Source mechanisms and dynamics of volcanic pyroclastic emissions : a perspective from Doppler radar (VOLDORAD) and other geophysical data

Sébastien Valade

N° d'Ordre : D.U. 2222

UNIVERSITE BLAISE PASCAL

U.F.R. Sciences et Technologies

ECOLE DOCTORALE DES SCIENCES FONDAMENTALES
N° 710

THESE

Présentée pour obtenir le grade de
DOCTEUR D'UNIVERSITE
Spécialité : Volcanologie

Par **Sébastien VALADE**
Master

Dynamique des émissions pyroclastiques et mécanismes à la source : approche couplée par radar Doppler (VOLDORAD) et autres signaux géophysiques

Source mechanisms and dynamics of volcanic pyroclastic emissions: a perspective from Doppler radar (VOLDORAD) and other geophysical data

Soutenue publiquement le 27 janvier 2012, devant la commission d'examen composée de:

Jean-François LENAT	LMV, Université Blaise Pascal (Fr)	Président du Jury
Maurizio RIPEPE	Università degli Studi di Firenze (It)	Rapporteur
William ROSE	Michigan Technological University (US)	Rapporteur
Philippe LESAGE	ISTerre, Université de Savoie (Fr)	Examinateur
Franck DONNADIEU	LMV, Université Blaise Pascal (Fr)	Directeur de thèse
Andrew HARRIS	LMV, Université Blaise Pascal (Fr)	Directeur de thèse

Remerciements

Il est rare qu'un travail soit le fruit d'une personne isolée, et il est certain que celui-ci n'aurait pu voir le jour sans l'intervention de nombreuses personnes, que je souhaite très vivement remercier à travers ces quelques mots. Et diable qu'il est difficile de trouver les bons !

En premier lieu, j'aimerais remercier aussi chaleureusement que sincèrement Franck Donnadieu, qui tout au long de cette aventure, m'a encadré, conseillé et épaulé. Merci d'avoir accompagné mes premiers pas dans ce monde de recherche, d'avoir toujours été à l'écoute, et de m'avoir toujours incité à prendre du recul dans les moments difficiles. Merci enfin, pour les nombreuses occasions que tu m'as données de partir en mission. Merci également à Andy Harris qui a co-encadré cette thèse, et qui m'a apporté de précieux conseils lors de la rédaction des articles notamment.

Je dois également un grand merci à tous les membres du jury, qui ont pris le temps à la fois d'évaluer mon travail, mais également d'effectuer le déplacement depuis leurs contrées parfois lointaines afin d'être présents à ma soutenance. Un chaleureux merci donc, à Philippe Lesage venu des contreforts Alpins de Savoie, à Maurizio Ripepe venu des terres toscanes outre-Alpes, ainsi qu'à William Rose venu des Grands Lacs d'outre-Atlantique. Un grand merci également à Jean-François Lénat, qui a accepté de présider ce jury, ainsi qu'à mes encadrants Franck et Andy.

Nombreux sont ceux qui à diverses occasions, m'ont apporté leur idées et leurs conseils, communiqué leurs envies et leurs passions, influençant ainsi mon parcours et mon travail. J'ai maintenant le plaisir de pouvoir les en remercier…

Sur les chemins menant à la thèse, je souhaite tout d'abord remercier Hervé Leyrit, qui m'a le premier donné l'envie (tenace!) de me lancer dans la volcanologie, accompagnant mes premiers pas sur l'Etna (à Milo avec la joyeuse clique d'Igaliens, dont Cloé, Agnès, Odon, Pix, Louis-Marie, …). Jérôme Lecointre ensuite, qui m'a donné l'occasion de visiter le Ruapehu et le Taranaki, affirmant ainsi mon envie de poursuivre dans cette voie. Christian Montenat enfin, pour l'érudit qu'il incarne et qui inspire, pour ces missions en Afghanistan qui font rêver…

Sur les chemins de la thèse, je veux remercier Philippe Lesage, dont le nom ne trompe pas: ton expertise sur les données sismiques, autant que ton approche sereine, rigoureuse et amicale m'ont souvent apporté lumières sur les obscures profondeurs de l'Arenal! Un grand merci également à tous les "ticos" qui m'ont chaleureusement accueilli au Costa Rica: Mauricio Mora en premier lieu, qui m'a permis de passer l'été 2008 dans ce fabuleux pays (dans le cadre du projet VOLUME) et qui m'a initié aux curieux signaux sismiques de l'Arenal, à Guillermo Alvarado, ainsi qu'à Carlos et "el gato" qui m'ont emmené sur les volcans Costa Ricains (en partageant le "gallo pinto" au petit matin, et en m'enseignant les mots qu'on ne trouve pas dans le dico!). Un grand merci également à toute la "familia Duran" qui m'a hébergé pendant ces 3 mois, ainsi qu'à mes colocs Fabien et Agathe, tous devenus de bons amis.
Merci également à Ben Van Wyk de Vries et Olivier Roche pour m'avoir donné l'occasion de rendre visite aux volcans Chiliens (dans le cadre du projet ECOS-Sud – CONYCIT) en décembre 2008 & janvier 2009. Un très grand merci à Denis Legrand avec qui j'ai eu beaucoup de plaisir à parcourir les flancs du Llaima et du Villarica pour y installer stations sismiques et panneaux solaires. La mission sur l'Arenal en janvier 2009 m'a permis de voir VOLDORAD en action, et me donne l'occasion de remercier d'autre personnes : Franck, Sévérine Moune & Carlos Ramirez, pour les bons / longs moments passés sur les flancs de l'Arenal à épier son activité sous son épais chapeau nuageux, mais également pour les "cervezas" autour desquelles nous avons eu l'occasion de trinquer le soir venu. Merci également à Annie pour son chaleureux accueil dans son petit havre paradisiaque sur les côtes Costa Ricaines.
Sur les flancs de l'Etna en juillet 2009, j'ai eu l'occasion de partager de bons moments avec les collègues de l'OPGC (Claude Hervier, Patrick Fréville et Franck bien sûr!) et de l'INGV (Michele Prestifilippo et autres!), pour y installer VOLDORAD 2B… merci! Parmi les membres de l'OPGC, je tiens également à renouveler mes remerciements envers Jacques Fournet-Fayard pour son aide tout au

long du Master 2R, au cours duquel j'ai été immergé au cœur de "CALPV l'infernal". Merci à tous ceux qui sont à l'origine de VOLDORAD, et en particulier Jacques Kornprobst, G. Dubosclard, R. Cordesses et l'ensemble des membres du SDT de l'OPGC.
Mes remerciements vont également aux "permanents" du LMV, avec qui j'ai eu le plaisir d'échanger dans les bureaux, couloirs, et/ou salle de convivialité: Jean Battaglia (pour ces discussions "sismiques"), Jean-Luc Froger (pour Ophélia) et tous les membres de l'équipe volcano (Jean-Luc LP, Karim K, Philippe L, Ben VWV, Olivier R, Jean-François L, Tim D, Thierry M, etc.), mais également Tahar H. (pour ces discussions jazzy et ces bières au Poco), Régis D, Oleir S, Estelle K, ainsi que Cécile S, Marie-Christine A, et Véronique G pour leur aide lors des départs en missions notamment, Thierry H. pour les pépins informatiques, Eliane, Marlène, etc. !

Mes remerciements se tournent à présents vers mes compagnons thésards du labo, et en premier lieu vers ceux avec qui j'ai partagé mon bureau pendant trois ans. Giacomo: "il padrino", d'un calme à toute épreuve, pour nous avoir initié au rituel ô combien plaisant du caffè corto après le repas. Julia: pour ton amitié, ton soutien, ta complicité, pour avoir partagé ces moments de douce folie et pour avoir supporté mes caprices! Aude: pour avoir enduré ces derniers mois avec nous dans le bureau, pour avoir toujours eu une oreille attentive et des mots encourageants. Mathieu: parce que tu as été pour moi aussi bien un collègue (cher!), fin connaisseur de VOLDORAD avec qui les discussions ont toujours été riches et constructives, qu'un ami, encourageant, rassurant, et inspirant, ô combien merci! J'espère que l'on aura encore longtemps le plaisir de partager caffè et mousses, de parler de musique, d'avions de chasses, et bien plus encore ! Aurélien, ah mon coquin! Depuis le master, ton amitié, ta curiosité, ta générosité, tes idées (petites et grandes!) m'ont toujours énormément aidé, et il est certain que sans toi cette thèse aurait une autre allure, merci beaucoup… Un grand merci à tous les autres, thésards, masters & post-docs, qui mériteraient tous un paragraphe mais que je devrai me contenter de lister par manque de place. Parmi "les anciens" avec qui j'ai partagé mes débuts au labo : Noël, Julien, Célia, Yann, Hanika, Fanny, Kim, Guillaume, Seb, Bickette, Anaïs, Daniel, Marco, Nico, Lydie, Sarah, Marion, Ahmed, Séverine, David,… Et parmi les plus "jeunes" : Oscar, Yannick, Baptiste, Amélie, Asmaa, Gabi, Ahmad, Angel, Gareth, Gaby, Greg, Wu, Deniz, Elodie, Pierre, Julien et bien sûr la Smooth Surge Crew et ses légendaires riders: Max, Camille, Manon, Nina, Gautier, Gaétan, …

Et puis parce qu'une thèse c'est aussi et surtout les moments forts partagés à l'appart (apéros, bouffes et emmerdes du quotidien), je me dois de faire une grande ovation aux collocations rendues magiques grâce à des colocs magiques: rue des Petits Gras d'abord, avec Julien (Dragoulle le rouquin!), Damien (le bad boy roux de l'appart!), Katie (ay up duck!), David (Dai the welsh!); puis rue du Port, avec Gab (le dit "observateur de volumes et volutes de fortune"!) & Julien (l'inclassable!). Merci à vous…

Enfin, chacun conviendra que le point d'orgue d'une thèse c'est bien le pot qui suit la soutenance. Une journée qui marque presque autant que trois années. Je souhaiterais donc remercier les personnes qui sont venus de loin pour partager ce moment avec moi : les Igaliens ô combien précieux (Odon, Christian, Audrey & Benoit), les Toulousains irremplaçables (Sylvain, Kevin), Alex & Marie-Jo ("tatie & tonton" d'El Paso!), Maria & Bruno (from Bourges!), les membres du groupe mythique Blue Gin (Perrine, Philippe, Yoann, Alex, qui m'ont d'ailleurs accueilli dans leur groupe pour mon plus grand bonheur), les Clermontois (Cyril, Sylvain, Medou, Julie, …), Gilles & Pascal (quasi présents!), etc. Et parmi la garde rapprochée, ceux qui ne pouvaient être là mais qui me soutiennent depuis longtemps: Elise, Romain, Cloé, Agnès (qui détient la palme de la meilleur excuse puisque même jour même heure tu faisais face à ton propre jury de thèse!), …

Mes derniers mots se dirigent vers ma famille. Papa, Maman, Xavier, Marion, pour ce somptueux pot d'abord, mais bien au-delà pour votre soutien, encore et toujours, milles fois merci…

Enfin et surtout, Laura ("oh honey pie")… Pour ton soutien, ton réconfort, ta présence, pour avoir supporté mes doutes, mes angoisses, et mes absences (croissantes à mesure que la fin approchait), enfin pour croire en moi plus que je n'y parviens, merci, merci, merci... Quel doux euphémisme !

Abstract

This study investigates the dynamics of explosive volcanic eruptions, from the sub-surface source mechanisms through to the emission dynamics and downwind dispersal of tephra. To this end, we use a ground-based Doppler radar (VOLDORAD) which informs on the loading / velocimetry of the expelled ejecta. Data are integrated with complementary geophysical techniques, and numerical models are developed to simulate pyroclastic emissions, generate synthetic radar data, and in turn enhance our understanding of the underlying dynamical processes. Arenal (Costa Rica) is used as a case study volcano, where frequent mildly-explosive eruptions commonly expel ash plumes and ballistic projections up to a few hundred meters above the vent. Firstly, we combine seismic and radar data to investigate the link between conduit processes and pyroclastic emissions. A conceptual model is proposed to account for their complex interplay, whereby fractures through a rigid lava cap control the system's degassing, which in turn governs both the seismic and radar signals (the latter depending on the ash load carried by the gas). Secondly, we investigate the dynamics of pyroclastic emissions from the analysis of Doppler radargrams. Time-velocity distribution of the expelled tephra shows the signature of two distinct phenomena. Numerical modeling and computation of synthetic radargrams show that these are consistent with both ballistic projections and ash plume crossing the beam simultaneously, whose respective mass load can be derived. Inverse modeling using a near-neighborhood Monte Carlo procedure was used to find synthetic Doppler radargrams which best matched the observed ones. The results give constrains on eruptive parameters, such as the size, trajectory, exit velocities and source gas velocities of the ballistics, as well as the speed / direction of the ash cloud drifted by trade winds. Lastly, because Doppler radars are powerful tool for real-time all-weather monitoring of volcanic activity, we address issues relative to the operational radar monitoring of ash plumes. In particular, the ability to remotely quantify the mass proportions of ejecta either falling on the slopes of the volcano or prone to be ejected into the atmosphere, gives source eruptive parameters which may feed volcanic ash dispersal models.

***Keywords**: explosive eruption, emission dynamics, Doppler radar, seismology, Arenal, numerical modeling*

Résumé

Cette étude traite de la dynamique des éruptions volcaniques explosives, depuis les mécanismes de sub-surface jusqu'aux processus d'émission et de dispersion des pyroclastes. A cet effet un radar Doppler sol est utilisé (VOLDORAD), lequel renseigne sur la charge / vitesse des ejectas. Les données sont intégrées avec d'autres techniques géophysiques, et des modèles numériques sont développés afin de simuler les émissions pyroclastiques, générer des signaux radar synthétiques, pour finalement améliorer notre compréhension des processus qui leurs sont sous-jacents. L'Arenal (Costa Rica) est utilisé comme volcan cible, où de fréquentes éruptions de faible magnitude émettent des panaches de cendres et des projections balistiques jusqu'à quelques centaines de mètres au-dessus de l'évent. Dans un premier temps, nous combinons des données sismiques et radar afin d'explorer la relation entre les processus de conduit et les émissions pyroclastiques. Leurs interactions complexes sont interprétées via un modèle conceptuel, lequel décrit les fractures parsemant le bouchon de lave comme responsables du dégazage du système, et en retour des signaux sismiques et radar collectés (ces derniers dépendants de la charge en cendres des émissions de gaz). Par ailleurs, nous investiguons la dynamique des émissions pyroclastiques à travers l'étude de radargrammes Doppler. La distribution spatio-temporelle de la vitesse des ejectas indique l'existence de deux phénomènes aux dynamiques distinctes. Des modélisations numériques permettant la reconstruction de signaux synthétiques indiquent qu'il s'agit de l'émission simultanée de blocs balistiques et de panaches de cendres. Une procédure d'inversion de type Monte Carlo couplée d'un algorithme d'optimisation permet de retrouver les radargrammes synthétiques qui reproduisent au mieux ceux observés. Les résultats apportent des contraintes sur divers paramètres éruptifs, tels que les tailles, trajectoires, vitesses des ejectas et des gaz, ainsi que la vitesse / direction de dispersion des panaches de cendres par le vent. Enfin, nous discutons du potentiel des radars Doppler appliqués à la surveillance opérationnelle des émissions volcaniques. En particulier, la possibilité de quantifier les masses éjectées dans l'atmosphère ou retombant sur les flancs du volcan, fournit des paramètres éruptifs à la source pouvant alimenter les modèles de dispersion de panaches de cendres.

***Mots clefs:** dynamisme éruptif, éruption explosive, radar Doppler, sismologie, Arenal, modélisation numérique*

CONTENTS

Introduction

One of the greatest challenges in volcanology is to understand the mechanisms operating within the volcanic edifice in order to better explain and forecast the resulting surface activity. However, understanding the underlying mechanisms that drive volcanic eruptions is particularly complex, as these involve a combination of processes which are commonly interdependent, and integrated over large spatial and temporal scales. Typically, these range from deeply rooted mechanisms (magma transport, bubble nucleation and coalescence, …), through to shallow conduit processes (gas exsolution, magma degassing, cristalization, viscous shear…) and near surface processes (magma fragmentation, cristalization, …), which ultimately result in a variety of volcanic phenomena (lava jet and fountains, ash plumes, …). Over the years a tremendous amount of studies have been carried out to gain insights into these processes, resulting is a wealth of data which includes field observations, geophysical and geochemical data, as well as laboratory analogue and numerical modeling.

The aim of this study is to investigate the explosive eruptive mechanisms driving the activity of persistently active volcanoes, where frequent small-scale transient eruptions are observed. More specifically, we intend to constrain both the shallow subsurface processes and the dynamics of the resulting pyroclastic emissions.

Bearing in mind the obvious hazards which arise with such investigation, remote sensing techniques turn out to be very powerful tools which enable quantitative measurements of volcanic phenomena. Using Arenal (Costa Rica) as a case study volcano, we combine various remote sensing tools to unravel the subsurface source mechanisms and dynamics of the subsequent pyroclastic emissions. In particular, we use a ground-based Doppler radar (VOLDORAD, Volcano Doppler Radar), which was specifically designed for the sounding of volcanic eruptive jets. The first studies carried out with this instrument investigated Strombolian-type eruptive activity recorded at Etna, providing for the first time *in-situ* measurements on both the kinetics (*Dubosclard et al.*, 1999, 2004; *Gouhier and Donnadieu* 2010, 2011) and the mass loading (*Gouhier and Donnadieu*, 2008) of eruptive lava jets. This study is the first to investigate more explosive Vulcanian-type mechanisms, with frequent emissions of small scale ash plumes. It involves data from three recording campaigns carried out at Arenal, in 2004, 2005 and 2009 respectively.

The first chapter of this manuscript is an introductory chapter which sets the background of the study. It gives a review of the existing remote sensing techniques devoted to the study of volcanic explosive activity, with particular emphasis made on the need for integration amongst them. It then describes Arenal volcano, its eruptive activity, and the geophysical studies which have been carried out so far. Lastly, it presents VOLDORAD, by giving some technical and theoretical elements needed to understand the study.

After this introductory chapter, the manuscript is composed of three parts, arranged in an order reflecting the sequence from *sub-surface* source mechanisms, to *surface* dynamics of pyroclastic emissions, through to *dispersal* of tephra emission downwind.

In the first part (Chapter II), we investigate the source conditions of pyroclastic emissions at Arenal, by cross-analysis of seismic and radar data (*Valade et al.*, 2012). We propose a conceptual model to account for their complex interplay, whereby fractures through a rigid lava cap control the system's degassing, which in turn governs both the seismic and radar signals (the latter depending on the ash load carried by the gas).

In the second part, which comprises Chapters III, IV and V, we focus on the dynamics of pyroclastic emissions as seen by Doppler radar.

- Chapter III presents the development of a new tool, entitled Doppler radargram, which enables a synoptic visualization of the information held in the Doppler radar data (namely the velocimetry and mass loading evolution of ejecta through time and space). In particular, we find that this reveals distinct dynamics, which imprint on Doppler radargrams with distinctive Doppler signatures that betray distinct eruptive dynamics. We show that these are attributed to the simultaneous projection of both ballistic particles and ash plume (*Valade and Donnadieu*, 2011).
- Chapter IV is devoted to the numerical modeling of both ballistic projections and ash plumes crossing the radar beam, and to the simulation of the resulting radar signal. We carry out parametric tests to understand what factors control for the most part the Doppler signatures, and how the Doppler radargram of eruptive events can be interpreted to withdraw information on the eruptive dynamics.
- Chapter V presents the application of inversion modeling procedures, to search for the model input parameters which are best able to reproduce the observed Doppler radargrams.

The third and last part (Chapter VI) is dedicated to the real-time monitoring and tracking of ash clouds, from vent to downwind dispersal. The chapter is threefold:

- we first simulate ash plume transit paths through the radar beam using geometrical shape to retrieve the 3D transport vector of wind-drifted ash plumes (*Donnadieu, Valade & Moune, 2011*),
- we then discuss the recent permanent installation of VOLDORAD 2B on the flanks of Mt. Etna, and address the challenges / potential set of parameters that can be used to provide real-time notifications on tephra emissions (*Donnadieu et al.*, in prep),
- we finally highlight how the integration of ground-based (in particular Doppler radar, infrared cameras) and satellite-based sensors can act as a powerful observational suite of tools (*Gouhier et al.*, 2011).

Chapter I

Background

I.1. Monitoring eruptive dynamics and products from source to dispersal: *a review of remote sensing techniques*

Remote sensing, expressed in the simplest terms, refers to the acquisition of information concerning an object or phenomenon without making physical contact with it. Its application and usefulness in volcanology is particularly manifest, as the objects and phenomena of interest may be extremely hazardous. In turn, there has been an increasing use of remote sensing systems to monitor volcanic activity (*McNutt et al., 2000*; *Mouginis-Mark et al.*, 2000; *Sparks*, 2003).

The basis for remote monitoring is that the examined object emits or reflects a mechanical or electromagnetic radiation, which can in turn be recorded by remote sensors. Passive sensors, will detect natural radiation emitted or reflected by the object (e.g. sunlight reflected and imprinted on a sensitive surface, such as Niépce's 1826 "heliography", known as the world's first photography, *Marignier*, 1999). On the other hand, active sensors will emit their own energy, and measure the radiation that is scattered by the target back to the sensor (e.g. Huelsmeyer's 1904 "telemobiloscope", which later became known as RADAR – RAdio Detection And Ranging – technology). Nowadays, a wide range of both active and passive remote sensing techniques exists to examine and monitor volcanic systems. These can record both mechanical and electromagnetic waves, spanning various spatial coverage (i.e. recorded area), spectral coverage (i.e. recorded frequency band), and time coverage (i.e. frequency of record), depending on the sensor's position (i.e. ground-based, air-borne or satellite based) and the target of interest (i.e. subsurface source processes, surface emissions processes, and distal dispersion processes).

We hereafter focus on the techniques which investigate the dynamics of an explosive eruption, from the source mechanisms operating within the shallow system, to the emission products / dynamics at the vent, and finally to the long-range dispersal and deposition of the eruptive products (Figure I.1). Reviewing the entire set of instruments and literature available would be a mammoth task. Instead, we point out the most significant techniques used, and particularly emphasize on those which lend themselves to ease of integration. In doing so, our aim is to show how the synergy of multiple techniques can provide the most complete possible view of the explosive eruptive processes, and how they can provide complementary

data to feed the Volcanic Ash Transport and Dispersion (VATD) models with the vital source parameters they require.

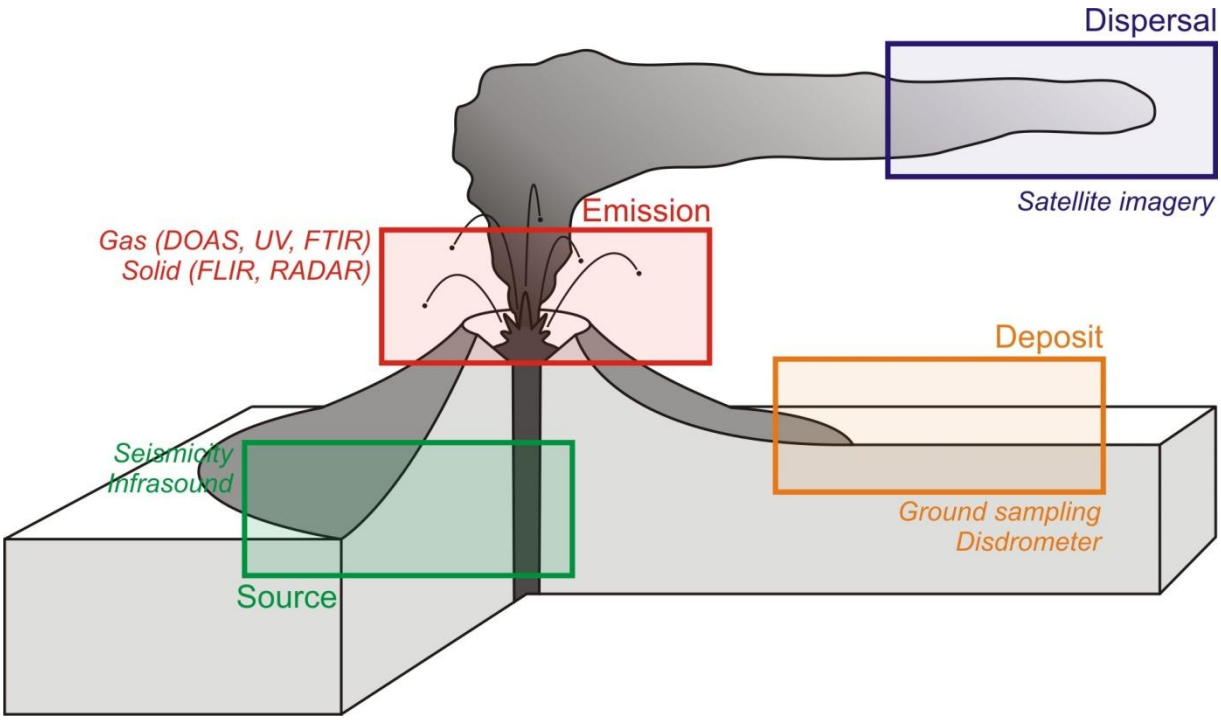

Figure I.1. Integration of remote sensing techniques to monitor the eruptive process from subsurface source mechanisms, to the emission, dispersal and deposition of the explosion products. The displayed techniques are reviewed below.

I.1.1. Monitoring the emission source mechanisms

Volcano seismology: insights into the hidden subsurface processes

Eruptive activity presupposes mass transfer from the earth's interior to its surface. This transfer is nearly always associated to seismicity, originating from the interaction between the fluid magma and the solid host rock (e.g. *Benoit and McNutt*, 1996). For this reason, volcano seismology has become one of the most useful and most widely used discipline to monitor and forecast eruptive activity (e.g. *Chouet*, 1996; *McNutt et al.*, 2000; *McNutt*, 2002). Volcano seismology studies have in turn overwhelmed the literature, using seismic data for a variety of purposes. The recognition of different types of earthquakes has been a key development in volcano seismology, which helped clarify what can be learned on the volcanic processes operating within the edifice. In turn, the classical volcano earthquake classifications (commonly based on the spectral signature of the signals, i.e. frequency content), can be read in terms of source processes which are thought to be predominant for each event type (*Johnson et al.*, 2009). Volcano-tectonic (VT) earthquakes for instance, are short-period (SP)

events (a.k.a. high-frequency (HF) events, >1 Hz to 50 Hz), attributed to brittle failure of rocks. Typically, as the ascending magma makes its way to the surface and fractures the surrounding rock, it generates numerous small-magnitude volcano-tectonic earthquakes which can image the magma migration (e.g. *Toda et al*, 2002; *Battaglia et al.*, 2005). On the other hand, long period (LP, 5 s to 1 s) events are commonly attributed to fluid flow within the volcano's plumbing system, which would induce seismogenic conduit oscillations (*Chouet*, 1996) or pore fluid decompression (laboratory analogue simulations, *Benson et al.*, 2008). Tremor signal is thought to be closely related to this mechanism. Although there has been a profusion of models to explain its origin, most agree that it likely involves complex interaction of magmatic fluids with the surrounding bedrock (see *Konstantinos and Schlindwein*, 2002 for a review). Explosion earthquakes have a spectral signature very close to that of LP events (*Hagerty et al.*, 2000), except that they display a higher frequency component which is attributed to an air phase (*Ripepe and Braun*, 1994). In turn, both LP and explosion quake signals are thought to have the same source mechanism (*Lesage et al.*, 2006), yet with differing source depth (*Mori et al.*, 1989): explosion quakes would occur at shallow levels within the conduit, allowing the propagation of an acoustic air wave which later couples to the ground as a high frequency seismic phase, whereas the LP events would occur at deeper level, impeding the propagation of the acoustic phase. Volcano infrasounds can provide an additional constrain to distinguish between the two (e.g. *Ruiz et al.*, 2006). At longer periods, broadband seismometers can detect very long period (VLP, 5 to 30 s) and ultra-long-period (ULP, 30 to 600 s) events, which are believed to be associated with long-duration source movement lasting several tens of seconds (e.g. *Neuberg et al.*, 1994; *Kawakatsu et al.*, 2000; *Sanderson et al.*, 2010).

During an eruptive event, the recorded seismic waves usually result from a complex superimposition of several physical processes (e.g. composite events, *Johnson et al.*, 2009). These are likely interdependent, and can include: (i) magma transfer within the plumbing system, inducing fragile rupture in the surrounding rocks (VT) and resonance with the channel walls (LP, tremor), (ii) surface degassing (high frequency jetting), with cycles of pressurization-depressurization associated with volumetric change (VLP, LP), (iii) fragmentation and expulsion of molten and brittle magma (LP, SP), (iv) induced rock falls (high frequency emergent waves), edifice inflation/deflation (VLP, ULP).

Seismic data thus appears as an immensely resourceful tool to shed a light on the processes operating within the edifice. The information however, is often so rich that it needs to be coupled with sister disciplines, such as infrasonic studies.

Volcano infrasounds: insights into the processes at the magma-air interface

Exploding volcanoes commonly produce acoustic air waves, ranging from audible frequencies (> 20 Hz) to infrasonic frequencies (< 20 Hz), inaudible to the human ear. These waves are in fact atmospheric pressure oscillations, which can be recorded by means of analog microbarometers or modern digital pressure transducers. The earliest volcano infrasound study was performed in the mid-1950s following Bezymianny's 1955 eruption (*Gorshkov,* 1959), and since then, the number of studies utilizing infrasounds has increased exponentially (see review by *Johnson and Ripepe,* 2011). Many have intended to understand the physical source mechanisms responsible for the generation of these infrasounds: at basaltic systems, they have constrained the gas bubble properties, ascent dynamics, and associated conduit phenomena (e.g. *Vergniolle and Brandeis,* 1994; *Vergniolle et al.,* 1996, 2004; *Ripepe and Gordeev,* 1999; *Ripepe et al.,* 1996; *Rowe et al.,* 2000; *Bouche et al.,* 2010), whereas at more silicic systems, they have outlined gas releases from dome fractures (*Yamasato,* 1998), dome uplift and vent inflation (*Yokoo et al.,* 2009; *Johnson and Lees,* 2010; *Yokoo and Iguchi,* 2010). In addition, they have been able to locate infrasound sources (e.g. *Ripepe and Marchetti,* 2002; *Johnson,* 2005; *Ripepe et al.,* 2004), quantify the gas outflux (e.g. *Johnson,* 2003), and constrain the explosion kinetic energy (e.g. *Gorshkov,* 1959; *Mauk,* 1983). On the other hand, theoretical formulation of the propagation of acoustic waves (e.g. *Garces,* 1997; 2000; *Garces and McNutt,* 1997) and experimental measurements of acoustic emissions (*Divoux et al.,* 2008) have provided complementary material to understand volcanic infrasounds. *Divoux et al.,* 2008 in particular, emphasized that the frequency of the signal gives a direct access to the bubble length. However, measuring the acoustic energy is not enough for obtaining a good estimate of the total energy release and any attempt to interpret the amplitude and energy of the acoustic signal would surely lead to strong misinterpretation.

Because both seismic and acoustic waves are mechanical waves, often generated by the same physical phenomena, the two disciplines should be conceived as sister disciplines (if not as a unique "seismoacoustic" discipline, e.g. *Arrowsmith et al.,* 2010). For this reason, a large number of studies have cross-correlated seismic and infrasonic data (see *Harris and Ripepe,* 2007 for a complete list referencing the studies up until 2005).

In summary, seismic and infrasonic data are able to provide insights into both the hidden subsurface processes and the magma-air interface processes. However, neither inform on the end emission products and dynamics, which call for another set of remote sensing techniques.

I.1.2. Monitoring the emission products and dynamics

I.1.2.1. Volcanic gaseous emissions

SO_2 emissions: COSPEC, DOAS and UV cameras

SO_2 emissions have become widely monitored on active volcanoes, as changes in SO_2 emissions can foresee changes in the volcanic system, and in turn foreshadow changes in the eruptive activity (e.g. *Malinconico*, 1987; *Daag et al.*, 1996; *Gardner and White*, 2002; *Edmonds et al.*, 2003). In particular, SO_2 flux can be considered as a proxy for magma flux, provided that there is complete exsolution of gas and lossless transport to the point of measurement (*Mori and Burton*, 2006). In turn, several authors have found correlation between SO_2 fluxes and volcanic tremor amplitude (e.g. *Leonardi et al.*, 2000; *Nadeau et al.*, 2000). Because of SO_2's low atmospheric concentrations and high abundance in volcanic plumes (*Andres and Rose*, 1995 and *Symonds et al.*, 1994, respectively), it appears as relatively easy specie to track remotely. Taking advantage of its selective absorption of UV light (*Moffat and Millan*, 1971; *Millan et al.*, 1976; *Platt*, 1994), a number of portable instruments have been developed since the early 1970s to measure volcanic SO_2 emissions. Correlation spectrometers (COSPEC, *Stoiber et al.*, 1983), and later compact UV spectrometers (e.g. *Galle et al.*, 2003), still remain the most widely used instruments by the volcanological community. UV spectrometers are better known as DOAS instruments, which in fact refer to the retrieval technique employed (Differential Optical Absorption Spectroscopy). Both COSPEC and DOAS however, scan transects of the volcanic plume, and recover SO_2 fluxes from wind speed calculations. Due to both the errors in wind speed estimations and the instrument small field of view, these instruments can suffer severe shortcomings if the measurements do not involve multiple instruments (e.g. *McGonigle et al.*, 2005; *Williams-Jones et al.*, 2006). More recently, UV cameras were developed to image SO_2 emissions (*Mori and Burton*, 2006; *Bluth et al.*, 2007), capturing large spatial extents in a single image. These are able to map quantitatively the spatial variations of SO_2 contents within volcanic plumes at unprecedented frequencies (2 Hz) and accuracy, heralding a breakthrough in our ability to monitor SO_2 emissions. In particular, SO_2 fluxes measured by UV cameras have shown to decrease prior to ash bearing eruptions at Sakurajima volcano (*Kazahaya et al.*, 2010), suggesting that sealing processes were operating between each eruption. Moreover, because UV absorbance by ash overwhelms that of SO_2, ash mass estimates and ash mass distributions within volcanic plumes can also be derived with UV

cameras (*Yamamoto et al.*, 2008). Henceforth depending on the optical thickness of the plume, the instrument will be able to retrieve information on either its SO_2 content or its tephra load.

Other gaseous species: FTIR

The Fourier Transform Infrared (FTIR) gas spectroscopy, which much like the COSPEC and DOAS techniques described previously, uses the spectral absorption lines from an infrared radiation source (magma, sun, or artificial source) to determine the identity of magmatic gas molecules (see *Opphenheimer et al.*, 1998 for review of the technique's early years). The significant advantage of FTIR methods however, is its ability to detect and measure relative abundances of several gases, including SO_2, HCl, HF, CO_2, CO, CH_4, SiF_4, N_2O and OCS). Because some species are present both in volcanic emissions and in air, atmospheric corrections need to be applied. Once combined with SO_2 fluxes inferred from DOAS measurements, fluxes of all species can then be determined. FTIR spectroscopy has successfully been applied to the analysis of volcanic fumaroles (*Mori et al.*, 1995), plumes (*Francis et al.*, 1998; *Burton et al.*, 2000; *Burton et al.*, 2003), and lava fountain (*Allard et al.*, 2005), shedding light onto their chemical gaseous composition, subsequent residence conditions of the deep magmatic sources, and exsolution depths of magmatic gases.

I.1.2.2. Volcanic pyroclastic emissions

Visible and thermal cameras: imaging of volcanic emissions

Visible and near-infrared photography / video analysis of surface volcanic activity, have proven to be to be an important tool to image the dynamics of pyroclastic emissions (e.g. *Chouet et al.*, 1974; *McGetchin et al.*, 1974; *Blackburn et al.*, 1976; *Sparks and Wilson*, 1982; *Ripepe et al.*, 1993; *Formenti et al.*, 2003). These however, in addition to the heavy tedious work they represent, preclude the simultaneous observation of both the small incandescent ballistic particles and the large buoyant ash plumes. Indeed, incandescent particles will be visible at night but the rapidly cooled ash particles forming the plume won't, whereas during daylight the ash plume is easier to see than individual blocks. Recently, thermal cameras (e.g. FLIR systems, Forward Looking InfraRed) have managed to overcome these shortcomings by operating in the infrared spectral bandwidth (7.5 - 13 μm) at high acquisition rate (30 Hz) (e.g. *Patrick et al.*, 2007). Most notably, they have provided insights into the dynamics of mild Strombolian eruption and the subsequent plume rise dynamics (*Patrick et al.*, 2007; *Patrick,*

2007). Also, they have enabled the imaging of the thermal and morphological structure of an active lava dome (*Sahetapy-Engel and Harris*, 2009).

Recently, a new imaging camera has been developed to detect and quantify ash (*Prata and Bernardo*, 2009). It uses the same concepts that are applied to satellite infrared measurements of volcanic ash plumes (*Prata*, 1989; *Prata and Barton*, 1993), which spectrally filter infrared radiations to discriminate volcanic ash from meteorological clouds. In turn, the camera enables retrievals of mass, particle radius and optical depth of ash eruption columns. The interaction between such instruments and ground-based Doppler radars (e.g. VOLDORAD) is likely to be very promising, as the two techniques can provide mutual feedbacks to constrain / calibrate their respective datasets (see further discussions in section VI.4.3). Note that a list of ground-based thermal deployments carried up until 2005 can be found in *Harris and Ripepe* (2007), and an exhaustive review of the information which can be retrieved from thermal imagery can be found in *Spampinato et al.* (2011).

However, using video imagery to study eruptive dynamics over long time periods will be very tiresome if not coupled with automated tracking algorithms (e.g. section VI.4.2). Moreover, the technique can image the eruptive dyamics but cannot retrieve *in situ* quantitative eruptive parameters in real time, such as the ejection velocity, mass load, etc. Last but not least, the technique will become totally inefficient under harsh, rainy weather. In turn, radar instruments appear particularly useful to overcome these shortcomings.

RADAR: quantitative monitoring of volcanic emissions

RADARs (Radio Detection And Ranging) are active remote sensing systems, which by contrast to passive remote sensing systems described previously, operate by radiating their own electromagnetic source, with wavelengths being millimetric to pluri-decimetric (mm, Ka, K, Ku, X, C, S or L-band), Figure I.2. Particles which intersect the radar beam scatter the electromagnetic radiation, part of it is scattered back to the radar which in turn records it. The backscattered signal is proportional to the number and size of the particles and therefore holds information on the mass (flux) of tephra. Moreover, because most radar systems use Doppler shift-based techniques, these are able to measure the moving targets' along-beam velocity.

The development of radar systems was first motivated by its potential military use during the first half of the 20th century, and was then rapidly employed for meteorological purposes during the second half. Stationary weather radars have been used opportunistically since the late 1970s to track large volcanic eruptive clouds, but it was only during the late 1990s that

transportable radars were developed with the primary goal of studying eruption dynamics. We hereafter give an overview of both weather radars and volcanological radars, which have been applied to the study of volcanic emissions.

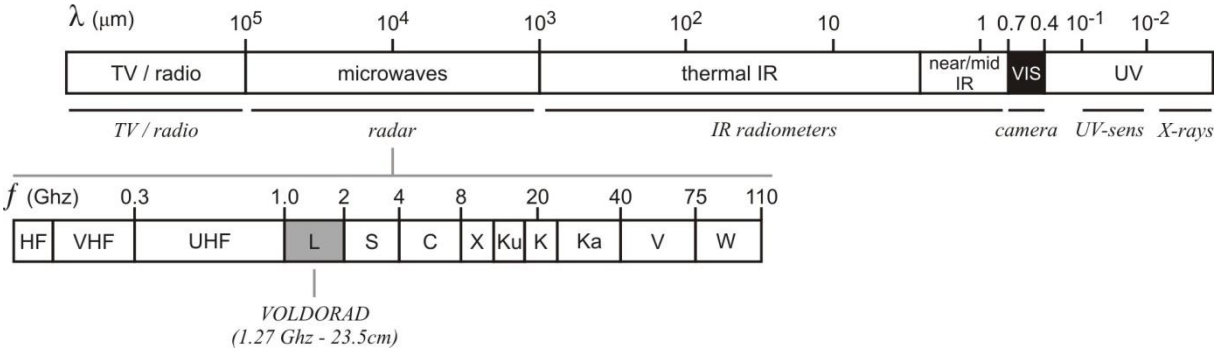

Figure I.2. Electromagnetic spectrum showing the spectral bands of most common radars (IEEE, Institute of Electrical and Electronics Engineers). Weather radars usually utilized for volcanic applications operate at wavelengths ranging typically from 1 – 8 cm (K, X, C, or S-band). VOLDORAD system operates at the wavelength of 23.5 cm (L-band).

Weather radars

One of the first volcanological use of radar, was that described by *Kienle and Shaw* (1979), who determined the width and heights of eruption clouds from Augustine volcano using Alaskan military radars. Shortly after, the Mt St. Helens eruptions of 1981 and 1982 emitted ash plumes which were monitored with U.S. weather radar (*Harris et al.*, 1981; *Harris and Rose*, 1983). Since then, a number of other volcanoes have been monitored with similar instruments: Mount Spurr (*Rose et al.*, 1995), Hekla (*Lacasse et al.*, 2004), Grímsvön (*Marzano et al.*, 2006, 2010a), Augustine (*Marzano et al.*, 2010b), or Eyjafjöll (*Marzano et al.*, 2011). The scanned reflectivity maps of these weather radar have been able to image the dispersal of the plume, and provide quantitative data on its spatial extent, height, and mass load, all vital information for international aviation routes which are endangered by eruption clouds. However because of their fixed position, the distance between the observing point and the eruption site may be quite large (< 500 km). In turn, weather radar will only be able to detect large plumes, and will generally detect only the uppermost portion of the cloud. The need to monitor smaller scale eruptive processes directly above the emission vent, has triggered the development of smaller transportable devices, specifically designed to monitor explosive volcanic activity.

Volcanological radars

During the mid-1990s, portable Doppler radar systems were constructed to be emplaced on volcano flanks and probe the region directly above the vent with a high spatial and temporal resolution. Two systems have been developed in parallel: a Frequency-Modulated Continuous Wave system (FMCW) operating in the K-band (commercial MVR, see *Hort and Seyfried*, 1998 for its first use), and a pulsed system operating in the L-band (VOLDORAD, designed at OPGC, see *Dubosclard et al.*, 1999 for its first use). VOLDORAD is the Doppler radar which has been used in this study; see section I.2 for further technical details. While the FMCW system offers an appreciable ease of transportability, its narrow field of view (1-3° beam width) precludes a synoptic view of the eruption, and its small wavelength (1.24 cm) may induce difficulties in the detection of ash under harsh rain condition (see *Vöge et al.*, 2005 for a comprehensive comparison between the two instruments). Nevertheless, over the past 10 years the two instruments have successfully monitored a variety of volcanoes, providing powerful insights into the eruptive dynamics of several eruption styles.

The MVR system has been used to investigate dome instabilities (Merapi, *Hort et al.*, 2006; *Voge and Hort*, 2008, 2009; *Voge et al.*, 2008), lava bubble outbursts by measuring explosion velocities at Stromboli and Erebus (*Urbanski et al.*, 2002; *Hort et al.*, 2003; *Scharff et al.*, 2008; *Gerst et al.*, 2006), retrieve 3D explosion velocity vector (*Hort et al.*, 2001, 2003; *Gerst et al.*, 2008; *Gerst*, 2010), and monitor eruptive dynamics and vent inflation prior to eruption at Santiaguito (*Hort et al.*, 2010; *Scharff et al.*, in press). On the other hand, VOLDORAD has provided valuable insights into Strombolian emissions at Etna (*Dubosclard et al.*, 1999, 2004; *Donnadieu et al.*, 2003; *Gouhier and Donnadieu*, 2010), enabled the systematic retrieval of ejecta velocities (*Gouhier and Donnadieu*, 2011), and has made possible the estimation of the mass loading of strombolian explosion using an inversion algorithm developed by *Gouhier and Donadieu* (2008). Moreover, insights into ash cloud dynamics at Arenal volcano were given (*Donnadieu et al.*, 2005; *Mora et al.*, 2009; *Donnadieu et al.*, 2011; *Valade and Donnadieu*, 2011), as well as constraints on the source eruptive mechanism throughout a cross-correlation of radar and seismic data (*Valade et al.*, 2012). A review of the recordings obtained with VOLDORAD in various types of volcanic activity (i.e. Strombolian and Vulcanian), observed at several volcanoes (i.e. Etna, Popocatepetl, Arenal and Yasur), can be found in *Donnadieu* (2012).

I.1.3. Monitoring the emission dispersal

Satellite sensors: dispersal and properties of the volcanic plumes

Tracking the properties and the dispersal of volcanic emissions over long distances require instruments with very large spatial coverage, which satellites only are capable of providing. Satellite-based remote sensing systems have been abundantly used for volcanic applications, with concepts very similar (if not identical) to the ground-based techniques described previously. Bearing in mind the profusion of these systems, we just aim at giving some key examples of satellite-based studies concerning emissions of volcanic products in the atmosphere (hence excluding ground thermal hotspots such as lava flows). Indeed, the satellite-based sensors currently used to monitor volcanic emissions span a large range of wavelengths (UV, IR and Microwave), with a variety of spatial (m to km) and temporal (minutes to days) resolutions depending on the object of interest (see *Francis and Rothery*, 2000; *Ramsey and Flynn*, 2004, and *Thomas and Watson*, 2009 for reviews). Infrared systems mainly focus on the discrimination of volcanic ash from non-volcanic atmospheric clouds (e.g. *Prata*, 1989), the retrieval of ash radius and mass loading (e.g. *Wen and Rose*, 1994), or the plume height altitude (e.g. *Glaze et al.*, 1989). Ultraviolet systems on the other hand, are more commonly devoted to volcanic SO_2 retrieval (e.g. *Bluth et al.*, 1994; *Gouhier and Coppola*, 2010). Lidar sensors finally, have the ability to retrieve information along plume vertical profiles: particle sizes, aerosol types, plume height and thickness (*Carn et al.*, 2008), and more recently, ash mass load (*Chazette et al.*, 2012).

HVOS (*HotVolc Observing System*), recently developed at OPGC (*Observatoire de Physique du Globe de Clermont-Ferrand*), is dedicated to the real-time acquisition and processing of geostationary satellite data (e.g. METEOSAT). It provides via a web base interface real-time quantitative data on ground thermal anomalies, as well as volcanic emissions such as SO_2 and ash (*Labazuy et al.*, in press).

I.1.4. Monitoring the emission deposits

Tephra ground-sampling: insights into fragmentation mechanisms

Textural and chemical analysis of eruptive pyroclasts collected in the viscinity of the eruptive vent, may provide substantial information on conduit processes, magma storage, ascent and fragmentation mechanisms (e.g. *Lautze and Houghton*, 2007). Although this discipline is not a remote sensing one, we believe it is important to mention it, as the approach can be coupled

with geophysical data to give insights into explosion processes. In particular, textural / chemical data from ejecta at Villarica volcano have been combined with thermal, seismic, and infrasonic data (*Gurioli et al.*, 2008). The combination of techniques have shed a light onto the shallow conduit dynamics at this basaltic center, which appears tapped by a largely degassed column through which fresh batches of magma occasionally rise and burst at the surface. When the tephra is transported within an ash plume, the tephra deposit can be mapped, and can be used to infer the dynamics, intensity, plume height (*Burden et al.*, 2011) and erupted mass of past eruptions (e.g. *Eychenne et al.*, 2011).

Disdrometer-like instruments: access the particle size distribution of falling tephra

The traditional ground sampling of tephra described above cannot provide real-time information on the eruptive event. However, characterizing the particle size distribution of the erupted material is of first order importance to forecast its spatial dispersion in the atmosphere (see section I.1.6). An effective approach to constrain the particle size distribution of falling tephra, is the use of disdrometers (e.g. Pludix, *Scollo et al.*, 2005). These instruments analyze the settling velocities of falling tephra, from which they infer their size and number to rapidly reconstruct a particle size distribution. Coupled with satellite data which recovers the fine portion of the distribution (e.g. *Wen and Rose*, 1994), a complete particle size distribution may be constructed (e.g. *Bonnadonna et al.*, 2011).

I.1.5. The need for multidisciplinary efforts

I.1.5.1. Need for integration of observational data sets

The above review gives a flavor of the remote sensing techniques applied to the monitoring of eruptive processes and products. Although not exhaustive, it gives a cheering idea of the pieces of information each technique provides, and yet gives a concurrent frightening idea of the amount of underlying data. Indeed, although when taken individually each technique highlights a specific part of the "global picture", it is also apparent that application of any single analysis can never fully constrain the volcanic system in its whole. As emphasized by *Harris and Ripepe* (2007), "*the most effective approach to understanding the dynamics of an explosive volcanic eruption and the structure of the feeder system that drives it, is through synergy of multiple data sets, each data set providing different pieces of information about the physical processes that drive the activity*". Henceforth in parallel to the tremendous advances

in the monitoring techniques and the data acquisition / analysis capabilities, an increasing effort is needed for data integration and assimilation (e.g. *McNutt et al.*, 2000; *Sparks*, 2003).

Multi-parametric monitoring has proved to be successful to forecast large eruptions. The eruption of Mount Pinatubo in 1991 for instance, was monitored using a large set of techniques (e.g. the Integrated Mobile Volcano Monitoring System developed by the USGS), which led to a timely evacuation of several thousands of people (*Punongbayan et al.*, 1996). A few years later, the Soufrière Hills eruption (Montserrat) further demonstrated the advantages of integrated data, and led to an interpretation of cyclic pressurization of magma in the upper conduit (*Voight et al.*, 1999). The cross-correlation of techniques to monitor smaller eruptive events however, is perhaps even more challenging. Synergy between seismic and infrasonic records is now a long-established exercise, which *Harris and Ripepe* (2007) have traced up to 1959 with the work on Gorshov on Bezymianny volcano (*Gorshkov*, 1959). Only recently has a third discipline mingled with the working pair, with the add-in of thermal infrared data at Stromboli in 1999 (*Ripepe et al.*, 2001, 2002). Since then, an increasing number of studies have cross-correlated various data sets at a variety of volcanoes.

I.1.5.2. Need for interaction between observational data and modeling

"*Modern physical volcanology is situated between two different research approaches: multi-disciplinary data acquisition in field and laboratory settings, and analytical and computer-based multi-parameter modelling*", *Neuberg* (2006). The above comment outlines the counterpart to the multi-parametric integration praised previously: the need to have the observational data sets interact with models (analogical, theoretical, or numerical).
Indeed, enhanced understanding of the collected data sets and underlying dynamical processes requires feedbacks between observed and modeled data (e.g. report on the IAVCEI workshop on explosive volcanism by *Donnadieu et al.*, 2009). In other words, the observational data should be put in perspective with numerical models that (i) simulate the studied phenomena, and (ii) generate synthetic signals similar to the collected data.

The study presented here attempts to apply both approaches expressed in Neuberg's comment: carry out a multi-disciplinary correlation of geophysical data (mainly seismic and Doppler radar, *Valade et al.*, 2012), and develop numerical models to reproduce the observed data set (*Valade and Donnadieu*, 2011; *Valade et al.*, in prep).

I.1.6. **Volcanic ash threat to aviation:** a need for assessment of source eruptive parameters

The threat volcanic ash represents to both human health and aviation safety is a well-known issue, which has now been addressed for several decades (e.g. *Miller and Casadevall*, 2000; *Baxter*, 1999; *Gudmundsson*, 2011). Following aviation incidents in the beginning 1980s, and in conjunction with the speedy and sustained growth in air traffic, the International Civil Aviation Organization (ICAO) created the International Airways Volcano Watch (IAVW), which in turn established nine Volcanic Ash Advisory Centers (VAACs) around the world to issue specialized advisories to the aviation community concerning ash threats. Various Volcanic Ash Transport and Dispersion (VATD) models have been developed, and are currently being used by VAACs to forecast the downstream location, concentration, and fallout of volcanic particles (e.g. *Stohl et al.*, 2010). These often account for complex microphysical processes describing the plume evolution through time and space, but require input parameters which describe the volcanic activity and products near the emission source. Unfortunately, the accurate assessment of such source terms remains extremely difficult, and thus constitutes one of the largest uncertainties in the model predictions (errors may reach 1 order of magnitude, thus dramatically undermine the prediction of ash dispersal, e.g. *Kaminski et al.*, 2011) .

The recent 2010 eruption of Eyjafjoll volcano, Iceland, provides the most compelling illustration of this issue. As the ash plume drifted southward towards the European air space, the VAACs were asked to use VATD models to forecast the ash propagation downwind over hours to days, and thus assess the potential hazards to aircrafts. Due to both the lack of detailed source parameters (i.e. eruptive mass flux, particle size distribution, plume height), and the pre-existing safety limits of ash concentration in the atmosphere, the event caused an unprecedented closure of the European air space. It thus appears that improving our ability to assess quantitatively source eruptive parameters, and in turn feed VATD models with realistic inputs, is a fundamental and challenging objective for hazard mitigation.

In the late 1990s, the IAVW highlighted the need for more accurate source parameters to improve the VATD model accuracy. In 2007, the *Eruption Source Parameters Workgroup* convened to provide an assessment of the key source parameters, the way they may interact, and the average values which can be expected at a number of active volcanoes worldwide (*Mastin et al.*, 2009). The highlighted parameters were: (i) the plume height, (ii) the mass

eruption rate, (iii) the eruption duration, and (iv) the mass fraction of fine particles (≤ 63 μm). In 2010, a post-crisis analysis of the Eyjafjoll eruption led in conjunction between the remote sensing, modeling, and VAAC communities (*Zehner*, 2010), concluded that these same parameters lacked both in precision and in real-time acquisition, and that they were responsible for the large discrepancies in the model outputs. In particular, they emphasize that "*the experience […] demonstrates that there is a substantial lack of combining sophisticated transport models with the wealth of new earth observation data for improved eruption plume predictions*".

This study offers the possibility to assess how portable ground-based Doppler radars can contribute to the retrieval of some of the key source parameters required, more specifically: the eruption duration, the mass eruption rate, and the mass fraction of the fine particles prone to be ejected in the atmosphere (*Valade and Donnadieu*, 2011; *Donnadieu et al.*, in prep.).

I.2. VOLDORAD: Volcano Doppler Radar

VOLDORAD, literally Volcano DOppler RADar, is a ground-based pulsed Doppler radar, specifically designed by the *Observatoire Physique du Globe de Clermont-Ferrand* (OPGC, France) for active remote sensing of volcanic eruption jets and plumes. As of now, three versions of the radar exist: (1) the prototype VOLDORAD 1 was used for the first time at Etna in 1998 (*Dubosclard et al.*, 1999, 2004); (2) an improved, more compact and modular version (VOLDORAD 2) was utilized in 6 campaigns at Etna, Arenal, Popocatépetl and Yasur (*Donnadieu et al.*, 2003, 2005, 2009), and a clone of this radar now permanently monitors Etna's summit craters (VOLDORAD 2B) in the frame of a research agreement between OPGC and INGV (see VOLDORAD web site for details[1]). Because it has been extensively used during this study, we hereafter detail the main technical characteristics of VOLDORAD 2, and consider the fundamental data acquisition and processing techniques.

I.2.1. Technical characteristics

The VOLDORAD 2 system comprises (Figure I.3): 1- a 60*60*60 cm unit managing the generation, transmission, reception of the electromagnetic waves and signal pre-processing, 2- a directional antenna system (adjustable in site and azimuth) linked to the radar via a switch box (transmission-reception switch and pre-amplifiers), 3- a control PC on which the radar echoes are visualized/recorded in real time, and 4- a 1500W electric generator supplying power to the whole system (200 W consumption in average). The complete system can be transported in a four-wheel-drive vehicle, and set up near an eruptive vent.

[1] VOLDORAD web site: http://wwwobs.univ-bpclermont.fr/SO/televolc/voldorad/

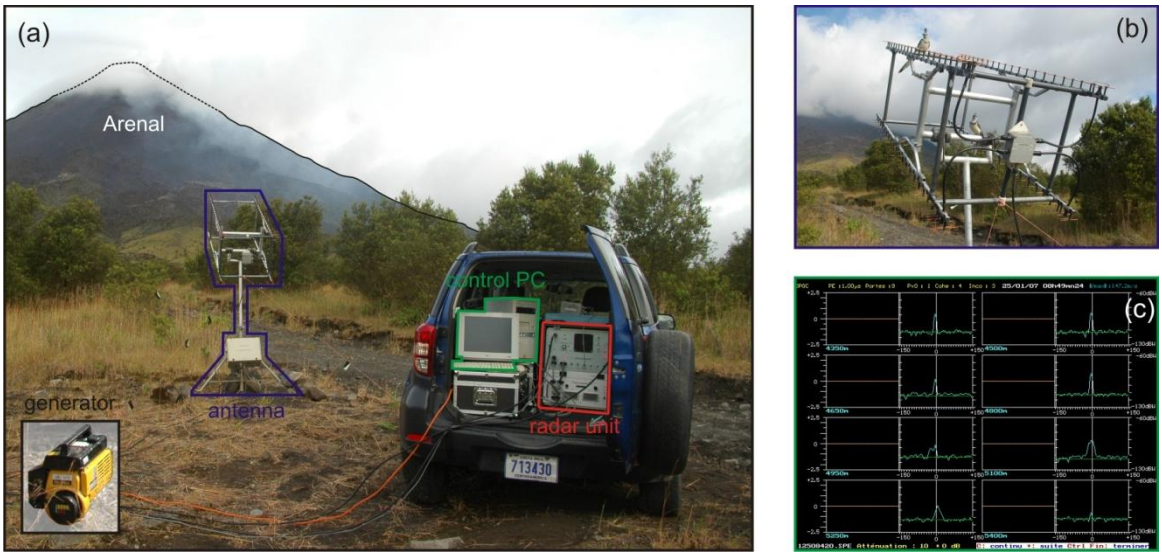

Figure I.3. a) VOLDORAD 2B complete set of devices: radar unit, control PC, antenna tripod, and electric generator; b) four Yagi-antenna array; c) snapshot of the control PC screen, displaying the real-time acquisition of Doppler spectra in successive range gates.

The antenna radiation pattern describes the relative variation of the transmitted power as a function of the angular direction from the antenna axis. The beam pattern of VOLDORAD's antenna array is composed of a main lobe, defining the direction of the maximum radiated energy, and side lobes, which are radiations in undesired directions. The beam width (or aperture angle), is defined as the angular range in which half of the maximum power is transmitted/received (equivalent to -3 dB of the peak power). In the case of VOLDORAD, the beam can thus be defined as conical with an ***aperture angle*** (α) of 9°.

The medium-power (60 W) and large working wavelength ($\lambda\psi$= 23.5 cm) of the radar respectively enable it to operate at medium distance ranges (0.3 – 11 km) and under all weather conditions (little atmospheric attenuation). The frequency of the transmitted electromagnetic wave (f_t) is of 1274 MHz (i.e. L-band, for Large-band radar, defined between 1 – 2 GHz by the Institute of Electrical and Electronics Engineers – IEEE). The polarization is horizontal.

Because VOLDORAD is a pulsed Doppler radar, it is possible to define distinct sampling volumes within the radar beam, which are referred to as ***range gates*** or range bins. The radial resolution of these gates (i.e. along-beam depth), depends on the pulse duration (τ), and their site and azimuthal resolution depend on the distance to the radar and on the beam aperture (α). Throughout the entire study, the range gates will be referenced by the radial distance of their center to the radar (e.g. gates 2247 to 2727 m at Arenal, Figure I.4). At Arenal, the pulse

duration was set to 0.8 µs, which corresponds to a radial range resolution of 120 m, i.e. half the travel distance of the transmitted wave during a pulse (cτ/2, where *c* is the celerity of light). So for instance, gate 2607 m goes along-beam from 2547 m to 2667 m. As for the site and azimuthal resolutions, they equal ca. 410 m for the gate located above the vent. The volume of the 2607 m bin can be calculated as ca. $15.8 \cdot 10^6$ m^3 ($V = \pi R^2 \alpha^2 c\tau/8$, where R = 2607 m is the gate's radial distance from the radar, α is the beam aperture in radian, and τ = 0.8 µs is the pulse duration).

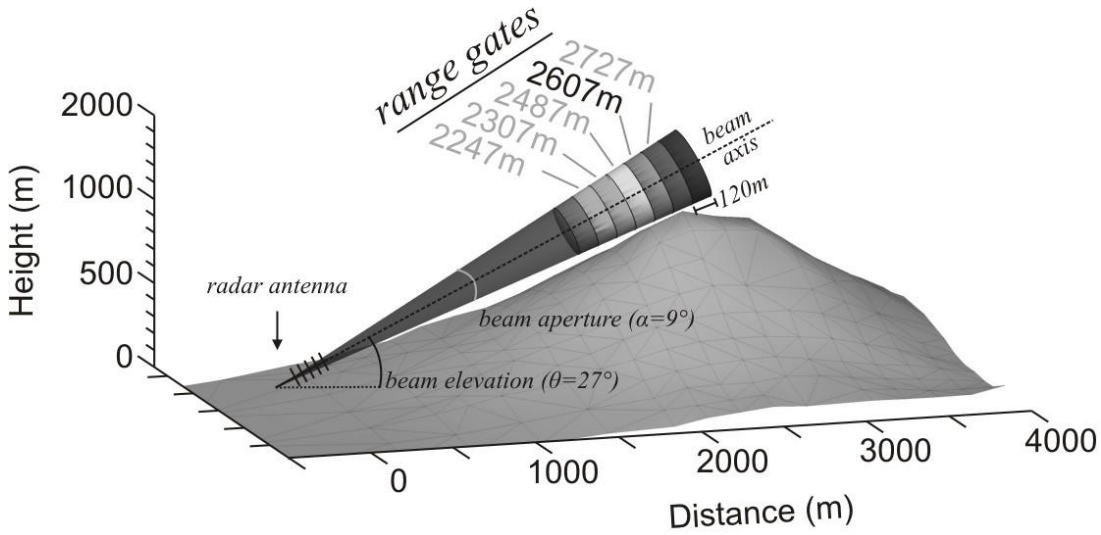

Figure I.4. Illustration of the radar beam and the successive sampling volumes (range gates) which can be defined within it. (Note that only 7 gates are represented here, but that 11 are actually recorded.)

The main characteristics and operating parameters of VOLDORAD are summarized below.

Technical characteristic of VOLDORAD 2	**Symbol**	**Value**
Transmitted frequency (GHz)	f_t	1.274
Wavelength (cm)	λ	23.5
Transmitted peak power (W)	P_t	60
Pulse repetition interval (µs)	t_r	50 – 100 or 100 – 200
Pulse duration (µs)	τ	0.4 – 1.5
Radial range resolution (m)	R	60 – 225
Observation distance (km)	L	0.3 - 11
Beam width (°)	α	9
Power consumption (W)	C	200
System total weight (kg)	W	110

Table I-1. Technical characteristics of VOLDORAD 2.

I.2.2. Theoretical considerations

Electromagnetic pulses (duration τ) are periodically transmitted (pulse repetition t_r) towards the summit via a directive antenna which concentrates the energy in a narrow beam. Volcanic ejecta crossing the beam scatter this electromagnetic signal, part of which is scattered back towards the radar. The way the electromagnetic signal is scattered depends on the relationship between the radar wavelength (λ) and the particle size (D) and shape. For small spherical particles ($D << \lambda$), the Rayleigh scattering theory applies, whereby the backscattered power is proportional to the sixth power of the particle diameter ($P \propto D^6$). On the other hand, for large particles (roughly $D \geq \lambda/4$), the Rayleigh scattering no longer holds and the Mie scattering theory needs to be applied (*Mie*, 1908). In this case, the scattered power becomes a complex function of the transmitted frequency and the considered location around the particle (see *Gouhier*, 2008 for details).

The returned echoes constitute time series, which are time-sequenced in coincidence with the travel time to identify the range gates. These are then processed (Fast Fourier Transform) in real-time to retrieve information: 1- the backscattered power (P), which is a complex function of the number and size of the ejecta crossing the range gates, and 2- the radial velocity of the ejecta, which is related to the frequency content of the backscattered echoes. Let us briefly summarize how these are acquired.

I.2.2.1. Backscattered power

The echo-power received (P_r) by the radar is a complex function of the radar's characteristics (C_r, accounting for the antenna properties, transmitted power, wavelength, etc.), the physical properties of the targets (η, depending on their number, sizes, shapes, composition, etc.), as well as the slant distance (r) and the attenuation (L) of the medium between the radar and the target (the latter being neglected at VOLDORAD's wavelength). The measured received power is thus given by the radar equation (e.g. *Sauvageot*, 1992):

$$P_r = C_r L^2 \frac{\eta}{r^2} \qquad \text{I.1}$$

where P_r is the recorded backscattered power expressed in mW or dBmW, and (η) is the radar reflectivity, defined as the sum of the backscattering cross section (σ_{bsk}) of the individual particles per unit sampling volume (V_s):

$$\eta = \sum_{i=1}^{n} \frac{\sigma_{bsk(i)}}{V_S} \qquad \text{I.2}$$

Note that (P_r) depends on the radar characteristics, and thus cannot be compared with the power values from other radars (even if they probed the same eruptive jet). In order to do so, the radar reflectivity factor (Z) is commonly used because it only characterizes the target (*Sauvageot*, 1992):

$$Z = \frac{\eta\, \lambda^4}{\pi^5\, |K^2|}\, 10^{18} \qquad \text{I.3}$$

where (K) is the dielectric factor characterizing the target (e.g. *Adams et al.*, 1996), and Z is expressed in $mm^6.m^{-3}$ (equivalent to a concentration). For convenience, Z is commonly converted to logarithmic units as follows: $Z_{(dBZ)} = 10.log\ Z_{(mm^6.m^{-3})}$.

I.2.2.2. Radial velocity

Doppler systems enable the comparison between the transmitted frequency (f_t) and the received frequency (f_r) backscattered by moving targets. The difference between the two is referred as the Doppler shift (Δf), a.k.a. Doppler Effect (discovered by Christian Doppler in 1842), and is used to infer the radial velocity (V_r) of the backscattering sources (i.e. along-beam velocity):

$$V_r = \frac{-\lambda\, \Delta f}{2} \qquad \text{I.4}$$

Hence particles with a radial (along-beam) component of motion towards the radar will have negative radial velocities, whereas particles having an along-beam component of motion away from the radar will have positive velocities.

I.2.2.3. Doppler spectra aquisition

Both the backscattered power (P_r) and the radial velocity (V_r) are plotted in real-time on the control PC as Doppler spectra (Figure I.5). These represent, for each range gate and at each sampling step the Power Spectral Density, i.e. the distribution of backscattered power (y-axis) as a function of the radial velocity (x-axis). In other words, these can be regarded as distributions of the mass load as a function of particle velocities within successive volumes of the radar beam.

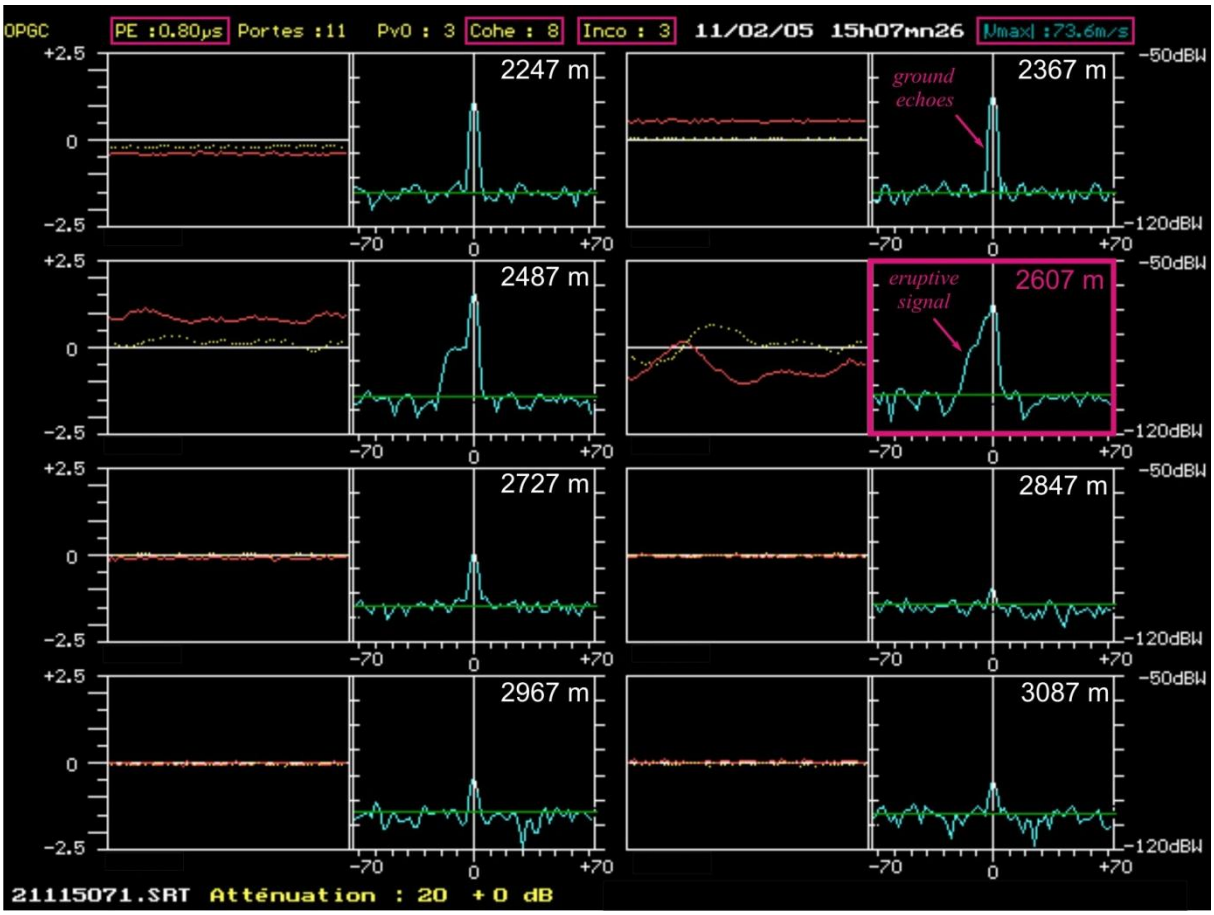

Figure I.5. VOLDORAD real time acquisition of Doppler spectra in successive range gates during the an eruptive event recorded at Arenal on February 11, 2005 (15:07:26 UTC). Doppler spectra (e.g. outlined by the pink box) display the backscattered power P_r (y-axis, in dBmW) as a function of the radial velocity V_r (x-axis, in m/s). Mean noise power in each spectrum is indicated by a horizontal green line. The spectral peak at V_r=0 m/s results from ground-echoes, later suppressed in post-processing of the signal. Eruptive signal appears notably in the gate 2607 m (located above the main eruptive vent), with signal mainly in the negative portion of the spectra, indicating that ejecta in that gate have a radial component of motion towards the radar. Plots to the left of each Doppler spectrum display each component of the complex signals recieved (i.e. real and imaginary part). Acquisition parameters are displayed at the top of the screen: the pulse duration (PE = 0.8 µs) infers a gate radial depth of 120 m, the number of coherent integrations (Cohe = 8) infers a maximum radial velocity (|Vmax|) recorded by a Doppler spectrum of 73.6 m/s, and the number of incoherent integrations (Inco = 3) infers that the spectra are displayed every ~0.44 seconds.

The acquisition rate of one set of Doppler spectra depends on the number of *incoherent integrations* (N_i), which defines the number of consecutive Doppler spectra which are averaged to obtain a mean spectrum. The highest acquisition rate is consequently obtained with 1 incoherent integration (~ 0.14 s^{-1}). The maximum radial velocity that can be recorded by the Doppler radar on the other hand (V_{max}) depends on the number of *coherent integrations* (N_c) (i.e. number of returned radar echoes integrated) and the pulse repetition interval (t_r):

$$V_{max} = \frac{\lambda}{4\, t_r\, N_c} \qquad \text{I.5}$$

where λ is the radar wavelength (0.235 m). Most of the time, N_c was set to 8 and t_r to 100 µs, leading to a velocity range up to about 74 m/s. Because a Doppler spectra is made of 64

spectral lines (31 to the left of the central line, and 32 to the right), the spectral resolution of the velocity axis is with these setting is ~2.3 m/s.

For further details on VOLDORAD, the reader is referred to *Donnadieu et al.* (2003).

I.2.3. Doppler spectra processing

Processing of Doppler spectra consists in extracting the main spectral features to characterize the loading and velocity properties of the target in the beam, i.e. in our case the volcanic ejecta. Two sets of parameters are classically computed, depending on which side of the spectra is processed (Figure I.6): positive parameters (indexed by a plus, e.g. P_+, V_{+max}, etc.) inform on the particles with a radial component of motion away from the radar, and negative parameters (indexed by a minus, e.g. P_-, V_{-max}, etc.) on particles with a radial component of motion towards the radar. In addition to these, we define parameters which are computed over the full spectrum (e.g. P, E_k).

Note that because the spectra are computed in each range gate, the spectral parameters we derive from them will have a subscript indicating in which range gate it has been computed (e.g. P_{2607} will refer to the backscattered power in gate 2607 m, ca. $P_{-2607} + P_{+2607}$).

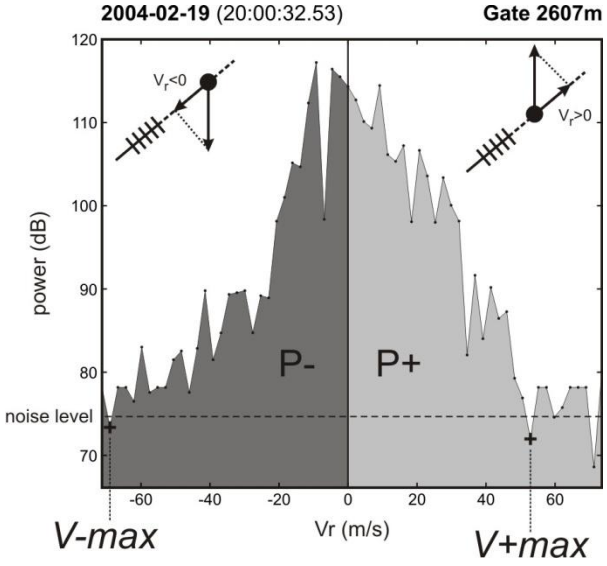

Figure I.6. Typical Doppler spectrum recorded at 20:00:32.5 (UTC) in gate 2607 m, where the backscattered power is displayed as a function of the radial velocity V_r of the target (i.e. component of the velocity vector along the antenna beam direction). The main spectral parameters processed in each side of the spectrum (P_+, P_-, V_{+max}, V_{-max}) are annotated. The indexes (+) and (-) refer to ejecta with the radial component of motion of away and towards the antenna respectively.

We may distinguish three types of spectral parameters: those analyzing the spectrum's backscattered power, those analyzing its velocities, and those which combine both to tell

about the kinetic energy of the spectrum. Their computation is performed in a *Borland Pascal* coded algorithm (CALPV). We hereafter detail how these are calculated.

The main spectral parameters providing information on the backscattered power (and by extension, on the mass loading of the ejecta), are computed as follows:

$$P+ = \sum_{i=1}^{max} p(i) \qquad \text{and} \qquad P- = \sum_{i=-1}^{min} p_i \tag{I.6}$$

$$P = \sum_{i=\min}^{max} p(i) \tag{I.7}$$

$$P_{tot} = \sum_{g=1}^{n} P(g) \tag{I.8}$$

where (i) refers to a spectral line in a Doppler spectrum (ranging from *min* = -31 to *max* = 32), $p(i)$ is the power displayed at the corresponding spectral line, (g) refers to the successive range gates in sampled in the beam, and (n) to the number of range gates considered. Therefore, (P_+) and (P_-) refer to power backscattered by the particles moving respectively away and towards the radar within a given range gate, and (P) to the power backscattered by all particles within this gate ($P \approx P_+ + P_-$), e.g. *Dubosclard et al.*, 2004. On the other hand, we introduced the new parameter (P_{tot}) in CALPV, which refers to the total backscattered power in all the range gates considered during the processing. P_{tot} can consequently be considered as a proxy for the maximum quantity of ash contained inside the beam.

The maximum radial velocities (V_{+max}) and (V_{-max}) of the ejecta, are defined as the velocity value $V_r(i)$, at which the corresponding power value $p(i)$ drops below the noise value (Figure I.6). Recall that these are radial velocities, hence they correspond to the projection of the true velocity vector on the slant line radar-scatterer in the beam.

Lastly, because the Doppler spectrum holds information on both the mass load and velocity of the ejecta within each gate, we can compute a proxy to the kinetic energy of the ejecta (E_k). This new parameter implemented in the *Borland Pascal* CALPV algorithm is computed as:

$$E_k = \sum_{i=i_{-max}}^{i_{+max}} p(i) \cdot V_r(i)^2 \tag{I.9}$$

where (i) refers to a spectral line in a Doppler spectrum, (i_{-max}) and (i_{+max}) correspond to the spectral line of V_{-max} and V_{+max} respectively, and $p(i)$ and $V_r(i)$ refer respectively to the power backscattered by particles with radial velocity between $V_r(i)$ and $V_r(i+1)$.

The Doppler spectra are processed through time, thus providing a value for each of these parameters, at each time step. We can then build time series from these parameters to show how they evolve through time (Figure I.7).

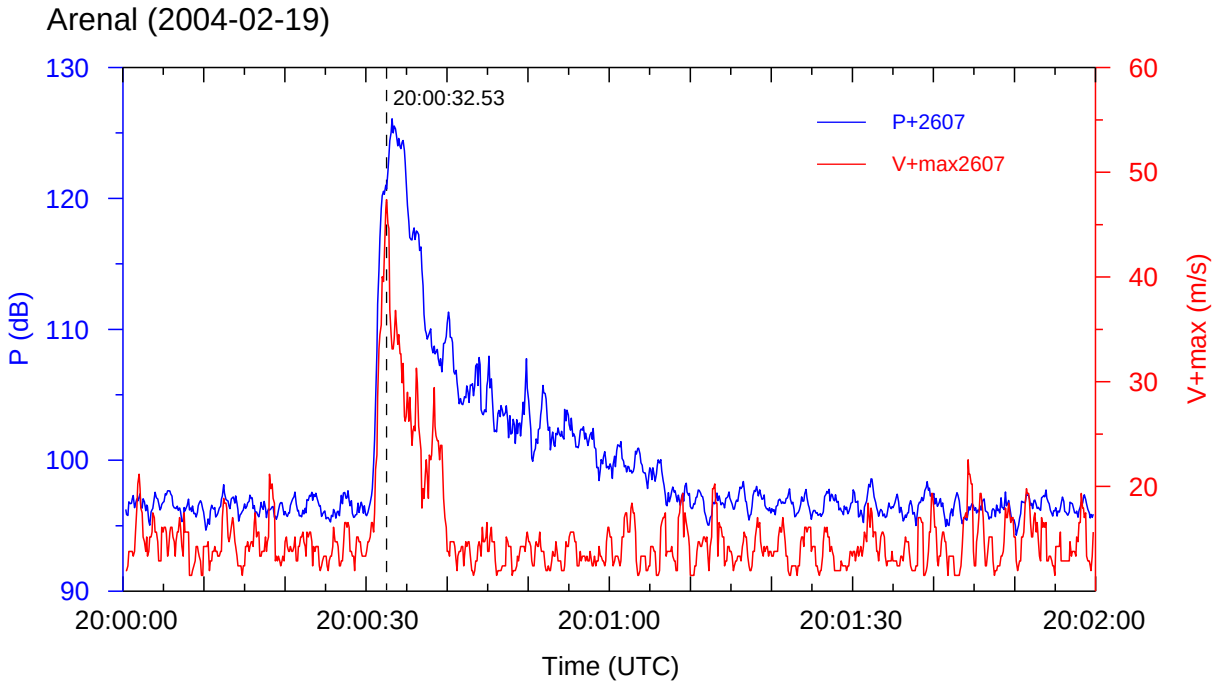

Figure I.7. Time series of two radar parameters (P_{+2607} and V_{+2607}) from gate 2607 m, recorded during an eruptive event at Arenal on February 19, 2004. The data is processed with 1 incoherent integration (i.e. time step ca. 0.14 s), and the time series are smoothed using a running-average with a window width of 5. The dashed line indicates the time at which the spectrum displayed in Figure I.6 is extracted.

I.2.4. Recording campaigns at Arenal volcano (Costa Rica)

VOLDORAD has monitored Arenal's eruptive activity during three field campaigns, in 2004, 2005 and 2009 successively. The 2004 and 2005 field campaigns were short, lasting respectively 8 and 11 days in February of each year. The campaign in 2009 (in which I was involved in) on the other hand, lasted 47 days, from January 17 till March 4. The radar settings and subsequent sounding conditions were set to be identical in all three campaigns (with the exception of the second part of the 2009 campaign, as explicated further down).

VOLDORAD was installed on Arenal's western flank, 2.6 km (slant distance) west and downwind of the active crater (C). Data were acquired at ~12 Hz in 11 range gates between ca. 2 and 3 km from the radar. The pulse duration (τ) was set at 0.8 µs, giving range gates with a radial resolution of 120 m. Two range gates were located directly above the active crater: gates 2607 and 2727 m. Moreover as ash plumes were drifted by trade winds, their

displacements could be recorded in up to 7 range gates (>720 m) before they passed beyond the beam. Raw data were recorded in SRT format.

Between January 25 and March 4, 2009, VOLDORAD was stored in a shelter at the entrance of Arenal National Park. Located 4150 m (slant-wise) from the active crater, it continuously monitored Arenal's activity (despite frequent electric power break-downs). The radial resolution of the range gates was increased to 135 m. For storage memory space of the PC disk, data were recorded in SPE format, whereby only the power values of the spectra (averaged over 3 spectra, i.e. 3 incoherent integrations, time step ca. 0.44 s) were saved.

I.3. ARENAL: a case study volcano

I.3.1. Arenal's eruptive history and current activity

Arenal volcano is located in Costa Rica, in a convergent margin setting related to three tectonic plates (whereby the Cocos and Nazca plates dive under the Caribbean plate), Figure I.8. The volcano (10.463°N, 84.703°W) is part of the Central American magmatic arc (*Carr and Stoiber*, 1977), and more specifically, part of the Cordillera Volcánica de Guanacaste province (CVG) of the northwest-trending Costa Rican volcanic arc (CRVA). It is the youngest cone of the Arenal–Chatosystem (~7000 years old, *Soto and Alvarado*, 2006), a 12-km-long SE–NW-trending volcanic alignment.

Today, at least 7000 people live within a 6 km radius of Arenal, mainly in the town of La Fortuna. Only 4 km to the west of the volcano, extends Lake Arenal, created in 1979 after the building of the Sangregado Dam to supply Costa Rica with hydroelectricity (nearly 50% of the country electric power).

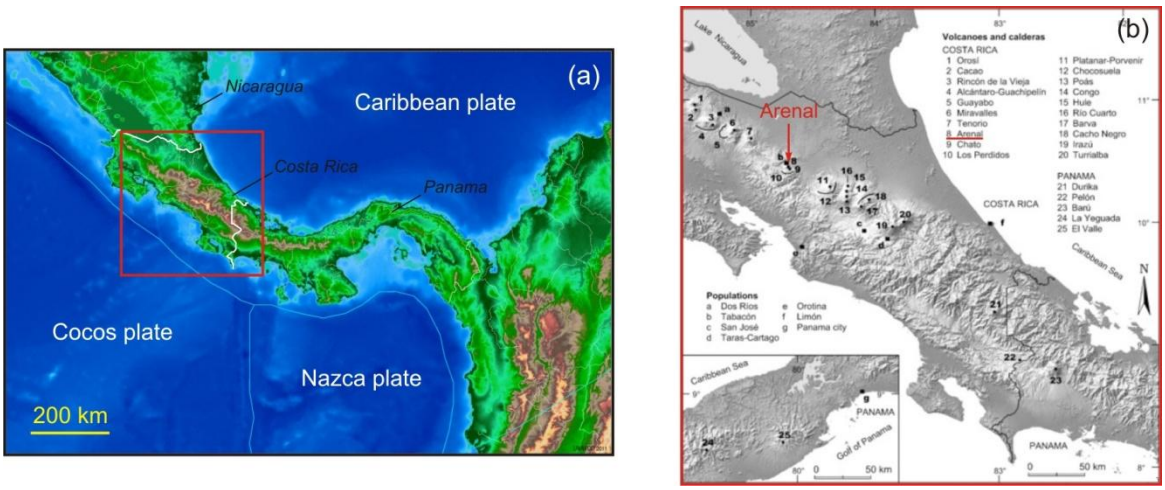

Figure I.8. Geographical location of Costa Rica and Arenal. (a) image created from UNAVCO's mapping tool (http://jules.unavco.org/Voyager/Earth); (b) courtesy of Guillermo Alvarado, NASA source image.

Arenal can be defined as a small basaltic andesite stratovolcano, approximately 1.1 km in height and 1710 m above sea level, with total volume of ca. 7.2 km^3 (*Alvarado and Soto*, 2002; *Wadge et al.*, 2006). One of the first studies to look at the chronostratigraphy of Arenal was done by *Malavassi* (1979). Since then a number of authors have refined it, with the latest in date being that of *Soto and Alvarado* (2006), who constrained its history with several excellent chronological datings. It has begun to erupt around 7000 years B.P., and has since then erupted a variety of products spanning a wide range of phreatomagmatic to magmatic

phenomena (*Soto et al.*, 1998). On July 29, 1968, after nearly 450 years of dormancy, Arenal erupted violently marking the onset of an ongoing continuous eruptive activity. We hereafter describe the activity experienced since then, referring the reader to the work of *Soto and Alvarado* (2006) for a review of the eruptive history prior to the 1968 eruption.

Arenal's reawakening in 1968 was marked by a lateral blast eruption, which destroyed two nearby villages and killed 78 people (*Melson and Sáenz*, 1968; *Alvarado et al.*, 2006). Several papers have focused on the assessment of the eruption kinetic energy, deriving notably the velocities of expelled ballistic blocks (which likely exceeded 350 m/s, e.g. *Minakami et al.*, 1969; *Fudali and Melson*, 1972; *Steinberg and Lorenz*, 1983). The eruption opened a 1-km long radial fissure running west from the summit, feeding three new explosion craters (namely craters A, B, and C) and leaving the old summit vent (crater D) inactive ever since. From 1968 to 1973, a series of lava flows were erupted from Crater A (*Wadge*, 1983). After a few months hiatus, the effusive activity shifted to Crater C (nearly 400 m higher up the volcano), where it still remains as of today. Up until 1983, almost continuous aa-blocky lava flows of basaltic andesite composition outpoured from the crater (*Cigolini et al.*, 1984). In 1984 however, the activity became much more explosive with frequent Vulcanian-type explosions (*Van der Laat and Carr*, 1989), and between 1987 and 1990, numerous column-collapse pyroclastic flows were reported (*Cole et al.*, 2005). Since the late 1980s however, the eruptive mass rate has significantly decreased, from 0.6 m^3/s (1980 – 1988) to 0.086 m^3/s (2000 – 2005, *Wadge et al.*, 2006), Figure I.9a. Except for sporadic partial collapses of the crater wall (in 1993, 1998, 2000, 2001, *Alvarado and Soto*, 2002), there has been a markedly reduction in explosive activity since 1998 (tephra fall mass < 1 $g.m^{-2}.day^{-1}$, *Cole et al.*, 2005, Figure I.9b). This decreasing activity is believed to have allowed lava to accumulate at the summit, leading to the development of a mainly rigid, degassed magma body in the upper portion of the conduit (*Cole et al.*, 2005). In particular, this could explain the progressive shift from "Strombolian-like" eruptions associated with the reported "lava pool" (e.g. *Cigolini et al.*, 1984; *Alvarado and Soto*, 2002), to more "Vulcanian-like" eruptions associated to a more viscous lava cap (or plug) tapping the conduit. This is supported from tephra clast analyses, which attest the fragmentation of a rigid degassed magma with only minor molten component (*Cole et al.*, 2005).

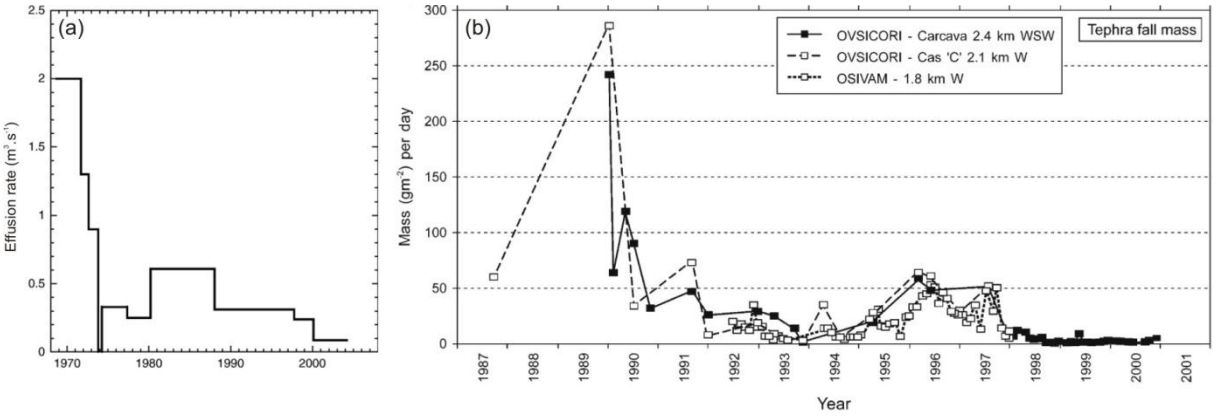

Figure I.9. (a). Lava effusion rate versus time at Arenal (from Wadge et al., 2006). (b) Tephra mass per day per m^2 versus time, for different collectors on the western flank of Arenal (from Cole et al., 2005). Both plots show the progressive decrease in eruptive activity at Arenal.

Today, crater A and B are completely covered by lava flows from crater C, and crater D is about to be buried as well (Figure I.10). Rather than a simple open lava pool, it seems that crater C should be regarded as a broad active region from which viscous lava flows are continuously fed. Regular explosions, several times per day, generate tephra columns that can rise up to a few hundred meters above the crater, and can be drifted by easterly winds up to a distance of 5 km West of the crater (*Cole et al.*, 2005). Ballistic bombs associated with these explosions are visible at night, and can be ejected up to a few hundred meters from the crater.

The OSIVAM observatory (*Observatorio Sismológico y Vulcanológico de Arenal y Miravalles*) that monitors seismic and volcanic activity at Arenal is operated by the Department of Geology of the *Instituto Costarricense de Electricidad* (ICE). Seismic activity is also recorded with short-period and broad-band seismometers by both the OVISCORI (*Observatorio Vulcanológico y Sismológico de Costa Rica*) and the UCR (*Universidad de Costa Rica*).

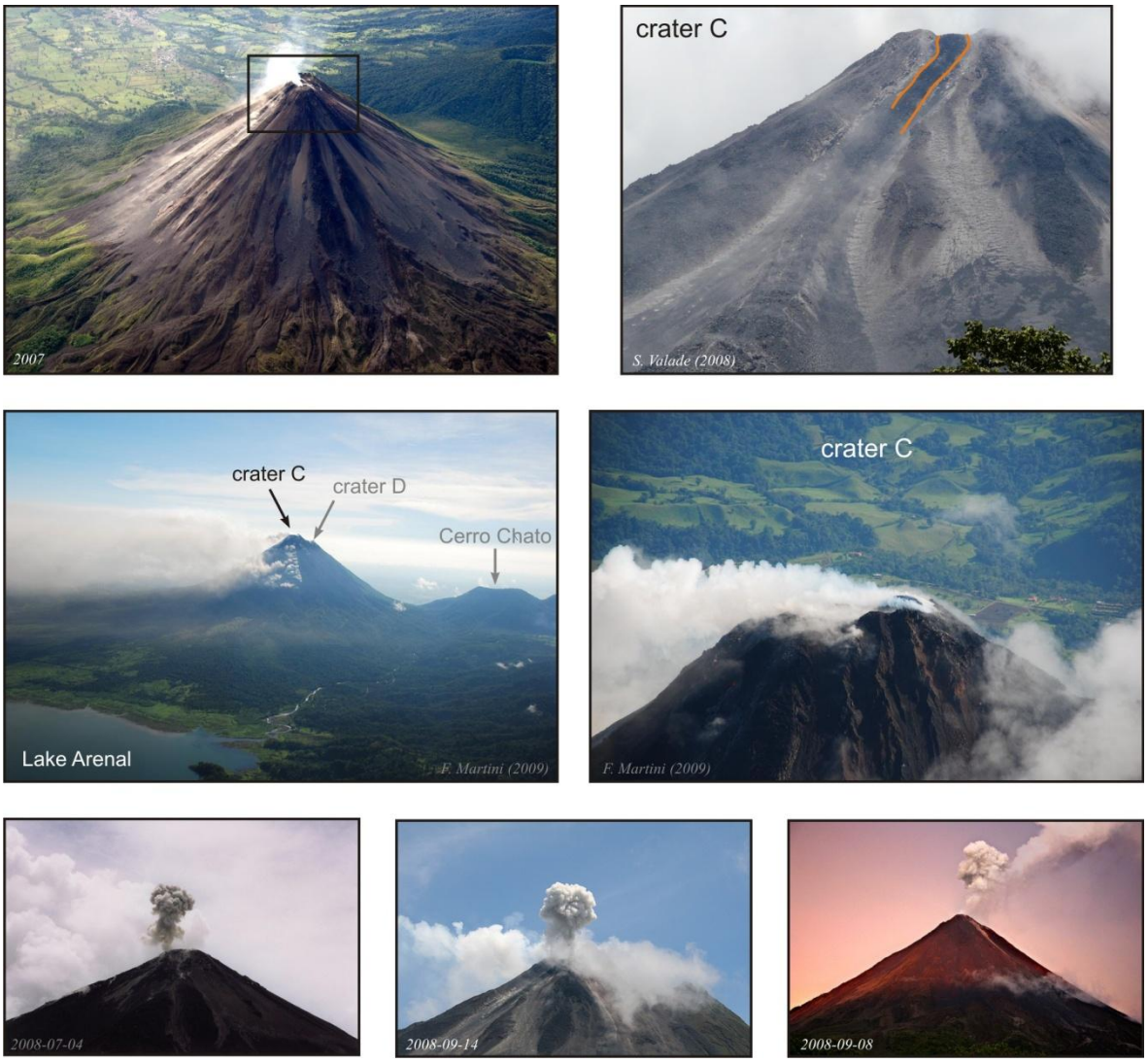

Figure I.10. Photo-board of Arenal's actual morphology and activity. The date at which the picture was taken and its author are annotated when known, elsewise the pictures are anonymous (downloaded from Flickr). Activity is concentrated in crater C, from which blocky basaltic-andesitic lavas continuously effuse. In addition, small ash plumes are emitted several times per day, usually ascending ≤ 1-3 km above the crater.

I.3.2. Geophysical studies at Arenal

Several geophysical studies have been carried out on Arenal volcano since its tragic reawakening in 1968. A large number of these are seismological studies, launched with the pioneering contributions of the Japanese community during the late 1960s and 1970s (*Soto,* 2007). *Minakami et al*. (1969) and later *Matumoto* (1975) in particular, were the first to distinguish different types of seismic events at Arenal, including volcano-tectonic, LP, and tremor signals of various types. In the following years, several studies have further described the waveform and frequency content of the seismic signals (*Alvarado and Barquero,* 1987; *Morales et al.*, 1988; *Barquero et al.*, 1992; *Métaxian et al.*, 1996; *Alvarado et al.*, 1997),

pointing out the variability of seismic events at Arenal. *Melson* (1989) and *Barboza and Melson* (1990), introduced a classification based on the correlation with audible sounds: "whoosh" events, associated with a progressive 10 – 50 second-long sound (much like that of a jet airplane), and "chugging" events, associated to rhythmic gas release sounds (similar to that of a locomotive). These terms are still used as of today, and identified at a number of volcanoes (e.g. Karymsky volcano, *Johnson et al.*, 1998; Sangay volcano, *Lees and Ruiz*, 2007). The first time-frequency analysis were performed by *Benoit and McNutt* (1997) and *Garcés et al*. (1998), and highlighted for the first time the progressive shifting of the spectral peaks of tremor (i.e. frequency glidings). *Lesage et al*. (2006) proposed a model that accounts for most characteristics of the tremor signal at Arenal. Investigation of the shallow velocity structure of Arenal was performed by *Mora et al*. (2001, 2003, 2006), and study of how it might affect the location of sources was done by *Métaxian et al.* (2009). More recently, *Davi et al.* (2010, 2011) carried out moment tensors inversions of both explosive long-period events and tremor events to retrieve their respective source mechanism.

Seismic data have been correlated with infrasonic data at Arenal by *Hagerty et al.* (2000), who achieved a detailed analysis of the waveforms to give constraints on the generation of these signals. *Williams-Jones et al*. (2001) on the other hand, cross-correlated seismic data with both SO_2 fluxes (from COSPEC data) and Earth tides to investigate the link between degassing, seismicity, and the influence of cyclic drivers.

In the recent year, satellite-borne sensors have been used to monitor the growth and magma budget of Arenal, using either Lidar sensors (*Hofton et al.*, 2006) or radar interferometry (*Wadge et al.*, 2006). Very recently, *Ebmeier et al.* (2010) constructed radar interferograms to measure the deformation of the volcano, and were able to reveal a steady downslope movement of its western flank.

The study presented hereafter is an innovative geophysical study, which uses both between seismic data and ground-based Doppler radar data recorded at Arenal. In doing so, we correlate for the first time quantitative information regarding both the pyroclastic emissions and the subsurface processes that drive the explosions.

Chapter II

Source mechanisms of explosive activity:

linking sub-surface and surface activity at Arenal

II.1. Introduction

One of the fundamental objectives of volcanology is to understand the mechanisms operating within the volcanic edifice in order to better explain/forecast the resulting surface activity. In this aim a growing number of techniques have been developed over the past century to monitor volcanic phenomena. As techniques have been developed and tested, their datasets and respective studies have increased, leading to a growing need for integration among them. Consequently more and more fields of studies are being cross-correlated, and are constantly challenging our interpretative models which often appear too simplistic to successfully explain the complexity of the eruptive behaviours and datasets.

Many volcanoes worldwide exhibit quasi-continuous activity with small-scale, short-lived, transient eruptions, yet a simple classification of their eruption style and behaviour is not trivial (Figure II.1). Persistent volcanism associated to low viscosity magmas has been largely described by multidisciplinary studies on Stromboli (Italy), Erebus (Antartica) and Villarica (Chile), where eruptive activity is generally characterized by the bursting of overpressurized gas slugs at the magma free surface (*Strombolian activity,* e.g. *Blackburn et al.,* 1976). On the other hand of the spectra, persistent high-viscosity volcanism has been documented by eruptions of the Soufriere Hills Volcano (Montserrat) and Mount St Helens (USA), where eruptive phenomenon is thought to be the result of a steady accumulation of pressure under a viscous dome obstructing the conduit (*Vulcanian activity,* e.g. *Self et al.,* 1979). In between these two end-member cases, however, are a number of volcanoes whose activity fit either both or neither models. Among them and to mention only a few are: Arenal (Costa Rica), Karymsky (Russia), Santiaguito (Guatemala), and Colima (Mexico).

In this chapter, we cross-correlate LB seismic data with radar data, in hope to gain insight into the subsurface source mechanisms (e.g. source conditions and fragmentation mechanisms operating in the shallow conduit system) and the subsequent surface pyroclastic emissions (e.g. mass loading and dynamics) that generate the repeated, mildly explosive activity of Arenal (Costa Rica). The data used in the study mainly come from the 2005 recording campaign. The results are published in the *Journal of Geophysical Research* (*Valade et al.,* 2012). We hereafter present the tools and methodology developed, describe the results, and present the conceptual model which is believed to explain the eruptive activity at Arenal and the associated geophysical signals.

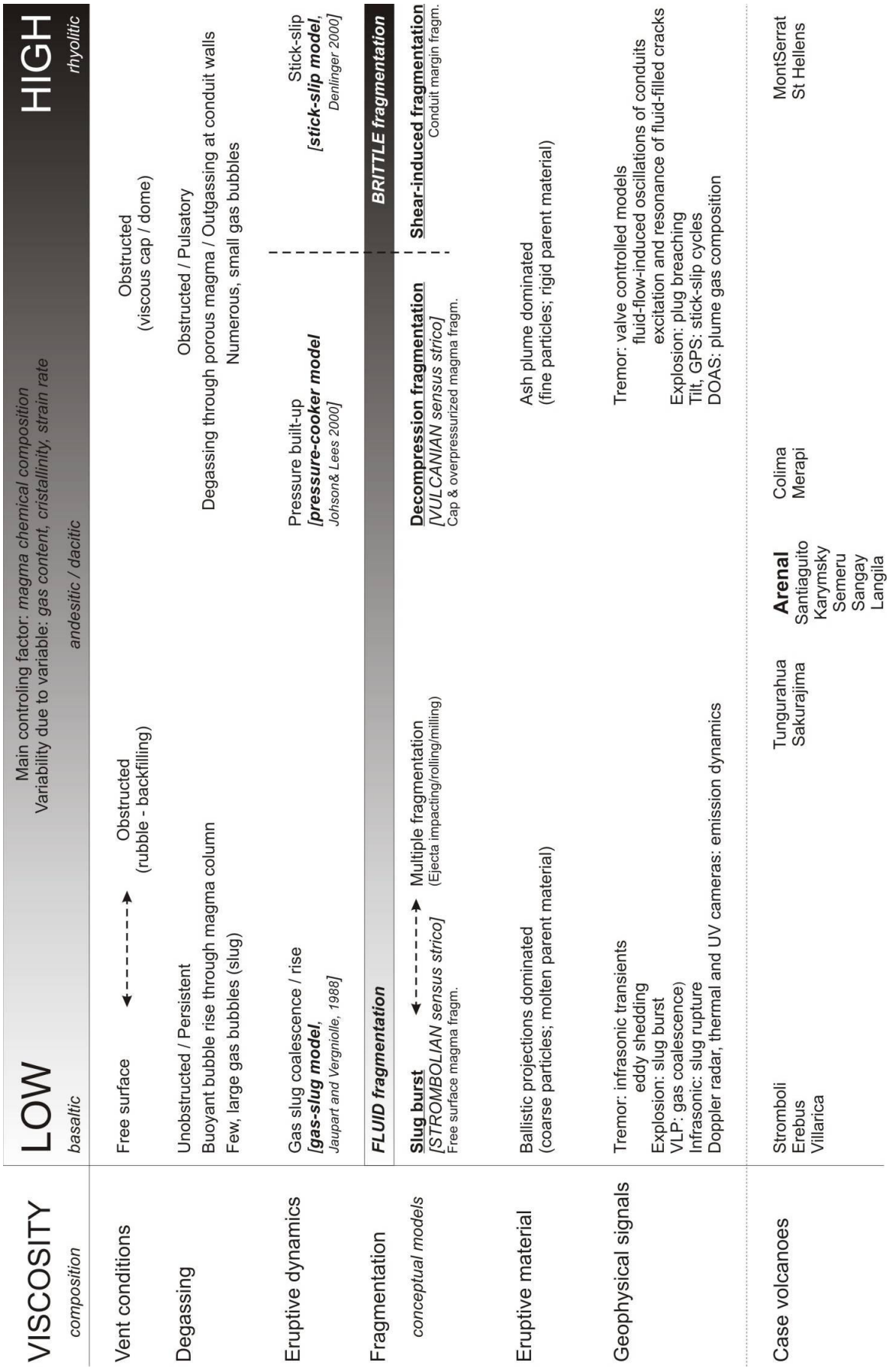

Figure II.1. Shallow conduit processes (source conditions, fragmentation mechanisms and eruptive dynamics) of persistently active systems encountering discrete (non-sustained) eruptive events.

II.2. Methodology and tools

Linking surface and subsurface activity requires usage of adequate sets of parameters, capable of providing substantial information on the physical processes in operation. Figure II.2 gives a schematic view of the methodology and tools deployed to carry out this cross-correlation study. Below, we detail the "Data Processing" and "Data Analysis" steps.

II.2.1. Data processing

Radar data. The raw radar data were first processed (see section I.2.3), and the eruptive events identified. This operation needs to be carefully performed, in order to set aside the non-eruptive signals (rain fall, noise due to antenna movements, etc.). During the 11-day field campaign in 2005, a total of 132 eruptive events were recorded (*Pouchol*, 2005). Various parameters were extracted for each event (power, velocity, impulsivity …), and archived in a data base (see Data Analysis section II.2.2). Certain key parameters were used as "indexes" to classify the events: by event size (based on a mass loading proxy: P_{tot} maximum amplitude), or depending on the onset delay between the radar and seismic signal. Such indexes enabled the possibility to set weights to the various events (e.g. rightmost column in Figure II.5), and analyse subsets of events taking those into account (e.g. scatter plot Figure II.7).

Seismic data. Once tephra emissions were identified with the radar data, the coeval seismic signal was considered, and the event type was annotated within the data base: tremor (harmonic or spasmodic), explosion quakes (or "whoosh" if the coda evolves into harmonic tremor), high frequency events, or volcano-tectonic events. This classification was based on the work of *Lesage et al.*, 2006 and the *Universidad de Costa Rica* (see section II.3 for details on their specific characteristics). A number of parameters were then extracted for each seismic event associated to a tephra emission (see Data Analysis, section II.2.2).

Acoustic data. Acoustic measurements were carried out during this recording campaign (*Fourel and Vergniolle*, unpublished), but unfortunately the data is extremely noisy. Several frequency bands were considered, ranging from 0.2 Hz to 50 Hz, to see whether any signals were found associated to the radar emissions. Unfortunately, too few events were recorded to be used in this study. Most explosions in 2005 involved small gas volumes and very low overpressures ($<1.26 \cdot 10^5$ Pa, *Fourel and Vergniolle* unpublished), with low ejections velocities (radar data), attesting a period of low activity at Arenal.

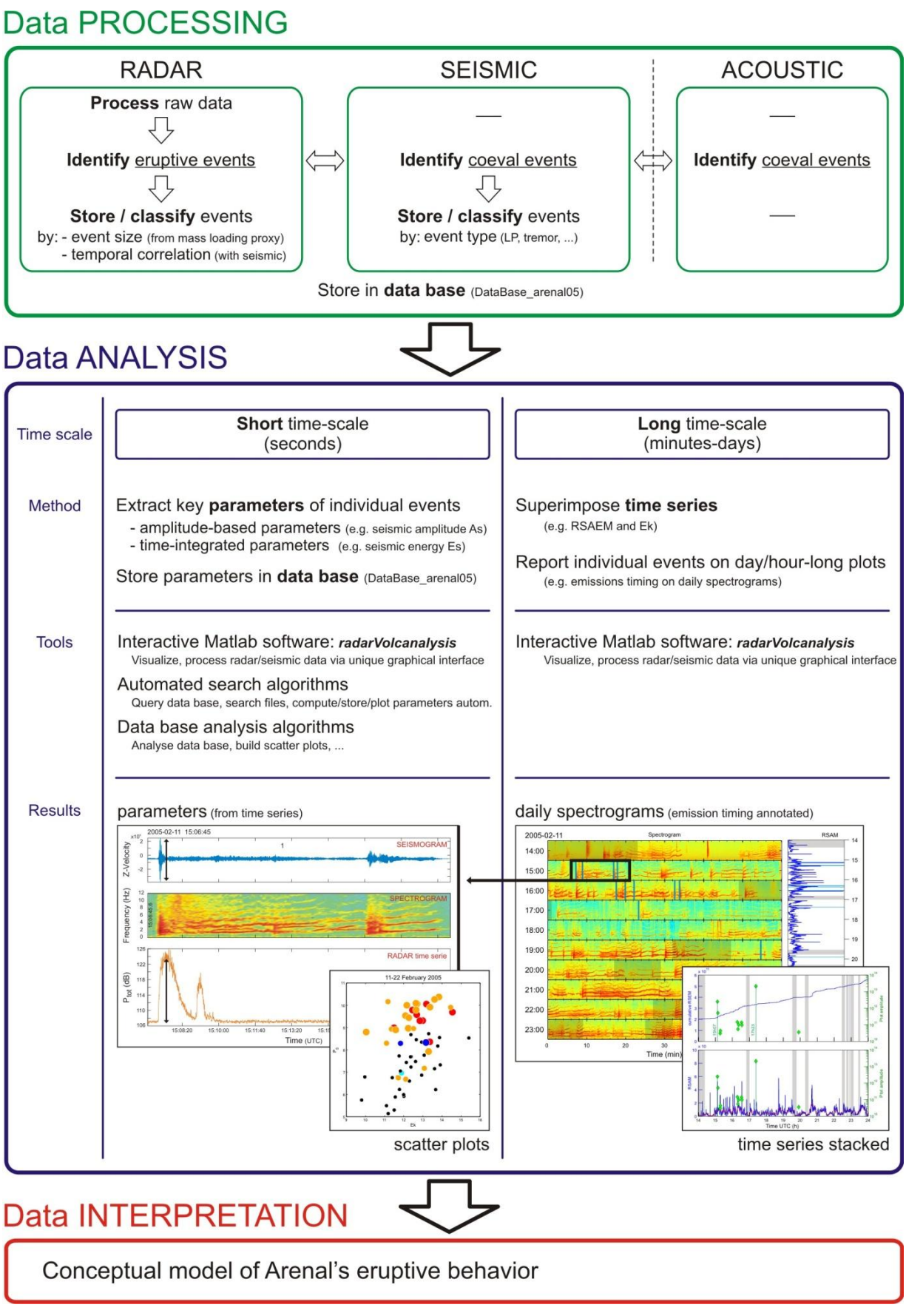

Figure II.2. Methodology and tools developed to carry out the cross-correlation study on Arenal's eruptive behavior.

II.2.2. Data analysis

Once the raw data have been processed and the eruptive events have been identified / classified, the data analysis can start. The data were studied at different time scales: 1- at the time of the eruptive event, in order to study the seismo-radar signature *during* the pyroclastic emission, and 2- in the minutes to hours preceding the eruption, in order to understand the seismo-radar activity that may *lead* to the pyroclastic emissions. We hereafter point out the main tools developed to carry out this study.

II.2.2.1. Interactive Matlab software: *Seismo_Radar_Correlation*

Seismo_Radar_Correlation is a user-friendly, *Matlab*-based software, specifically developed to display the different data types (radar, seismic and acoustic) on a unique graphical interface (Figure II.3). It provides several tools that allow the user to select, filter, resample, zoom and pick on sections of both records, either simultaneously or separately. The software also enables the application of high resolution time-frequency methods (*Lesage*, 2009) to extract the main features from both seismic and radar data, and to export them into a data base. Note that the seismic data processing part of the software uses the same functions as *Seismo_Volcanalysis*, a software developed by Philippe Lesage (*Lesage*, 2009).

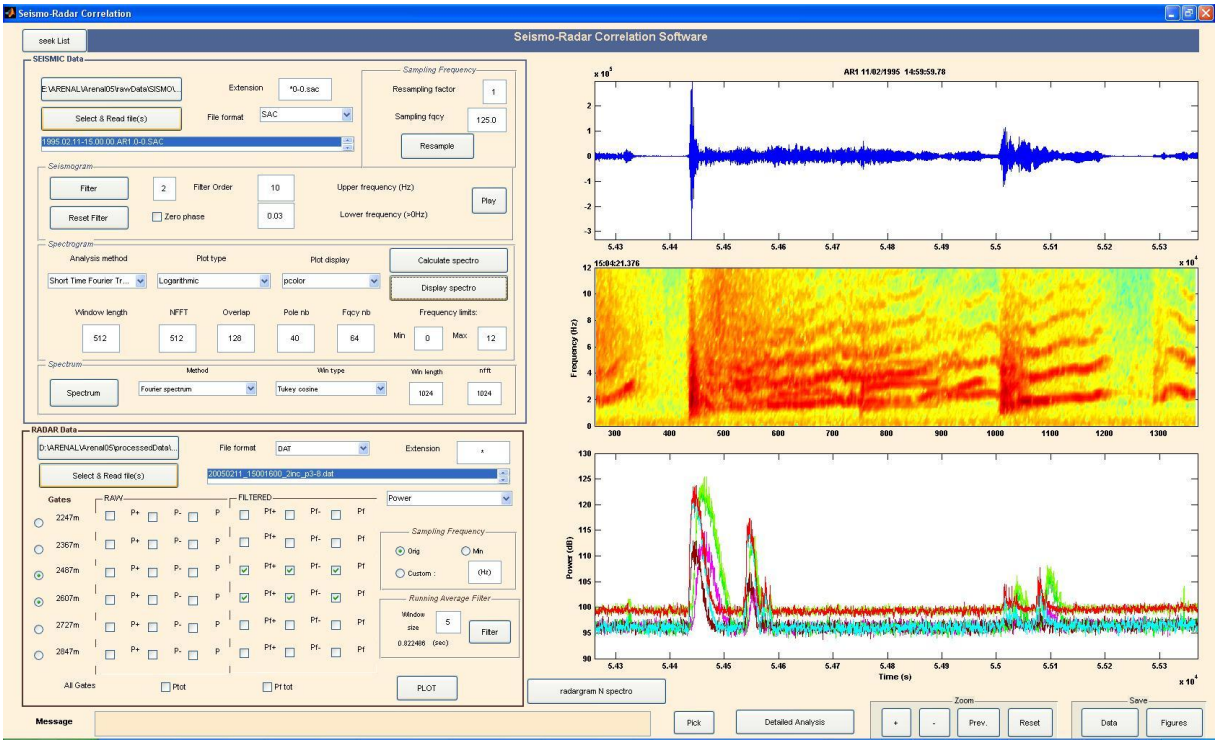

Figure II.3. Snap-shot of the main interface of Seismo_Radar_Correlation software.

II.2.2.2. Automated search algorithms

When a large number of eruptive events have to be analyzed, collecting a given parameter (e.g. signal amplitude) on each event individually and for each data type is extremely tedious and time consuming. To fasten this operation, we have developed algorithms which enable automatic collection of parameters.

The user may query the data base (*DataBase_arenal05*) to select specific events (e.g. events of certain intensity or of certain type). The algorithms then use the date/time information of each event to seek for the appropriate raw data file which contains it (i.e. the one which covers the time period during which the event is recorded). Once it is located, it builds a time series with the requested data, and computes/collects the requested parameter (e.g. signal amplitude). The user may choose to have the algorithms automatically save plots of the time series and the collected parameter (Figure II.4), and automatically store the parameter's value in a seperate data base.

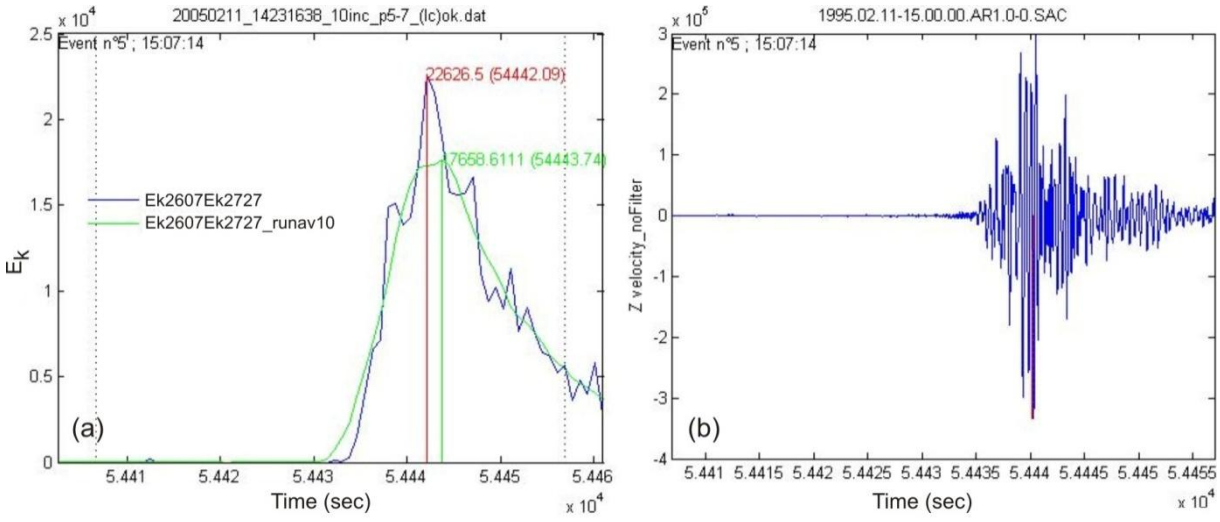

Figure II.4. Typical plots obtained from the automated search algorithms, illustrating the automatic collection of parameters from different data types for a given eruptive event. (a) radar time series of $E_{k\ 2607}$ + $E_{k\ 2727}$ (blue) and its maximum amplitude (red), along with a running average of it (time window = 10) and the associated maximum amplitude (green). (b) seismic trace (vertical component), and maximum amplitude collected (red). Both plots correspond to the eruptive event recorded at Arenal, on February 11, 2005, at 15:07:14 (event referenced as n°5 in the data base, Figure II.5). Note that all information related to the search is automatically plotted: the ordinate axis's name indicates the queried parameters (e.g. vertical seismic amplitude, no frequency filter), the plot title indicates the raw file used to build the time series, the plotted event's number / time stored in the data base are annotated (top left), the time range searched is indicated (vertical dotted lines), as well as the value and time of the collected maximum amplitudes (time – in seconds from midnight – are annotated within parenthesis).

II.2.2.3. Data base: *DataBase_arenal2005*

A large data base has been built to gather the quantitative parameters extracted from the radar, seismic and acoustic data, relative to each of the recorded eruptive events (132).

DataBase_arenal05

			Event Number	Subset		RADAR			
				Tick	Num	File Nb inco	Heure ONSET sec	Heure ONSET hh:mm:ss	Ev.Size
Year	Month	Day		* NB			* NB	* NB	
2005	2	11	5	x	1	2inco	54432	**15:07:15**	**3**
2005	2	11	6	x	2	2inco	54534	**15:08:54**	**3**
2005	2	11	7	x	3	2inco	55015	15:16:55	1
2005	2	11	8			2inco	55071	15:17:51	1
2005	2	11	9	x	4	2inco	58654	16:17:34	2
2005	2	11	10			2inco	58792	16:19:52	1
2005	2	11	11	x	5	2inco	58928	16:22:08	2
2005	2	11	12	x	6	2inco	59554	16:32:34	1
2005	2	11	13	x	7	2inco	59628	16:33:48	1
2005	2	11	14	x	8	2inco	62599	**17:23:19**	**3**
2005	2	11	15			2inco	71681.22	19:54:41	1

~100C

150L

Figure II.5. Snap-shot of the data base (~ 150 x 100 cells) built to gather the quantitative data extracted with Seismo_Radar_Correlation software. Notice for instance the* event size index *(rightmost column, based on P_{tot} maximum amplitude), used to build subsets of eruptive events based on the mass loading of the tephra emissions.

II.2.2.3.1. Parameters stored in data base

We summarize these parameters in two categories, which we describe hereafter.

Amplitude-based parameters

These parameters correspond to the maximum amplitude collected in the time-series of a given data type. We can mention for example: the maximum amplitude of P_{tot} curve (see section I.2.3), which depends on the maximum quantity of tephra contained inside the beam during an eruptive event (i.e. proxy to the mass load of the tephra emission); or the maximum amplitude of the seismic trace (i.e. proxy to the "magnitude" of the seismic event). We have also tested more complex amplitude-based parameters, which used several amplitudes to compute a single parameter. For instance, the peak amplitude of the $P_{+\ 2607}$ and $V_{+max\ 2607}$ time series of a given eruptive event (Figure II.6a), can be used as proxies to the mass (m) and velocity (v) factors in Newton's equation for the kinetic energy $E = \frac{1}{2} \cdot m \cdot v^2$. The resulting value can then be used as a kinetic index (I_k) of the given eruptive event, which can later be compared with seismic parameter characterising that same event (e.g. Figure II.7).

Time-integrated parameters

Time-integrated parameters refer to parameters computed over a given time range. We can mention for example the seismic energy E_s (defined as the sum of the squared signal over the sample interval), the seismic power P_s (defined as the seismic energy E_s divided by the time interval over which it has been computed, e.g. Figure II.7), or the kinetic index ($I_{k\,2}$) (defined as the sum of the product between the power curve $P_{+\ 2607}$ and the squared velocity curve $V_{+max\ 2607}$, e.g. Figure II.6b).

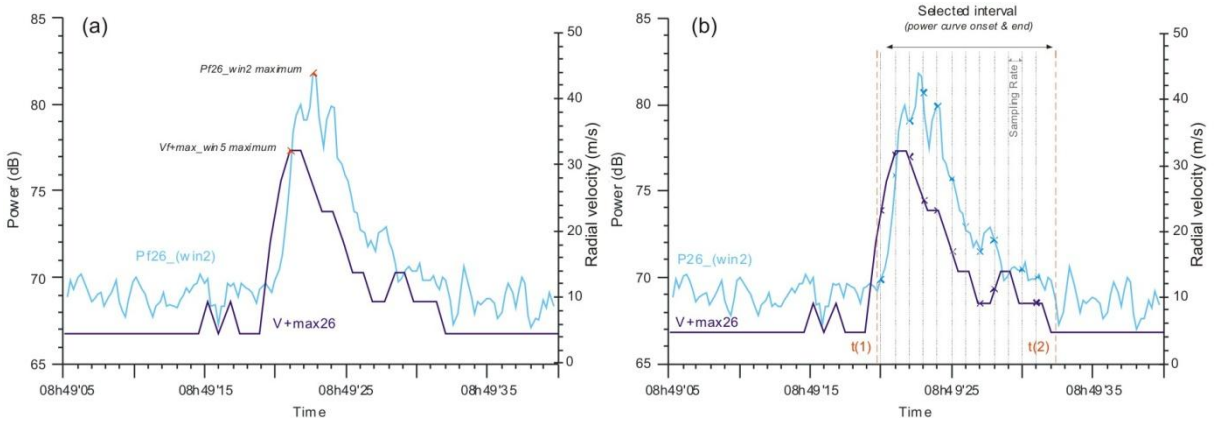

Figure II.6. Illustration of the two types of parameters collected: (a) amplitude-based parameters, and (b) time-integrated parameters. From these a number of other parameters can be derived, such as kinetic indexes: I_k (product of the peak amplitudes of $P_{+\ 2607}$ and $V_{+max\ 2607}$, from plot* a*), and I_{k2} (time integrated product of $P_{+\ 2607}$ and $V_{+max\ 2607}$ squared, from plot* b*). The subscript "f" in the labels of the time series, indicates the fact that the original time series have been filtered with a running average, and the numeric value after the subscript "_win" indicates the window length used.

II.2.2.3.2. Algorithms for data base analysis

Algorithms were developed to probe the data base and plot the data contained within it. Figure II.7 is an illustration of a typical scatter plot, which compares the seismic power (P_s) and the kinetic index (I_k), computed over of a large number of events. Notice how the event classifications described earlier (section II.2.1) are taken into account inside the plot: the dot-colors refer to different seismic event types, and dot-sizes refer to an index based on the delay between the radar event and the seismic counterpart.

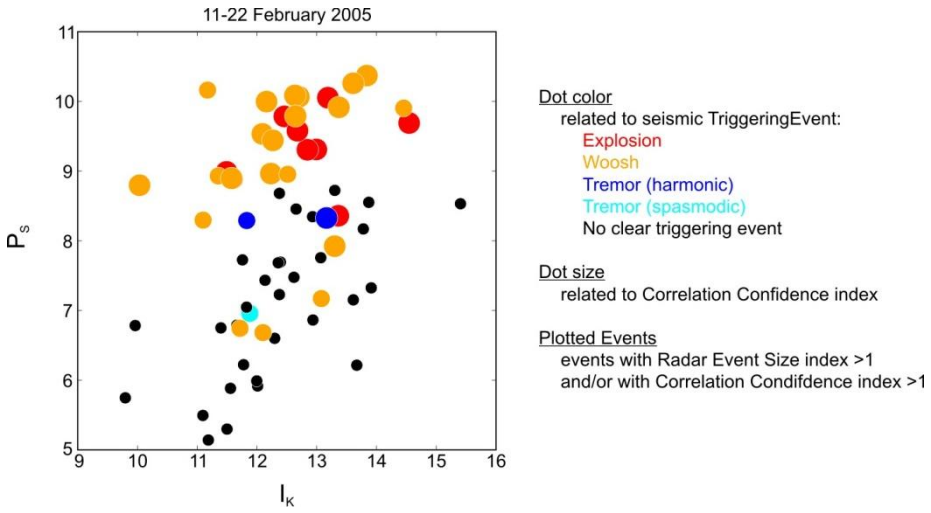

Figure II.7. Typical scatter plot constructed from the data contained inside the data base DataBase_arenal2005. The algorithms developed enable the possibility to select the data to plot depending on various criteria, either qualitative (e.g. seismic event types), or quantitative (e.g. event size Index, based on the amplitude of P_{tot} curve).

In the following section, we discuss the results obtained with the tools described above, and propose a conceptual model to explain Arenal's eruptive activity (*Valade et al.*, 2012).

II.3. Explosion mechanisms at Arenal volcano, Costa Rica: *an interpretation from integration of seismic and Doppler radar data*

The following section is published in *Journal of Geophysical Research* (*Valade et al.*, 2012), with the following list of authors: S. Valade, F. Donnadieu, P. Lesage, M. M. Mora, A. Harris, and G. E. Alvarado. The architecture of the section is kept identical to that of the printed format (appendix D), but the content has been complemented with some additional material that is not included in the publication.

Journal of Geophysical Research

Explosion mechanisms at Arenal volcano, Costa Rica: an interpretation from integration of seismic and Doppler radar data

S. Valade, F. Donnadieu, P. Lesage, M. M. Mora, A. Harris, and G. E. Alvarado.

Received 23 June 2011; revised 15 November 2011; accepted 17 November 2011; published 21 January 2012.

II.3.1. Abstract

We execute an integrated analysis of broad-band seismic and Doppler radar data to gain insights into the subsurface mechanisms that drive repetitive, mildly explosive activity of Arenal (Costa Rica). We find large variability of both seismic and radar waveforms, and non-systematic relationships between the two. Seismic recordings display long-lasting tremor sequences and numerous explosion quakes. Radar measurements show that tephra emissions are poorly correlated, both in time and energy, to the seismic activity. Tephra emissions were found in association with explosion quakes, but also during episodes of tremor and seismic quiescence. Moreover, the exit velocity, mass-loading, and kinetic energy of the emissions show no clear relationship with the coeval seismic amplitude and frequency content. We propose a conceptual source model whereby degassing is controlled by opening and closing of fractures which cross-cut a rigid cap atop the conduit. When the fracture's strength is overcome by the building gas pressure below, it suddenly opens and high velocity gas escapes, producing high-frequency elastic waves typical of explosion quakes. Gas release also occurs in relation to periodic opening and closure of the fractures to produce repetitive

pressure pulses: this being the source of tremor. In both cases, varying quantities of fragmented material may be carried by the gas, which can be detected by the radar if their concentration is high enough. Moreover, the highly variable, constantly changing state of lava cap (e.g. thickness, fracture network and gas permeability) results in non-repeatable source conditions, and explains the complex relationship between tephra emissions and associated seismic signals.

II.3.2. Introduction

Arenal, a small stratovolcano (1,710 m a.s.l.) located in northern Costa Rica, has experienced near continuous effusive and explosive activity since its reactivation in 1968 (*Minakami and al*., 1969; *Cigolini and Borgia*, 1980). Since 1975, the activity has been concentrated in crater C, from which blocky basaltic-andesitic lavas continuously effuse (*Cigolini et al*., 1984; *Murillo and Ruiz*, 2004). In addition, pyroclastic flows and numerous small ash plumes (ascending $\leq$ 1-3 km above the crater) are emitted recurrently (*Cole et al*., 2005). The frequency of ash emissions in the 1980's and 1990's was nearly one event every 30 minutes (*Williams-Jones et al*., 2001), but this frequency has been progressively decreasing so that only a few per day were recorded during the time of our recording campaign in 2005. Arenal's lava discharge rate also fell from ~2 m^3/s in the 1980's to between 0.1 and 0.2 m^3/s in 2004 (*Wadge et al*., 2006), and a rigid degassed plug capping the conduit has developed (*Cole et al*., 2005).

A number of geophysical studies have been carried at Arenal in order to constrain its shallow structure and the mechanisms operating within it. Studies using seismic data have constrained the shallow velocity structure of the edifice (*Mora et al*., 2006), as well as the source mechanism of both tremor (*Benoit and McNutt*, 1997; *Lesage et al*., 2006) and long period signals (*Davi et al*., 2010). *Hagerty et al*. (2000) cross-correlated seismic and acoustic data, and achieved a detailed analysis of the waveforms to give further constraints on the generation of these signals. *Williams-Jones et al*. (2001) cross-correlated seismic data with both SO_2 fluxes (from COSPEC data) and Earth tides to investigate the link between degassing, seismicity, and the influence of cyclic drivers. No study, however, has been able to cross-correlate quantitative information regarding both the pyroclastic emissions and subsurface processes that drive the explosions.

We here quantify the exit velocity, mass-loading and kinetic energy proxies of pyroclastic emissions using ground-based Doppler radar (VOLDORAD), which we cross-correlate with broad band seismic data. We use these data to constrain a conceptual model which accounts for the complex interplay between tremor, explosion earthquakes and tephra emissions recorded in this study.

II.3.3. Background: seismic activity at Arenal

Arenal exhibits intense and varied seismic activity, including tremor, explosion quakes, long-period (LP) events, rockfall events, and (rarer) volcano-tectonic events. Tremor is the most common signal, it being recorded several hours per day on average. Two types of tremor are commonly distinguished depending on the way the energy is distributed across the spectra (*McNutt*, 2002): when the energy is evenly distributed with no dominant peak (generally confined to the 1-6 Hz band at Arenal), it is referred to as "spasmodic tremor"; if the spectra contains several regularly spaced peaks, composed of a fundamental frequency and its overtones, it is termed "harmonic tremor". The fundamental frequency at Arenal is generally in the range 0.9-2 Hz (*Hagerty et al*., 2000; *Mora*, 2003), and the frequencies of overtones are integer multiples of it. Tremor at Arenal shows striking characteristics, such as (*Lesage et al*., 2006): frequency gliding episodes (whereby the fundamental and corresponding harmonic frequencies fluctuate in time while maintaining their regular spacing, e.g. *Benoit and McNutt*, 1997; *Garcés et al*., 1998; *Hagerty et al*., 2000), frequency jumps (with either positive or negative increments), progressive transitions from spasmodic to harmonic tremor (with variable quantities of harmonic overtones), and coexistence of multiple frequency systems (with distinct spectral peaks and independent gliding). Several source models have been proposed to explain tremor at many volcanoes worldwide; at Arenal the clarinet model defined by *Lesage et al*. (2006) appears to be well-adapted to describe the complex behavior of the tremor. In particular, harmonic and spasmodic tremor are thought to have the same source mechanism, i.e. intermittent flow of gas through fractures in the cap atop the conduit. Frequency gliding is attributed to pressure fluctuations in the magmatic conduits (*Neuberg*, 2000; *Lesage et al*., 2006), which in turn depends on the state of the plug (i.e. its gas-permeability). The coexistence of different frequency systems, each evolving independently, may be the expression of different resonators, i.e. different conduits in the shallow feeding system.

Long-period (LP) transients and explosion quakes are regularly superimposed on the nearly continuous tremor, and are both characterized by spindle-shaped envelopes and narrow band-width (1-3 Hz) frequencies (*Chouet*, 1996; *Hagerty et al*., 2000). The coda may in some cases evolve into harmonic tremor (*Barquero et al*., 1992; *Benoit and McNutt*, 1997; *Hagerty et al*., 2000). Both LP and explosion quake signals are thought to have the same source mechanism, but with differing source depths. Following *Mori et al*. (1989), explosion quakes should occur at shallow levels within the conduit, allowing the propagation of an acoustic air wave which couples back to the ground as a high frequency seismic phase which arrives shortly after the P-wave onset. LP events, on the other hand, should occur at greater depths in the conduit, preventing the propagation of an acoustic air wave. Because there is probably no fundamental difference in their mechanisms, we follow *Lesage et al*. (2006) and consider both LP events and explosion quakes as part of the same type of event, defined as "explosion quakes". Note that this term will refer to this particular seismic signal, regardless of whether it is accompanied by tephra emission or not. On the contrary, the term "eruptive event" will refer to tephra emission, regardless of the presence and type of associated seismic signal.

High frequency events are also frequently observed and show a progressive onset followed by a progressive decay, generally lasting 50-180 sec. Energy is well staggered between 5-35 Hz with no dominant frequency and a sharp onset in the 5-15 Hz band. At Arenal, radar signals are always recorded ahead of these seismic signals. *Johnson and Lees* (2000) described similar events at Karymsky volcano, and suggested that they may result from energetic gas jetting when the vent is unobstructed by debris.

Volcano-tectonic events are less frequent at Arenal as the open state of the vent prevents the accumulation of high stresses. The rarity of such events also suggests the absence of a vast and shallow magma storage body (*Mora*, 2003).

II.3.4. Data acquisition and processing

VOLDORAD 2 (Volcano Doppler Radar) is a ground-based, pulsed, Doppler radar specifically designed for active remote sensing of volcanic pyroclastic emissions (*Dubosclard et al*., 1999, 2004; *Donnadieu et al.*, 2003, 2005, 2011; *Gouhier and Donnadieu* 2008, 2010; *Valade and Donnadieu*, 2011). It was set up at an altitude of about 690 m a.s.l, around 2.3 km west, and downwind, of active crater C (Figure II.8a), from where we recorded activity for

several hours per day between February 10 and 22, 2005. The antenna beam was pointed in the crater azimuth, and then lowered until ground echoes appeared in the Doppler spectra, indicating that the base of the beam was aligned with Arenal's summit. At Arenal, there is no deep crater, but rather an irregular dome-like surface. This ensures that the beam skims the eruptive vent. The radar should thus capture all ash emissions, provided the particle concentration is above the detection threshold (ca. 15 g/m^3 for 1 mm particles, *Donnadieu et al.*, 2011). The radar beam is divided into successive sampling volumes, termed range gates, whose radial resolution depend on the pulse duration (τ), and whose location and azimuthal resolution depend on the beam aperture (conical 9° beam width) and the distance to the radar. During the recording campaign, data were recorded in range gates with radial resolutions of 120 m (τ = 0.8 μs), and with slant distances ranging between 2007 and 2847 m (i.e. between gates G_{2007} and G_{2847}). Two range gates were located above the active crater area: gates G_{2607} and G_{2727} (Figure II.8a). Volcanic ejecta crossing the beam scatter the electromagnetic signal repeatedly transmitted by the radar (sampling rate 100 μs^{-1}), part of which is scattered back to the radar and can be recorded. Real-time processing of this signal gives information on: (1) the backscattered power (which is a complex function of the number and size of the ejecta, and so is a proxy for the mass loading of the pyroclastic emissions), and (2) the radial velocity of the ejecta (i.e. the component of the exit velocity projected along the beam axis). These data are displayed for each range gate as Doppler spectra, representing the backscattered power (P in dB) versus the radial velocity (V_r in m/s). Processing of the Doppler spectra gives, for each range gate, two sets of parameters: positive parameters, which refer to signal backscattered by particles with a radial component of motion away from the radar, and negative parameters, which refer to particles with a radial motion towards the radar.

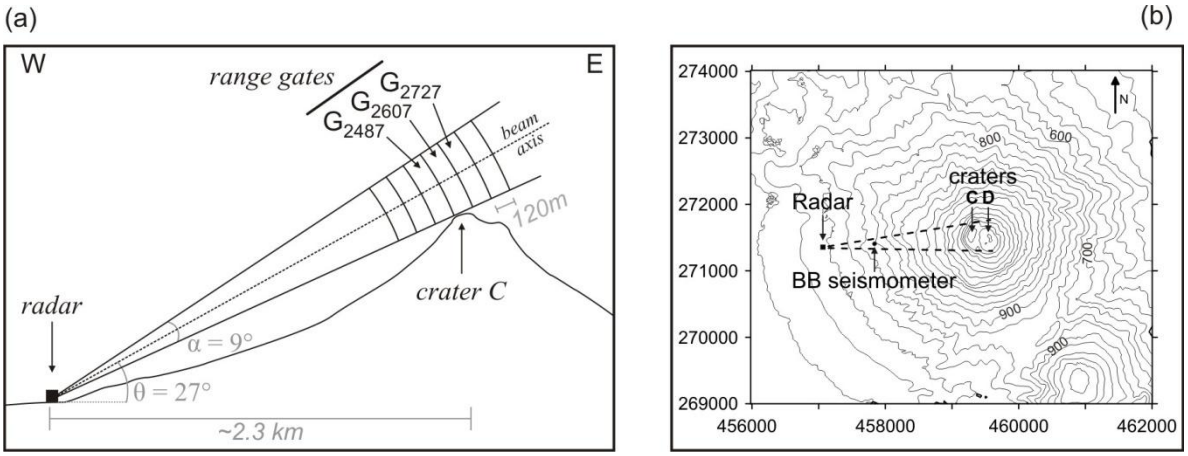

Figure II.8. (a) Radar beam geometry during the recording campaign. (b) Location map of the broad-band seismometer and Doppler radar. At the time of the recording campaign in February 2005, the estimated altitude of crater C is 1710 m a.s.l (Wadge et al., 2006).

For each range gate, the following parameters were defined and calculated: backscattered powers (P_+, P_-, and $P = P_+ + P_-$), and maxima of radial velocities (V_{+max}, V_{-max}) (*Dubosclard et al.*, 2004). We also implemented a proxy for the kinetic energy E_k of the tephra emission following:

$$E_k = \int_{V-\max}^{V+\max} (P(V) \cdot V^2).dV \qquad \text{II.1}$$

in which V_r is the radial velocity of particles and $P(V_r)$ is the power backscattered by all particles with radial velocity V_r.

Seismic observations were carried out 1.8 km west of the active crater using a permanent 30-sec GURALP CMG-6TD broadband seismometer (Figure II.8b). The vertical component was generally used, because tremor and explosion quakes are mainly composed of Rayleigh waves (*Mora et al.*, 2006; *Zobin et al.*, 2009), which are polarized in the vertical plane.

Detailed analyses of radar and seismic data were carried out using *Matlab*-based software (*Mora et al.*, 2009), we specifically designed for the purpose of this study. This software enables the display of the different data types on a graphical interface and the application of high resolution time-frequency methods (*Lesage et al.*, 2009) to extract the main features from the different geophysical data sets collected. During the 11-day-long field campaign, a total of 132 eruptive events were recorded by the radar, from which we defined a subset of 68 events comprising medium- and large-amplitude radar events, and/or the events having a good seismo-radar temporal correlation.

II.3.5. Results

We herein consider the correlation between radar and seismic records on two distinct time-scales: (1) over the time scale of seconds to minutes, to analyze the coeval seismic and radar signals during individual pyroclastic emissions, and (2) at the time scale of several hours, to understand how subsurface and surface activity may interact on longer time scales.

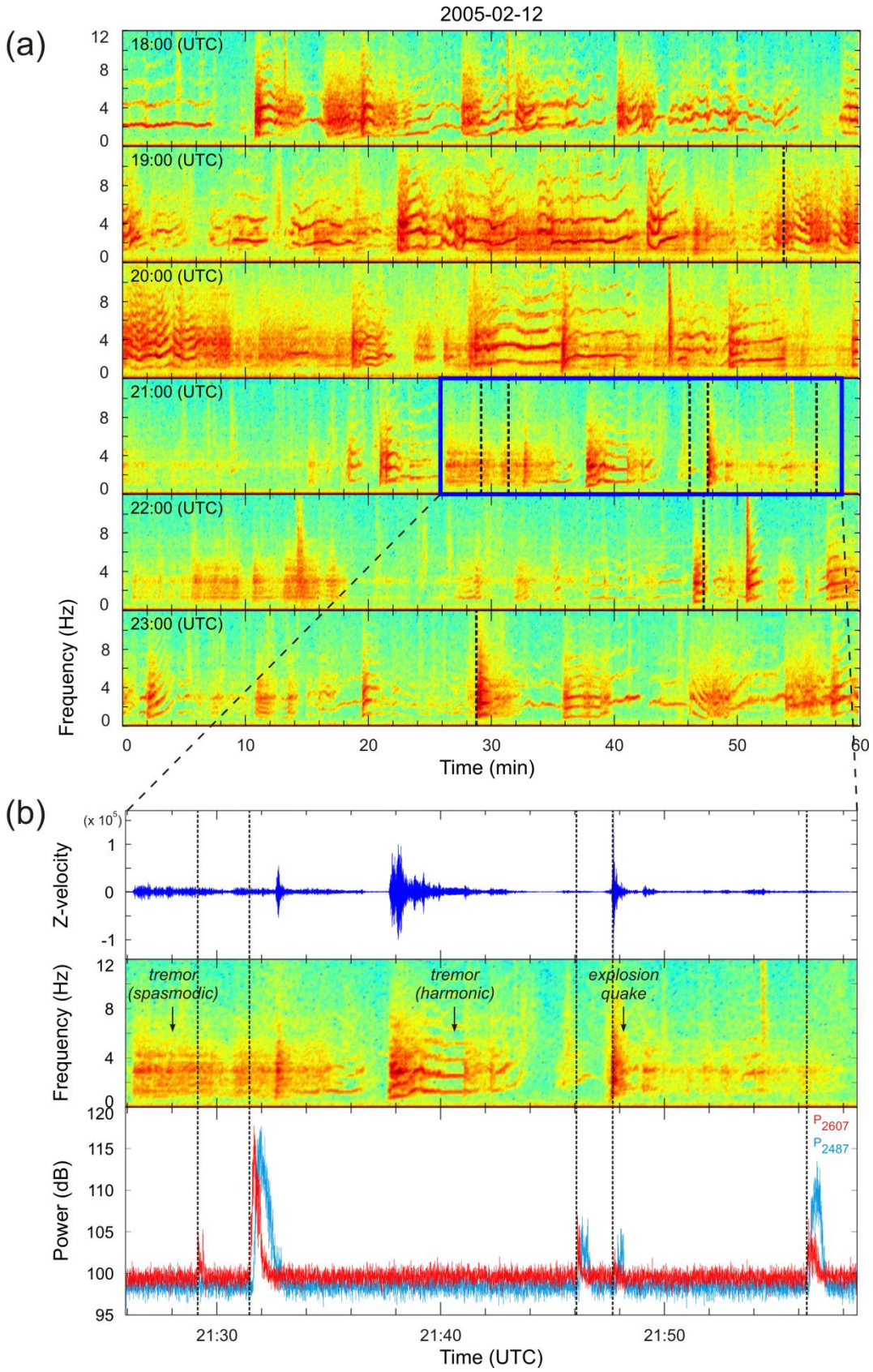

Figure II.9.(a) Spectrograms of the seismic signal recorded on February 12, 2005 from 18:00 to 24:00 UTC. Each line corresponds to one hour. Vertical dashed lines indicate radar eruptive events. The sequence enclosed by the box is enlarged in (b), which presents from top to bottom: the seismic trace (vertical component), the corresponding Fourier spectrogram, and the power backscattered to the radar in gates G_{2607} (red) and G_{2487} (blue).

II.3.5.1. Short-term correlation between seismic and radar observations

Spectrograms were computed from the seismic data, and radar signals recorded during emissions were traced over it to visualize how surface and sub-surface activity were related on short time scales (Figure II.9). Figure II.9a shows spectrograms from six consecutive hours of seismic data recorded on the 12th February 2005, with eruptive events detected by the radar being indicated by vertical dashed lines. The figure illustrates the variety of seismic activity discussed in Section II.3.3, with sequences of both harmonic and spasmodic tremor, multiple frequency systems that glide independently, numerous explosion quakes, and periods of quiescence all being apparent. Surprisingly, the surface tephra emissions are poorly correlated with this seismic activity. Indeed, tephra emissions detected by the radar are not always associated with distinct seismic events, and emissions can be found associated with explosion quakes (e.g. 23:28:48 UTC), in the middle of tremor sequences (e.g. 21:31:29 UTC), and during periods of very weak seismic activity (e.g. 21:56:23 UTC). This observation applies throughout the entire record in which, of the 68 radar events subset, ~44 % of the signals are associated with explosion quakes, ~43 % occur during episodes of tremor, and ~13 % occur during periods when only background seismic noise is recorded. Figure II.9b shows a magnification of the sequence identified by the box in Figure II.9a, and highlights that the strongest ash emissions (i.e. the events giving the highest backscattered power, such as that occurring at 21:31:29 UTC) do not occur when they are most expected (i.e. during high amplitude explosion quakes, at 21:37:30 UTC, for example).

Hence, it seems that there is no simple relationship between tephra emission and coeval seismic events. Pyroclast emissions do not have a unique repetitive seismic signature and, more importantly, emissions cannot always be identified by the seismic signals alone, even for emissions with high mass loadings.

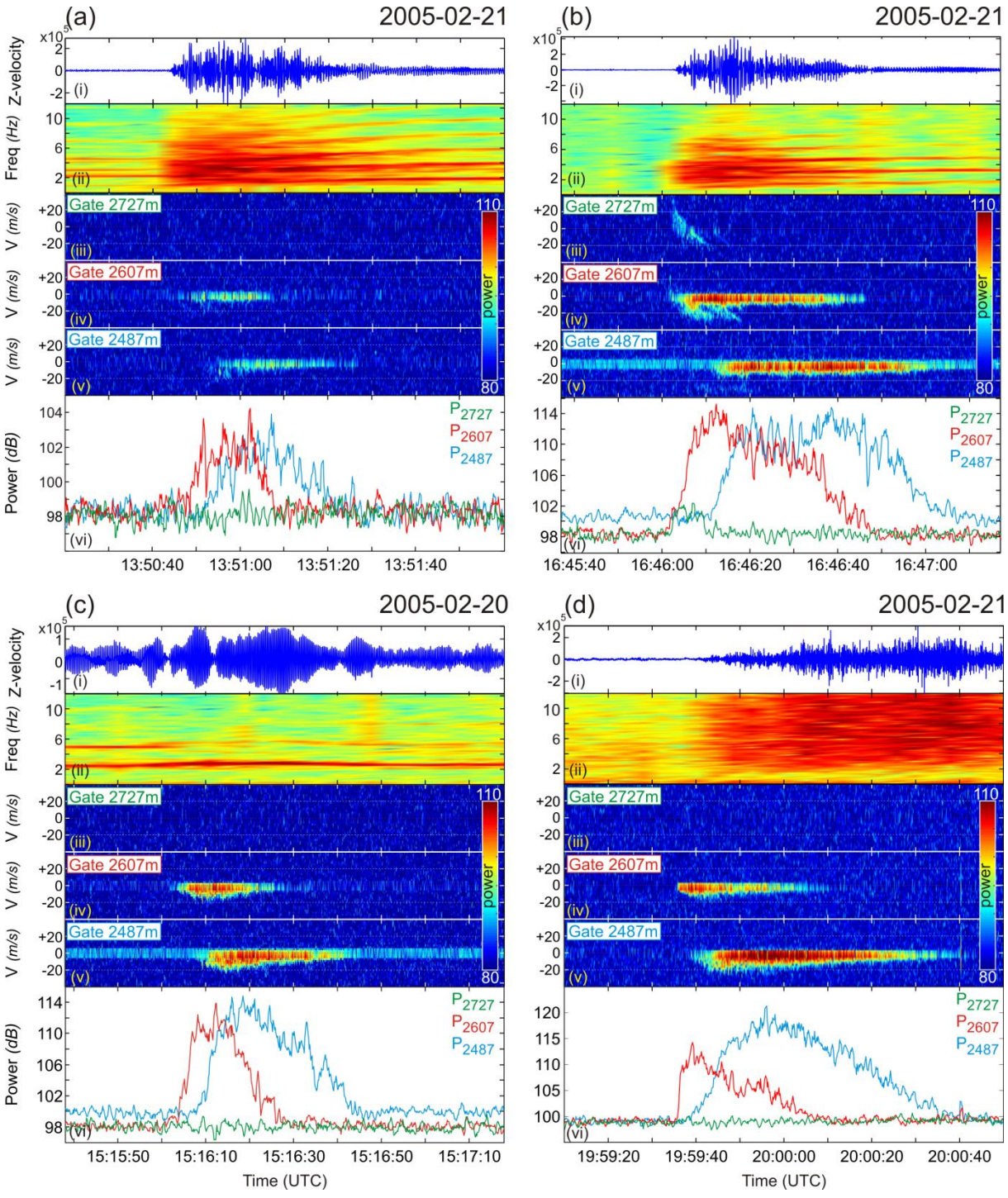

Figure II.10. Four representative seismic events and the associated radar signal: a) and b) explosion quakes, c) harmonic tremor, d) no seismic signal at emission onset, post-onset high frequency signal only. Each panel displays from top to bottom: (i) the seismic record, (ii) the seismic spectrogram, (iii - v) the Doppler radargrams (time-velocity distribution of backscattered radar signal) in gates G_{2727}, G_{2607}, and G_{2487}, and (vi) the corresponding time series of backscattered power in gates G_{2727} (green), G_{2607} (red), and G_{2487} (blue).

The radar signals and associated seismic records show a large variability in their respective characteristics. Radar signals show variable backscattered power (varying by more than 30 dB), particle velocities, and Doppler signatures (i.e. time-velocity distribution of the power), which respectively reflect the diversity of the emissions' mass loading, impulsivity and dynamics. Figure II.10 displays, for several eruptive events, (i) the seismic trace, (ii) its spectrogram, (iii-v) the Doppler radargrams (time-velocity distribution of backscattered power) for gates G_{2727}, G_{2607}, G_{2487}, and (vi) the radar backscattered power time series for the same gates. Examples (a) and (b) are explosion quakes with similar seismic amplitudes, durations and spectral contents. However, the corresponding radar signals are quite different in terms of both backscattered power and radial velocity. While the event given in Figure II.10a has a maximum backscattered power that is +7 dB above the noise level and has no positive velocities, the event of Figure II.10b has a higher backscattered power (+17 dB), and radial velocities that exceed 20 m/s. Moreover, the radargrams exhibit distinctive Doppler signatures. Event (b) shows distinctive diagonal streaks during the first few tens of seconds following the eruptive event onset, which is not the case for event (a). These streaks are short-lived (~10 s), are spread across a large velocity range (reaching more than +20 m/s and -20 m/s in gates G_{2727} and G_{2607}, respectively), and seem to superimpose a longer–lived signal (tens of seconds) with low negative radial velocities (less than -10 m/s). *Valade and Donnadieu* (2011) have modeled these short-lived diagonal streaks and show that they result from ballistic blocks crossing the range gates (see Chapter IV). The longer-lived signal (observed in events (a) to (d)) instead results from the slow transit of the ash plume through the beam. Hence, although the two events (a) and (b) have similar seismic signals, the differences in the radar signals reveal two emissions with very different properties, in terms of mass loading, duration, impulsivity and eruptive dynamics. An interpretative sketch of the dynamics of these two events in terms of spatial motion within the range gates, is given in Figure II.11. In the case of the event in Figure II.10c, a strong radar signal (maximum recorded power ~ +17 dB, similar to event (b)) occurs without perturbing the harmonic tremor. The event of Figure II.10d produces an even stronger signal (with a maximum recorded power of +22 dB). This event is not preceded by any seismic signal, but is followed by a high frequency emergent seismic waveform which begins a few seconds after the radar signal onset. The seismic signal could be interpreted as a rockfall signal, however we doubt that the associated radar signal results from a rockfall-generated cloud. Indeed, the radar signal onset is very impulsive (i.e. sharp P_{2607} increase) and exhibits strong backscattered power (+22 dB), suggesting that a highly concentrated ash plume rapidly entered the beam. In

the case of rockfall-originated clouds, we expect much less backscattered power due to both: (i) the fine granulometry of the elutriated material, and (ii) the low particle concentration (compared to ash plumes resulting from an explosive event). Moreover, the radar signal begins before the seismic signal, which is not consistent with a cloud of rockfall-origin. During the recording campaign of 2005, rockfalls were concentrated in a ravine perpendicular to the radar beam axis. This location would increase the time needed for the cloud to rise from its source and drift into the beam. Hence we conclude that this was a highly loaded ash plume, emitted without an associated seismic signal (unlike events (a) and (b)).

All of these observations show that the mass loading (i.e. backscattered power), exit velocities, and dynamics of the tephra emissions at Arenal are highly variable, and do not show apparent correlation with the coeval seismic signal amplitudes or spectral contents.

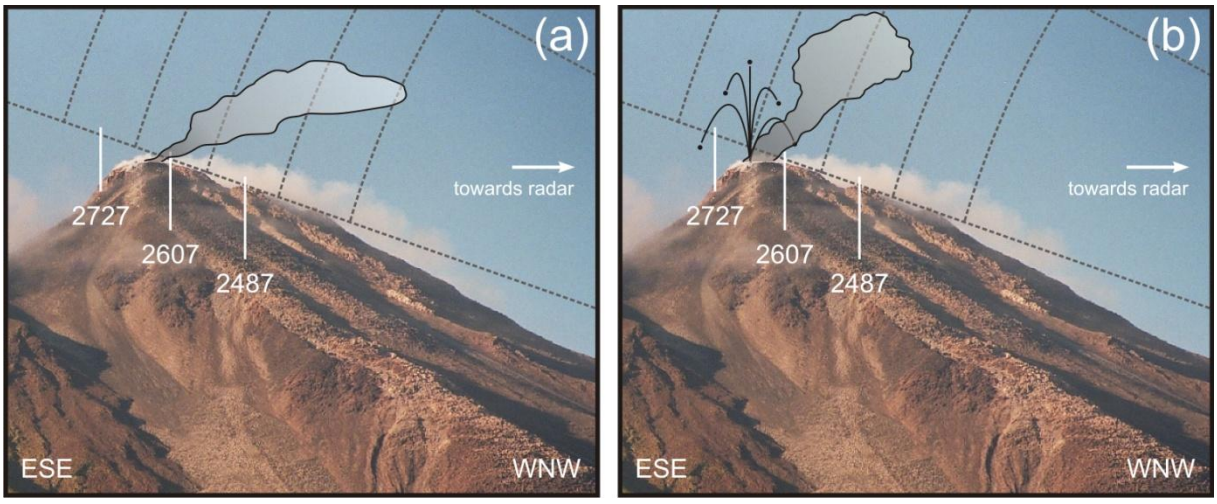

Figure II.11. Schematic illustration of pyroclastic emission dynamics, interpreted in terms of spatial motion in the radar range gates. (a) Weakly loaded ash plume drifts in trade winds towards the radar, resulting in Doppler radargrams which exhibit low negative velocities and low backscattered power (e.g. Figure II.10a iii-v). (b) Strongly loaded ash plume accompanied by ballistic projections. In this case (e.g. Figure II.10b), the resulting radargrams show up as an additional signal to the plume signature described previously; the ballistics causing diagonal streaks which exhibit high positive velocities (mostly in gate 2727 m) that progressively shift towards negative velocities.

It is worth noting that both paired and pulsed emissions are commonly observed. Paired eruptions refer to eruptions less than 3 minutes apart and represent 22 % of all the recorded radar events. In most cases, the second event's power amplitude is similar to, or lower than, that of the first (e.g. Figure II.9b 21:46 UTC); only in some rare cases is it significantly higher (e.g. Figure II.9b 21:29 UTC). The eruptive sequence shown in Figure II.12 shows a striking example of two paired eruptions, highlighting the delay which can be observed between successive tephra emissions. Indeed, at 15:07:15 UTC a powerful radar signal is recorded and

is clearly associated with an explosion quake of large amplitude which evolves into harmonic tremor. Shortly after however (15:08:54 UTC), a strong second radar pulse is recorded, yet with no clear seismic counterpart. A similar pattern (i.e. first pulse with seismic "triggering event" followed by a second pulse without) is observed only 10 min later, highlighting the ability for the system to regenerate overpressures over short time scales.

Pulsed emissions, on the other hand, refer to eruptive events which comprise several pulses, spaced by a few seconds only, as evidenced by the successive streaks in Figure II.10b (iv). From a seismic point of view, these pulses are not recorded, highlighting once again the complex relationship linking the pyroclastic emissions and the coeval seismic signals at Arenal.

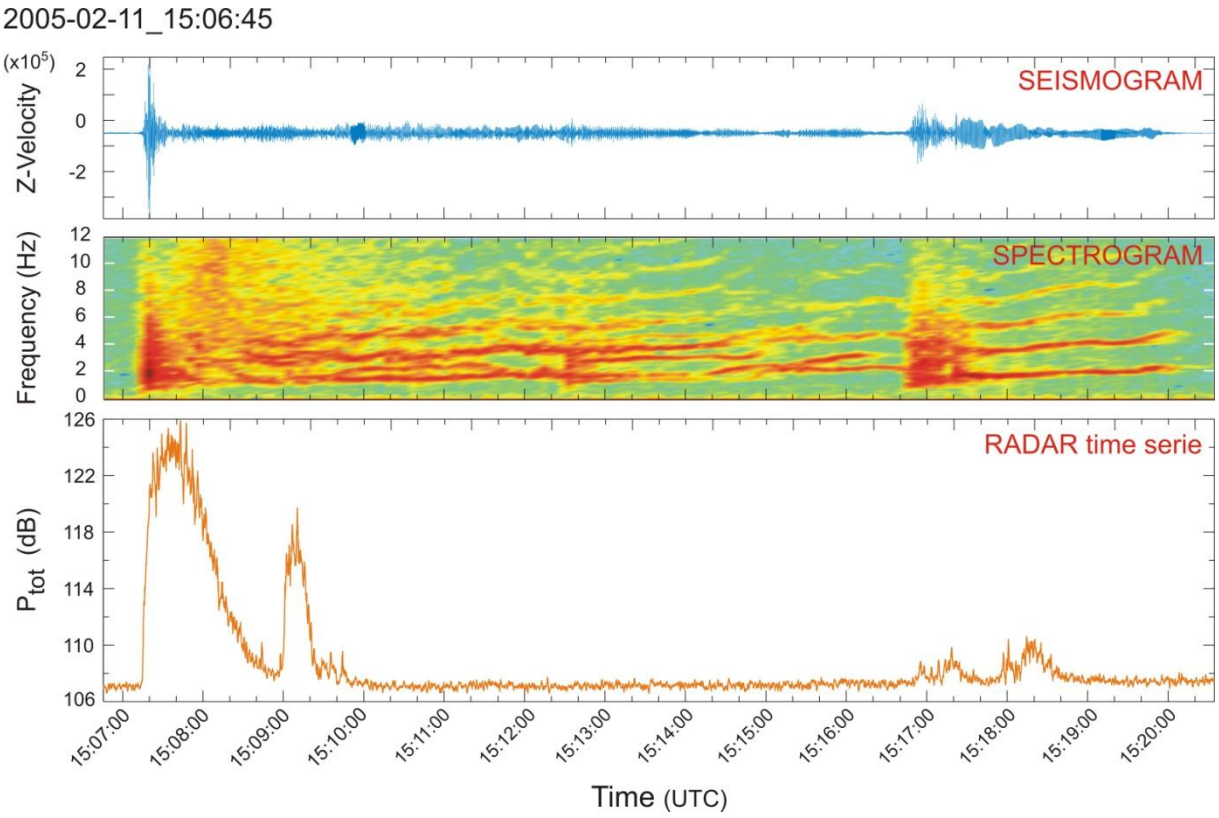

Figure II.12. Eruptive sequence recorded at Arenal on February 11, 2005. Top plot: vertical velocity seismogram. Middle plot: spectrogram of the velocity seismic trace. Bottom plot: radar P_{tot} time series (i.e. backscattered power from all the range gates).

Careful observation of the harmonic tremor in the eruptive sequence of Figure II.12 reveals several systems of overtones with independent frequency gliding. Indeed, the harmonic tremor inherited from the first explosion is overlapped at 15:12:30 UTC by another whoosh which has its own set of frequencies. Both frequency systems evolve independently with time, with an overall increasing trend (positive frequency gliding). *Lesage et al.* (2006) suggest that the coexistence of different frequency systems evolving independently may be the expression

of different resonators, in other words different conduits in which pressure fluctuations may evolve independently depending on the state of the vent at the surface.

Seismic and radar energy proxies were computed for all pyroclastic emissions associated with explosion quake seismic signals. The maximum seismic amplitude (vertical component, A_s) was considered as a suitable proxy for the intensity of the sub-surface process. The use of seismic amplitudes (i.e. velocity trace amplitude) rather than seismic energies (i.e. time-integration of the squared velocity) was preferred because many explosion quakes occurred during background tremor (e.g. Figure II.10c), which makes the estimation of the explosion energy problematic. For the radar signal, we computed the kinetic energy, as defined in Section II.3.4, for the two gates above the active crater (i.e. $E_{k\ 2607}$ and $E_{k\ 2727}$), and define their sum as the kinetic energy (E_k) of the pyroclastic emissions. Figure II.13 displays the maximum seismic amplitude versus the maximum kinetic energy for these events. The data points show a positive trend, which is particularly apparent in the cluster of points in the upper left corner of the plot (i.e. those having A_s between 10^5 and 10^6, and E_k between 10^3 and 10^4, in arbitrary units). The events of this cluster share an emergent onset, a relatively weak power amplitude (< 12 dB), and low radial velocities (< 16 m/s). Despite this weak positive trend, Figure II.13 shows a wide scatter of data points indicating that the ratio between subsurface seismic energy and surface kinetic energy is highly variable. For example, although the events in Figure II.10a and b (respectively indexed 100 and 104 in Figure II.13) have similar seismic amplitudes, they have considerably different kinetic energy values. Whatever the type of energy proxies used for the seismic and radar signals (signal amplitudes, time-integrated energies, various frequency bands ...), they all show similarly poor correlation. This suggests poor scaling between the seismic energy and the energy of the subsequent emission. Similar observations were reported by *Johnson et al.* (2005) at Tungurahua. Nevertheless, pyroclastic emissions may be the result of long pressurization processes, which can only be revealed by examining data records on longer time-scales, as reported next.

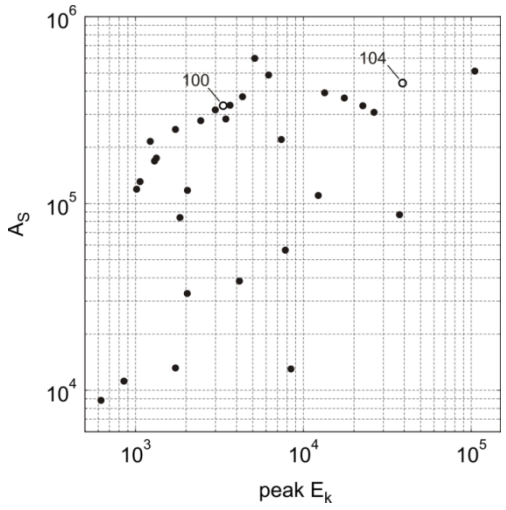

Figure II.13. Maximum seismic amplitude A_s (vertical velocity component) versus radar peak amplitude of the kinetic energy proxy E_k, for all the tephra emissions associated to explosion quake events. Values of A_s and E_k are in arbitrary units. Events indexed 100 and 104 refer respectively to the events displayed in Figure II.10a and b.

II.3.5.2. Long-term correlation between seismic and radar observations

The time-averaged amplitude of the seismic trace, termed RSAM (Real-time Seismic Amplitude Measurement, *Endo and Murray*, 1991), has proved capable of revealing long-term cyclic patterns (e.g. *Denlinger and Hoblitt*, 1999). The cumulative squared amplitude of the seismic trace, or cumulative RSEM (Real-Time Seismic Energy Measurement, *De la Cruz-Reyna and Reyes-Dávila*, 2001), enables a better visualization of the seismic energy release rate through time. RSAM, RSEM and E_k time series were thus computed and plotted together to search for relationships between the seismic activity and the tephra emissions on time scales of several hours. Figure II.14a and b show 10 hours of continuous seismic and radar recordings on the 16th February 2005. The RSAM plot displays successive transients with sharp onsets followed by slow decays, which mostly relate to tremor amplitude fluctuations. When an explosion quake triggers a tremor sequence, the RSAM shows a high peak marking the transient onset. The cumulative RSEM curve, on the other hand, shows a gradual increase, punctuated by sudden increments (or steps) when strong explosion quakes are recorded. Similarly, the E_k curve shows successive peaks (or steps in the cumulative E_k curve), indicating the occurrence of pyroclastic emissions with strong kinetic energies. Comparison of Figure II.14a and b shows poor correlation between the seismic and radar signals: neither the fluctuations (i.e. amplitude oscillations in the RSAM and E_k curves), nor the sudden energy releases (i.e. the steps in the RSEM and E_k cumulative curves), show correlation in time or amplitude. This was observed throughout the entire recording period,

indicating that there is no simple relationship between the energy of tephra emissions and the energy of seismic vibrations, even on daily time scales.

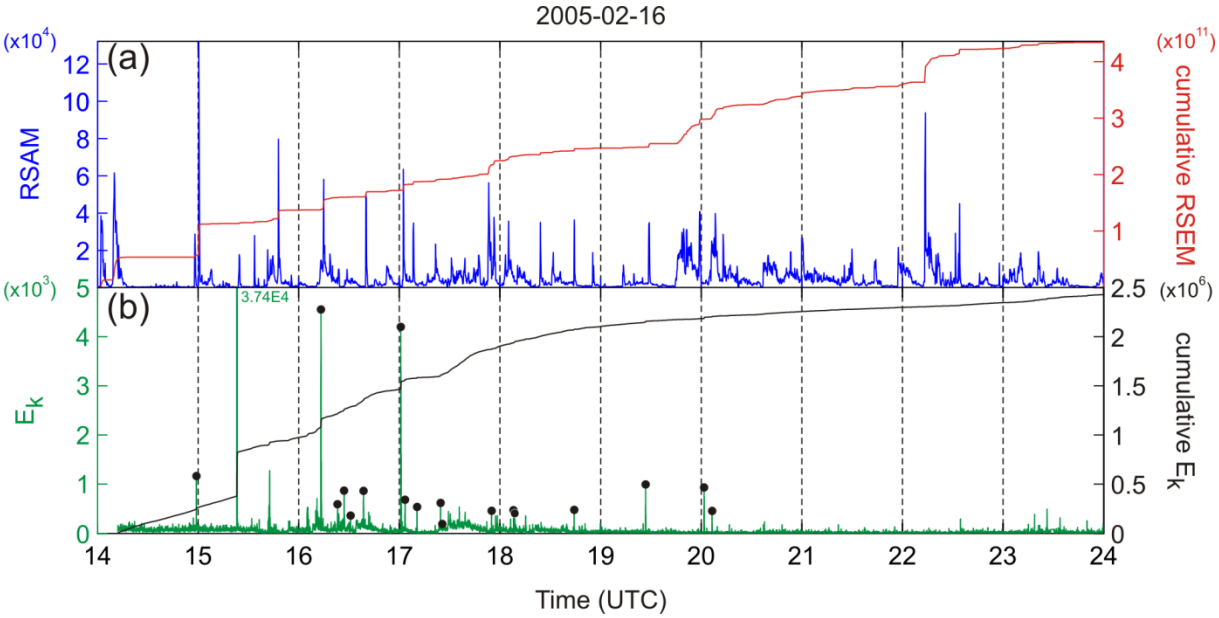

Figure II.14. (a) RSAM and cumulative RSEM recorded on the 16th February 2005, and (b) radar kinetic energy (E_k) with its cumulative curve. The kinetic energy curve (E_k) is filtered with a running average, and the recorded eruptive events are indicated by black dots. The peaks which are not topped by black dots are non-eruptive peaks (e.g. rain, noise …). For visualization purposes the E_k ordinate axis was clipped at $E_k = 5 \times 10^3$, truncating the major radar event at 15:23 UTC ($E_k = 3.74 \times 10^4$, in arbitrary units).

Classically, exit velocities of volcanic ejecta are thought to be related to overpressures in the volcanic conduit prior to the explosion (*Wilson*, 1980). If pressure builds-up progressively beneath a cap which obstructs degassing, and if this pressure is released during eruptive events, then the longer the repose intervals between successive eruptions, the longer the period of pressurization and, thus, exit velocities should be higher. Note that this statement holds only if we assume that passive degassing is minor compared to the degassing during an explosion. We consequently investigated whether the measured exit velocities were proportional to the repose interval separating successive emissions. Figure II.15 plots the maximum positive radial velocity recorded in gate G_{2607} as a function of repose time, and shows a wide scatter, indicating no correlation between repose time and exit velocity. This suggests that overpressures do not increase steadily during repose intervals, probably because of the fractured nature of the lava cap which allows gas to escape between eruptive events. Figure II.15b displays the maximum power recorded in gate G_{2607} as a function of repose time. Again no correlation is observed, which indicates that ejecta mass loadings do not appear to be controlled by the duration of repose.

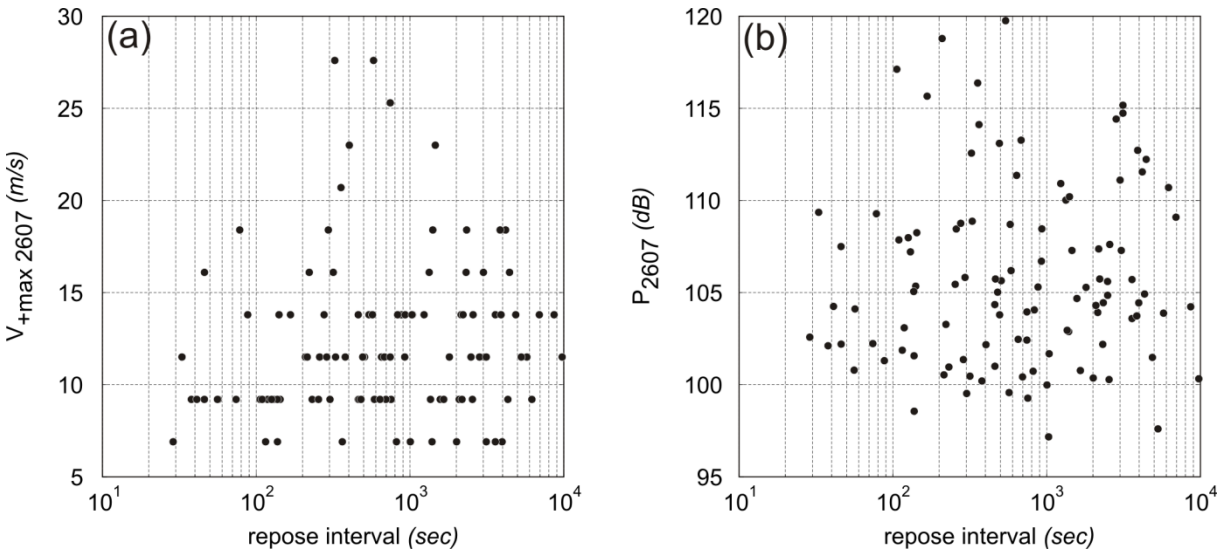

Figure II.15. Relationship between the repose interval separating successive tephra emissions and (a) their maximum radial velocities, (b) their maximum backscattered power. Values are taken from the main gate G_{2607}.

In summary, analysis of simultaneous seismic and radar recordings show complex, non-repeatable relationships, on both short and long time scales. Tephra emissions are not systematically associated with a specific type of seismic signal (Figure II.9), and show variable properties (i.e. mass loading, exit velocity, dynamics) that do not correlate with seismic amplitude or spectral content (Figure II.10). When considering the emissions associated with explosion quakes, poor scaling is found between the kinetic energy of the emission and the amplitude of the seismic signal (Figure II.13). Even on daily time scales, we find that the energy of the emissions do not correlate with fluctuations in the seismic amplitude and energy (Figure II.14).

II.3.5.3. Glance at data from other recording campaigns

Although the intensity of Arenal's eruptive activity has been clearly decreasing since the late 1990s (*Wadge et al.*, 2006), its activity during the 2005 campaign was relatively weak in comparison to the usual activity (Mauricio Mora, personal communication). In 2009, another recording campaign was carried out with the deployment of similar seismic and radar instrumentation. The collected seismic and radar data were analyzed with the tools described in section II.2. The analysis shows the same variability which was observed with the data from the 2005 campaign. Figure II.16 intends to illustrate this variability, with scatter plots showing the lack of relationship between the seismic amplitude and various radar parameters extracted from the gate above the main vent (i.e. kinetic index E_k, backscattered power P, and

maximum positive radial velocity V_{+max}, from gate 4148 m). Note that the events presented in these plots have been selected on the basis of their seismic amplitude (courtesy of Philippe Lesage). Similar plots have been constructed with a number of other parameters (such as the seismic energy, radar parameters from other gates, etc.), but all show the same scattering. The same observation holds for the data from the 2004 campaign at Arenal, which also show dispersion between the seismic amplitude and the radar power of several events (*Donnadieu et al.*, 2006). Thus we can conclude that the highly variable relationship between seismic and radar data not only holds for the 2005 campaign, but for the 2004 and 2009 campaigns as well.

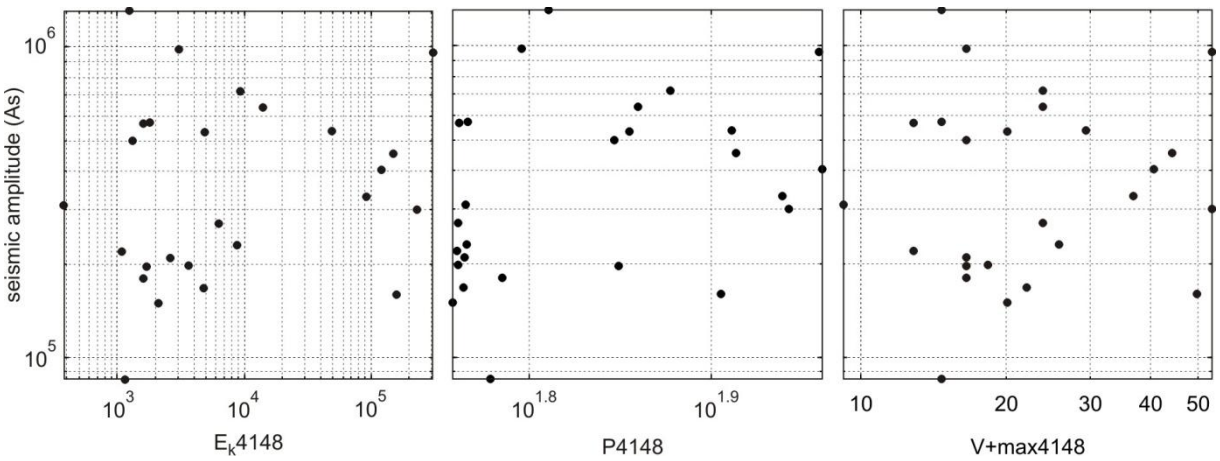

Figure II.16. Relationship between the seismic amplitude and various radar parameters (extracted from gate 4148 m located above the eruptive vent): from left to right, kinetic energy, the total backscattered power in the gate, and the maximum positive radial velocity. The events plotted were collected between January 27 and February 25, 2009.

II.3.6. Existing models for Arenal-type eruptive activity and associated geophysical signals

Several models have been proposed to account for the style of repeated, mildly explosive eruptive activity and associated geophysical signals at persistently active volcanoes such as Arenal. The physical processes involved in each model depend mainly on the magma viscosity. The bubble-bursting model is widely accepted at volcanoes with low-viscosity magmas. Laboratory experiments (*Jaupart and Vergniolle*, 1988; *Ozerov*, 2010) model the phenomenon as bubbles rising up the conduit to burst intermittently at the surface. This mechanism, however, requires low viscosity magma (10^3 and 10^5 Pa/s, *Ozerov*, 2010) if the slugs that generate the explosion are to ascend buoyantly through the magma column and burst at the free surface. At Arenal these conditions are not fulfilled: average viscosities of

lavas close to the crater range between 10^5 and 10^6 Pa/s (*Cigolini and Borgia*, 1980; *Cigolini et al*., 1984; *Bertolino et al*., 2009), and the vent is capped by a degassed, cooled plug of lava (*Cole et al*., 2005).

The pressure build-up model is often invoked to explain repeated, discrete, short-lived explosions characteristic of the Vulcanian activity. These are attributed to the steady build-up of pressure below a plug obstructing the conduit, which is suddenly released when the plug's resistance threshold is overcome (*Stix et al*., 1997; *Melnik and Sparks*, 2002; *Yokoo et al*., 2009). This sudden failure and decompression causes both brittle failure of the plug and rupture of numerous small gas bubbles trapped in the viscous melt, both of which generate fine ash. At Arenal, petrological observations show that a rigid degassed cap has progressively developed and muzzled the summit vent (*Cole et al*., 2005). *Cole et al*. (2005) studied tephra clast morphologies and reported a dominance of blocky textured clasts over fluidal ones, thus arguing for fragmentation of rigid degassed magma with only a minor molten component, typical of vulcanian-type explosions. The presence of such a degassed body could act as a plug, which blocks the vent and impedes the release of gas.

The idea that such plugs can possess a network of fractures has led several authors to believe that the small pathways represented by the fractures can control the degassing periodicity and, in turn, the associated geophysical signals (*Hellweg*, 2000; *Johnson and Lees*, 2000; *Lesage et al*., 2006). The soda-bottle model was proposed by *Hellweg* (2000) as a possible source model for Lascar's harmonic tremor and cyclic degassing behavior. Following *Soltzberg et al*. (1997), *Hellweg* (2000) described how a small opening in a soda bottle may generate cycles of pressure drop beneath the cap, which triggers bubble nucleation and ascent. *Johnson et al*., (1998) and *Johnson and Lees* (2000), on the other hand, proposed a mechanism analogous to a pressure-cooker for Karymsky, in which the plug atop the conduit acts as a valve. In this case, harmonic tremor is the result of rhythmic gas release through the valve, producing source pulses that are sufficiently regular to generate harmonics. More recently, *Lesage et al*. (2006) proposed a process similar to that of a clarinet to explain Arenal's tremor. This model is close to the pressure-cooker idea of *Johnson and Lees* (2000) in the sense that both suggest that gas periodically escapes through fractures in a solid plug. The clarinet model, however, includes a stabilization mechanism for the pressure pulses. As fractures open intermittently, pressure waves are emitted in the conduit, which allow a standing pressure wave to be maintained. This, in turn, controls the pressure state below the plug and consequently the fracture oscillations. This feedback is thought to be an efficient way to produce pressure

transients with a stable repeating period, responsible for the harmonic tremor (*Rust et al.*, 2008). Lack of period stability, however (if rubble chokes the fractures for instance), would result in spasmodic tremor. If the repeat frequency slowly varies with time, the spectral peaks will also vary, and appear as frequency gliding episodes. Nevertheless, if the clarinet-model is an adequate model for the source of tremor at Arenal, it does not explain the source mechanisms of the explosion quakes.

Stick-slip movement of the uppermost part of the conduit has been proposed as a possible conduit model for several volcanoes with high-viscosity magmas, such as Soufriere Hills (Montserrat) and Santiaguito (Guatemala). *Denlinger and Hoblitt* (1999) first suggested that the cyclic eruptive behavior at Soufriere Hills might be controlled by boundary conditions along the upper part of the conduit, where stick–slip boundary conditions would generate periodic conduit flow. Field evidence (at Santiaguito, Guatemala, *Bluth and Rose*, 2004) and numerical modeling (*Gonnermann and Manga*, 2003) have suggested that non-explosive fragmentation of magma near conduit walls (where strong shear-stress is expected) could generate fine ash during slip events and result in repetitive ash plumes during stick-slip cycles, a hypothesis which was supported by a ring-shaped vent structure and ash emission patterns observed at Santiaguito (*Bluth and Rose*, 2004; *Sahetapy-Engel and al.*, 2008, 2009). Santiaguito, in particular, is very similar to Arenal in terms of eruptive style, intensity and frequency. Both volcanoes show repeated low energy explosions (several per day), sending ash-plumes up to $\leq$ 1-4 km, occasionally generating small pyroclastic flows, with a viscous lava cap plugging a conduit from which lava flows continuously extrude. However, at Arenal the characteristic vent structure and emission pattern reported for Santiaguito have not been observed. Furthermore, the constantly evolving crater morphology and the multiplicity of the feeding conduits at Arenal suggest that the persistence of such annular stick-slip zones is unlikely. However, we cannot exclude the possibility that shear-induced fragmentation may occur locally, along limited surfaces of conduit walls.

In summary, pressure build-up under a viscous degassed cap, which is crosscut by fractures, seems the most adequate model to characterize the eruptive periodicity and associated tremor signal at Arenal. Nevertheless, the mechanism explaining the explosion quakes, and the way these are related to the pyroclastic emissions remains unclear. Hence for now, no model can fully account for the complexity of Arenal's activity.

II.3.7. Discussion

The joint observation of gas and ash emissions by seismic and Doppler radar measurements reveals complex behavior at Arenal. The seismicity displays a great diversity of event types, which include tremor (both spasmodic and harmonic, with complex frequency gliding episodes) and explosion quakes (of variable amplitude, sometimes followed by a harmonic tremor coda). The radar measurements also reveal great variability in the mass loading and exit velocities of pyroclastic emissions. However, there is poor correlation with the seismicity, and while some mild explosion quakes observed in the seismic records are not accompanied by ash emission, some radar events are not coeval with a seismic signal. Sometimes ash emissions occur during harmonic tremor, or are associated with high frequency [5-35 Hz] seismic events. When pyroclastic emissions and explosion quakes are concomitant, low correlation is obtained between the kinetic energy of the emission and the seismic amplitude. Moreover, no clear relationship can be observed between repose time and exit velocity of solid particles or mass loading of the plume. All of these observations point to a mechanism of gas and ash emission that is highly variable and probably very sensitive to small perturbations in the system.

II.3.7.1. Conceptual model

To explain these observations, we propose the conceptual model of Figure II.17. According to this model, fractures in the solid plug control degassing, which in turn controls the seismic signal. If gas release is frequent and intermittent, repetitive pressure pulses will generate low-frequency tremor signal, whereas if gas release is sudden, flow induced vibrations will generate high-frequency explosion quake signals. We hereafter define an explosion as the release of a given volume of gas, more or less laden with solid particles, through a fracture in the solid plug which becomes suddenly opened to release the gas pressure. We suggest that the high-frequency components of the associated seismic signal (i.e. the explosion quake) result mainly from the interaction between the pressurized turbulent flow of gas and the rough channel walls.

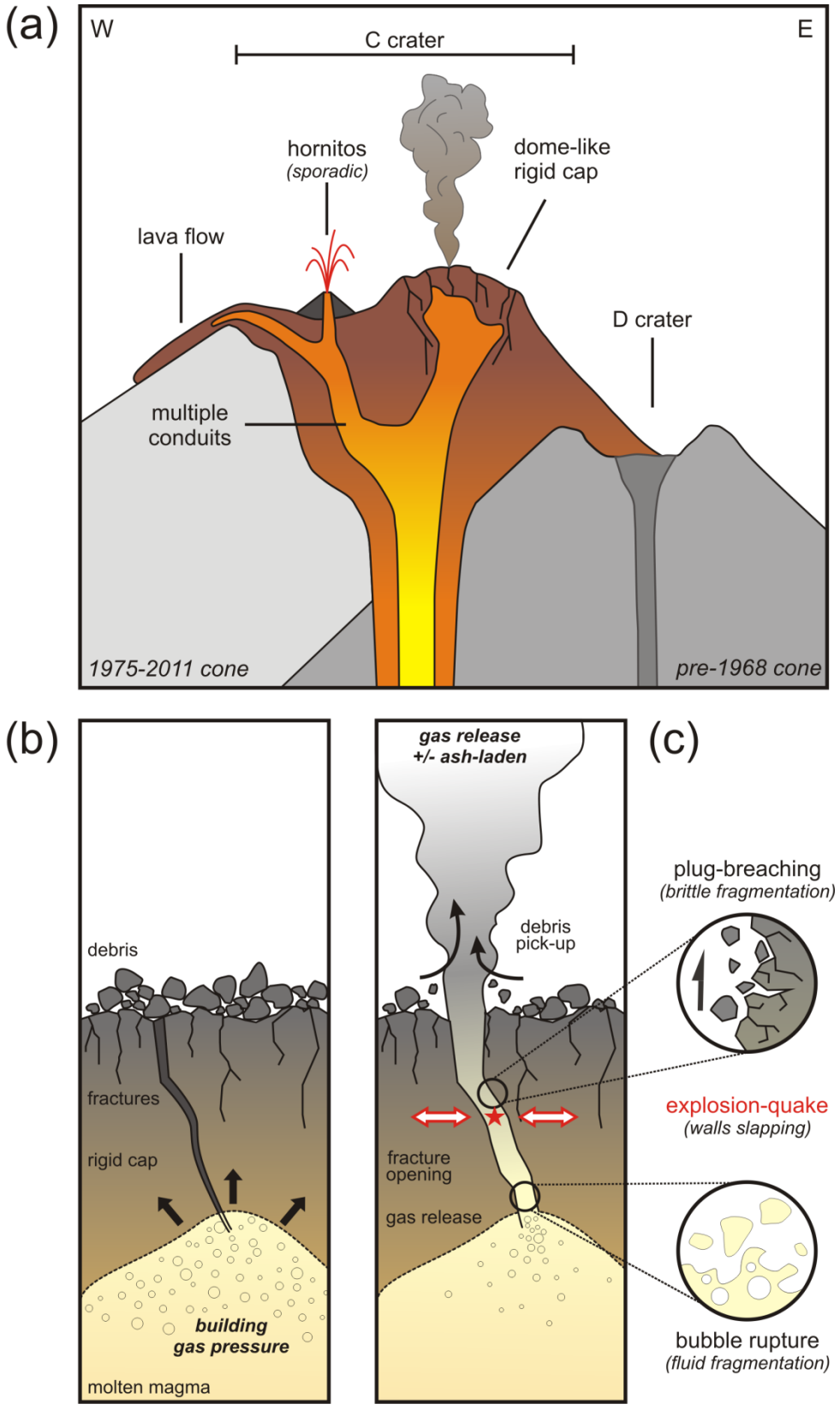

Figure II.17. Sketch of Arenal's shallow structure (a), and conceptual model of the mechanism of gas and ash emissions at Arenal. (b) Pressure builds up under a viscous degassed cap crosscut by fractures. (c) When the fracture strength is overcome, the gas is suddenly released: fracture walls slap together, triggering high frequency seismic vibrations characteristic of the explosion quake signals. The turbulent gas may in turn pull out varying quantities of pyroclasts, which can be detected by the radar if enough is expelled. The expelled tephra may result from syn-eruptive fragmentation (brittle or fluid fragmentation), or may result from remobilization of loose fragmented material residing atop the cap, or within its permeable fractures.

Two mechanisms of flow-induced vibration can be considered, whereby hydrodynamic flow instabilities and oscillations occur at the channel walls (*Rust et al.*, 2008). In the first case, the fluid flow in a thin channel generates roll waves (i.e. waves of channel thickness variation) in the elastic walls when the flow speed is higher than

$$U_{crit\,roll} \approx \beta \sqrt{\frac{\rho_s}{\rho_f}} \frac{H}{L} \qquad \text{II.2}$$

where β is the shear wave velocity of the walls, $\frac{\rho_s}{\rho_f}$ the rock to fluid density ratio, and H and L are the thickness and length of the channel, respectively. If we consider typical rock property values of β = 1 km/s and ρ_s = 2000 kg/m^3, with a gas density (ρ_f) of 300 kg/m^3 (H_20 at 500 °C and 50 MPa) and, because the fracture is closed at the beginning of the explosion, H~0 so that the ratio $\frac{H}{L}$ is small (~10^{-5} to 10^{-3}) during the fracture aperture, the threshold condition for roll waves to be generated is easily met. However the channel must be long enough for these instabilities to develop.

The second mechanism is the excitation of normal modes of the conduit walls. Instability occurs when the flow velocity is higher than

$$U_{crit\,wall} \approx fL \qquad \text{II.3}$$

where f is the modal frequency and L the characteristic length, or width, of the channel. *Rust et al.* (2008) carried out laboratory experiments of gas flow between an elastic membrane and a rigid plate to show that the amplitude of oscillations increases with increased flow speed (when $U > U_{crit\,wall}$). In another experiment where air was forced to flow through a slit in a block of gelatine, they showed that at very high flow velocities, the channel walls slap together producing large and non-periodic high-frequency elastic waves. We propose that this process could be considered as an analogue for the explosion quakes at Arenal (Figure II.17c). In the case of strong explosions, the fracture and part of the plug are destroyed and the conduit remains partly open. However, for most explosions in 2005 at Arenal, the gas volume and pressure associated with each explosive event was small, so that the fractures were not, or only slightly, damaged by the gas flow and so that they could close again after the event.

The turbulent gas flow may entrain varying quantities of pyroclasts, and depending on its mass loading, may be recorded by the radar. Explosions expelling only gas will not be detected by the radar (and thus will result in explosion quakes without a coeval radar signal, e.g. Figure II.9b, 21:38 UTC). On the other hand, those expelling ash-laden gas flow will

produce a radar echo (i.e. explosion quakes with coeval radar signal, Figure II.9a, 23:29 UTC). Depending on the fracture strength and the underlying gas pressure, the pyroclasts will not necessarily be expelled all at once, and may result in paired eruptions (i.e. eruptions that are ≤ 3 minutes apart, Figure II.9b at 21:29 and 21:46 UTC) or pulsed emissions (i.e. pulses ≤ 10 seconds apart, Figure II.10b iv). In most cases, the second event releases less tephra than the first, ejecting the remaining unevacuated material. The short time lapse separating each eruptive event (minutes to tens of minutes, Figure II.9) suggests a high capacity for the system to regenerate overpressure over a very short time scale.

When the gas-flow is intermittent through the fractures of the solid plug, it is believed to act as the source mechanism of tremor (*Lesage et al.*, 2006; *Rust et al.*, 2008). It results from the periodic opening and closure of the fracture triggered by pressure oscillations associated with standing waves in the conduit. The periodic pulses generate evenly spaced spectral peaks by a Dirac comb effect. This is consistent with the results of moment tensor inversion of tremor waveforms which have been interpreted as the opening and closure of a shallow crack (*Davi et al.*, 2011). It is also consistent with the repeated large amplitude oscillations (1-2 s) observed in many radar signals associated with ash emissions that suggest staccato pressure release (*Donnadieu et al.*, 2008), and with recent observations of correlation between SO_2 emission rate and tremor amplitude at Fuego volcano (*Nadeau et al.*, 2011). Furthermore, it explains the frequently observed tremor-like coda of explosions, which occur if the fracture can still act as a valve and if the residual pressure below the plug is high enough after the explosion, or if another crack is opened by the main event. During this kind of post-explosive tremor, the pressure is progressively released by the gas escaping through the fracture. Therefore, the gas flow rate in the upper part of the conduit decreases, the average wave velocity in the resonating conduit increases and thus the fundamental frequency and overtones of the tremor also increases. Simultaneously, the pressure reduction induces an increase of gas exsolution of the magma that tends to counterbalance the gas loss. However, the characteristic time of exsolution and gas transfer inside the conduit is larger than that of the gas loss through the fracture. As a consequence, the dominant effect is a pressure release during the first minutes after mild explosions. This process gives an explanation to the positive frequency gliding observed in the post-explosion tremor (e.g. Figure II.9a, 23:02 UTC). On the other hand, during tremors that are not associated with explosion, either constant frequency content, or positive / negative frequency gliding can be obtained according to the balance between gas escape through the plug and gas input in the resonating conduit from exsolution and transfer.

II.3.7.2. Model sensitivity to evolving summit conditions

All the mechanisms considered in the model described above are quite sensitive to small changes of the state of the conduit and plug. In open-system volcanoes such as Arenal, shallow system conditions may evolve rapidly, causing high temporal variability in both the seismic and radar waveforms associated with explosions. In particular, the presence of a solidified cap, its rheology, heterogeneous fracturing, thickness, debris residing above it, and consequently its permeability to gas, may evolve over time scales ranging from days to seconds (e.g. disruption following an explosion). Variable degrees of "gas-tightness" cause variable gas output through the plug fractures, and thus result in complex frequency gliding episodes in the tremor signal (Figure II.9). Temporal variations in fracture strength cause differential mechanical responses to pressure increases from one event to another. Consequently, gas and ash may be expelled from one or several fractures (or vents) simultaneously or at slightly delayed intervals, and the eruption focus may change from one event to another. In this context, the partitioning of the total eruptive energy (i.e. its distribution amongst the various types of energy: kinetic and seismic, see *Gerst,* 2010), is likely to vary significantly, and will thus act as a contributing factor to the lack of seismo-radar correlation. The variation in explosion depth, in particular, is likely to have a major impact as it strongly controls the coupling efficiency of the elastic energy radiated into the ground and atmosphere (*Johnson and Aster*, 2005). Deep explosions (i.e. ~200 m, *Davi et al.*, 2010) may produce strong seismic signals and low radar signals (exiting of the fragmented material is impeded), and vice versa for shallow explosions. Eventually, due to the distance between the vent and the seismometers, very shallow explosions might not be recorded seismically if they are not strong enough. This may provide an explanation to the occurrence of eruptions unrecorded by seismometers (*Williams-Jones et al.*, 2001), and to radar events which show high exit velocities with no coeval seismic counterpart.

Furthermore, explosions may fragment variable quantities of magma, either molten (i.e. fluidal fragmentation of juvenile magma) or solid (i.e. breaching of the solid plug) (Figure II.17c), as attested by tephra clast analysis (*Cole et al.*, 2005). In turn, the turbulent gas flow may entrain varying quantities of pyroclasts from the plug fracture system, which may be unrecorded by the radar if the ash load is too low. Moreover, magma fragmentation and tephra emissions may not necessarily be synchronous with explosions-quake signals. Indeed, magma fragmentation may result from viscous shear near the conduit walls (*Gonnermann and Manga,* 2003) or from elastic shocks during conduit wall fracturing (even at low strain rate,

Lavallée et al., 2011), and loose particles may remain in the permeable fractured regions to be entrained in ensuing events (*Sahetapy-Engel et al.*, 2009). Ash emissions can thus result from remobilization of loose, previously fragmented material residing atop the lava cap and/or in the fractured region of conduit walls, remobilized during degassing events (e.g. tremor episodes, Figure II.10c).

II.3.7.3. Perspectives

Further geophysical studies are needed to constrain the conceptual model proposed here. Acoustic measurements were carried out during this recording campaign, but unfortunately the data were extremely noisy and thus unusable. Nevertheless, acoustic records are likely to hold crucial information on the mechanical processes operating in both the magmatic conduit and the magma-air interface (e.g. *Hagerty et al.*, 2000). Thus further seismo-acoustic measurements, coupled with coincident Doppler measurements, would greatly increase our ability to constrain a shallow system model. Because the mechanism of the eruptions is thought to be closely related to degassing processes, coincident gas flux measurements would also be helpful. In particular, SO_2 fluxes measured by UV cameras have shown to decrease prior to ash bearing eruptions at Sakurajima (*Kazahaya et al.*, 2010), which suggests that sealing processes were operating between each eruption. Coupling gas flux and radar measurements is thus likely to be very promising. These additional geophysical measurements, if performed continuously over a long period, should allow us to better analyze the variability of the geophysical signals over longer time scales. Such studies may help to further constrain the complex processes, patterns and feedbacks operating in the shallow system of Arenal, and to better understand the mechanism and evolution of its persistent activity.

II.3.8. Conclusion

Joint observation of tephra emissions and subsurface processes was carried out at Arenal using broad-band seismometers and a ground-based Doppler radar to quantify surface tephra emissions. Cross-correlation of both signals shows complex, non-repeatable relationships. Indeed, tephra emissions are not systematically associated to a unique type of seismic event, and seem to occur with no clear correlation with the tremor amplitude fluctuation, the seismic

energy release rate, nor the repose time between successive emissions. Moreover, poor correlations are found between the features of both signals (e.g. kinetic energies, backscattered powers, exit velocities of radar signals, versus seismic amplitude, frequency content). We propose a conceptual model that accounts for the generation of the tremor, the explosion quakes, and their relationship with tephra emissions. We suggest that fractures through a solid cap tapping the conduit control degassing of the shallow system, which in turn control the seismic waveforms and tephra emissions. If the gas release is intermittent, it will produce repetitive pressure pulses and thus generate low-frequency tremor signal. On the contrary if gas is suddenly released after the fracture's strength has been overcome by the underlying pressure, flow induced vibrations will generate high-frequency, explosion quake signal. Depending on the amount of fragmented material carried by the gas, the degassing event will either be accompanied by a radar signal (i.e. ash-laden gas output), or not (i.e. ash-free gas output). The variable shallow system conditions (plug thickness, rheology, fracturing, permeability) are likely to be reset on short time-scales, and thus result in non-repetitive conditions that may account for the variability of the gas and ash emission mechanisms (and resulting seismic and radar signals).

II.4. Conclusion

We carried out a cross-correlation of broadband seismic data and ground-based Doppler radar data obtained at Arenal (Costa Rica) in February 2005 and 2009. Our aim was to gain insight into the subsurface source processes (i.e. mechanisms operating in the shallow conduit system) and the subsequent pyroclastic emissions (i.e. tephra emission mass loading and dynamics) that characterize the transitory, mildly explosive activity at Arenal. To do so, a number of tools were developed, such as an interactive software (*Seismo_Radar_Correlation*, to display / process both data types), automated search algorithms (to query data base / extract meaningful parameters), or data base analysis algorithms (to construct plots from data base).

Extensive study of radar and seismic waveforms has revealed a non-systematic relationship among them, both exhibiting a large variety of behaviors and features, with no clear pattern on radar signals that can be associated to specific seismic signals. Unexpectedly, pyroclast emissions do not have a unique seismic signature, as they are encountered in association with explosion-type events, during episodes of tremor, and even during aseismic intervals. On longer time-scales, radar events' amplitudes show no correlation with the seismic energy release rate (RSEM, RSAM), nor with the repose time intervals. Energy proxies of coeval radar and seismic eruptive signals show significant scattering indicating that the ratio of the seismic/radar energy is highly variable. The tephra emission's intensity (mass-loading, exit velocity) thus seems only weakly correlated to the seismic energy generated by the explosion, suggesting that the seismic energy might not be a good indicator of the intensity of surface emissions at Arenal.

A conceptual model was proposed to account for the generation of tremor, explosion quakes, and their relationship with tephra emissions. It is based on the idea that fractures cross-cut the rigid lava cap, and thus control the shallow system's degassing. The degassing regime in turn dictates the type of seismic signal generated: (i) intermittent gas release will produce repetitive pressure pulses and act as the source of tremor, whereas (ii) sudden gas release will cause fracture walls to slap one against the other, generating explosion quake signals. Variable amounts of tephra may be entrained by the gas, thus controlling whether the seismic event will be accompanied by a radar signal or not. These mechanisms however, are highly sensitive to small changes of the state of the conduit and lava cap, causing high variability in both the seismic and radar waveforms.

Chapter III

Dynamics of pyroclastic emissions

III.1. Introduction

Gaining insights into the internal dynamics of pyroclastic emissions requires in-situ quantitative measurements of the eruptive jets, which can only be achieved by remote sensing techniques. Ground-based thermal cameras (FLIR) in particular, have provided powerful insights into the dynamics of mild strombolian eruption and the subsequent plume rise dynamics (*Patrick,* 2007; *Patrick et al.,* 2007). On the other hand, ultraviolet ground based cameras, have proved to be capable of imaging the distribution of ash within weak Vulcanian ash plumes (*Yamamoto et al.,* 2008). Recently, *Gouhier and Donnadieu* (2010) carried out a statistical analysis of the geometry of Doppler spectra, which were recorded by VOLDORAD on Strombolian explosions at Etna. In doing so, they were able to constrain the geometrical features of Strombolian lava jets, and provide constraints on shallow conduit processes.

In this chapter, we develop a tool to visualize the evolution of the Doppler spectra through time. This type of representation, hereafter entitled ***Doppler radargram***, enables the possibility to study how pyroclasts transiting through the beam evolve in both time and velocity. We show that radargrams of several eruptive events reveal distinct ***Doppler signatures***, pointing out distinct eruptive dynamics (*Valade and Donnadieu,* 2011). A statistical analysis is then carried out to assess the variability of these Doppler signatures over a number of eruptive events, and discuss their implications for both the ejections dynamics and the shallow source processes.

III.2. Doppler radargrams

III.2.1. Construction of Doppler radargrams

The elementary information the radar acquires at each time step is shown in a ***Doppler spectrum***, which holds the information on the velocity distribution of the ejected mass load in each range gate (see Chapter I for details). Processing of the spectra through time gives time series of useful parameters, such as the backscattered power, the maximum radial velocities, or the kinetic energy (see Chapter II for examples on their use). Such time series however have several disadvantages: (i) they come from post-processing of radar data, and consequently may alter the raw information the radar provides due to imperfection in the processing algorithms, and (ii) they show the evolution through time of only one information (e.g. power, velocity …), and thus fail to show the interaction between the various parameters through time. In particular, the evolution of the shape of Doppler spectra informs on the evolution of the mass-velocity distribution through time and space (when considering several range gates). Although the spectra from each range gate can be read at each time step from raw source files, this precludes from a synoptic view of the eruptive event. To overcome this issue, we construct an image visualization of their evolution, hereafter entitled *Doppler radargrams*.

Computing ***Doppler radargrams*** simply consists in the juxtaposition through time of the Doppler spectra[2] (Figure III.1). These radargrams consequently express the time-velocity distribution of the backscattered power, each point holding the information on how much material (color code) moves, at a certain velocity (y-value), at a certain time (x-value), in a given range gate. All the useful information given by the radar (velocimetry, mass loading, shape of spectra and evolution through the gates) is plotted at once, and represents the ***Doppler signature*** of the ejecta crossing the beam.

[2] Recall that a spectrum is constructed from processing of raw radar data, and can ultimately result from the integration of several spectra if the number of "incoherent" integrations chosen is higher than one (see section I.2.2). All the data presented in this chapter has been computed with one incoherent integration, ensuring the highest temporal resolution possible (time step ca. 0.14 s).

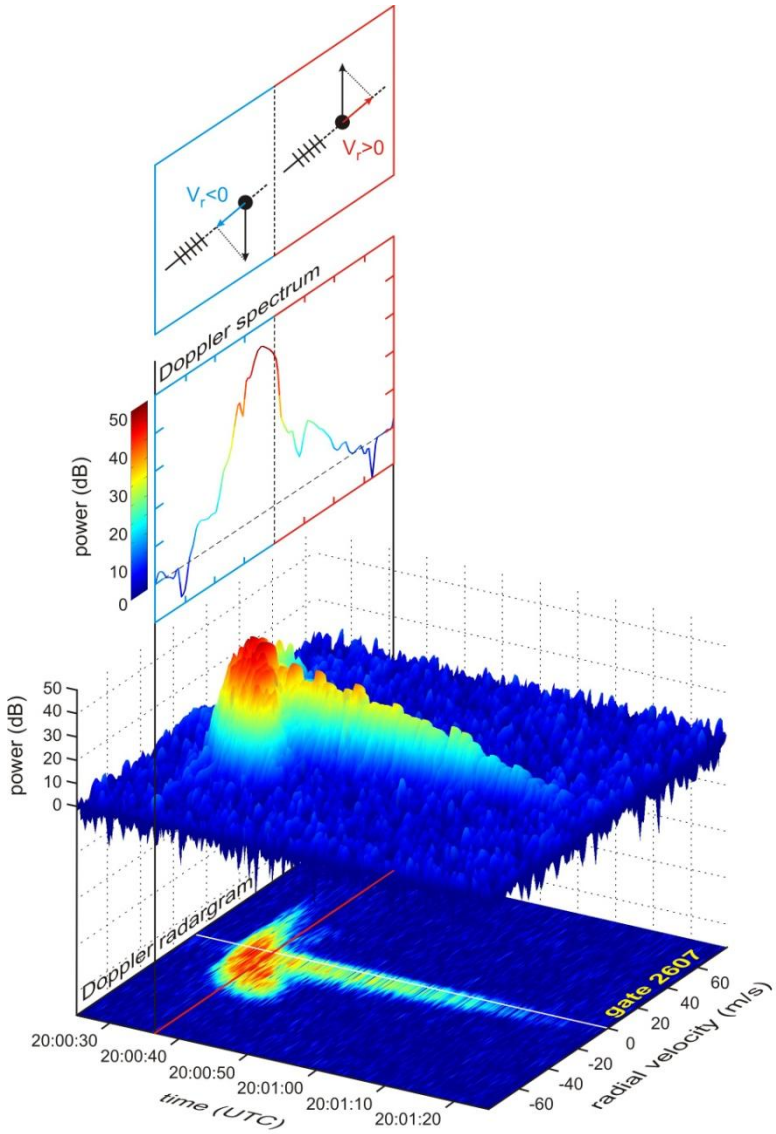

Figure III.1. Illustration of how a Doppler radargram (bottom) is constructed, i.e. from the juxtaposition in time of successive Doppler spectrum (top) recorded in a given range gate. Positive radial velocities (right) refer to particles moving away from the radar antenna, negative radial velocities (left) to particles moving towards it, and backscattered power is related to the number and size of the particles in the range gate.

III.2.2. Strengths and weaknesses of radargrams

As it has been said above, radargrams have the immense advantage of displaying all the information the radar is able to furnish at once, without altering the raw information. Nevertheless, the strength of a radargram is also one of its weaknesses. Indeed, because the data is power-weighted using a color code, the pixels having low power values (i.e. low mass load) will not appear clearly. This issue is particularly problematic when a precise value of the maximum velocities is wanted.

Figure III.2 intends to illustrate the problem. On the radargram (Figure III.2a), the pixels above ~40 m/s exhibit low power, which may lead the observer to estimate maximum velocities below 50 m/s. The time series of the maximum positive velocity V_{+max} however (Figure 2c), peaks at 52.9 m/s (20:00:32.5 UTC). The Doppler spectrum extracted at that specific time (Figure III.2b) shows that this value is meaningful, in the sense that it is not noise but eruptive signal indeed. On the other hand, these time series tend to be noisy, especially out of eruptive signals. Although imperfect, the processing algorithm of Doppler spectra have the advantage of being able to extrapolate maximum velocities of aliased spectra; moreover, erroneous data points in the eruptive signal can be smoothed by running average over a small window or preferably by incoherent integrations (3 for instance).

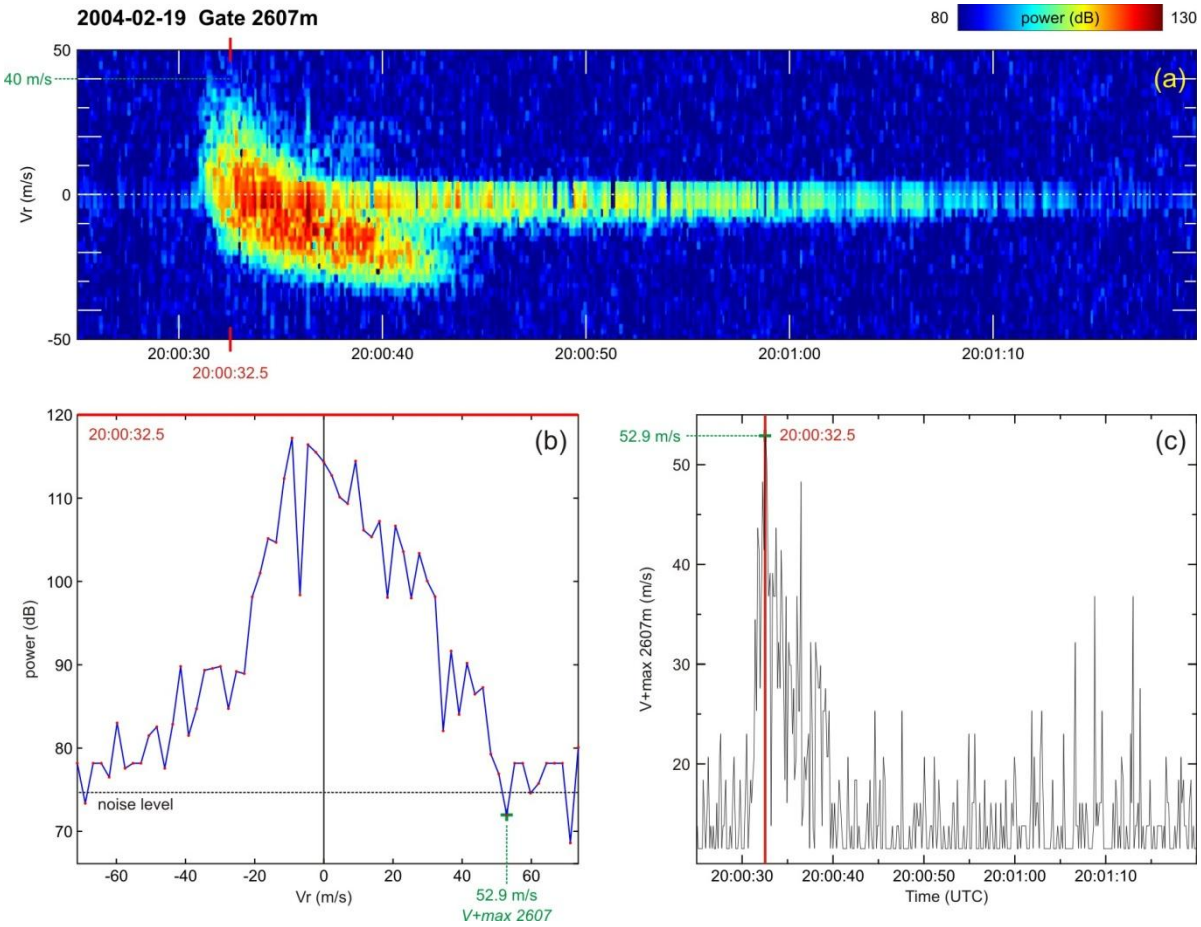

Figure III.2. Illustration of the strengths and weaknesses of both Doppler radargram (a) and time series (c). Radargrams display unprocessed Doppler spectra, but because the pixels are power-weighted, those with low power do not clearly come out from the noise: this may lead to underestimation of maximum radial velocities (V_{+max}). On the other hand, time series display data which come from automated processing of the Doppler spectra (b): as a consequence, these may appear noisy (especially V_{+max} time series, e.g. plot c). The data is processed with one incoherent integration (time step ca. 0.14 s).

Henceforth, reading maximum velocities from the radargram color distribution tends to give underestimated values, but reading them from the time series tends to be problematic as these can be very noisy. The user may try to avoid the problem by playing with the radargram color

code, or by extracting Doppler spectra at selected times (both possible in the ***RadargramBuilder*** software presented in appendix B). The best solution however is to interact with both the radargrams and time series, and use them as distinct tools which complement one another.

III.3. Ballistics and ash plume discriminated by Doppler radar *(Valade and Donnadieu, 2011)*

The following section is published in *Geophysical Research Letters* (*Valade and Donnadieu,* 2011). The cover image of the journal (Volume 38, No. 22) is devoted to the publication, as well as an article in the *EOS Research Spotlight* section (*Balcerak,* 2012). Appendix E holds the printed format of the article, as well as the journal cover and the EOS article. The architecture of this section is kept identical to that of the publication, but the content has been complemented with some additional material that is not included in the published article.

Geophysical Research Letters

Ballistics and ash plumes discriminated by Doppler radar

Sébastien Valade and Franck Donnadieu

Received 23 August 2011; revised 12 October 2011; accepted 12 October 2011; published 16 November 2011.

III.3.1. Abstract

Small scale eruptive ash plumes at Arenal volcano (Costa Rica) were recorded using a ground-based Doppler radar (VOLDORAD). The time-velocity distribution of the mass load (i.e. Doppler radargrams) exhibits two contrasted dynamics recorded simultaneously, evidenced by distinctive velocities, life spans, and transit speeds through the radar beam. Synthetic Doppler radargrams computed with a simple ballistic model indicate that the short-lived signal is consistent with the instantaneous projection of ballistics blocks accompanying the ash plume emission. The mass of centimeter- to decimeter-sized ballistics is confidently estimated at 0.5–7 tons, whereas the ash plume mass is loosely constrained at $5.8 \cdot 10^2$ tons, assuming a particle diameter of 2 mm close to the vent. These quantitative estimates of the mass proportion either falling on the slopes of the volcano or ejected into the atmosphere could help in the modeling and monitoring of tephra dispersal.

III.3.2. Introduction

Small-scale volcanic eruptions commonly expel a wide range of pyroclast sizes, ranging from coarse blocks with ballistic trajectories, to fine ash driven away within ash plumes. As both the plume and the ballistics are emitted simultaneously, it is often difficult to discriminate and to collect quantitative data on both phenomena. Thermal (*Patrick*, 2007; *Marchetti et al.*, 2009) and ultraviolet imagery (*Yamamoto et al.*, 2008) have provided powerful insights into the dynamics of mild strombolian and vulcanian eruptions, shedding light onto the plume rise dynamics and the relative ash / ballistics distribution of the ejecta. In this paper, we describe similar small-scale transient eruptions at Arenal (Costa Rica), monitored with a ground-based Doppler radar (VOLDORAD) (*Dubosclard et al.*, 2004; *Donnadieu et al.*, 2005). The radar provides quantitative information on exit velocities and mass loading of the ejecta. We show that the time-velocity distribution of the mass load (i.e. Doppler radargram) reveals two distinct dynamics, which discriminates the ballistics and the ash plume transiting through the radar beam. We compute synthetic Doppler radargrams by numerical modeling of the ballistics, and constrain the dynamics and mass loadings of both the ballistics and the ash plume. Such characterization of the near-vent eruptive dynamics has strong potential applications, as the degree of fragmentation and the mass proportion injected into the atmosphere are of interest for hazard mitigation issues.

III.3.3. Radar data acquisition

VOLDORAD is a ground-based, pulsed Doppler radar, specifically designed for active remote sensing of volcanic jets and plumes (*Dubosclard et al.*, 2004). The radar was set 2.4 km West of Arenal's active crater C, at an altitude of 685 m. The 27° antenna elevation enabled the beam to skim the summit crater (Figure III.3). The spatial resolution is defined by the beam aperture (9°) and the radial depth (120 m) of the successive volumes (range gates) sampled in the beam, referenced by their radial distance to the radar (e.g. 2247 to 2727 m). When volcanic ejecta cross the beam, they scatter some energy of the pulsed electromagnetic waves (100 μs^{-1}) back to the radar. Doppler spectra (acquired at 0.14 s^{-1}), express the power backscattered by the ejecta during the pulse duration (0.8 μs) as a function of their radial velocity (Figure III.4a). The backscattered power is a complex function of the number and size of the ejecta. The measured radial velocities inferred from the frequency shift between the transmitted and the backscattered signal correspond to the along-beam components of the

ejecta velocities. Positive and negative radial velocities are induced by particles having a radial component of motion respectively away from and towards the radar. Consequently, in the range gates up the vent, ascending ballistics generate mainly positive radial velocities, whereas falling blocks tend to produce negative radial velocities. The juxtaposition of Doppler spectra constitute Doppler radargrams (Figure III.4b), which reveal the evolution through time (x-axis) of both the velocities (y-axis) and echo power (color scale) of the ejecta in each range gate. All the useful spatio-temporal information characterizing the target (velocimetry, mass loading, shape of spectra, evolution through the gates) is plotted at once and constitute its Doppler signature.

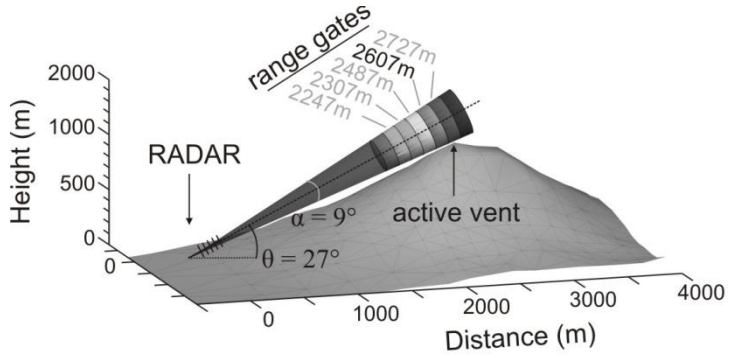

Figure III.3. Geometry of the radar sounding at Arenal showing the sampled volumes in the beam. The radar was set up at an altitude of 685 m, 2.4 km West and downwind of the active crater.

III.3.4. Results

Figure III.4b shows the Doppler signature of an eruptive event recorded on February 19, 2004 at 20:00:31 UT. The recording shows two distinct features, characterized by contrasted dynamics, i.e. different life spans, radial velocities, and transit speeds through the radar range gates. The first feature is a short-lived (<15 s) impulsive signal, first appearing at 2607 m as a curved streak. It spreads on a large velocity range (both positive and negative velocities), and transits rapidly through the beam (~3-4 s per gate in average). In the gates above the vent and uphill (i.e. 2607 m and 2727 m), it exhibits sharp onsets, with relatively high positive velocities (> +40 m/s) and high backscattered power (~34 dB in gate 2607 m) reached in <2 s. In both gates, the peak echo power shifts progressively from positive to negative velocities in ~10-13 s (e.g. reaches -30 m/s in gate 2607 m at 20:00:44 UTC). In the gates downhill from the vent however (i.e. 2487 m to 2247 m), only negative velocities are recorded: in gate 2487 m for instance, the onset velocity is of -25 m/s, and reaches -48 m/s in ~5 s. Contrastingly, the second feature is a longer-lived signal (≥60 s), whose Doppler signature differs significantly from the short-lived signal: the onsets of both the echo power and the Doppler velocities are

progressive, the peak power is 50 times lower (~17 dB), the range of Doppler velocities is similar in all range gates (0 to -15 m/s), the signal lasts 1-2 minutes (e.g. ~84 s in gate 2367 m), and it transits slowly throughout the range gates (~15-20 s per gate in average) with decreasing amplitude. Such Doppler signature is characteristic of an ash plume entrained towards the radar by the wind whose transport speed can be determined in 3-D (*Donnadieu et al.*, 2011).

The occurrence of these two features is observed in several recordings of eruptive events, either simultaneously (e.g. Figure III.4), or independently. The differences in the Doppler signature of both point out different dynamics, which suggests that the radar records more than just an ash plume. We hereafter model the short-lived part of the signal to explain its origin.

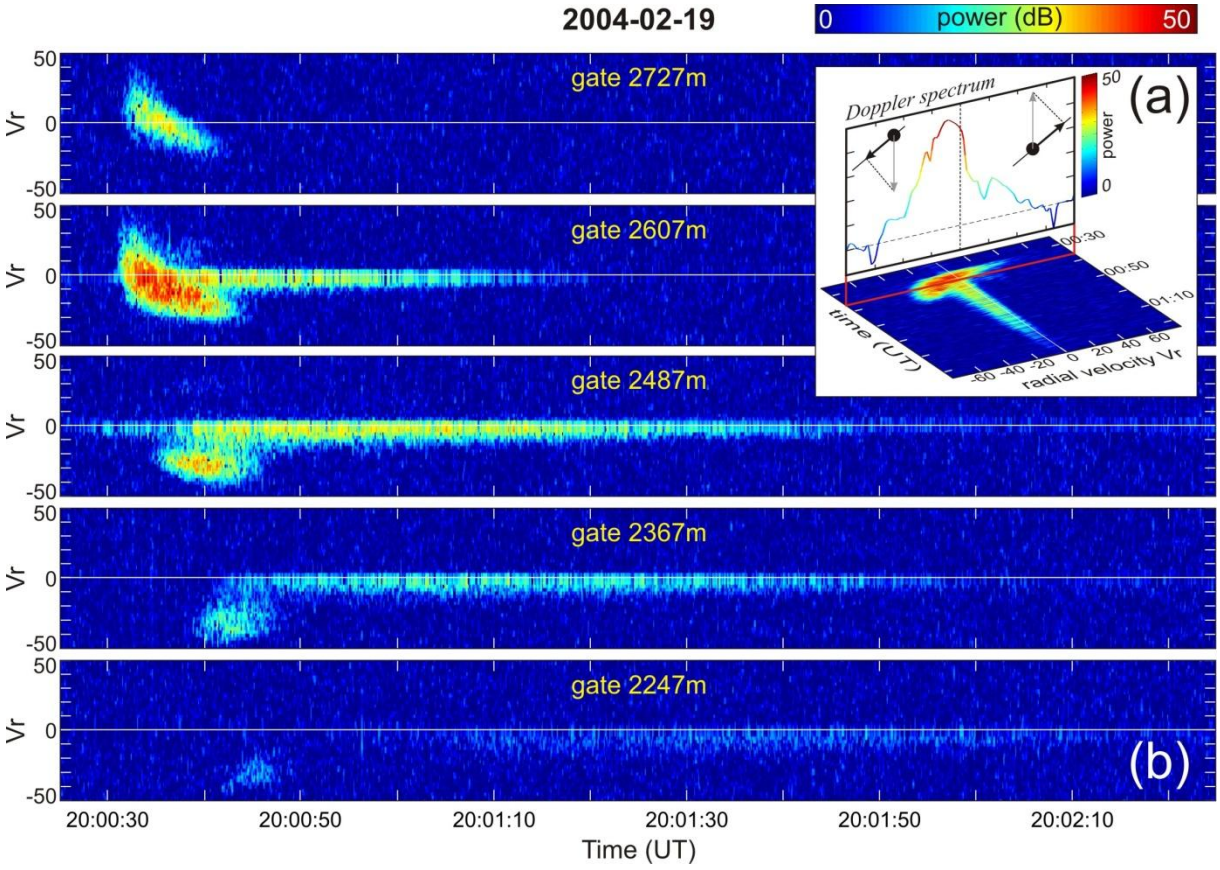

Figure III.4. Doppler radargrams recorded during an ash plume emission at Arenal on February 19, 2004 at 20:00:31 UT. (a) The Doppler radargram is built from the succession through time of Doppler spectra. The echo power in the spectrum (dB arbitrary units) is related to the number and size of the particles in the range gate. Positive (right part of the spectrum) and negative (left part) radial velocities correspond to particles with an along-beam velocity component respectively away from the radar antenna and towards it. (b) Doppler radargrams recorded in gates 2247 m to 2727 m, revealing the spatio-temporal evolution of two contrasted event dynamics: the short-lived signal with rapidly changing radial velocities and quickly transiting through the range gates is induced by ballistics, whereas the longer-lived signal with low negative velocities is induced by the wind-drifted ash plume.

III.3.5. Interpretation and discussion

Mild explosions typically occur several times a day at Arenal, resulting in small ash-plumes rising to a few hundreds of meters above the vent (*Cole et al.*, 2005). They are sometime accompanied by blocks impacting the volcano upper slopes, and visible at night as incandescent ballistic projections. We show below with a simple model example that the features of the short-lived signal are consistent with ballistic projections, and we discuss the mass loadings of both the ballistics and the ash plume.

III.3.5.1. Modeling ballistic projections

We use the 2-D model of *Dubosclard et al.* (2004), to compute the ballistic trajectories of ejecta and the associated synthetic echo power in each range gate. Spherical particles are instantaneously released at selected angles with a velocity depending on the initial gas velocity. Their trajectories are determined by solving the equations of motion under the influence of gas drag and gravity (see *Dubosclard et al.*, 2004 for details on the driving equations). The synthetic Doppler spectra are then constructed at each time step by splitting particle radial velocities into classes, and summing the backscattered powers of the particles in each velocity class (*Gouhier and Donnadieu*, 2010). To reconstruct the evolution of the Doppler signature in the different range gates, Doppler spectra are juxtaposed in time, and a color scale is used for the echo amplitude. Note that this admittedly simple ballistic model was not intended to recover the true eruptive parameters by matching the exact time-velocity distribution of the echo power (which would require inversion procedures, subject of ongoing work), but only to reproduce the main characteristics of the Doppler signature of the short-lived signal using realistic block size and gas velocities.

Figure III.5 shows an example of synthetic Doppler signature produced by spheres of 0.1 m in diameter, launched within a vertical cone 60° wide, with an initial gas velocity of 105 m/s. The Doppler radargrams successfully reproduce the main characteristics of the short-lived signal observed in Figure III.4b, in particular the transit times, the shape and the number of range gates crossed. The sharp onset in positive velocities at gates 2607 m and 2727 m (+44 and +37 m/s respectively) is successfully reproduced, as well as the decay towards negative velocities during about 10 s. The obtained characteristic curved shape can henceforth be interpreted as mostly resulting from the progressive bending of the ballistic trajectories through the radar beam. As for the gates closer to the radar, the simulation reproduces the

onset at moderate and increasing negative radial velocities (-14 m/s in gate 2487 m), the signal onset in the next gate again at higher radial velocities (-27.5 m/s in gate 2367 m), and the progressive diminution of signal duration at increasing distances from the vent (~10.5 s in gate 2487 m against ~1 s in gate 2247 m). Because of the voluntarily simple model, several features of lower importance are not reproduced well: (i) the synthetic power is not as high as the recorded power because of the small number of particles launched in the model; (ii) the spectral width is too narrow, probably because only one particle size and 2-D trajectories are considered. Nevertheless, the reasonable match of the synthetic and observed Doppler signatures strengthens the origin of the short-lived signal as being the instantaneous projection of ballistic blocks crossing the successive range gates.

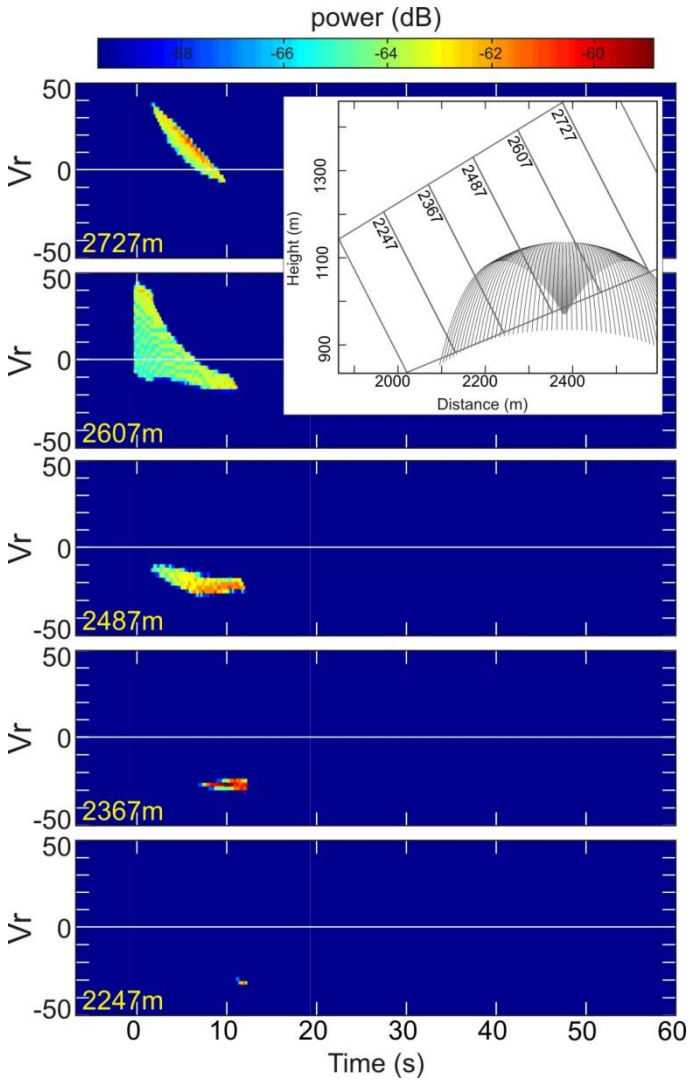

Figure III.5. Example of synthetic Doppler radargrams generated with a 2-D ballistic model (Dubosclard et al., 2004; Gouhier and Donnadieu, 2010). 60 spherical particles of diameter 0.1 m were uniformly released in a vertical cone of 60° aperture, with an initial gas velocity of 105 m/s. The source is 20 m below the 2607 m range gate, at x = 2381 m and y = 966 m from the radar. The main features of the short-lived signal observed in Figure 2 are reproduced, indicating its ballistic origin.

III.3.5.2. Constraints on mass loadings

Radar recordings (Figure III.4b) have shown that ballistics emitted simultaneously with an ash plume could be discriminated by their distinctive Doppler signature. Using the Mie scattering theory (*Gouhier and Donnadieu*, 2008), the peak echo power of both signals can then be used to constrain the respective masses and volumes of tephra comprising the ballistics and the plume.

Figure III.6 shows the solutions for the reflectivity factors close to those measured during the emissions of the ballistics and the ash plume (74.5 and 57.5 dBZ respectively) for various particle diameters assumed. The strong power values observed in the short-lived signal (Figure III.4b) suggest that they were produced by coarse ballistic particles (blocks), because large particles backscatter much more energy than fine ones. At Arenal, we can expect blocks of at least 0.1 m in diameter to be expelled with ballistic trajectories, as suggested by power inversions of linear streaks observed in several radargrams which are attributed to individual blocks (see section III.3.5.4, Figure III.9). If we consider block sizes ranging between 0.04–1 m and 1700 kg/m^3 in density, the mass of ballistics would fall in the range 0.5–7 tons, i.e. a DRE volume of ballistics of 0.2–2.8 m^3 (density of 2500 kg/m^3). Comparatively, *Cole et al.* (2005) give crude estimates of the total tephra volume of individual explosions at Arenal in the region 10–50 m^3.

For finer grain size distributions, the inferred mass becomes critically dependent on the assumed diameter (Figure III.6). Accessing the particle size distribution within the ash plume near the vent is particularly challenging, so we used the coarsest diameter (2 mm) of particles collected by *Cole et al.* (2005) between 2 and 3 km downwind of the vent. Assuming a density of 1000 kg/m^3 (2 mm andesitic ash, *Bonadonna and Phillips*, 2003), the estimated mass is in the order of 5.8x10^2 tons. Our value likely represents an upper limit for the mass of ash in the plume because (i) the particle size distribution above the vent is highly polydisperse with a diameter mode certainly coarser than the assumed 2 mm diameter, and (ii) the particle shapes are likely to deviate from the spherical assumption of the Mie theory, which increases the energy backscattered to the radar (e.g. *Sauvageot*, 1992). To a lesser extent, the ash mass estimate is slightly underestimated because the duration of the ash emission exceeds the plume transit time through the range gates, unlike the ejection of ballistics. More precise estimation of the mass loading of ash plumes would require more stringent constraints on the grain size distribution close to the vent.

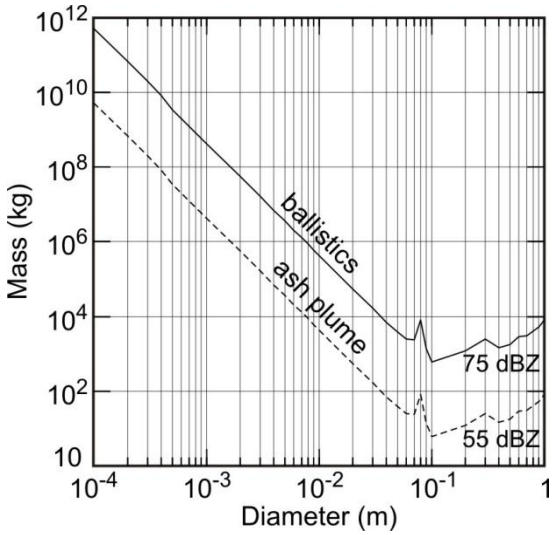

Figure III.6. Mass estimates of both the ballistics and the ash plume as a function of an assumed average particle diameter. The curves indicate the solutions for two reflectivity factors at 75 dBZ and 55 dBZ, respectively deduced from the backscattered power of the ballistics and the ash plume. Masses are inferred from the Mie scattering theory, with an assumed material density of 1700 kg/m^3. Mass estimates are well constrained in the case of centimeter- to decimeter-sized ballistics, whereas in the case of the ash plume, they critically depend on the assumed diameter because of the finer grain size distribution.

III.3.5.3. Mass estimations sensitivity

III.3.5.3.1. Mass sensitivity to particle density

The mass estimations presented previously, of both the ballistics and the ash plume, were computed using fixed particle densities (1700 kg/m^3 and 1000 kg/m^3 respectively). It may seem absurd to use fixed densities for such a wide range of particle diameters (Figure III.6). Indeed, the density of volcanic particles is known to vary depending on their size and related porosity (*Bonnadonna and Phillips*, 2003). *Eychenne* (2012) shows that the density varies with the particle diameter following a sigmoidal trend, which can be expressed as follows:

$$\rho_d = \left(1.29 + \frac{1.29}{1+0.6e^{-1.3d}}\right)\cdot 10^3 \qquad \text{III.1}$$

where ρ is the density (kg/m^3) calculated at the radius d expressed in phi units (where d(phi) = -log$_2$[d(mm)]).

To assess the sensitivity of our mass estimates with respect to the density variation, we've computed new mass estimates (Figure III.7), using the diameter-dependent densities defined above. The results show that even though the density nearly doubles between the extreme of the considered diameter range (2570 kg/m^3 at 0.1 mm, 1290 kg/m^3 at 1 m), the estimated masses computed considering this variation (blue curve) are within a factor of 2 from those computed with fixed density (red curve).

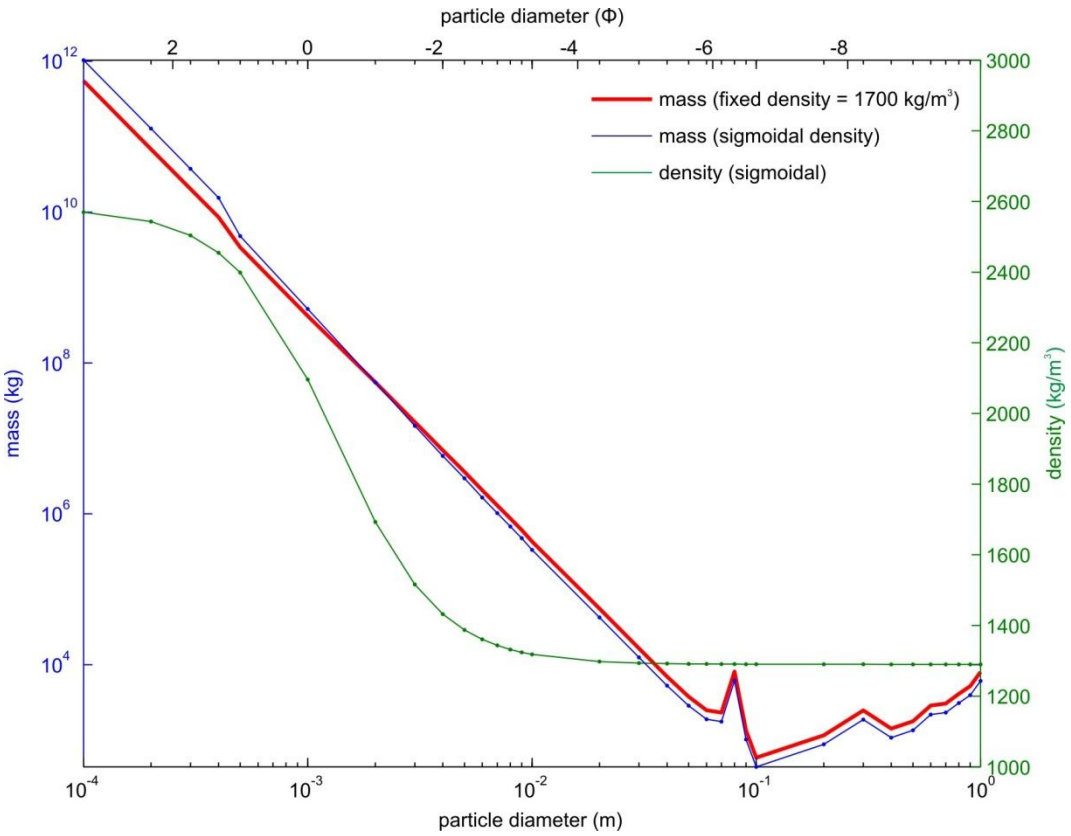

Figure III.7. Mass sensitivity to particle density variation. Both the red and blue curves give mass estimations for a reflectivity factor of 75 dBZ. The red curve is computed with a fixed density of 1700 kg/m3, whereas the blue curve uses a density which varies depending on the particle diameter (green curve).

III.3.5.3.2. Mass and reflectivity sensitivity to incomplete beam filling

Figure III.8 shows the influence that the beam filling has on the power and reflectivity factor recorded by the radar, with constant particle number and size. The plot shows that if the plume fills only 10 % of the gate volume, then the radar reflectivity factor characterizing the plume (i.e. only the volume filled by particle inside the considered range gate) will be 10 dB higher than if it had filled the range gate completely. However, the computed power has the same value whatever the volume fraction filled by the plume, because the number of particles is kept constant[3]. Therefore, because the plume mass estimates are derived by matching a power value (e.g. peak power), it is not impacted by the volume effectively filled by particle inside the range gate. However it must be remembered that only the particles in the considered range gate(s) at the chosen time are taken into count. For instance, strong errors on

[3] Note that we do not consider the multiple-scattering, nor the variable wave penetration that might arise and affect the radar signal when considering plumes of variable particle concentration.

mass estimates will occur if the plume is much larger than the beam width, or if the plume emission time is much longer than its transit time in the gate (*Gouhier and Donnadieu*, 2008).

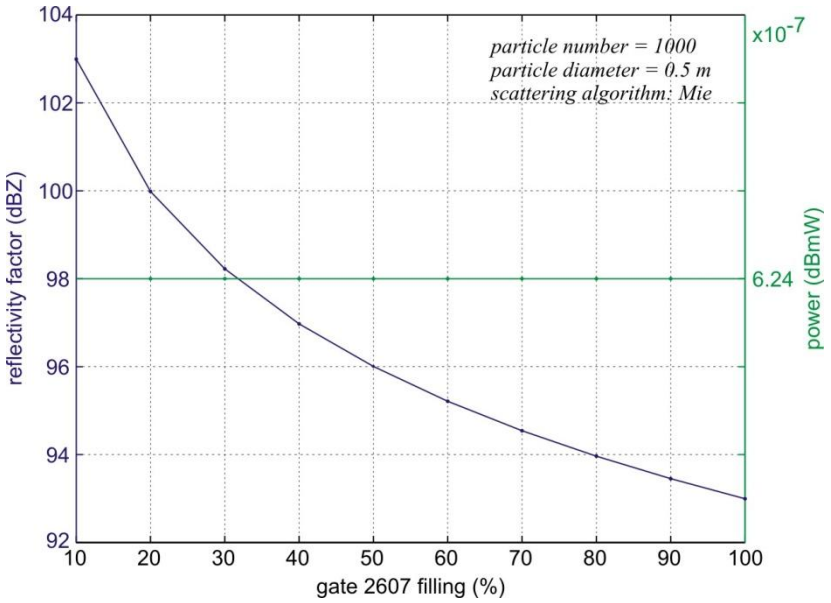

Figure III.8. Sensitivity of both the reflectivity factor characterizing the plume and the power recorded by the radar to the volume fraction occupied by the plume within a given gate, at constant size / number of particles. The reference volume used is that of gate 2607 m.

III.3.5.3.3. Mass sensitivity to particle sphericity

Deriving mass estimates from the backscattered radar power requires formulation of the electromagnetic scattering theory. However, the effects of non-sphericity of the particles on the scattering behavior (and by extension on the mass estimates) cannot be addressed simply, because no general formulation of the theory exists in this case. We give below elements of reply which can be found in the literature, for both large and small ratios of wavelength to particle size (λ/D).

(1) When the ratio of wavelength to particle size is large enough (e.g. λ/D ~ 10-100), Gan's extension (1912) of Rayleigh's theory gives formulation of the scattering behavior of ellipsoidal-shaped particles. Following the work of *Atlas et al.* (1953) on backscattering of radar waves on deformed hydrometeors, *Sauvageot* (1992) [p.101-102] conclude that "*in a general manner, the sphericity deviations with random orientation increase the backscattering [...] with respect to an equivalent spherical population*" by approximately one order of magnitude. In our case, this would lead to mass overestimation of small particles (<1 cm).

(2) When the ratio of wavelength to particle size is small (e.g. $\lambda/D \sim 10^{-1}$-1) on the other hand, no theoretical description of the diffusion behavior is known (e.g. *Bohren and Huffman*, 1983). Consequently, abundant experimental studies have investigated the scattering of light by randomly orientated, non-spherical particles. In particular, *Holland and Gagne* (1970) find that the predicted mass scattering coefficient from the *Mie* theory (1908) at back-scattering angles, may overestimate by almost an order of magnitude the experimental results (unpolarized light λ = 400-500 nm through an air-particle jet, with irregular plate-like shaped particles of ~0.25 µs). More recent works (*Volten et al.*, 2001; *Volten et al.*, 2005) have confirmed these first findings using a range of aerosols, and in particular with volcanic ash. However, these results are difficult to extrapolate to our conditions because of the very low λ/D ratios used in these studies (e.g. 10^{-1}-1 for *Holland and Gagne*, 1970).

Deriving more accurate backscattering behaviors (provided shape and size distribution of volcanic particles is constrained, which is not the case at the moment), would require a quantified characterization of the backscattering properties of volcanic particles as a function of their complex shapes (roughness), chemistry etc., and direct solving of Maxwell's equations, using numerical methods (e.g. T-matrix method, *Mishchenko et al.*, 1996). These however, usually require substantial execution times on a computer and assumptions on the particle shapes and size. So, the theoretical/experimental investigations on the effects of the irregular shapes of volcanic particles on the retrieved mass would be an entire new work, assuming advances are also made to fully characterize the shapes of volcanic particles over the whole range of sizes, and their variability among eruptions.

III.3.5.4. Constraints on the diameter of ballistic blocks

A few eruptive events exhibit ballistic signals which appear on the radargrams as very narrow oblique streaks (Figure III.9, left). Such narrowness, along with the fact that most streaks have similar power values and they are consistent with simulated ballistic trajectories, strongly suggests that these are in fact generated by individual blocks. The power inversion of these streaks can thus give constraints on the size of the blocks expelled during such events.

The mean power value of these streaks is obtained by automatic extraction of the peak power value on each Doppler spectrum (Figure III.9, right), and computation of the mean value. We then use the radar equation for point targets (i.e. single scatterer), and vary the particle

diameter until the obtained synthetic power matches the recorded one. The results suggest that the streaks highlighted in Figure III.9 (yellow markers) were generated by blocks having a diameter of ~0.088 m in gates 2847, 2727, and 2487 m.

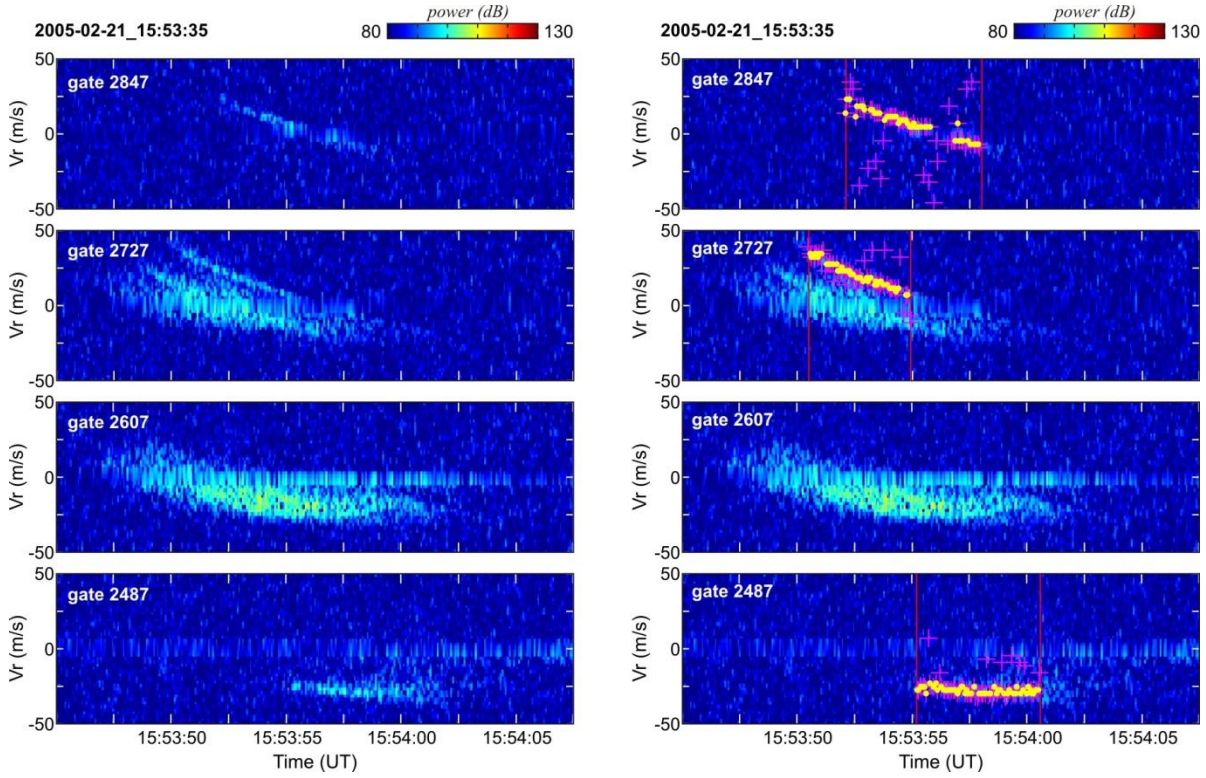

Figure III.9. Ballistic signal characterized by narrow streaks, and attributed to the expulsion of individual blocks. The right hand plot shows the automated collection of the mean streak power: pink crosses correspond to the peak values picked on the Doppler spectrum at each time step, and the yellow dots are the filtered values which are retained to compute the mean power of the streaks. The filtering procedure consists in collecting the values found within a chosen velocity range, on both sides of the least-square fit line computed from the picked values (pink crosses).

III.3.6. Conclusions

Ground-based Doppler radars allow the discrimination of ballistics and ash plumes expelled simultaneously. The Doppler radar signatures show two distinct dynamics characterized by different evolutions of the velocity range with time, distinct durations and transit speeds through the radar range gates. In the event analyzed, the ballistics are released instantaneously and transit through 3 range gates in <10 s at radial velocities exceeding 40 m/s. The mass of centimeter- to decimeter-sized ballistics is confidently estimated at 0.5–7 tons. Contrastingly, the ash plume emission lasts several tens of seconds, exhibits lower along-beam velocities (< 15 m/s in the radar direction) and longer transit times in the beam, depending on the wind speed and direction. Because the inferred mass becomes critically dependent on the assumed

diameters for infra-centimeter particles, the ash plume mass is loosely constrained at $5.8 \cdot 10^2$ tons assuming an average diameter of 2 mm above the vent. The ability to remotely discriminate ballistics and ash plumes expelled simultaneously opens a way to better constrain the eruption mechanisms and source parameters. In particular, refining the mass fraction prone to be ejected in the atmosphere during large eruptions would help in the modeling and monitoring of tephra dispersal. Furthermore, inversion procedures to obtain numerical models matching the exact time-velocity distribution of the echo power in the observed signal, are the subject of ongoing research (see Chapter V). These will enable the retrieval of initial eruptive parameters, such as initial gas velocities, particle size distribution, ejecta trajectories, and exit velocities.

III.4. Statistical analysis of the Doppler signature of ballistics and plume

The Doppler radar VOLDORAD 2 has monitored Arenal's eruptive activity during three field campaigns, in 2004, 2005 and 2009 successively. The 2004 and 2005 field campaigns were short, lasting respectively 8 and 11 days in February of each year. The campaign in 2009 on the other hand, lasted 47 days: from January 17 till January 26, the radar was operated daily from the same spot as in 2004 and 2005 using a generator; and from then on until March 4, the radar monitored continuously the volcanic activity from Arenal's park entrance office. Despite many interruptions in electric power, a relatively continuous dataset can be exploited. The signals having the best signal-to-noise ratio were extracted from the complete data set, giving a subset of 45 events. We hereafter carry a statistical analysis of the Doppler signature of these eruptive events, and comment the implications for the eruptive mechanisms.

III.4.1. Relative proportions and temporal relationships of ballistic emissions and ash plumes

III.4.1.1. Relative proportions of ballistics and ash plumes

We have previously showed that ballistics and ash plumes had distinct Doppler signatures, evidenced by distinct life spans, exit velocities, and transit velocities through the radar beam. The occurrence of the ballistics and ash clouds is observed in several recordings of eruptive events, either simultaneously, or independently. Figure III.10 shows the distribution of the events involving ballistics only (red), ash plume only (blue), and those involving both ballistics and ash plume (green) during the three field campaigns. Note that the 45 events referenced are only a subset of all the recorded events, and represent the most powerful and/or interesting events for our purposes. For instance, a few weak ash plumes were recorded during the 2004 campaign, but because these were judged too weak to appear in the subset, no ash plume event appears for this campaign in Figure III.10.

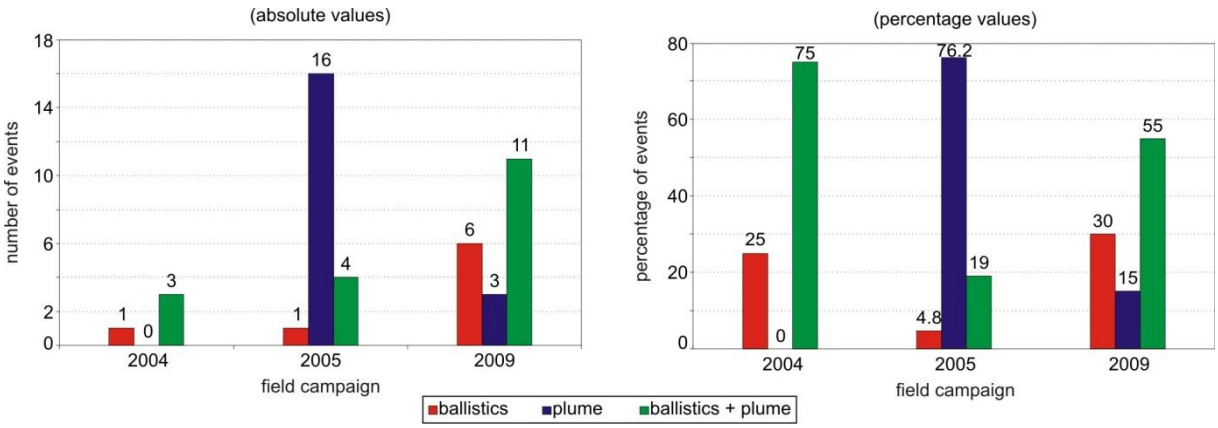

Figure III.10. Distribution of the type of eruptive events recorded with the radar during three field campaigns at Arenal. The left plot counts the number of events in each category, while the right plot counts the proportion of each category in each campaign.

It is clear from Figure III.10 that the eruptive events recorded during the three field campaigns do not have the same phenomenology. In 2004 and 2009, a majority of events involved powerful ballistic projections (i.e. ballistics only or ballistics and plume, Figure III.11a, which sum to 100 % and 85 % respectively), with only few involving just an ash plume (0 % and 15 % respectively). In 2005, when the activity was low however, the opposite is observed: the majority of events do not involve ballistics (76.2 % with just the ash plume), and when ballistics are involved, these are very weak in intensity (e.g. Figure III.11b). The interpretations which can be made on the eruptive mechanisms based on this observation are discussed further down.

III.4.1.2. Temporal relationship between ballistics and ash plumes

Interestingly, when an eruptive event shows the signature of an ash plume and ballistic projections, the first signal to appear is not systematically the same (as noticed by *Donnadieu et al.* (2004), IAVCEI, for the 2004 campaign). In some cases, the ballistic projections appear first on the radargram, and are shortly (or simultaneously) followed by the ash plume (Figure III.12a). In other cases contrastingly, the ash plume emission precedes the ballistics (Figure III.12b), sometimes by several tens of seconds. Note that in that case, the onset of the ballistic projections and the ash plume does not necessarily come from the same gate (e.g. Figure III.13). *Sahetapy-Engel et al.* (2008) report similar observations from Santiaguito volcano: thermal waveforms evidence the emission of small gas puffs more or less ash laden, which may precede the main eruptive emission. Discussions on the implications this observation has on eruptive mechanisms are addressed below.

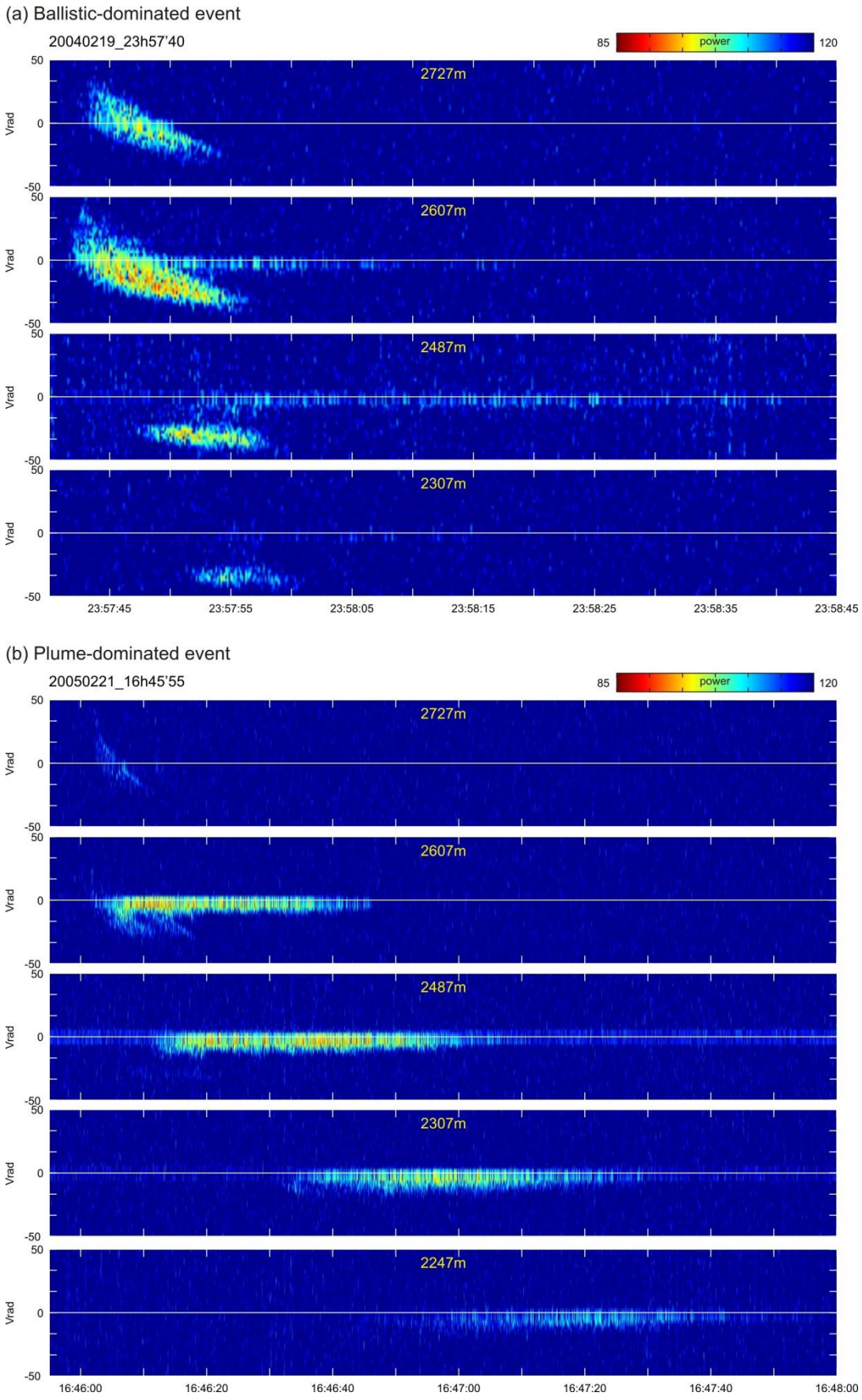

Figure III.11. Two eruptive events, respectively dominated by (a) ballistic projections, and (b) an ash plume (b). The predominance of one over the other is evidenced by their respective Doppler signature: the short-lived part of the signal is of ballistic origin, while the long-lived part is induced by the ash plume.

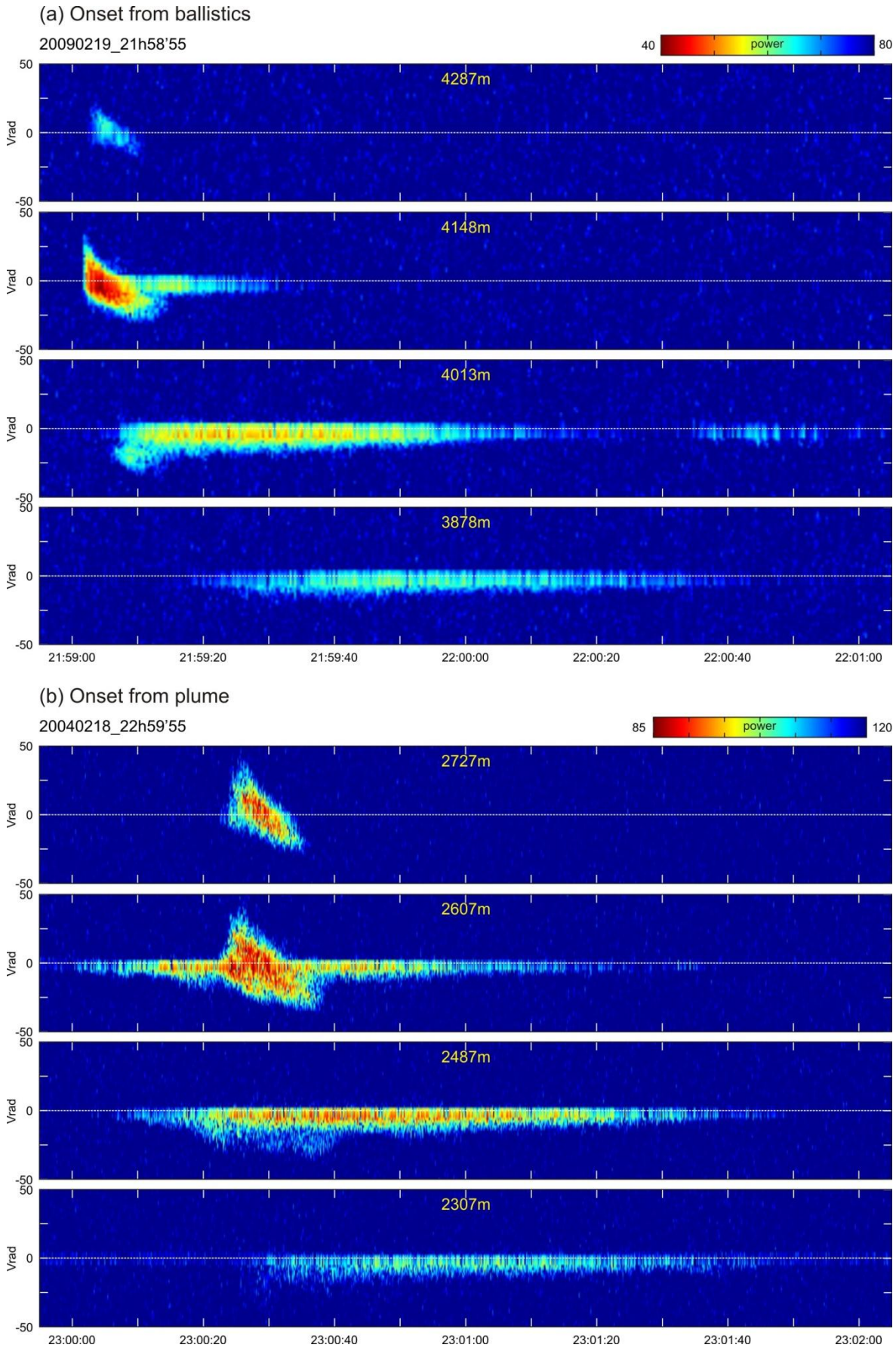

Figure III.12. Eruptive events, with onsets coming respectively (a) from the ballistics, and (b) from the plume.

III.4.2. Variability in the Doppler signature of ballistics and ash plumes

The discriminative characteristics of the ballistics' and the plumes' Doppler signature have been discussed in section III.3 of this chapter (*Valade and Donnadieu*, 2011). Based on a representative eruptive event, we showed that both had different dynamics, which were revealed on the radargrams by distinctive radial velocities, life spans, and transit speeds through the beam. We hereafter present a more complete view of these characteristics, based on the radargram analysis of the 45 events collected during the 2004, 2005 and 2009 field campaigns. By doing so, we intend to show how radargrams can be powerful to reveal the variability in eruptive dynamics.

The procedure to collect these characteristics was semi-automated: the date and time of the events of interest were stored in an Excel sheet, and the *RadargramBuilder* software (appendix B) successively computed the radargrams, allowing the user to pick on the radargram image the value of interest, and automatically store it in a data base. Note that the values presented here are picked directly from the radargram, not from the power nor velocity time series. The values may consequently suffer from slight underestimations, as discussed in section III.2.2. For example, velocities seen on the radargram are weighted by the power, thus the highest velocities with low power do not appear clearly. Nevertheless, except for aliased spectra, the error in estimation is generally in the order of a few percents (see Figure III.2), which is largely acceptable for our purpose.

Figure III.13 shows how radargrams are segmented, how the different parts are referred to, and what parameters are picked.

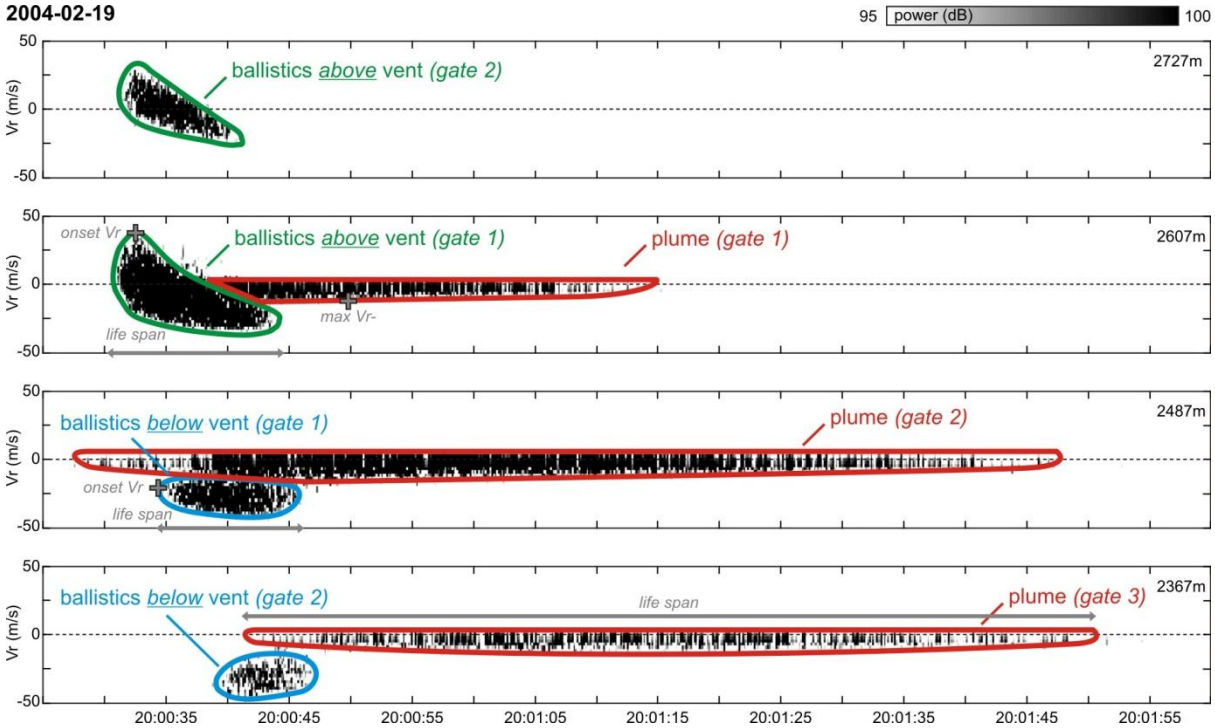

Figure III.13. Schematic view of how radargrams are segmented: ballistics entering the gates above the vent imprint as impulsive oblique streaks (green), those entering the gates below (down the beam) as short-lived signals staggered in the negative velocities (blue), and the ash plume on the other hand imprints as an emergent long-lived signal (red). Because the studied radargrams were computed with data from several recording campaigns, the gates in which these features are observed are not systematically the same. For this reason, the first gate in which a given feature is observed is named gate 1, and the numbering increases as the gate of appearance is further away from the vent.

III.4.2.1. Doppler signature of ballistic projections

The ballistics are seen on radargrams as a short-lived signal, which exhibits high and contrasted Doppler velocities, and which transits rapidly through the ranges gates. Due to the beam inclination however, the ballistics entering the gates up the vent do not have the same Doppler signature as those entering the gates down-beam from the vent, towards the radar. While the former imprint on the radargrams as oblique streaks (green in Figure III.13), the latter imprint as more horizontal streaks with negative radial velocities (blue in Figure III.13). This is illustrated in Figure III.14, which shows a simulation of ballistic projections through the radar beam. Two particles with distinct ejection angles are tracked in order to understand how the evolution of their trajectory and true speed (indicated by the color code) are imprinted on the Doppler radargrams. Particles enter the beam with a true speed of ~50 m/s.

Let us briefly comment the successive markers annotated on the figure. Markers labeled A① to A③ track the particle travelling towards the radar, and markers B① to B② the particle travelling away from the radar:

A① The left-most particle in the ejection cone (i.e. 110° from the horizontal) enters gate 2607 m at high speed, yet imprints on the radargram with a radial velocity $V_r = 0$ m/s. This results from the fact that when the particle enters the gate its trajectory is nearly perpendicular to the beam.

A①–A② The particle speed decreases as gravity takes over momentum (i.e. color shift from red to blue). Moreover, due to the parabolic trajectory of the particle it becomes progressively more tangent to the beam axis, resulting in an increasing radial velocity (in absolute values, i.e. from 0 to ca. -16 m/s). This sketches an oblique streak, characteristic of the gates above and up-beam from the vent (e.g. signal outlined in green in Figure III.13).

A② The particle enters gate 2487 m, i.e. the first gate below and down-beam with respect to the eruptive vent.

A②–A③ The particle speed increases once again upon falling due to gravity, causing the radial velocity to increase slightly during the first two seconds (~6.2 – 8.2 s). The radial velocity then becomes constant (ca. -22 m/s), sketching a horizontal streak characteristic of the ballistic signal in the gates below the vent (e.g. signal outlined in blue in Figure III.13).

A③ The particle enters gate 2367 m. Notice that the onset radial velocity in that gate is the same as the maximum velocity in gate 2487, indicating that the particle is falling at constant radial speed (although the particle is accelerating) and constant angle.

B① The particle at the right-most of the ejection cone (i.e. 70° from the horizontal) enters gate 2727 m with a high radial velocity $V_r = 30$ m/s, due to both its high traveling speed and the small angle to the radar beam.

B② The particle exits gate 2727 m with a trajectory nearly perpendicular to beam axis, resulting in a radial velocity close to $V_r = 0$ m/s. The progressive decrease from 30 m/s to 0 m/s sketches a diagonal streak, typical of the ballistic signal in the gates uphill from the vent (e.g. signal outlined in green in Figure III.13).

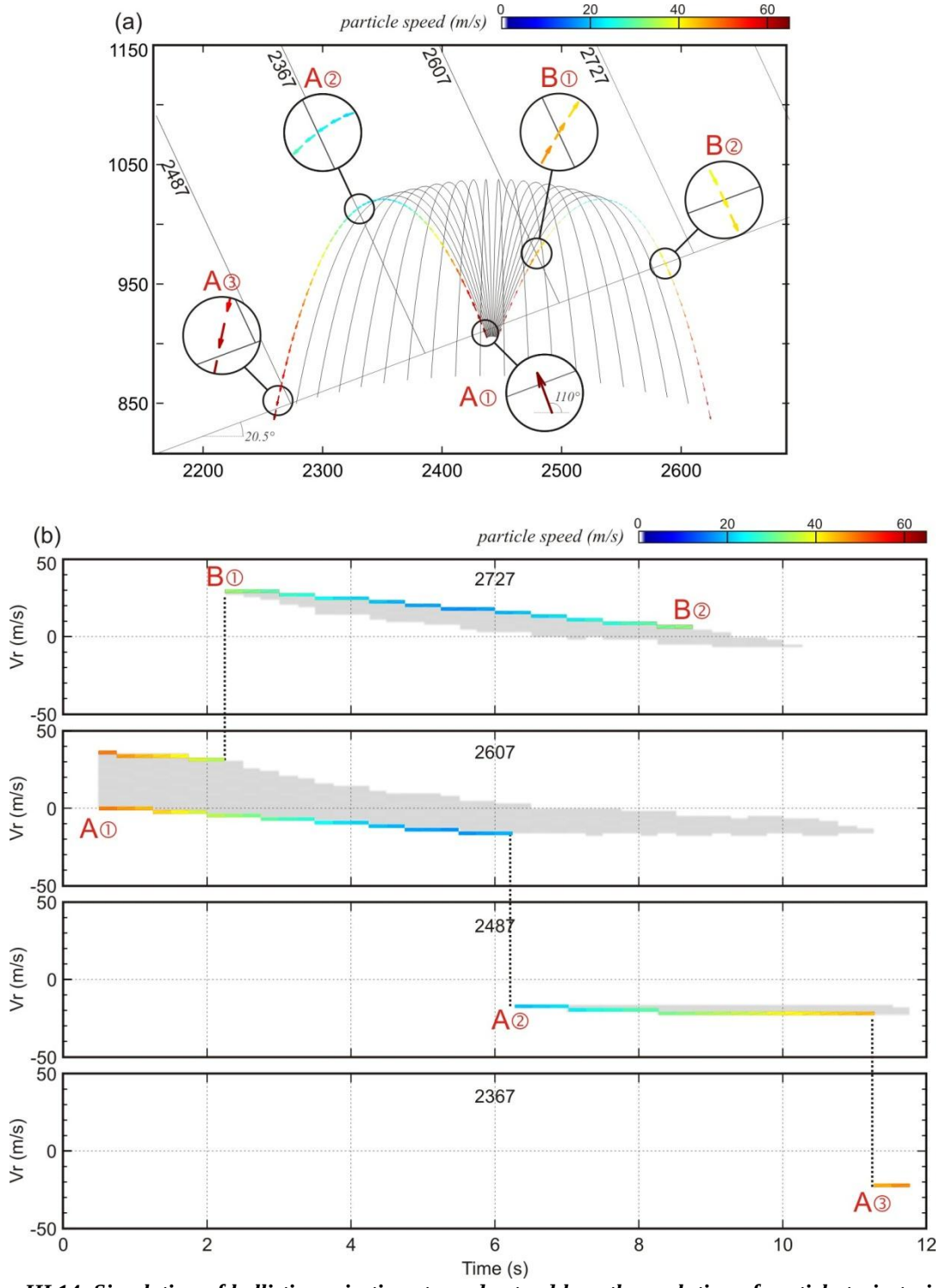

Figure III.14. Simulation of ballistic projections to understand how the evolution of particle trajectories and speeds are imprinted on Doppler radargrams. (a) Particles of 0.1 m in diameter are launched with initial gas velocity of 100 m/s, at ejection angles ranging from 70° to 110° from the horizontal (counter-clockwise), and enter the beam with a speed of ca. 50 m/s. The velocity vectors of the two particles launched at 70° and 110° (labeled B and A respectively), are plotted at each time step by colored arrows (the length and color being related to the particle speed). (b) Synthetic Doppler radargrams resulting from the ballistic projections illustrated in (a). The colored streaks are generated by the two particles launched at 70° and 110°, respectively, with colors referring to the particle speed. Magnification of the particles' trajectory are shown at key timings, i.e. when particles transit from one gate to another (A①,②,③ and B①,②).

Let us now describe the characteristics of the ballistics' signal in the gates above and below the vent, based on the analysis of 45 recorded radargrams.

III.4.2.1.1. Characteristics of the ballistics' signal in the gates **above** *the vent (up-beam)*

Peak onset velocities

Figure III.15a shows that the peak onset radial velocity of the ballistics' signal in the gate above the vent (i.e. maximum radial velocity V_r, gate n°1, see Figure III.13) are staggered between +10 and +60 m/s. However, the value at +60 m/s is in fact underestimated because the Doppler velocities exceed the velocity range fixed at the time of the recording (ranging from up to +59 m/s only). A reconstruction of aliased spectra is used to extrapolate the maximum velocity, which gives a maximum velocity of ca. 80-90 m/s for that event (*Donnadieu et al.*, 2005). Notice that the ballistics may enter two more gates away from the vent (i.e. gates 2 and 3). The maximum positive velocity in those gates may either be higher or lower than in the first gate of appearance (i.e. gate 1). This is mostly likely due to the geometry of the eruptive jet and the position of the vent, which will dictate the particle trajectories and in turn the radial velocities recorded by the radar (see Figure III.14).

It is also interesting to mention that the time it takes for the signal to reach its peak V_{r+} value may vary. In most cases, the onset is sudden (i.e. peak value reached in <1 s), which suggests that the ballistics are instantaneously released (e.g. Figure III.12a). More rarely, the peak value is reached within a few seconds, suggesting that ballistics' emission may be progressive (e.g. Figure III.12b). The observer must be careful, as once again, this is dependent on the geometry of both the sounding conditions (e.g. beam angle) and the eruptive jet (e.g. inclination).

Life spans

Figure III.15b shows that the life spans of the ballistics' signal in the gate above the vent are staggered between 5 and 17 s. Comparatively, particles ejected instantaneously can stay up to 11 seconds in the gate above the vent (see simulation in Figure III.14), suggesting that the lifespan can be interpreted in terms of height reached by the particle within the gate (and thus signal duration in that gate) rather than emission duration. Notice also that when the ballistics enter several gates, in almost all cases the signal lasts longer in the gate directly above the vent (gate 1) than in those further away (gate 2 and 3). This results from the fact that in the gate directly above the vent, the particles ejected nearly vertically remain in that gate during both their ascent and descent (see Figure III.14). In turn, this yields a longer life span to the

signal in that gate than in those further away, where the particle trajectories tend to cross the gates on the bias.

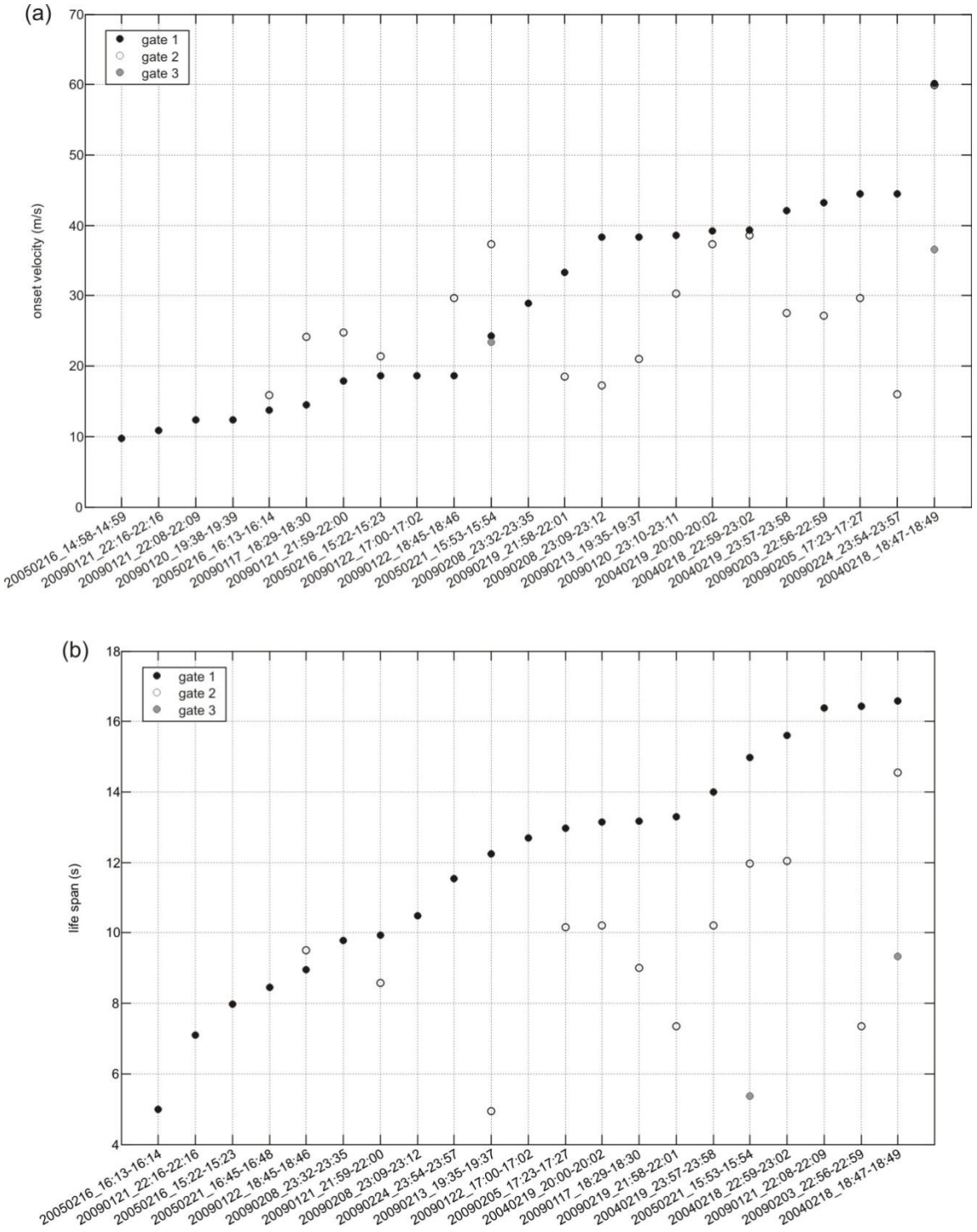

Figure III.15. (a) Peak onset radial velocities, and (b) life spans of the ballistics' Doppler signature in the gates above and up-beam from the vent, picked from the Doppler radargrams as shown in Figure III.13. The events are sorted according to the values from gate 1, i.e. the first gate in which the signal appears (which is not systematically gate 2607 m depending on the recording campaign and the subsequent sounding conditions). Gates 2 and 3 refer respectively to the second and third gates away from gate 1 (i.e. up-beam). Event 20040218_18:47 exhibits an onset velocity of +60 m/s, however this is an underestimation because the signal exceeds the Doppler spectral range (+59 m/s). Extrapolation of the Doppler spectra suggests an onset radial velocity of +80 m/s for that event (Donnadieu et al., 2005).

III.4.2.1.2. Characteristics of the ballistics' signal in the gates **below** *the vent (down-beam)*

Onset velocities

Figure III.16a shows the distribution of the ballistics' onset radial velocities in the gates down the beam away from the vent (i.e. blue outline in Figure III.13), which spread from -12.5 to -47 m/s. The onset velocities tend to increase (in absolute values) in the gates which are progressively further away from the vent. This is due to both the progressive bending of the ballistic trajectories (which tend to align with the beam axis, and thus result in higher radial velocities), and the acceleration of the particles upon its descent due to gravity (see simulation in Figure III.14, gates 2487 and 2367 m, markers A② and A③).

Life spans

The life spans of the ballistics entering the gates below the vent are showed in Figure III.16b. In the first gate in which the signal is observed (gate 1), these range between 5 and 21 s. Note that highest value plotted is in fact 25 s (20090122_23:54), but this value is excluded from the given range because the event is likely composed of several pulses, which are hard to distinguish one from another. In the gates further away from the vent (e.g. gates 2, 3 and 4) the signal lasts less than in gate 1, since fewer particles are able to enter the gate and their trajectories tend to cross the gates on the bias (e.g. gate 2367 in Figure III.14, marker A③).

Transit speeds

The distribution of the transit speeds of the ballistics crossing the successive gates down-beam from the vent is plotted in Figure III.16c. Apparent transit speeds are calculated by picking the onset delay between two successive gates, and dividing it by the range gate's radial depth. The figure shows that the transit speeds are high, staggered between 24 and 56 m/s. Note however that the obtained values are minimum estimates of the transit speeds, since the gate's radial depth is the minimum distance the ballistics must travel to cross the gate. For instance, the transit speed inferred from the onset delay between gates 2487 and 2367 m in the simulation (Figure III.14, markers A② and A③) would be estimated at 20 m/s (i.e. 120 m / 6 sec), when it should be in fact of 27.5 m/s (i.e. ~165 m traveled in 6 sec).

This rapid transit through the gates is characteristic of the Doppler signature of ballistic particles.

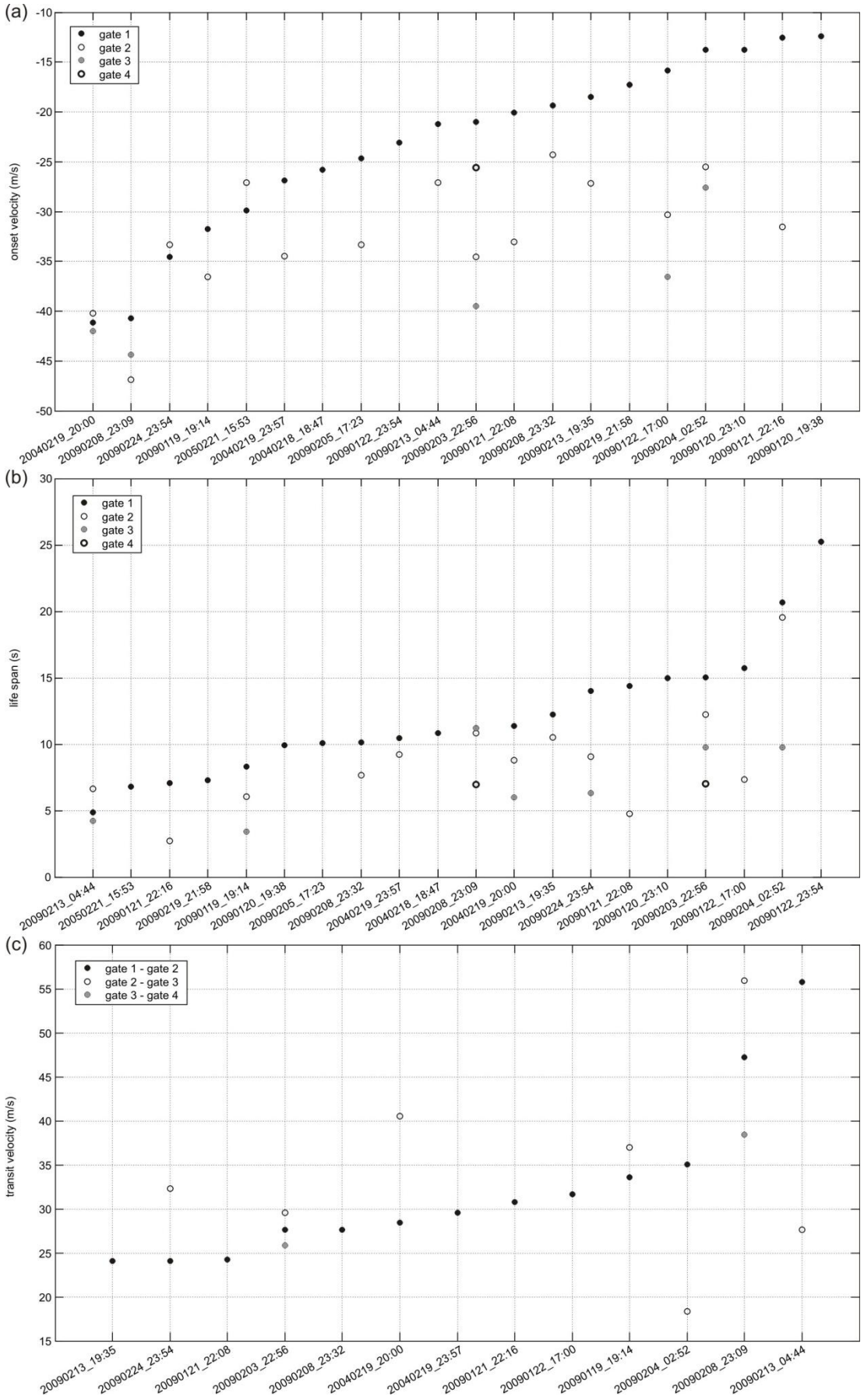

Figure III.16. (a) Onset radial velocities, (b) life spans, and (c) transit speeds of the ballistics' Doppler signature in the gates down the beam, picked from the radargrams as shown in Figure III.13.

III.4.2.2. Doppler signature of ash plumes

The ash plumes are seen on radargrams as long-lived signals, with low negative Doppler velocities, that transit slowly through the ranges gates. Let us give a statistical overview of these characteristics.

Maximum negative radial velocities

Figure III.17a displays the events exhibiting strong ash plumes signals, from which were picked the maximum negative radial velocities in the first gate of appearance (as illustrated in Figure III.13). The values are staggered between -10 and -30 m/s, but a few events with very weak plume signals (not displayed here), exhibit very low radial velocities < |-10| m/s. Notice that the highest value (|-33| m/s) is slightly apart from the general trend; this value however might be slightly overestimated because the plume signal of this event is difficult to distinguish from the ballistics.

As previously said, the events displayed in this figure are the strongest ash plume signals recorded, i.e. those which exhibit the highest backscattered power and consequently the strongest ash loading. We interpret the negative velocities presented here as resulting from both the drift of the ash plume towards the radar (easterly trade winds), and the sedimentation of the particles within the first hundreds of meters from the vent.

Life spans

The life spans of ash plume signals in the first three gates of appearance are presented in Figure III.17b. The plume signal may be observed in up to 6 gates, but only the first three were kept for graph readability. The life span of ash plume signals are long, staggered between ~20 and 160 seconds. Notice that the life spans in gate 1 are always shorter than in the gates further away from the vent due to the progressive plume expansion. When comparing the life spans in gates 2 and 3 however, the same observation does not hold: exiting of the plume from the beam (due to variable wind directions) becomes critical, and thus the life spans do not have repeatable relationships (e.g. life span in gate 3 longer than in gate 2). The sensitivity of the power diminution due to volumetric exiting of the plume from the radar beam can be found in section VI.2.

Transit speeds

The transit speed of the plume through the beam is more difficult to compute than that of the ballistics, mostly because of the signal onset is difficult to pick precisely since it is emergent.

We found that the transit speeds computed between gates 2 and 3 was the most relevant, because (i) the onset is not merged with the onset of the ballistics' signal (case of gate 1), and (ii) the onset is sharper than in the gates further away (e.g. gate 4 and beyond). Note however, that in addition to the ash plume drift by trade winds, the resulting values may be influenced by the plume expansion.

The transit speeds are displayed in Figure III.17c, and show low values ranging between 4 and 15 m/s. This slow transit is characteristic of the Doppler signature of ash plumes, which contrasts with the high transit speed of the ballistics' Doppler signature (> 25 m/s). In Chapter VI, we show that the onset times of the ash plume detection in each range gate can be used to infer the three dimensional transport speed of wind-drifted ash plumes (*Donnadieu et al.*, 2011).

III.4.2.3. Synoptic summary of the Doppler signature of ballistics and ash plumes

Based on the analysis of 45 Doppler radargrams recorded in 2004, 2005 and 2009, we were able to give a statistical overview of the Doppler signature of both ballistic projections and ash plumes. The two show contrasted dynamics with notable discriminative features. Ballistic projections imprint on the radargrams as a short-lived signal, characterized by a short life span (5-21s), a rapid transit speed through the range gates (24-56 m/s along-beam), and high contrasted radial velocities. In the gates above and up-beam from the vent, the Doppler signature appears as a diagonal streak, with an impulsive onset at high positive radial velocities (+10-80 m/s) that progressively shift towards negative values as the trajectories bend and become perpendicular to the beam axis. In the gates below and down-beam from vent on the other hand, the signal onsets at high negative radial velocities (-12.5 – -47 m/s), and sketches a more horizontal streak as the particles tend to reach a constant angle upon falling. Contrastingly, the Doppler signature of ash plumes is a long-lived signal, characterized by: a long life-span (20-160 s), low radial velocities (< -30 m/s) with emerging onset, and a slow transit through the range gates (4-15 m/s along-beam) as the plume gets drifted by trade winds towards the radar.

The chronology between the ballistics and the ash plume signals however seem to vary. Moreover, their respective proportions change from one recording campaign to the other. Below, we use these observations to provide an interpretation on the source eruptive mechanisms responsible for both phenomena.

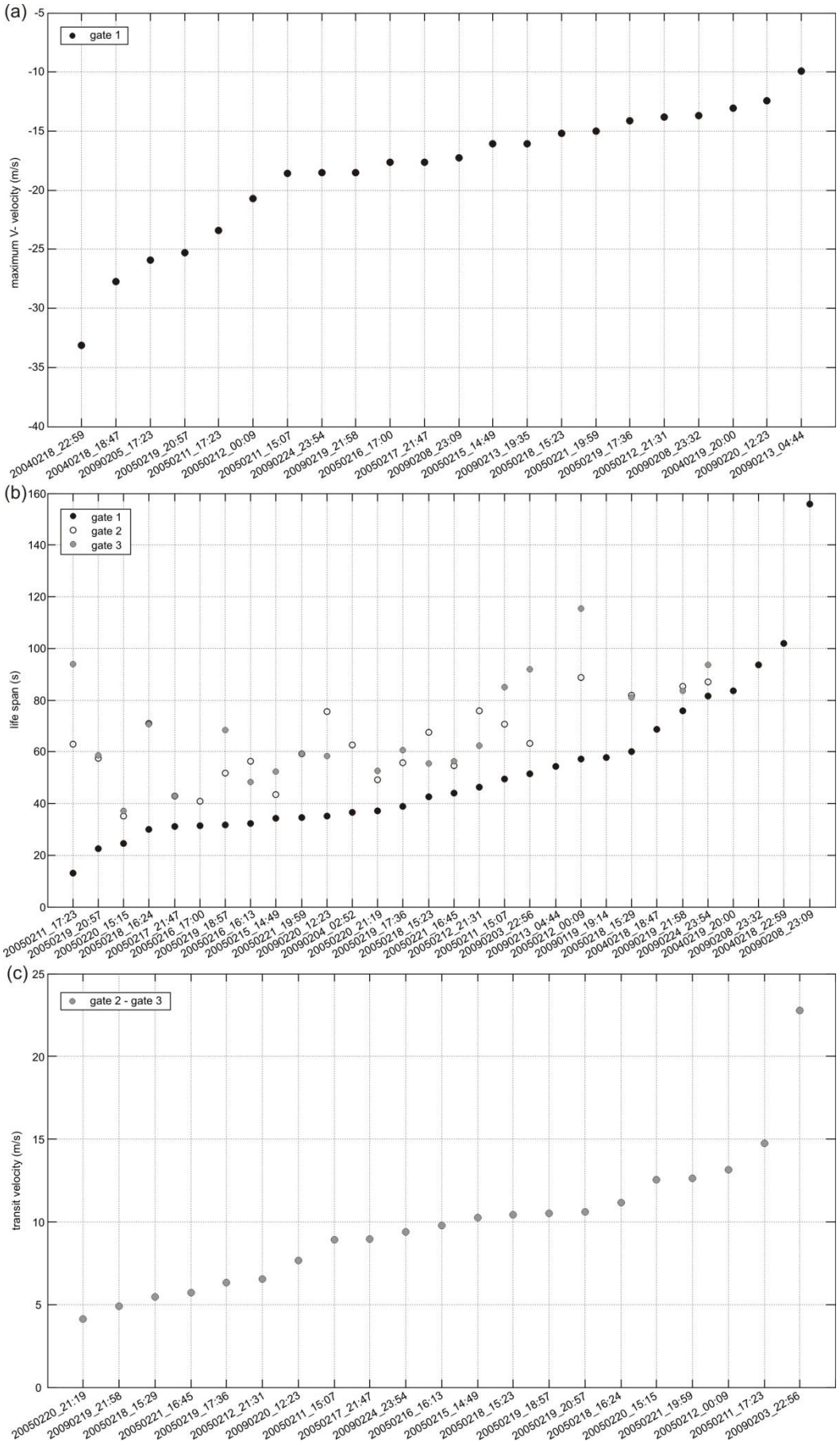

Figure III.17. Maximum negative radial velocities (a), life-spans (b), and transit velocities (c) of ash plumes.

III.4.3. Ballistics and plumes: discussions on source eruptive mechanisms

The proportion of events comprising ballistics or ash plumes is seen to vary from one recording campaign to another. Moreover, when an eruptive event expels both ballistics and an ash plume, the chronology of both events is not systematically the same. These observations question the source mechanisms responsible for both emission types at Arenal.

The magma fragmentation processes and the subsequent relative ash / bomb proportions, are believed to depend mainly on the magma viscosity and the distribution of bubbles within it (*Ozerov*, 2010). This assessment however, is likely to hold in volcanic settings where magma viscosities are relatively low, i.e. where bubbles can migrate buoyantly through the magma column. At Arenal however, the magma viscosity is high (in the range 10^5-10^6 Pa s, *Cigolini and Borgia*, 1980; *Cigolini et al.*, 1984; *Bertolino et al.*, 2009), and a viscous lava cap obstructs the conduit. The latter is believed to drive Vulcanian-type eruptive mechanisms (Chapter II), wherein conduit-sealing and cap-breaching would be responsible for the eruptive activity. In this context, it is likely that ballistic projections result from coarse fragmentation of the cap (e.g. breaching and "uncorking"), whereas ash plumes would result from a finer fragmentation of it. In both cases, fragmentation may involve varying proportions of "solid" and "fluid" magma (*Valade et al.*, 2012; *Cole et al.*, 2005). Sometimes, fragmentation may not necessarily be synchronous with tephra emission, and may result from ejection of previously fragmented debris residing atop the lava cap, or in its fractured permeable regions (e.g. conduit walls, *Sahetapy-Engel et al.*, 2009).

Bearing in mind these assumptions, the variable proportion of events comprising ballistics or ash plumes during the three recording campaigns (Figure III.10) can be interpreted in terms of source conditions/processes. The fact that the 2005 campaign exhibits very few ballistic events suggests that the cap was not breached significantly during the eruptive events, perhaps because it was significantly fractured and consequently permeable to gas, thus preventing from the accumulation of strong overpressures. This is in agreement with the long-lasting and interrupted tremor sequences observed (see Chapter II), which require stable, non-destructive, opening and close of the fractures cross-cutting the solid cap. It is also in agreement with the low overpressures recorded during this campaign (ca. $1.26 \cdot 10^5$ Pa, *Fourel and Vergniolle* unpublished), which prevented intense breaching of the cap. Contrastingly, the 2004 and 2009 campaigns exhibit more eruptive events with ballistic projections, suggesting that the system was probably more pressurized, leading to more intense uncorking of the rigid crust.

Variability in the cap thickness may also be a factor influencing the eruptive phenomenology, however as of today, we have no means to derive this information. All we can say is that the magma composition at Arenal shows remarkable stability (e.g. *Szramek et al.*, 2006), and that effusion rates between 1999 to 2004 were at their lowest since Arenal's reawakening in 1968 (ca. 0.1 m^3/s, *Wadge et al.*, 2006).

On the other hand, the fact that ash emission may precede ballistic projections (e.g. Figure III.12b), suggests that gas and ash may be expelled from one or several fractures or vents, which may exhibit variable mechanical response to overpressure. Similar to a pressure cooker's valve, the pressure underlying the cap may first be released as a high-frequency gas jet (more or less ash-laden), until the fracture strength is overcome, leading to a larger disruption of the fracture, more intense breaching of the brittle crust, and in turn expulsion of coarser particles with ballistic trajectories.

III.5. Conclusion

Doppler radargrams were constructed by stacking the *Doppler spectra* through time, and using a color scale to account for the backscattered power. The time-velocity distribution of the power thus describes the *Doppler signature* of the recorded target.

Distinct Doppler signatures are witnessed within the radargrams of eruptive events, with distinctive characteristics that betray distinct eruptive dynamics. The first is a short-lived signal, characterized by: a short life span (5-21s), a rapid transit speed through the range gates (24-56 m/s along-beam), high impulsive radial velocities (+10 – +80 m/s) progressively shifting towards negative values in the gates uphill the vent (sketching a characteristic oblique streak), and high negative values (-12.5 – -47 m/s) in the gates downhill the vent (sketching a more horizontal streak due to constant radial velocities). The second is a long-lived signal, contrastingly characterized by: a long life-span (20-160 s), low radial velocities (< -30 m/s) with emerging onset, and a slow transit through the range gates (4-15 m/s along-beam).

These distinct characteristics suggest that the short-lived signal is generated by the rapid transit of ballistic blocks through the range gates, while the long-lived signal results from the slow drifting of ash plumes by trade winds blowing towards the radar (*Valade and Donnadieu*, 2011; *Donnadieu et al.*, 2011).

Chapter IV

Forward modeling of pyroclastic emission

IV.1. Introduction

In order to understand what the recorded radar signals can actually tell us about the underlying pyroclastic emission dynamics, it is useful to simulate such emissions and reconstruct the synthetic radar signals from these. The modeling approach is thus twofold: one must (i) develop the numerical models which simulate the pyroclastic emission dynamics using the proper set of physical equations, and (ii) construct the synthetic signal which would be recorded by the radar, using the appropriate electromagnetic scattering equations. At this stage, because we (arbitrarily) define the source input parameters to our model, the modeling is termed ***forward modeling***.

As it has been shown in the previous chapter (Chapter III, *Valade and Donnadieu,* 2011), the Doppler radargrams of several eruptive events witness the emission of ballistics and ash plumes, which simultaneously transit through the radar beam. In the following chapter, we describe how both phenomena are modeled and how synthetic radargrams are generated. For the modeling of both the ballistics and the ash plume, the physical equations driving the particle motion are first described, after what parametric tests are presented to show how the main input parameters to these equations influence the resulting radar signal.

The equations driving respectively the ballistic- and ash plume-particles are entirely independent. Nevertheless, they are implemented in a unique *Matlab* code, and can be run simultaneously via a graphical user interface named ***eject3D*** (Figure IV.1). This software enables the user to easily and intuitively select the source input parameters of the driving equations. It also gives the possibility to select various types of graphical outputs, such as Doppler radargrams, particle trajectories through time and space, plot of the gate onset timings, etc… Further details may be found in appendix C.

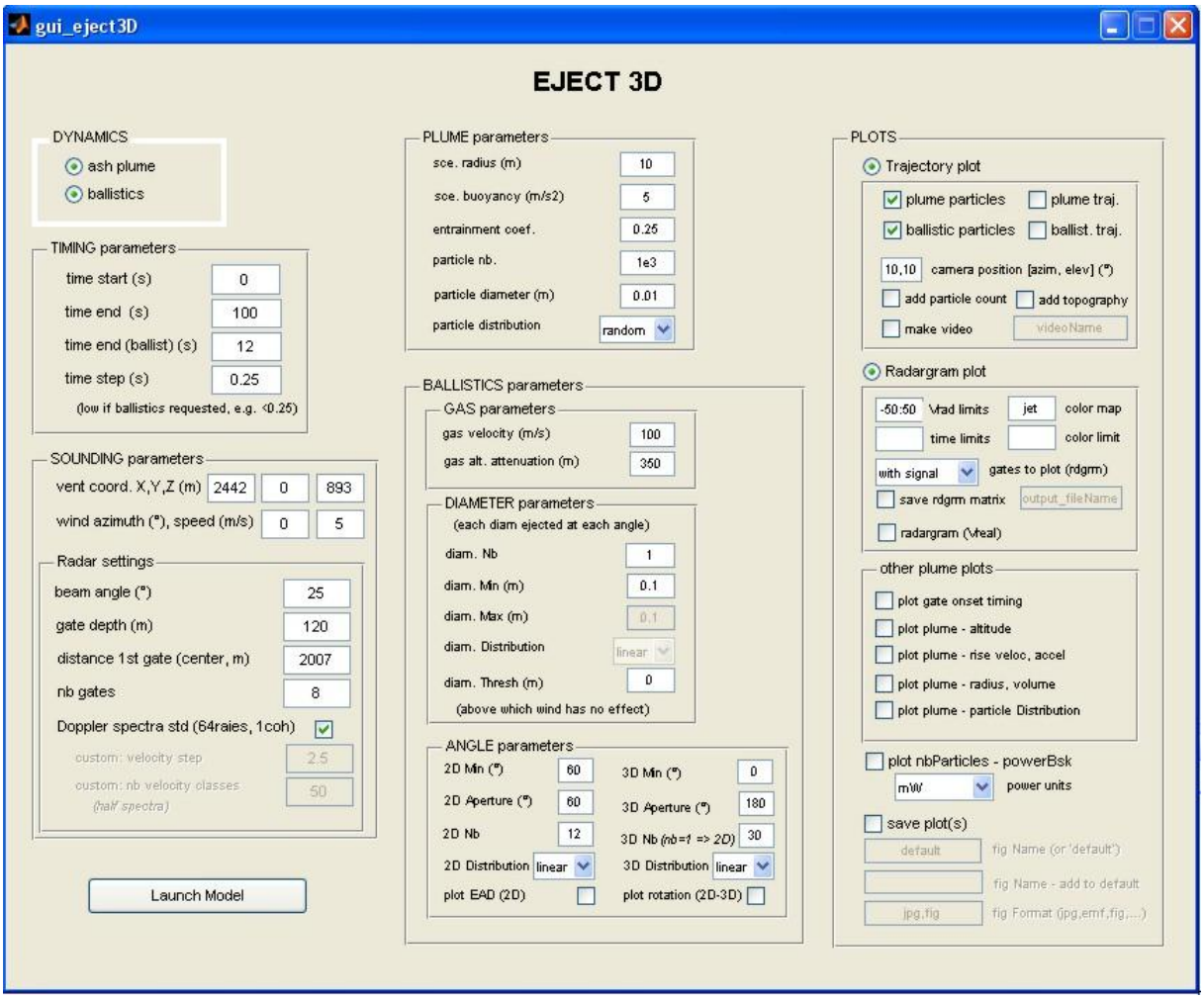

Figure IV.1. Snapshot of the graphical use interface controlling inputs and outputs to eject3D. ***Note that this interface enables the simulation of both ballistic projections and ash clouds.***

IV.1. Ballistic projection modeling

A 2D model simulating ballistic projections and the resulting radar echoes in a given gate was initially developed by *Dubosclard et al.* (2004), and later recoded in *Matlab* by *Gouhier and Donnadieu* (2010). We have built upon that and improved the model, in particular to simulate the projections in 3D. Let us describe hereafter the equations involved, the improvements made to the original code, and the model sensitivity to the main input parameters.

IV.1.1. Driving equations

Spherical particles of diameter (D) are launched instantaneously in a 2D plane, with an initial speed (V_{p0}) which is related to the initial gas velocity (V_{g0}) following *Steinberg and Babenko* (1978):

$$V_{p0}(D) = V_{g0} - k\sqrt{D} \qquad \text{IV.1}$$

where $k = \sqrt{4g\rho_m / 3C_d\rho_g} = 150$, g being the gravity, ρ_m and ρ_g the ejecta and gas densities, and C_d the drag coefficient (*Chouet et al.*, 1974). The moving particle of mass (m) is then subject to two opposing forces, the drag force (F_D) and the gravitational force (g), from which the equations of motion can be written as:

$$\frac{d^2x}{dt^2} = \frac{F_{Dx}}{m} \qquad \text{IV.2}$$

$$\frac{d^2z}{dt^2} = \frac{F_{Dz}}{m} - g$$

where (F_{Dx}) and (F_{Dz}) are the components of the drag force, and (g) is the acceleration due to gravity. The expression of the drag force (F_D) is given by *Chow* (1979) as:

$$F_D = \frac{1}{2}\rho_g A C_D (V_g - V_p)^2 \qquad \text{IV.3}$$

where (ρ_g) is the gas density (1.22 kg/m^3), (A) the cross-sectional area of the particle, (C_D) the particle drag coefficient, and (V_g), (V_p) the gas and particle velocities respectively. The gas velocity (V_g) is known to decrease exponentially (*Blackburn et al.*, 1976; *Patrick et al.*, 2007) with the distance to the vent (r), which can be expressed as:

$$V_g(r) = V_{g0} \cdot e^{(-\gamma r)} \qquad \text{IV.4}$$

where (γ) is the gas velocity decay rate. Being poorly known, (γ) was set to 0.013 as inferred from the best fit of height vs. velocity measurements carried out on eruptions at Stromboli using a FLIR camera (*Patrick et al.*, 2007). The drag coefficient (C_D), on the other hand, depends on the Reynolds number (Re), which is defined as:

$$Re = V_p \cdot \frac{D}{\eta} \qquad \text{IV.5}$$

where (η) is the gas viscosity ($1.49 \cdot 10^{-5}$ Pa s). The Reynolds number is used to derive the drag coefficient, the relationship between the two being given by experimental curves from *Goldstein* (1938). Note that these curves are suitable for spherical particles with subsonic speed, i.e. with Mach number < 0.5 (~175 m/s for air at T = 25°C and P = 1 atm). The effects

of higher particle speeds, or different particle shapes on the drag coefficient are addressed by *Mastin* (1991).

The system (equation IV.2) is then integrated numerically at each time step with a Runge-Kutta method (see *Chow* (1979) for detailed equations), in order to collect the particles' position (x, y) and velocity components (u_x, u_y). From there the algorithm locates its position in the radar beam (i.e. which range gate), computes its radial velocity (i.e. velocity component along the antenna beam direction) using trigonometrical relations, and calculates the power it backscatters to the radar using the Mie scattering theory (*Mie*, 1908) applied to the VOLDORAD case by *Gouhier and Donnadieu* (2008). Ultimately, synthetic Doppler spectra are constructed at each time step and in each gate, by (1) building classes from the radial velocities of the particles, and (2) summing the power backscattered by particles of each velocity class (*Gouhier and Donnadieu*, 2010).

IV.1.2. Improvements made to the algorithm

A number of improvements have been made to the original code described above. The entire architecture of the code has been recast (Figure IV.2), in order to (i) account for the improvements described hereafter, (ii) gain in computational time, and (iii) enable compatibility with the plume model (section IV.2), so that both ballistic particles and plume particles may be animated simultaneously in 3D via *eject3D* (see Appendix C). We hereafter point out the most relevant improvements made to the original code.

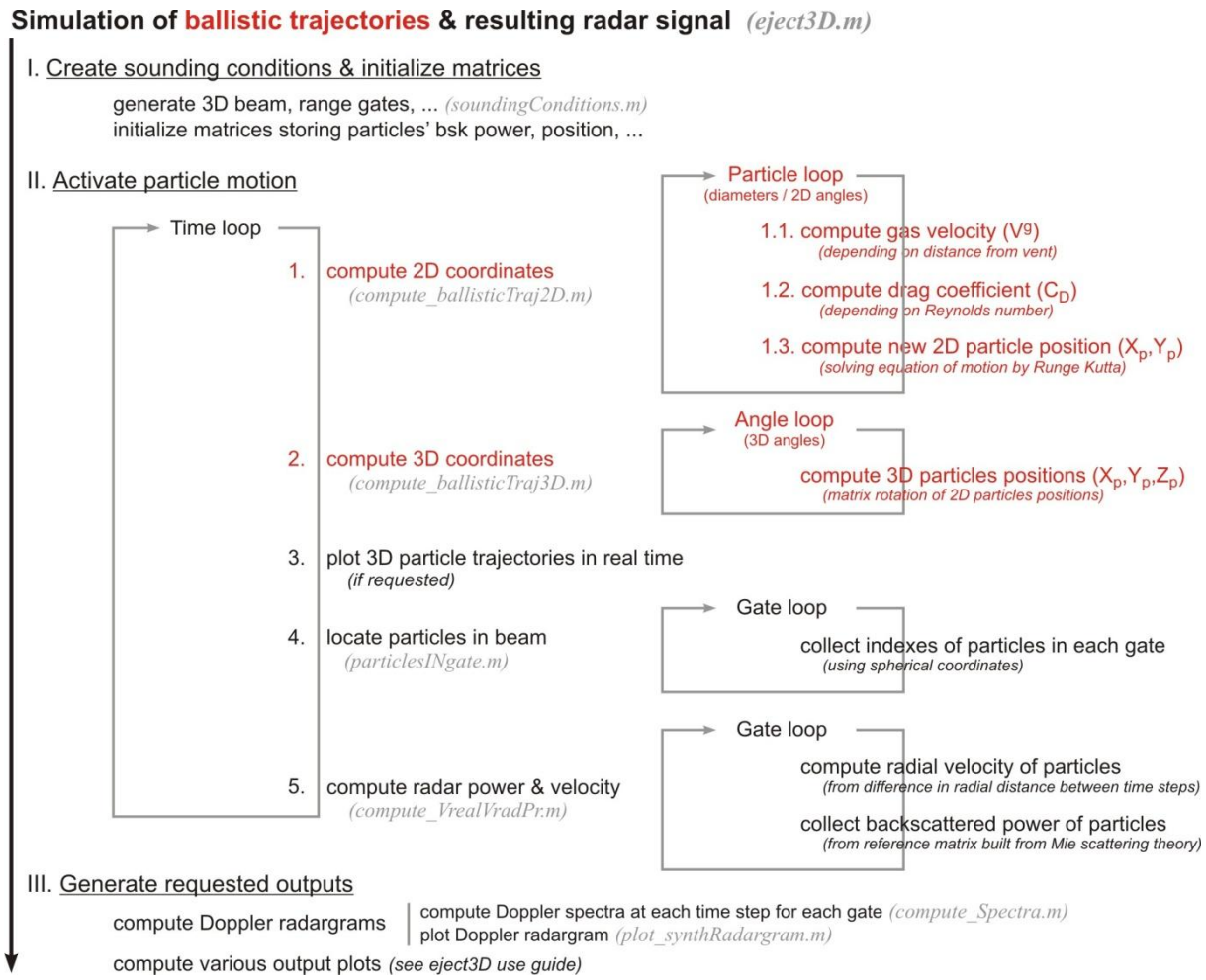

Figure IV.2. Architecture of eject3D, highlighting in red the section which specifically manages the simulation of ballistic projections.

IV.1.2.1. From 2D to 3D trajectories

The computational time of the model increases with both (i) the number of ejection angles demanded, and (ii) the number of particle diameters demanded, as each particle diameter is launched at each ejection angle. The running time can consequently increase dramatically if the user selects a polydisperse particle size distribution with a high number of ejection angles. For this reason, incorporating more complex equations dealing with 3D particle trajectories was not possible, as it would have resulted in tremendously high computational time. Instead, we compute particle trajectories in a 2D plane as described previsouly, and use rotation matrices to duplicate this plane into a number of others, thus reproducing trajectories in 3D (Figure IV.3).

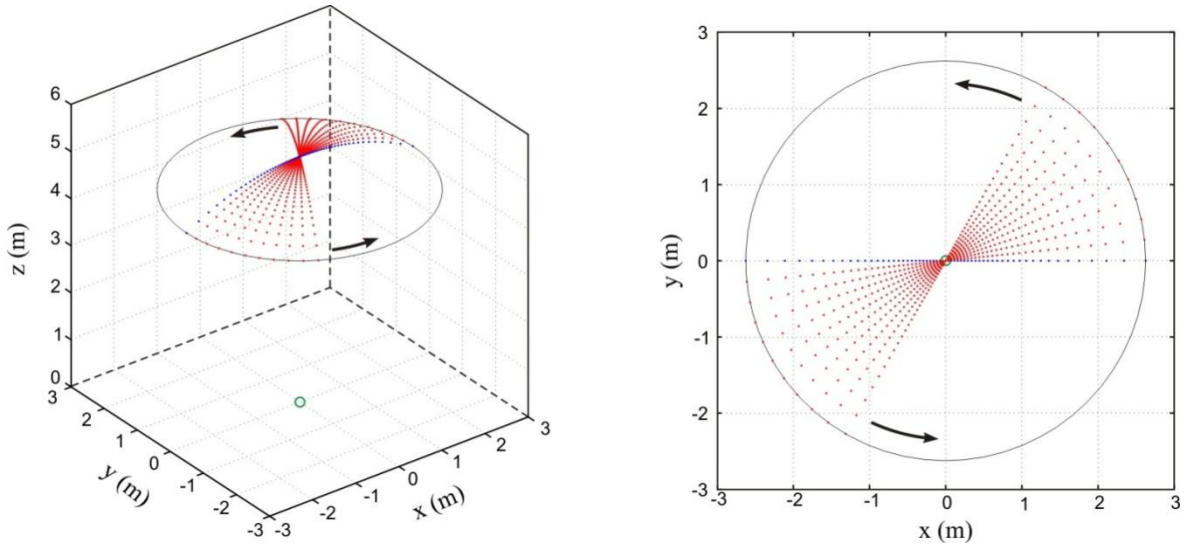

Figure IV.3. Rotation of particles contained in a vertical plane (blue dots), into a number of other planes which rotate around the jet axis (red dots). The origin of the coordinate system is the vent, i.e. the point from which particles are launched (green circle).

The rotation matrix around the z-axis in three-dimensions is written as follows:

$$R_z(\theta) = \begin{bmatrix} \cos\theta & -\sin\theta & 0 \\ \sin\theta & \cos\theta & 0 \\ 0 & 0 & 1 \end{bmatrix} \qquad \text{IV.6}$$

where θ is the rotation angle in radian, operating counter-clockwise when the rotation axis is pointing towards the observer and the coordinate system is right-handed (see arrows indicating the rotation in Figure IV.3). If the particles' coordinates {Xp, Yp, Zp} are initially stored in the matrix P defined as:

$$P = \begin{bmatrix} Xp \\ Yp \\ Zp \end{bmatrix} \qquad \text{IV.7}$$

then the particle coordinates after rotation {Xp_r, Yp_r, Zp_r} are computed from the product between matrices P and R_z, such as $P_r = P \cdot R_z$, where P_r is the resulting matrix defined as:

$$P_r = \begin{bmatrix} Xp_r \\ Yp_r \\ Zp_r \end{bmatrix} \qquad \text{IV.8}$$

Eject3D gives the possibility to define both the distribution of the angles in the vertical plane, as well as the distribution of the rotation angles in the horizontal plane (i.e. blue dots and red dots respectively in Figure IV.3). In doing so, the user may generate a wide range of eruptive jet geometry, including orientated jets (Figure IV.4). Note however that with this method,

unless the jet axis is vertical, the cross-section of the eruptive jet will not be circular (rotations are done with respect to the vertical axis z).

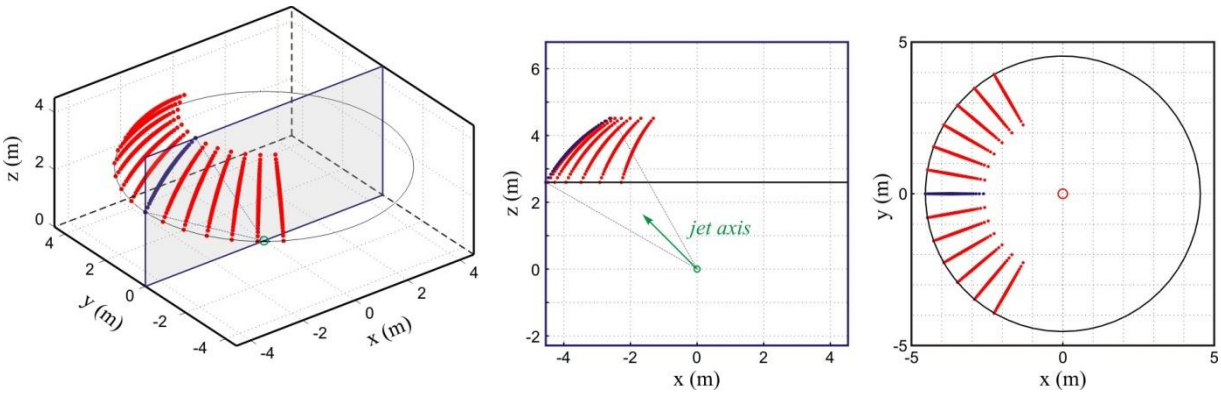

Figure IV.4. Asymmetrical eruptive jet constructed using rotation matrix.

The rotation operation described above is performed at each time step of the model run (i.e. step II.2 in Figure IV.2), immediately after the new particle coordinates in the initial vertical plane have been calculated via Runge Kutta. Once the rotation has been performed, the complete set of particles must be located in the 3D beam, and the radial velocity of each particle with respect to the radar must be derived. The methodology to perform these operations is detailed in section IV.2.1 of this chapter, which is dedicated to the description of the 3D-plume model.

Note that the particle rotation described above, incorporated into the newly developed *eject3D* code, significantly increases the number of particles accounted in the eruptive jet while decreasing significantly the computational time required (with respect to the original code).

IV.1.2.2. Ejection Angle Distribution (EAD)

Eject3D gives the possibility to choose the way the ejection angles within the eruptive jet are distributed, in both the vertical (xoy) and horizontal (yox) planes. In both cases, a minimum angle (α_{min}), an aperture angle (α_{ap}), and a number of angles (α_{nb}) within this aperture must be defined (Figure IV.5). The distribution of angles within the chosen aperture may be either uniform or Gaussian (independently in both the horizontal and vertical planes).

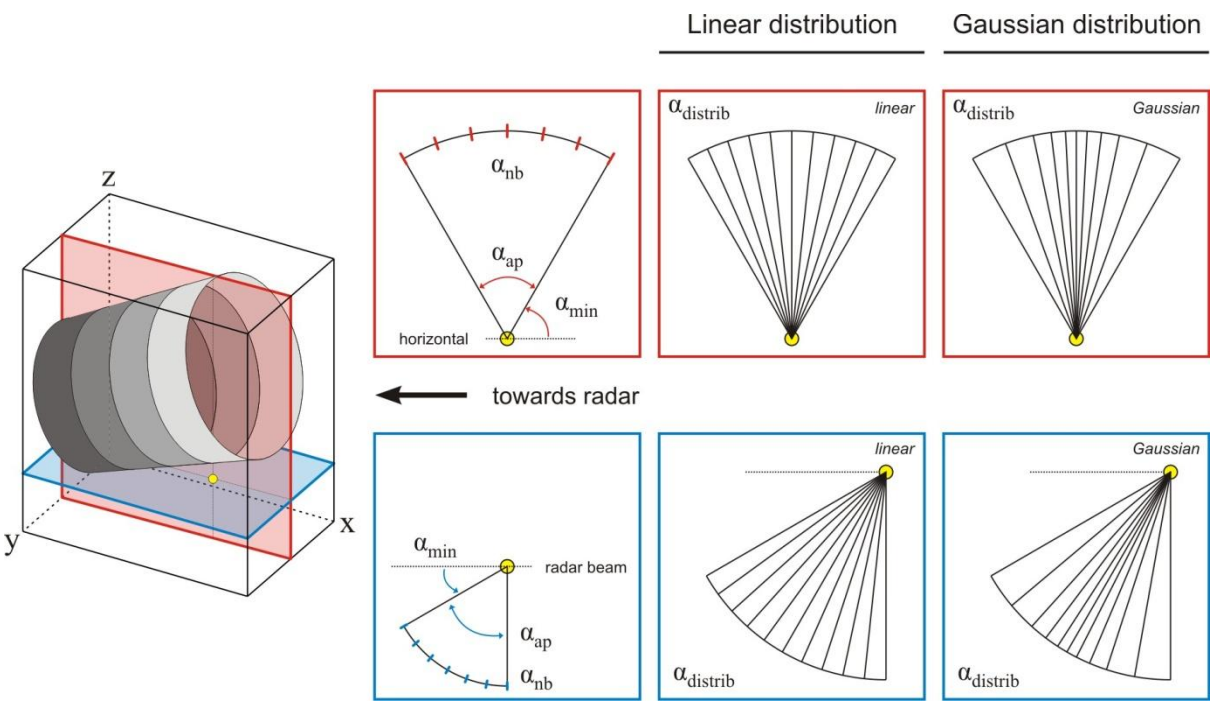

Figure IV.5. Definition of the ejection angles in the horizontal and vertical planes, using a minimum angle (α_{min}), an aperture angle (α_{ap}), a number of angles (α_{nb}), and a distribution of angles ($\alpha_{distrib}$, Gaussian or uniform).

Figure IV.6 shows an eruptive jet with angles in the vertical (xoy) plane distributed following uniform (a) and Gaussian (b)distributions, and rotated uniformly in the horizontal (yox) plane.

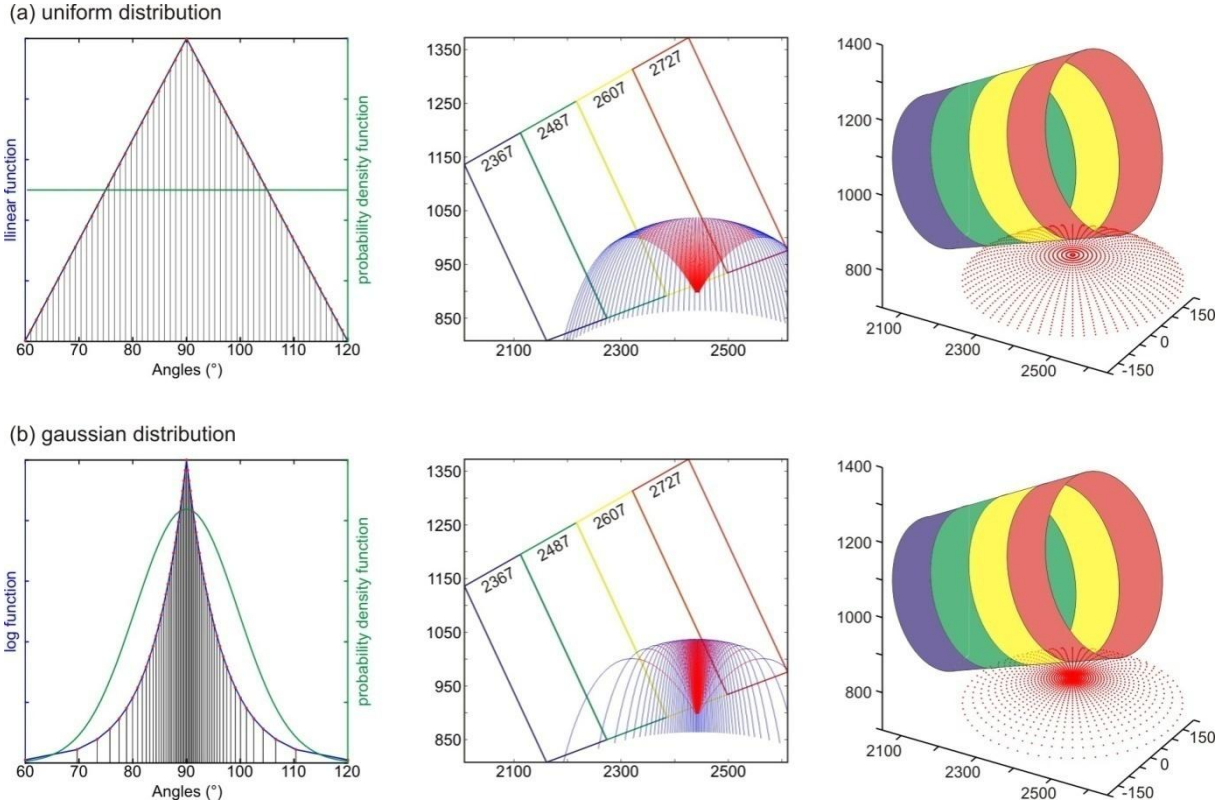

Figure IV.6. Simulated eruptive jets, with respectively linear (a) and Gaussian (b) distributions of ejection angles in the vertical (xoy) plane (middle panel). In both cases, the distribution is then rotated 180° around the (vertical) jet axis to simulate 3D dynamics.

IV.1.2.3. Particle Size Distribution (PSD)

Recall that a Doppler spectrum expresses the power backscattered to the radar (which depends on the number and size of the particles inside the range gate), as a function of the along-beam (radial) velocity of the ejecta. One can see that the shape of the Doppler spectrum, and by extension the shape of the Doppler radargram, is critically dependent on the particle size distribution (PSD) of the ejecta.

Various PSDs of volcanic ejecta have been considered in past studies: exponential (*Ripepe et al.*, 1993), lognormal (*Sheridan*, 1971; *Chouet et al.*, 1974; *McGetchin et al.*, 1974; *Self et al.*, 1974), Rosin Rammler (*Kittleman*, 1964; *Spieler* et al., 2003), Weibull (*Nakamura*, 1984; *Marzano* et al., 2006a, 2006b), polymodal (*Sheridan et al.*, 1987; *Riley et al.*, 2003) and sequential fragmentation/transport (SFT) (*Wohletz et al.*, 1989). However, a consensus on which PSD best characterizes Strombolian activity still lacks. Following *Gouhier and Donnadieu* (2008), we use a scaled Weibull function (equation IV.9), which enables the overall shape to be varied from exponential to Gaussian by means of three factors: shape (k), shift (Λ), and scale (N_{max}). The scaled Weibull distribution (S_w) is defined as:

$$S_w(D,k,\Lambda,N_{\max}) = \frac{f_w(D,k,\Lambda)}{\max[f_w(D,k,\Lambda)]} \cdot N_{\max} \qquad \text{IV.9}$$

where $f_w(D,k,\Lambda)$ is a probability function of particles of diameter (D), expressed as:

$$f_w(D,k,\Lambda) = \left(\frac{k}{\Lambda}\right) \cdot \left(\frac{D}{\Lambda}\right)^{(k-1)} \cdot \exp\left(\frac{-D}{\Lambda}\right)^{(k)} \qquad \text{IV.10}$$

where (k) defines the shape of the particle distribution: k = 1 for exponential, k = 3 for Gaussian, and 1 < k < 3 for log-normal. The shift factor (Λ) on the other hand, depends on both the mode (μ) and shape factor (k) of the distribution:

$$\Lambda = \mu \cdot \left(\frac{k-1}{k}\right)^{\frac{1}{k}} \qquad \text{IV.11}$$

Figure IV.7 shows the influence of these three factors on the shape of the particle distribution.

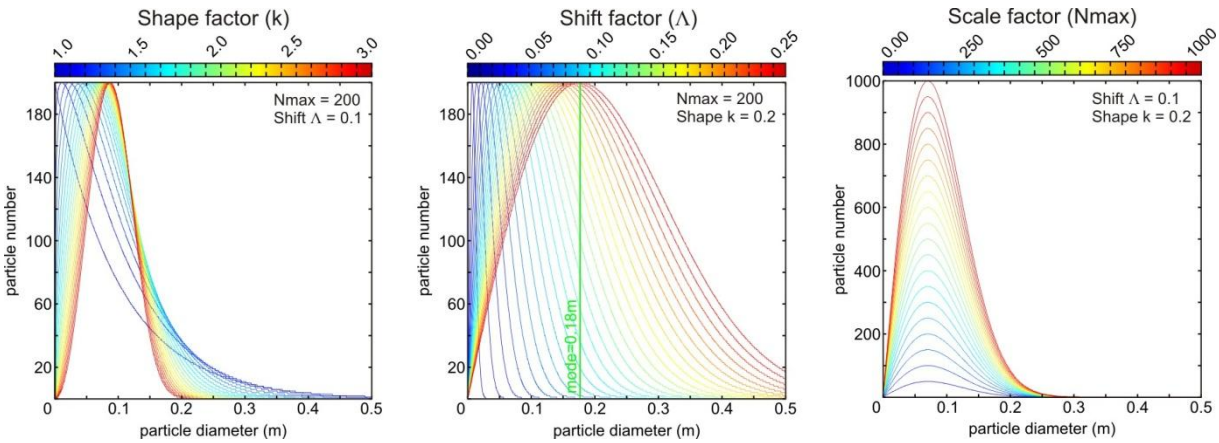

Figure IV.7. Factors defining the Weibull function, which in turn controls the shape of the particle size distribution. Notice in particular the shape factor (k), which enables to have distributions ranging from exponential (k = 1) to Gaussian distributions (k = 3), with intermediate lognormal distributions (1 < k < 3).

For each diameter in the PSD, the model launches one particle only, in each ejection angle of the initial vertical plane (i.e. Figure IV.6 - middle panel). The backscattered power attributed to this particle however, corresponds to the power backscattered by the *n* particles having this diameter in this ejection direction (i.e. ordinate value at a given diameter from the PSD). Henceforth, the particle size distribution defined above (e.g. Figure IV.7) is not the eruptive jet's PSD, but rather the PSD launched at each ejection angle. In turn, the eruptive jet's total PSD can be computed by multiplying the ejection angle PSD by the number of angles requested in the vertical and horizontal planes (i.e. α_{nb} in the red and blue plane respectively).

IV.1.2.4. Fine particles ballistic trajectories: gas velocity cutoff

A modification has to be made to the original code for it to reproduce ballistic trajectories even for small particles (diameter <5 cm). Indeed, we noticed that upon falling, particles tended to have their trajectories deviate away from the vent, a behavior which worsened as the size of the considered particles became smaller (Figure IV.8a). The reason for this is that the gas velocity driving the particles depends on the distance between the particle and the vent (equation IV.4). Consequently, as the particle fell back to the ground the gas velocity would tend to increase again (eventually prevailing over the gravity force), and thus modify its trajectory. To overcome this issue, we "cut" the gas velocity (i.e. set it to 0 m/s) once the particle has finished its ascent (i.e. height variation between two time steps is lower than a threshold value of 0.1 m, Figure IV.8b). In doing so, we assume that the eruptive event results from a single gas pulse.

Note that although in reality the trajectory of fine particles deviate much from true ballistic trajectories (because of their low inertia and entrainment by thermal convection for instance), it is convenient that fines behave ballistically in our simple model to facilitate the interpretation of radar signals.

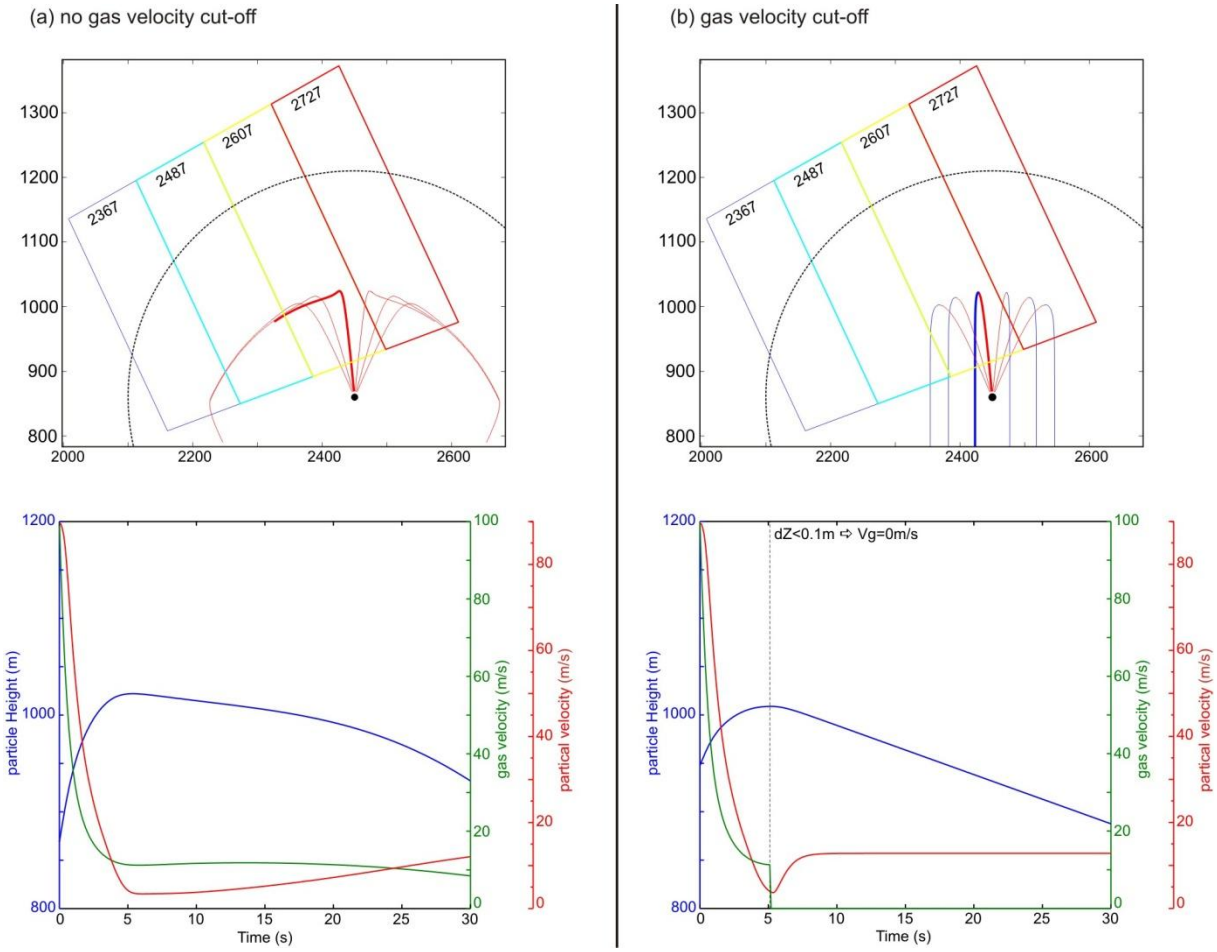

Figure IV.8. Particles 5 mm in diameter are thrown with an initial gas velocity of 100 m/s. The thickened trajectories in the top plots are those monitored in the bottom plots. (a) Throughout the entire computational time, the gas velocities vary with the distance to the vent (equation IV.4). Upon falling, particles exhibit non ballistic trajectories (top) due to gas velocity that increases (bottom), and thus prevails over gravity. (b) Once the particles have finished their ascent (i.e. altitude variation dZ < 0.1 m between two successive time steps), gas velocities are set to 0 m/s (blue trajectories in top plot). In that way, the trajectories of very small particles have a ballistic trajectory.

IV.1.2.5. Building radargrams from ballistic simulations

The initial code enabled the computation of synthetic Doppler spectra, one range gate at a time. In *eject3D*, by stacking Doppler spectra next to one another and by using a color scale for the echo power amplitude, we reconstruct synthetic Doppler radargrams to visualize the temporal evolution of the spectra in the different range gates (see section III.1 for details). The

user may select the gates to compute (e.g. select the gate number, or ask the program to plot only those with signal) without increasing the code's running time.
The new code also enables the user to plot radargrams displaying the true particle velocity rather than the radial velocity.

IV.1.3. Parametric tests of the ballistic model input parameters

A number of parametric tests have been carried out to understand which factors control, for the most part, the Doppler signature read on Doppler radargrams. We do not intend to present them all exhaustively, but rather to focus on those which demand particular insights.
In the following section, we assess the contribution of the eruptive jet's geometry (jet inclination, ejection angle distribution) and the ejecta particle size distribution (PSD) on the Doppler signature of radargrams, and we test the relationship between particle size and initial gas velocity on the maximum height reached by the ejecta. Note that all the tests described below are performed in 2D only. Indeed, converting the jet in 3D does not affect the radargram shape (i.e. time-velocity distribution). This results from the fact that the radargram's extreme radial velocities values (outlining the radargram shape) are obtained when the particles travel in the planes holding both the radar and the particles. The only change a 3D jet will make with respect to a 2D jet is to increase the number of particles travelling in various directions within the beam, consequently changing the power distribution within the radargram (rendered by colors variations) but not the radargram's shape.

IV.1.3.1. Model sensitivity to jet axis inclination

Figure IV.9 shows the influence of the eruptive jet's inclination on the radargrams of the different range gates. We see that the inclination of the jet axis (e.g. away or towards the radar, Figure IV.9 a and c) directly controls the shape of the radargrams in the gates crossed by the ballistics. All the gates lying up the beam from the vent exhibit radargrams having high positive onset velocities which progressively decrease towards negative velocities, sketching characteristic oblique signals. Contrastingly, the gates down the beam from the vent exhibit more horizontal signals with negative velocities only. (Note that a detailed step by step tracking of particles' speed, trajectory, and subsequent radargram signal is provided in Figure III.14).

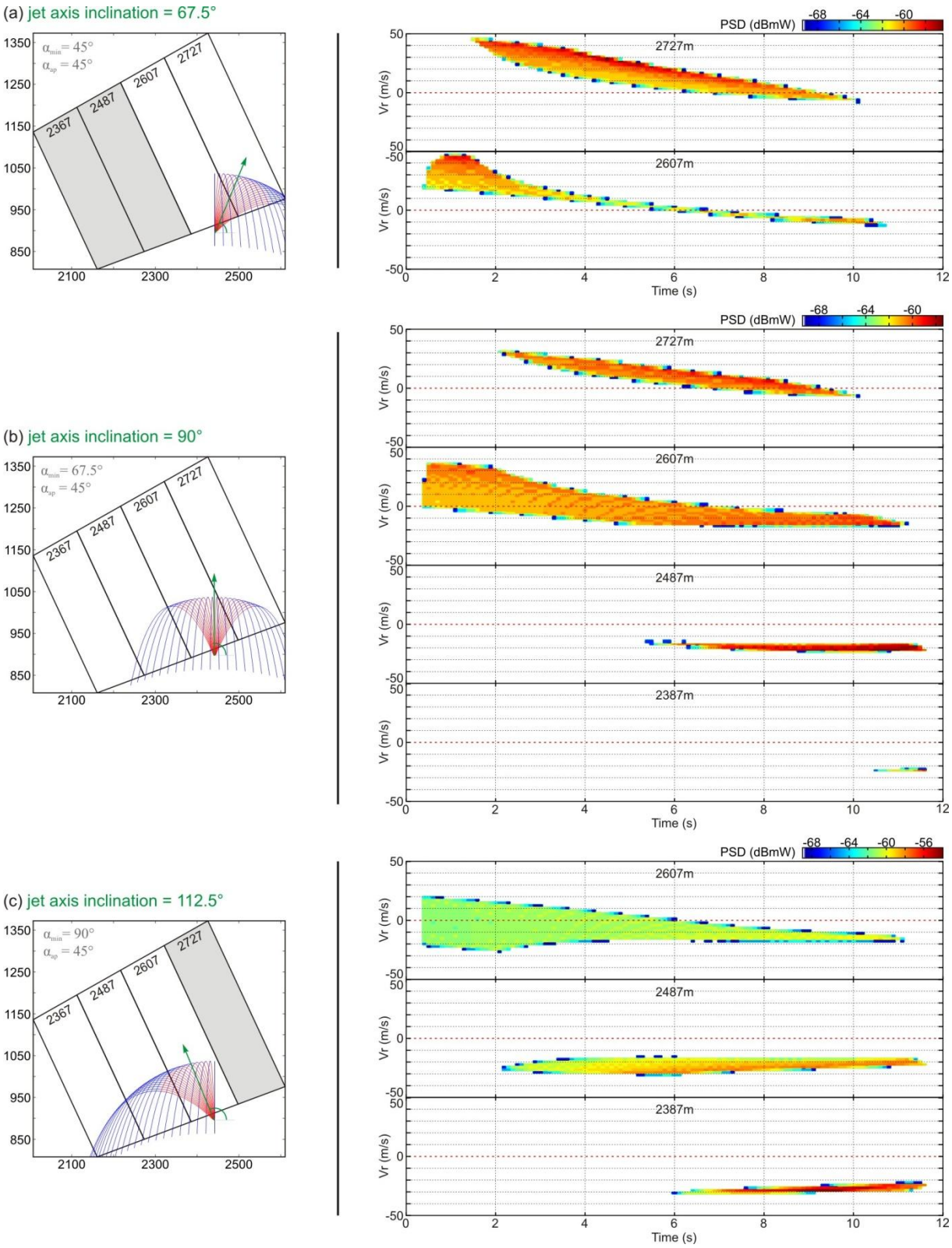

Figure IV.9. Illustration of the model's sensitivity to the jet axis inclination and its consequences on the Doppler signature. Particles of diameter 0.1 m are uniformly released in a cone of 45° aperture, with an initial gas velocity of 100 m/s (i.e. initial particle speed of 52.6 m/s using equation IV.1, entering gate 2607 m at 50 m/s). The jet axis inclination is measured from the horizontal, and is varied as follows: a) away from the radar (67.5°), b) vertically (90°), and c) towards the radar (112.5°). The radargrams of the gates in which particles enter (i.e. non-shadowed gates) are displayed to the right.

In turn, it is possible to retrieve information on the inclination of the eruptive jet (i.e. towards or away from the radar) solely from the observation of the shape of Doppler radargrams. Indeed, when a majority of gates exhibit radargrams shaped as oblique streaks then the jet axis is inclined away from the radar, whereas when a majority exhibit horizontal negative streaks then it is inclined towards it (Figure IV.10b and 10a respectively). In the intermediate case of a nearly vertical jet axis, more particles will tend to enter the gates down-beam than up-beam from the vent, due to the beam inclination.

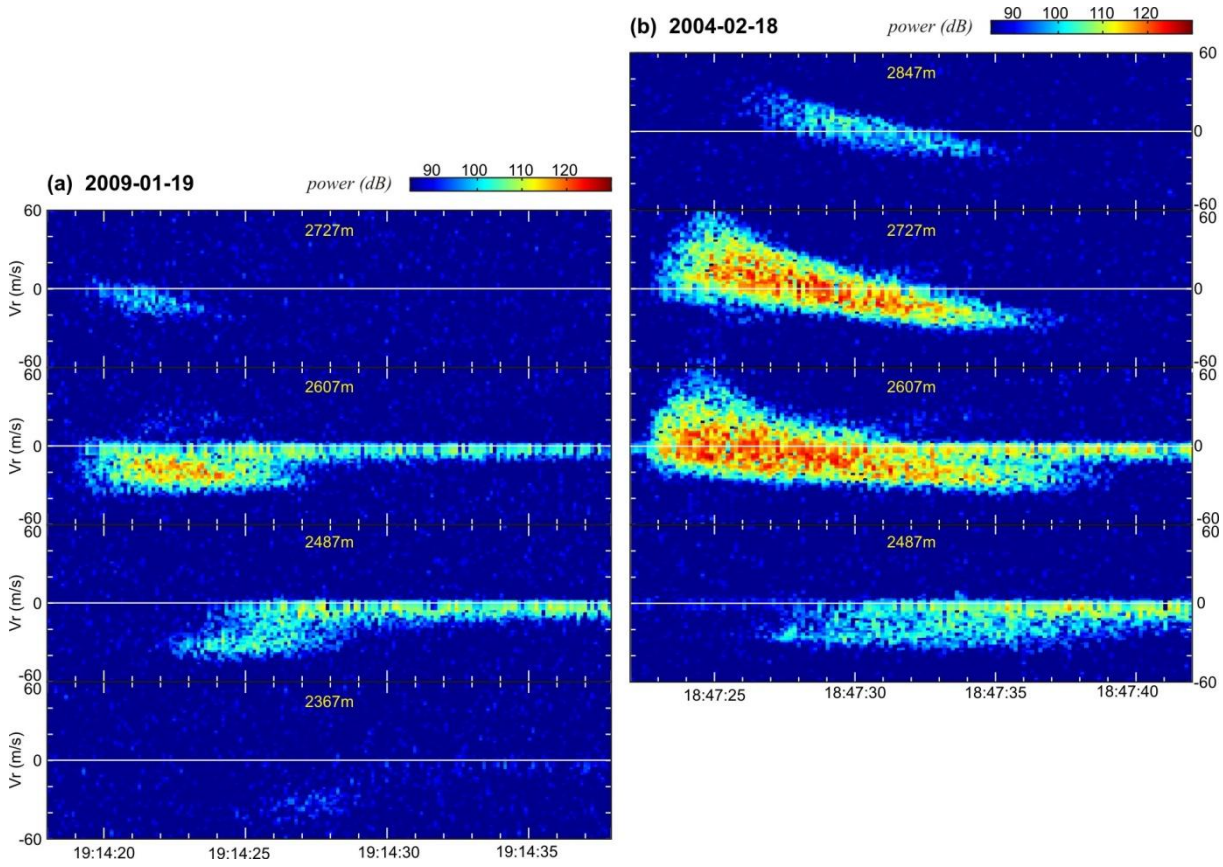

Figure IV.10. Recorded events during which the eruptive jet was likely inclined (a) towards, and (b) away from the radar.

Another important outcome to mention is that the maximum radial velocity value of the radargrams (i.e. V_{+max}) appears to be strongly dependent on the inclination of the jet, and thus not necessarily representative of the real ejection velocity. In particular, we see that at constant particle size (0.1 m) and source gas velocity (100 m/s), gate 2607 m located directly above the vent displays maximum positive radial velocities of +50, +35, and +20 m/s depending on the jet axis inclination (respectively away from the radar, vertical, and towards the radar), when the real particle speed is in fact of ~50 m/s upon entering the gate. If the jet is symmetric however and with a large aperture, then V_{+max} represents the real particle speed.

IV.1.3.2. Model sensitivity to Ejection Angle Distribution (EAD)

In the previous paragraph, particles were thrown uniformly inside the ejection cone. Here we assess the influence of the ejection angle distribution (EAD), by comparing jets with ejection angles following respectively uniform- and Gaussian-type distributions (Figure IV.11).

Figure IV.11 shows that the shapes of the radargrams are identical, whichever the ejection angle distribution. This results from the fact that maximum radial velocities are the same in each case, since the most tangent trajectories to the beam axis (i.e. those at the borders of the ejection cone) are the same. The power distributions within the radargrams, however, are not similar, and are clearly dependent on the ejection angle distribution: uniform EAD gives a more uniform time-velocity power distribution (Figure IV.11a), whereas Gaussian EAD gives a strongly non-uniform power distribution (Figure IV.11b). The radargram in gate 2607 m for instance, shows a band of very high power at its center, while its borders exhibit very low power. This directly witnesses the variable particle concentration within the jet, as the number of ejection angles decreases from the center to the borders. The increasing density of ejection angles from the side to the vertical is also clearly imaged in the radargrams of the gates up the beam (i.e. 2727 m): the highest echo power are associated with the lowest radial velocities because most ejecta have ascending trajectories very oblique to the beam. Notice that if the spacing between the ejection angles becomes too loose, the distribution of the particle radial velocities also become scarce, which may lead to signal discontinuity at the borders of the radargram (e.g. isolated streaks in Figure IV.11b resulting from the eccentric ejection angles at 60° and 120°). Note that the standard deviation of the Gaussian distribution may be adjusted in *eject3D* in order to control the spacing of the ejection angles from the center to the sides of the jet. In turn, this will have an effect on the power transition within the radargram, since it directly influences the radial velocity of the particles and their number (e.g. the isolated streaks in Figure IV.11b can be suppressed with a more uniform EAD).

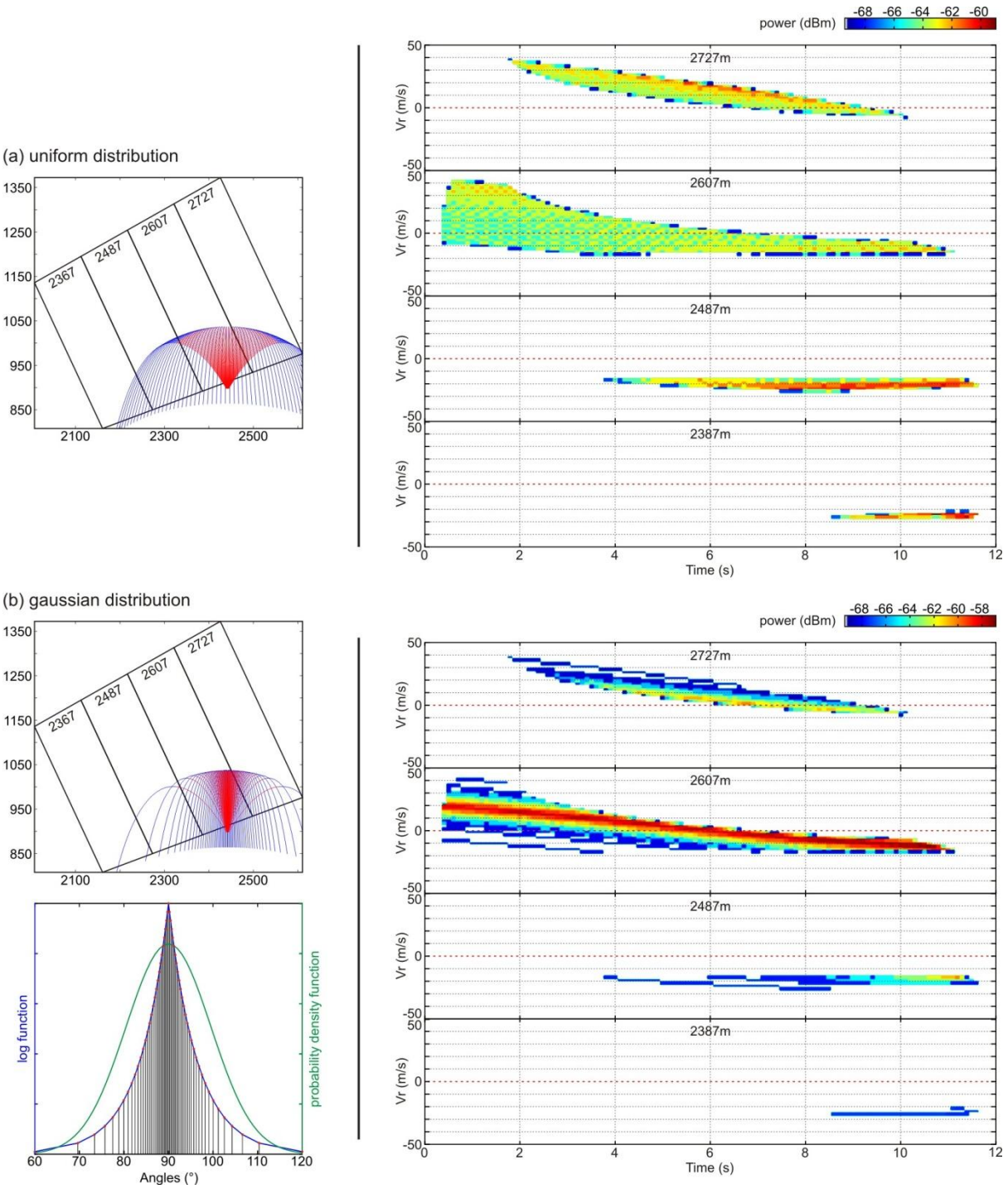

Figure IV.11. Illustration of the model's sensitivity to the ejection angle distribution (EAD), and its consequences on the Doppler signature. Particles of diameter 0.1 m are released with an initial gas velocity of 100 m/s. The ejection cone has an aperture of 60°, in which the ejection angles are distributed following a uniform-type distribution (linear) (a), and a Gaussian-type distribution (b).

The power distributions within the modeled radargrams however, poorly resemble those in the recorded radargrams (e.g. Figure III.4). Indeed, the high-power band in gate 2607 m (Figure IV.11b) is not curved like the overall shape of the radargram but clearly linear, indicating a constant decrease rate of the radial velocity (the same observation holds in gate 2727 m).

Moreover, the power distribution in gate 2607 m is closely related to the power distribution in the bordering gates 2727 and 2487 m: from t = 6 to 10 s for instance, the highest powers are associated to the highest radial velocities in gate 2607 m, whereas they are associated to the lowest velocities in gate 2727 m. This results from the fact that particles with vertical trajectories will imprint on radargrams as linear oblique streaks, which can enter successively gate 2607 m, 2727 m, and 2607 m again upon falling. Figure IV.12 illustrates this with a simulation in which two particles are ejected vertically: the smallest particle is ejected higher up and can enter gate 2727 m before falling back into gate 2607 m. Notice that both generate linear streaks in the synthetic radargram, thus reinforcing the idea that narrow streaks in observed radargrams are attributed to individual blocks (Figure IV.12b, see also section III.3.5.4, Figure III.9).

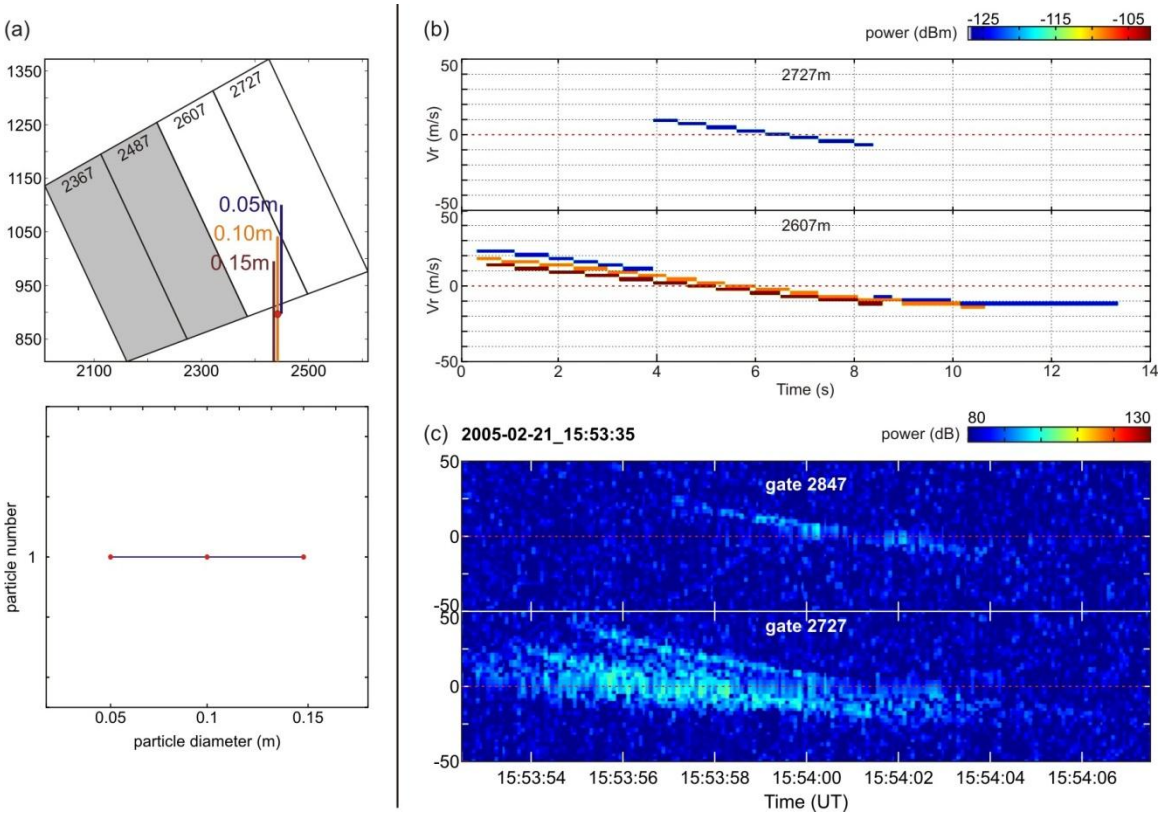

Figure IV.12. (a) Vertical ejection of three particles of 0.05, 0.1, and 0.15 m in diameter respectively, launched with an initial gas velocity of 100 m/s. All three are launched from the same vent position (red dot), with the colored vertical lines showing their ascent/descent trajectory. Notice how the smallest particle (blue, 0.05 m) enters successively gates 2607 m, 2727 m and 2607 m again upon falling. (b) The resulting synthetic radargram consists of linear oblique streaks, complementary between gate 2607 and 2727 m (much like the radargrams in Figure IV.11). (c) Linear streak observed in a radargram of an eruptive event at Arenal in 2005, which can confidently be attributed to an individual block.

IV.1.3.3. Model sensitivity to Particle Size Distribution (PSD)

Figure IV.13 shows the Doppler signature acquired for two distinct particle size distributions (PSD), respectively monodisperse and polydisperse. In the first case, particles have a single diameter of 10 cm, while in the second case particles range between 5 mm and 50 cm following a lognormal distribution (k = 2, mode = 10 cm, 20 distinct diameters). In both cases, the initial gas velocity is set to 100 m/s, and the ejection angles are uniformly distributed within an ejection cone 60° wide. As expected, the Doppler radargrams vary greatly whether the PSD is mono- or polydisperse: when PSD is polydisperse, both the radial velocities (in particular the positive velocities) and the backscattered power are higher than with monodisperse PSD.

The higher radial velocities are explained by the fact that smaller particles are ejected, which consequently travel faster for a given initial gas velocity. Note that this issue is particularly strong in the given example, since the smallest particles of the polydisperse distribution are 20 times smaller than those in the monodisperse distribution. The higher backscattered power on the other hand, results from a higher number of particles ejected when PSD is polydisperse: at each ejection angle, a particle of each diameter is thrown and its trajectory is computed. The resulting total backscattered power on a radargram pixel is the sum of the power backscattered by all particles having the same radial velocity at a given instant. Thus the pixel power value includes at least the power backscattered by particles with the same diameter and the same ejection angle (since they have the same trajectory and radial velocity all the time), but may also include occasionally the echo power from particles with a different diameter and/or ejection angle having by chance the same radial velocity at the considered instant. The computational time is consequently increased considerably (from seconds to minutes). For this reason, we assume the particle size distribution as monodisperse in the first inversion procedures carried in Chapter V. This choice is not entirely absurd because the primary objective is to match the velocity distribution of the radargrams rather than their power distribution. Furthermore, the shape of the recorded radargrams resulting from ballistic projections are likely to be predominantly controlled by a narrow PSD (likely centered around a coarse particle mode), as small particles (with high velocities) backscatter much less power than coarse particles.

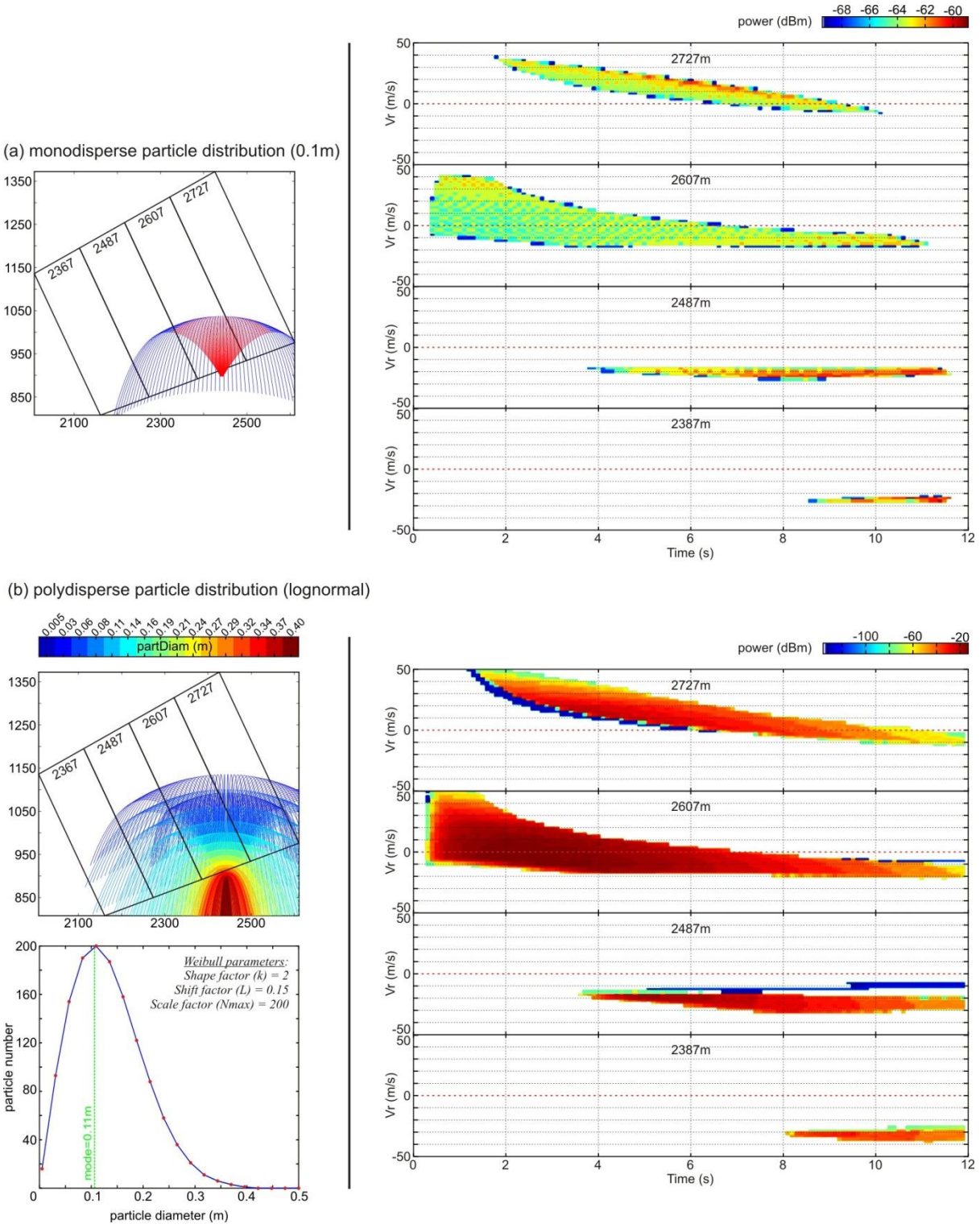

Figure IV.13. Illustration of the model's sensitivity to the particle size distribution (PSD), and its consequences on the Doppler signature. Particles are launched with an initial gas velocity of 100 m/s, within an ejection cone 60° wide, in which the ejection angles are distributed uniformly. The particle size distribution is: (a) monodisperse with a unique particle diameter of 10 cm, and (b) polydisperse, with a lognormal distribution of the diameters ranging between 0.005 m and 0.5 m (mode = 0.11 m).

IV.1.3.4. Particle rise with varying diameter and initial gas velocity

The maximum altitude reached by a particle depends on both its diameter, and the initial gas velocity. Figure IV.14 illustrates the maximum rise altitude of a particle ejected vertically, for diameters ranging between 0.005 – 0.5 m, and initial gas velocities varying between 50 and 250 m/s. Notice that for diameters below 0.1 m, the relationship changes drastically: the rise altitude strongly diminishes as the considered particle gets smaller. This attests of the importance of the drag forces acting on the particles, which affects particularly the small particles. The right hand plot in Figure IV.14 shows that if the drag forces are inactive (drag coefficient C_d forced to 0), this non-linear effect observed for small particles is lost and the height reached is significantly greater (although it has no physical meaning).

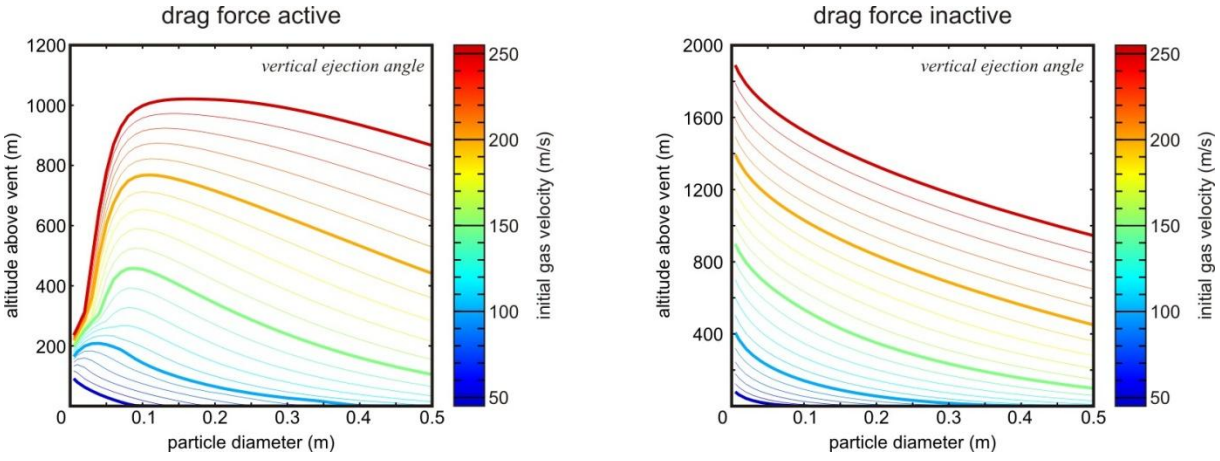

Figure IV.14. Relationship between the maximum altitudes reached by a particle ejected vertically above the vent, and the particle diameter and initial gas velocity. In the left-hand plot the drag forces are kept active (i.e. drag coefficient determined at each time step depending on the Reynolds number), while in the right-hand plot the drag forces are forced to be inactive. The thickened lines correspond to the values annotated next to the color bar.

Interestingly, the above observations help us understand the modeled trajectories / radargrams presented in Figure IV.13b, and gives us further insights into the observed radargams. Indeed, we can see that the smallest particles (diameter 0.005 m) exhibit unexpected trajectories, as these do not travel as high nor as far as the diameter immediately above (0.03 m): this is due to the effect of the drag force, which particularly affects the 0.01 m particle (see the 100 m/s curve in Figure IV.14-left). Moreover, we see that this peculiar behavior imprints on the radargram in gate 2487 m as an isolated blue streak (i.e. low power because of the very small diameter). Unlike the overall signal, this streak exhibits radial velocities which tend to decrease towards 0 m/s with time. Interestingly, it is a feature that is also observed in the radargrams of several eruptive events (Figure IV.15a). This should consequently be

interpreted as small particles which are expelled ballistically, but which, upon falling back to the ground, tend to decelerate rather accelerate (like it is expected for heavier particles, see simulation in Figure III.14). Consequently, the radial velocities of the small ballistic particles will tend to decrease towards V_r = 0 m/s (Figure IV.15a, pink arrow), rather than increase towards higher negative values like coarser particles would (Figure IV.15b, pink arrow).

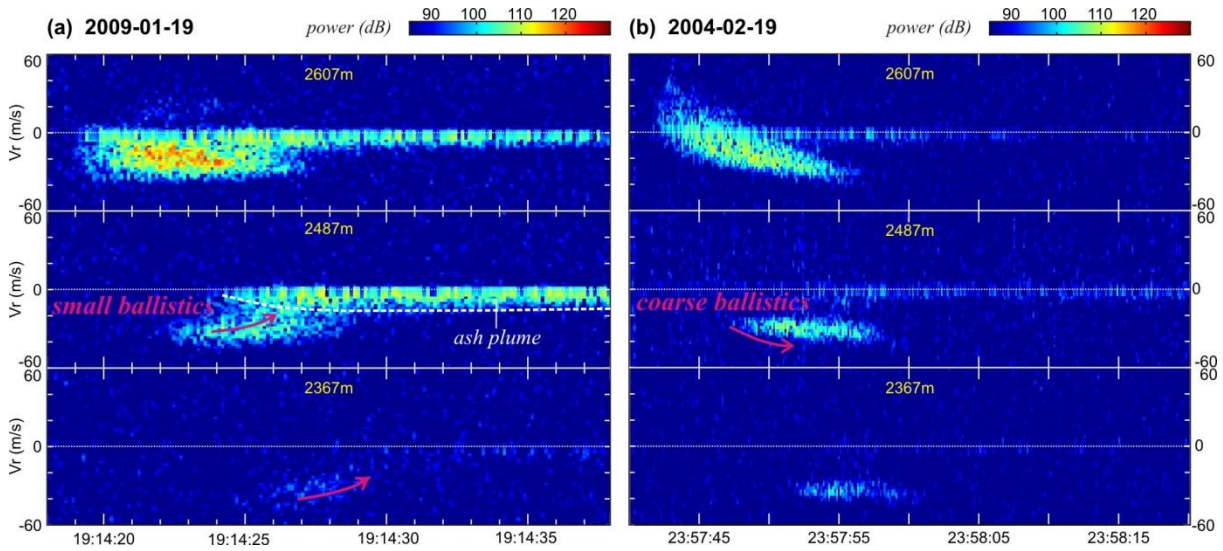

Figure IV.15. Radargrams showing different Doppler signatures of the ballistic particles entering the gates down-beam from the vent. Event (a) exhibits velocities which tend to decrease towards 0 m/s, whereas event (b) exhibits a much narrower signal which tends to increase towards higher negative radial velocities. This suggests that the ballistic particles in (a) are small (hence light, with low/decelerating speed upon falling), whereas in (b) particles are likely coarser (hence heavier, with high/accelerating speed upon falling).

IV.2. Ash plume modeling

Because eruptions at Arenal are short-lived (order of a few seconds, as suggested by ephemeral high positive velocities), and because the resulting plume may rise during tens of seconds, we consider the eruption plumes as non-sustained, finite volume releases. To better interpret the radar signal recorded by such unrooted plumes, we have modeled the migration of a cloud of particles, rising and expanding in three dimensions through the radar beam.

IV.2.1. Driving equations

The cloud's shape, rise rate and expansion rate are those defined for steady buoyant plumes (e.g. thermals). For axisymmetric thermals with circular cross-section, rising by buoyancy only through a static atmosphere, the height evolution with time z(t) was defined by *Yamamoto et al.,* 2008 (based on the work of *Morton et al*., 1956) as:

$$z = \left(\frac{4 g'_0 V_0}{3 \varepsilon^3 m} \right)^{1/4} t^{1/2} \qquad \text{IV.11}$$

where (g_0') defines the source buoyancy, (V_0) the volume of the thermal at the source, (ε) the entrainment constant, and (m) a factor characterizing the thermal's shape. Values for these constants are based on both field measurements and laboratory experiments of previous studies: $g_0' \approx 5$ m/s^2 (*Yamamoto et al.,* 2008), $\varepsilon = 0.25$ (defined for discrete thermals, *Scorer,* 1957; *Turner,* 1979), and m = 3 (defined for an oblate spheroid, *Turner,* 1979). The dependence of the horizontal radius (r) of the thermal with height on the other hand, is given by *Morton et al*. (1956) as follows:

$$r = \varepsilon z \qquad \text{IV.12}$$

Figure IV.16a shows the dependence of the plume's altitude with time, and Figure IV.16b shows the evolution of the plume radius and volume with time.

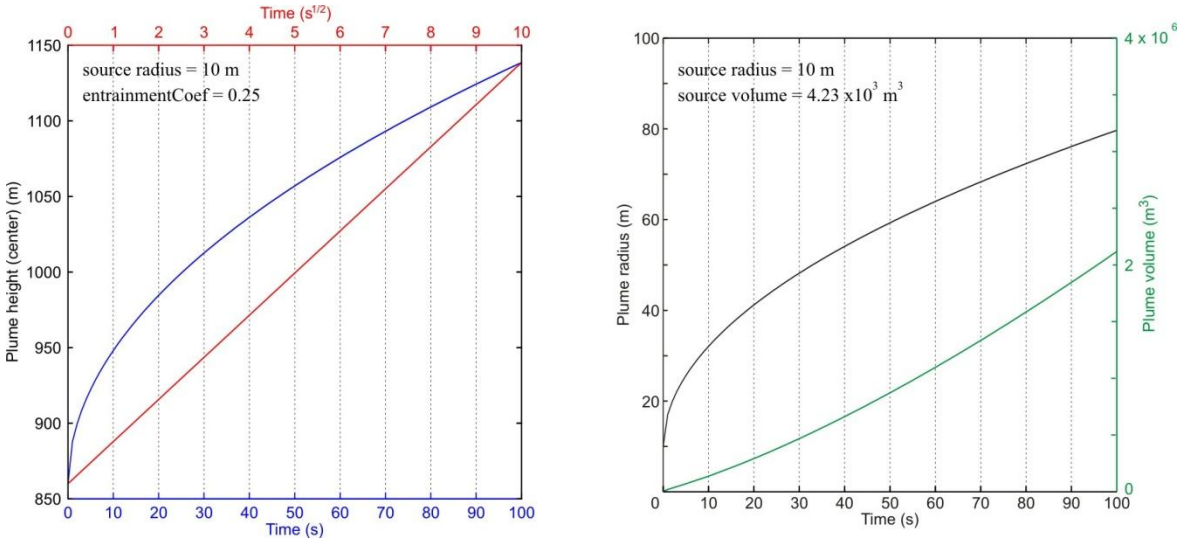

Figure IV.16. (a) Evolution of the modeled ash cloud center's height with time; the release altitude is located 850 m above the radar (reference altitude). Note that the linear dependence of the altitude with ($t^{1/2}$) (equation IV.11). (b) Evolution of the plume's radius and volume with time. The plume initial's radius is set to 10 m, and the entrainment constant set to 0.25 (typical value for a discrete thermal, Turner, 1979).

The particles in the model are initially (t = 0 s) distributed in a spheroid of radius (R_0), with a decreasing concentration of particles from the center to the borders (Figure IV.17). The spatial coordinates of each particle {x_p, y_p, z_p} are drawn randomly from a normal distribution with mean $\mu = 0$ (i.e. spheroid center) and standard deviation $\sigma = 1/3$, such as ~99.7% of the particles are contained inside the spheroid of radius R_0 (i.e. three standard deviations).

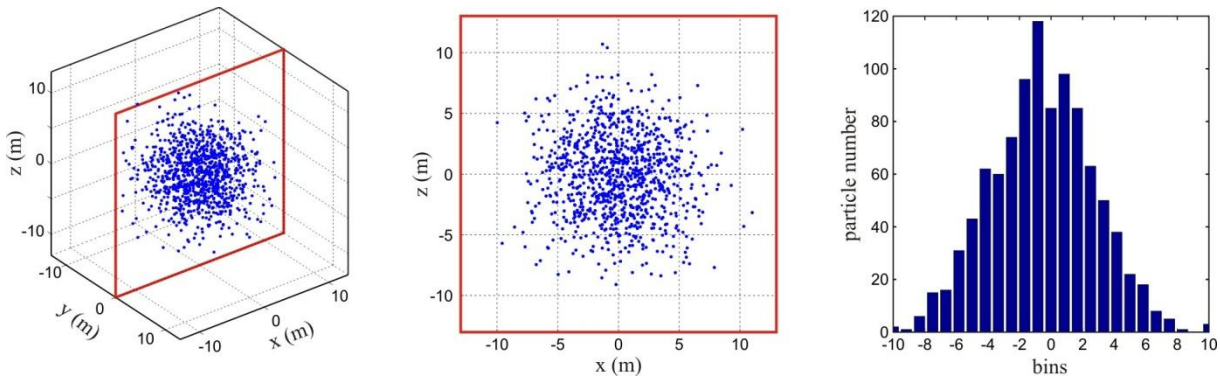

Figure IV.17. Particle distribution within the modeled ash cloud. In the given example, 1000 particles are distributed following a normal distribution (standard deviation σ = 1/3) around the center of the spheroid, 10 m in radius.

As the particle cloud rises above the vent (equation IV.11) its radius increases (equation IV.12), which is rendered by the spreading of each particle away from the spheroid center. Importantly, the particles keep their initial normal distribution within the expanding spheroid, no convection, turbulence, nor sedimentation processes are introduced in the algorithm.

In addition to the vertical rise of the cloud, a horizontal displacement component was implemented (affecting the plume center), in order to simulate the wind effect on the propagation of the plume, with varying wind speeds (W_s) and varying wind directions (W_a, azimuth angle measured relative to the beam axis).

At each time step, the particles are located within the beam to evaluate which gate they are in. To do so, we convert the Cartesian coordinates of the particle $\{x_p, y_p, z_p\}$ to spherical coordinates $\{r_p, \theta_p, \varphi_p\}$ and search in which range it is located, such as $r_p \in r_{lim}$, $\theta_p \in \theta_{lim}$ and $\varphi_p \in \varphi_{lim}$ (where $\{r_{lim}, \theta_{lim}, \varphi_{lim}\}$ define the gate's volume in spherical coordinates, as illustrated in Figure IV.18).

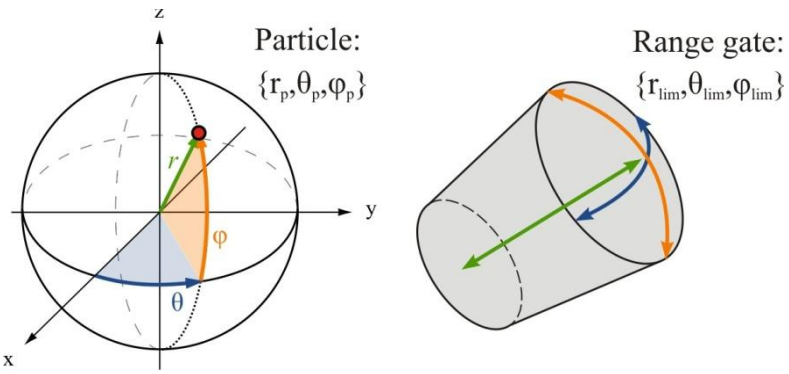

Figure IV.18. Locating the particles in the three-dimensional radar beam is done using spherical coordinates, with the radar as the origin of the coordinate system.

Once the particles are located, we determine the number of particles contained in each gate, and compute the backscattered power using the Rayleigh scattering equations, the particle size being small enough to ovoid the time consuming use of Mie scattering equations. The radial velocity of each particle on the other hand, is defined as the radial distance Δr_p travelled by the particle between two successive time steps.

The synthetic Doppler spectra are finally reconstructed at each time step and in each gate, by sorting the radial velocities of the particles into bins, and summing the power backscattered by all the particles in each bin. Ultimately, we reconstructed synthetic radargrams by plotting the Doppler spectra evolution through time. The overall architecture of the algorithm simulating the plume's evolution is illustrated below (Figure IV.19).

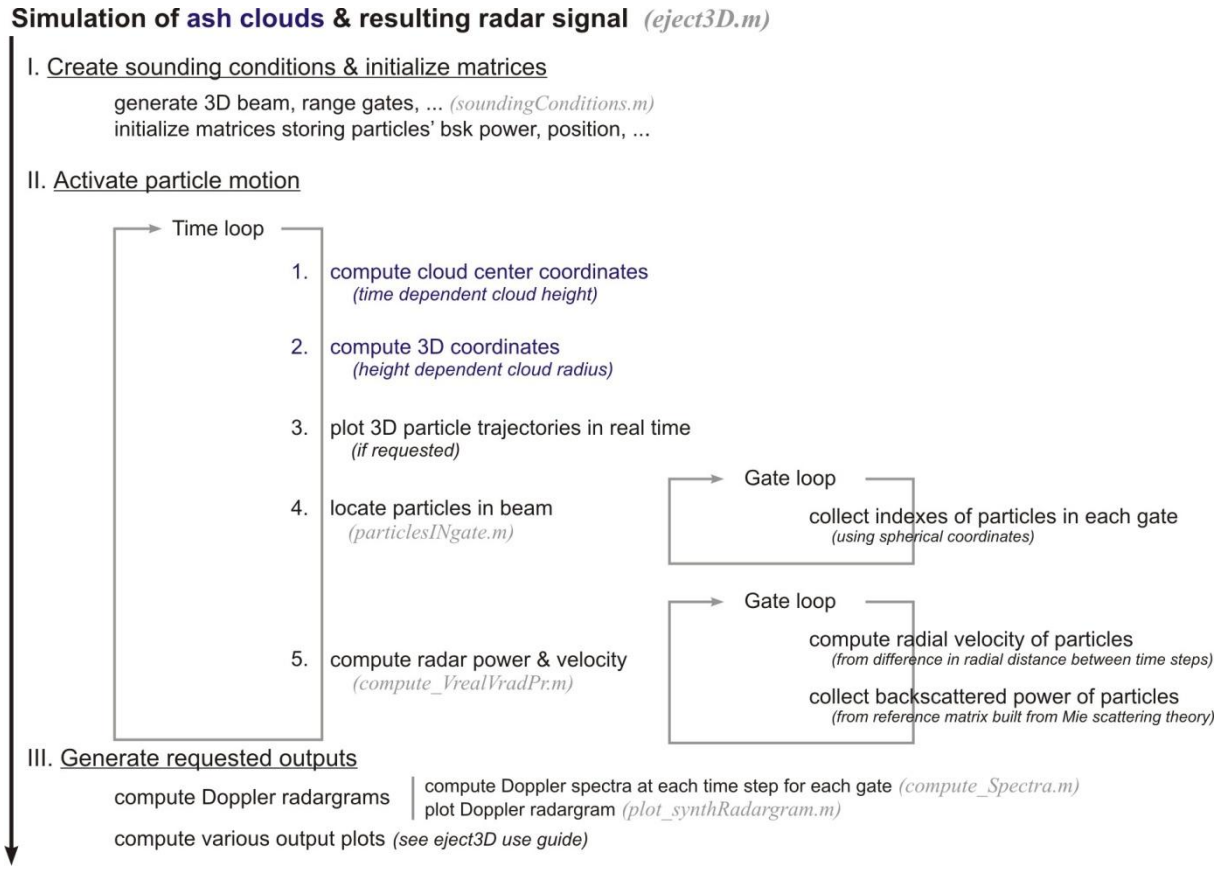

Figure IV.19. Architecture of eject3D, highlighting in blue the section which specifically manages the simulation of ash plumes.

Note that this simple model was not intended to reproduce the complexity of ash plume internal dynamics, but rather to test different parametric conditions for the transit of a spheroid plume having realistic size and speed, in order to better interpret the recorded radar signals.

IV.2.2. Rise dynamics of modeled and observed plume

Video analysis of an ash plume emitted at Arenal on February 19, 2004 at 23:57:37 UTC (*Doloire*, 2006; *Donnadieu et al.*, 2008) (Figure IV.20) indicates that momentum affects the initial stages of the plume rise (0-12 s), after what buoyancy controls the rise speed which becomes relatively constant (~7 m/s). We overlay the rise curves of both the observed and modeled plumes, in order to show that the dynamics of the modeled plume is similar to natural cases (Figure IV.20). Notice however that the rise speed of the observed plume appears much higher than that of the modeled plume (i.e. steeper curve), which results from the fact that cross-winds were blowing the plume towards the radar. As a consequence

apparent rise rate retrieved from the plume top seen on the video exaggerates the real rise rate of the plume due exclusively to buoyancy.

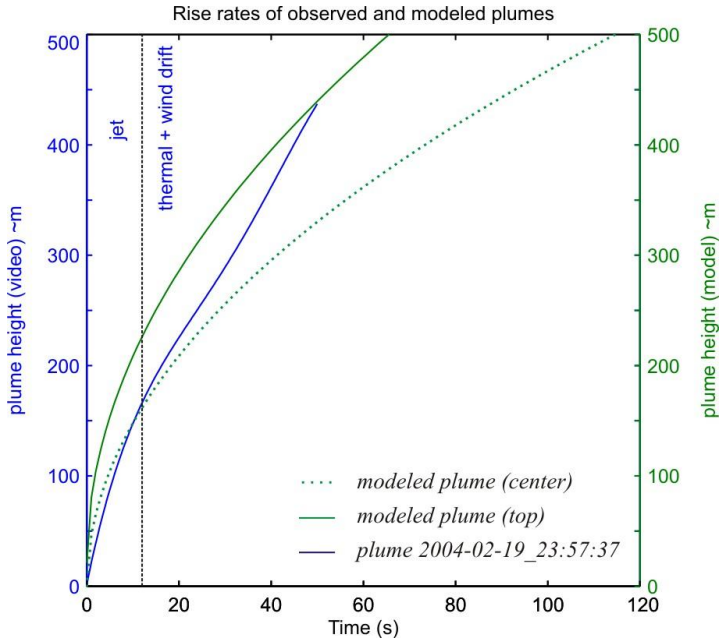

Figure IV.20. Comparison of the rise rates between a modeled plume (source radius = 20 m, entrainment coefficient = 0.25), and a real plume recorded on February 19, 2004 at 23:57:37 UTC (Donnadieu et al., 2008; video data processing by Doloire, 2006). The motion of the eruptive plume was recorded with a video camera operating in the visible, from which the plume top altitude variation with time was collected and fitted with a polynomial function.

IV.2.3. Parametric tests

The following section intends to assess the model sensitivity to various parameters used in the driving equations described above. In particular, we test the effect of the source radius (R_0) (and in turn the source volume, V_0), the source buoyancy (g_0'), and the entrainment coefficient (ε), all expressed in equation IV.11. We also describe the influence of the wind speed (W_s) and azimuth (W_a) on the Doppler signature of synthetic radargrams.

IV.2.3.1. Model sensitivity to source radius

Figure IV.21 shows how the source radius (R_0) affects the plume rise and the subsequent synthetic radar signal. The higher the radius value is, the higher the source volume (V_0) will be, which will in turn result in higher rise rates. With a 1 m source radius (Figure IV.21a), the plume rises only ~50 m above the vent in 100 seconds, with a maximum rise speed of ~4.9 m/s. With such low rise rates, the plume's ascent is overcome by cross-winds, and its trajectory becomes nearly horizontal. Consequently, its transit through the beam imprints on the radargram as narrow horizontal bands, having radial velocities V_r close to the implemented wind velocity W_s = 5 m/s (i.e. $V_r \approx W_s \cdot \cos(W_a)$, with W_a = wind azimuth angle measured relative to the beam axis = 0°). With a 10 m source radius on the other hand (Figure IV.21b), the cloud rises much higher (~280 m above the vent) and much faster (maximum rise speed = 28 m/s). Because the plume expansion is related to its height, the plume diameter has increased up to ~200 m at the end of the 100-second computational time. Such plume expansion results in a wider range of radial velocities expressed on the radargrams. In the gate immediately above the vent (2607 m), these neighbor positive values, and begin to draw a curveted shape, while radargrams of gates downwind image the plume horizontal motion by a constant velocity band over ca. 1 min. With source radii >10 m, the onset radial velocities become clearly positive, and the overall shape clearly curveted. Although the shape resembles the oblique streaks earlier identified as resulting from ballistic projections, the distinct life spans between those of "ballistic-origin", and those of "plume-origin", prevents from any confusion: the former last 17 s at the very most (Figure III.15b), while the latter last 40 s at the very least. Furthermore, the transit speeds and radial velocities are not comparable. Radial velocities in radargrams of ballistic-origin may reach up to 60 m/s (Figure III.15a), when those of plume-origin hardly reach 10 m/s (notice the different V_r axis limits in the synthetic plume radargrams and ballistic radargrams, e.g. Figure IV.21 and Figure IV.9 respectively).

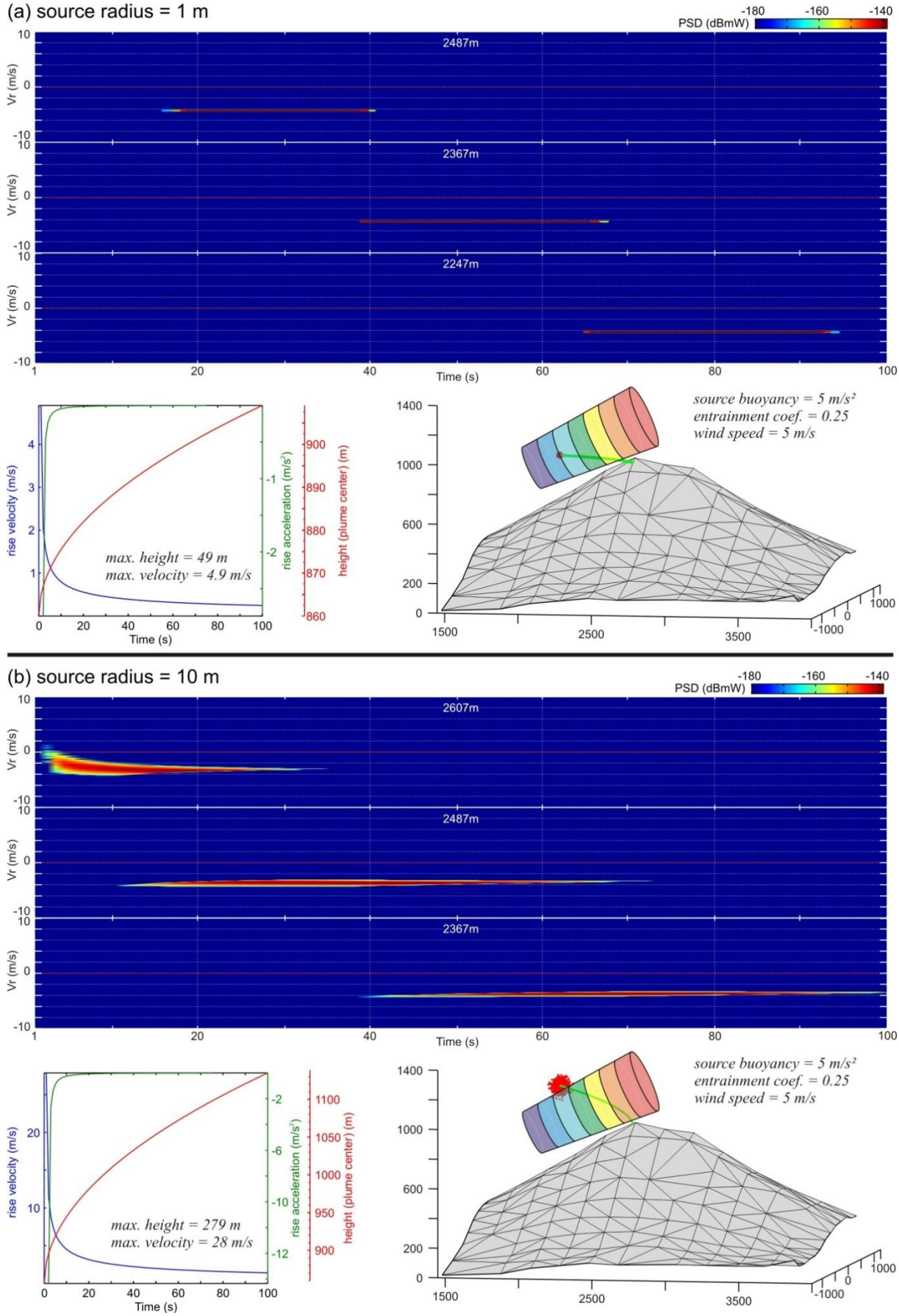

Figure IV.21. Model sensitivity to source radius (R_0). Only the first three gates in which the signal appears are represented on the radargrams.

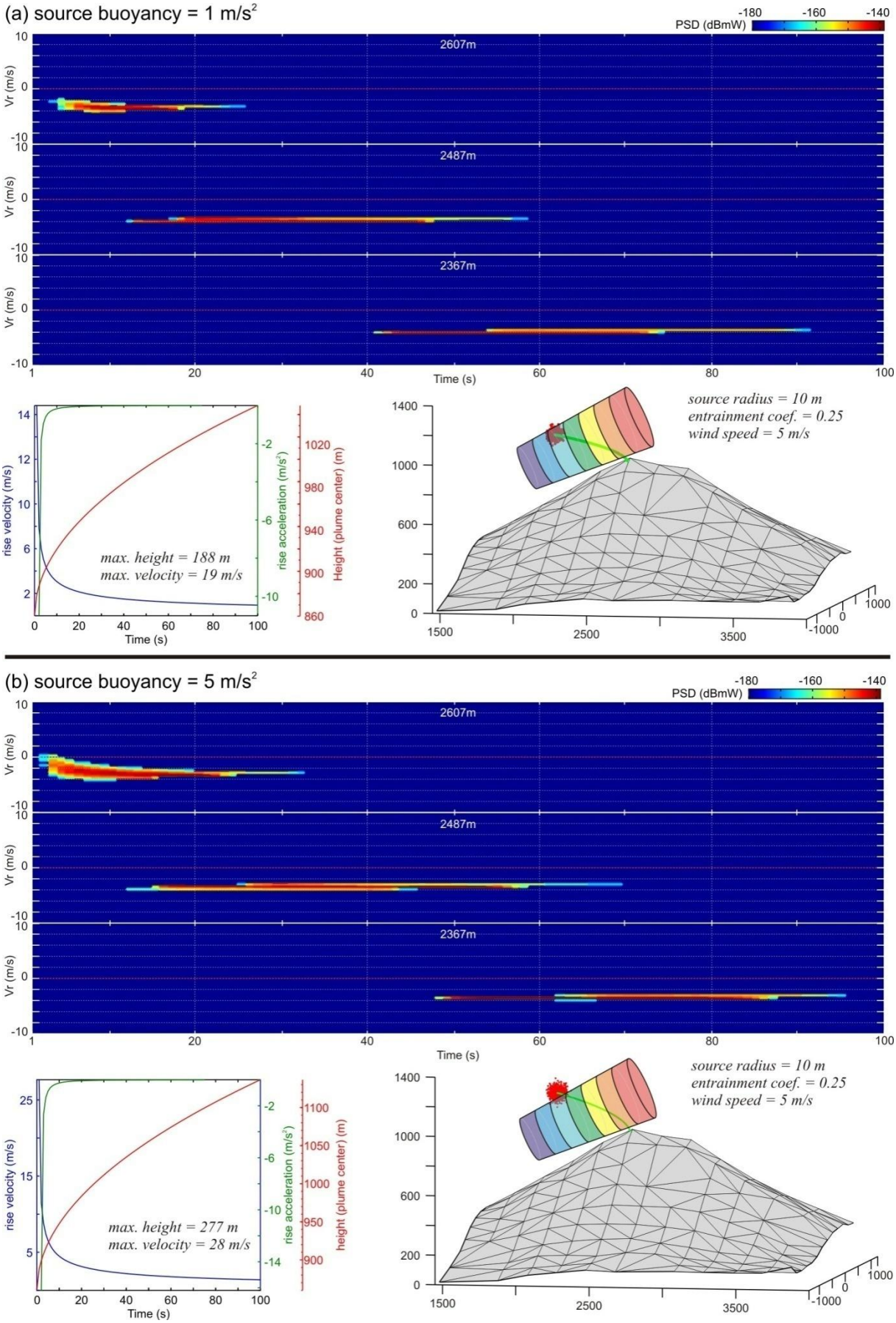

Figure IV.22. Model sensitivity to source buoyancy (g'_0). Only the first three gates in which the signal appears are shown on the radargrams.

IV.2.3.2. Model sensitivity to source buoyancy

The buoyancy depends on the density difference between the plume and the atmosphere. Measurements made by *Yamamoto et al.* (2008) on a thermal buoyant plume at Santiaguito volcano (Guatemala), suggested the source buoyancy (g_0') to be in the order of ~5 m/s^2. *Branan et al.* (2008) on the other hand, estimated the source buoyancy from initial values of the gas puff density (0.65 kg/m^3) and the atmospheric density (1.25 kg/m^3), and also obtained a value of ~5 m/s^2.

Figure IV.22 shows the influence of this parameter on the plume's ascent and on the resulting radar signal. As predicted from Equation IV.11, the source buoyancy value is proportional to the rise rate of the ash cloud: for g_0' = 1 m/s^2 (Figure IV.22a), the maximum height reached in 100 s is ~190 m (plume center above vent), hence nearly 100 m less than with g_0' = 5 m/s^2 (Figure IV.22b). These different rise rates result in slightly different radial velocities expressed on the radargrams of the first gate, with maxima respectively of -2 and 0 m/s.

IV.2.3.1. Model sensitivity to entrainment coefficient

The air entrainment coefficient (ε) controls the rate of air influx into the plume *Woods* (1988). In the review by *Sparks et al.* (1997), the entrainment coefficient value for a jet is given as approximately 0.06, while that for steady buoyant plumes is 0.09, and 0.25 for discrete thermals. *Yamamoto et al.* (2008) determined the entrainment constant to have the value ε = 0.22, for a plume at Santiaguito volcano described as propagating as a buoyant thermal. At Stromboli on the other hand, thermal video analysis carried by *Patrick* (2007) found mean air entrainment coefficients of 0.06–0.12 for gas thrust regimes, and 0.22 (±0.03) for buoyant regimes. We test in Figure IV.23 how the plume behaves for the two extreme values given by *Sparks et al.* (1997), i.e. for a jet- and thermal-type plume.

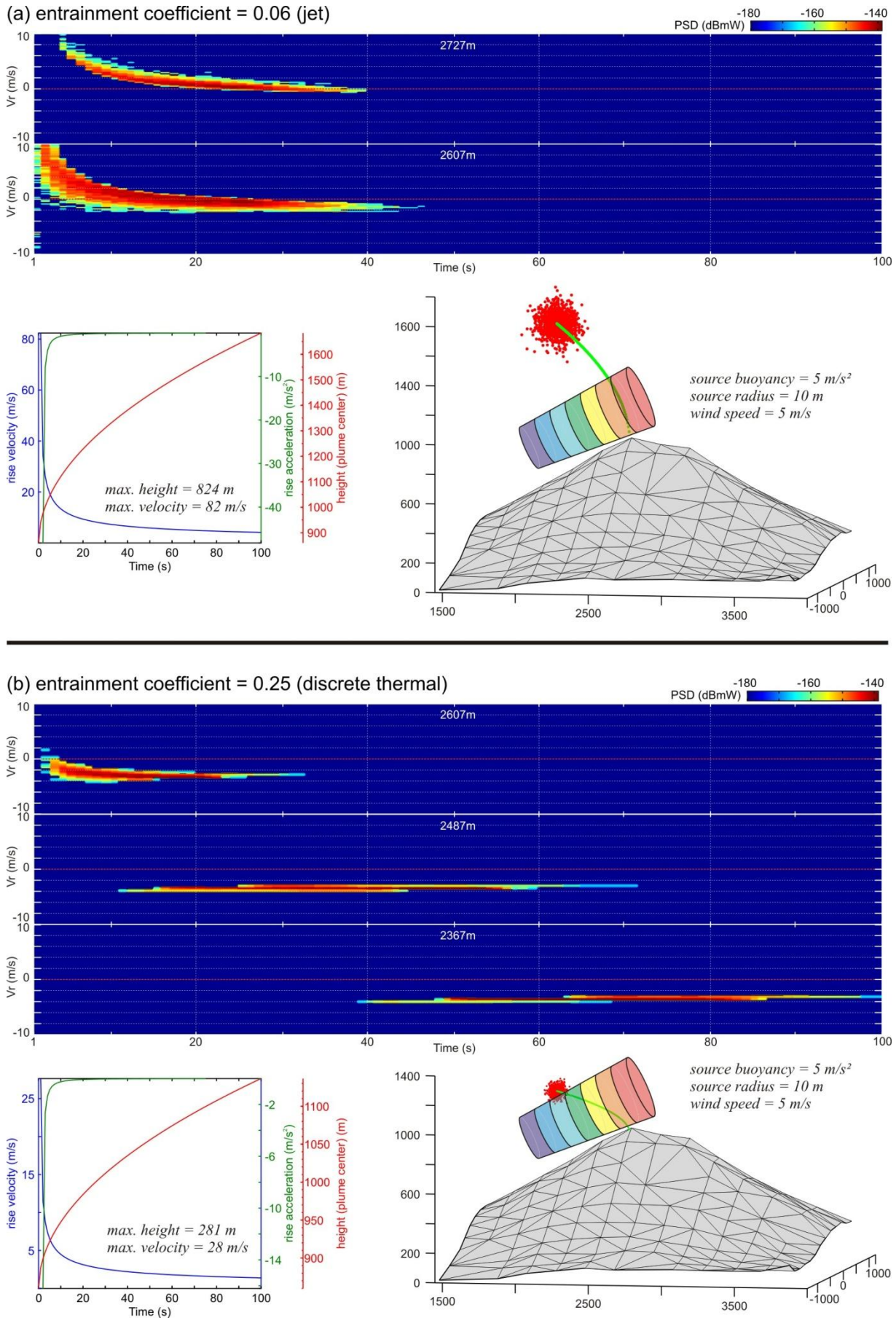

Figure IV.23. Model sensitivity to entrainment coefficient (ε).

Figure IV.23a shows a run with an entrainment coefficient set to 0.06, i.e. a value given for jets in the literature. It results with a plume having a very high rise rate: the maximum rise velocity is about 80 m/s (i.e. distance travelled by the plume center during the first two time steps), and the maximum altitude reached by the cloud (i.e. its center above the vent) is nearly 825 m in 100 s. With an entrainment constant of 0.25 on the other hand (Figure IV.23b), i.e. a value assigned to discrete thermals, the rise rate is much lower: maximum rise velocity = 28 m/s, and maximum rise height = 281 m.

The entrainment coefficient controls the rate of air influx, and should in turn control the plume dimension: a low coefficient should result in a small plume, and vice versa. Note however that this relationship is not valid in our model, because the plume's radius strictly depends on the plume's altitude (equation IV.12). This is an obvious shortcoming in the presented model, whose equations are suited for thermal plumes (*Yamamoto et al.*, 2008).

We've seen that the source radius, the source buoyancy, and the entrainment coefficient all affect the rise rate. To have a comparative view of their affect, we've plotted the maximum height reached by the plume center during a 100-second run (Figure IV.24). The results show that with a fixed source radius, the altitude is predominantly controlled by the entrainment coefficient rather than the source buoyancy.

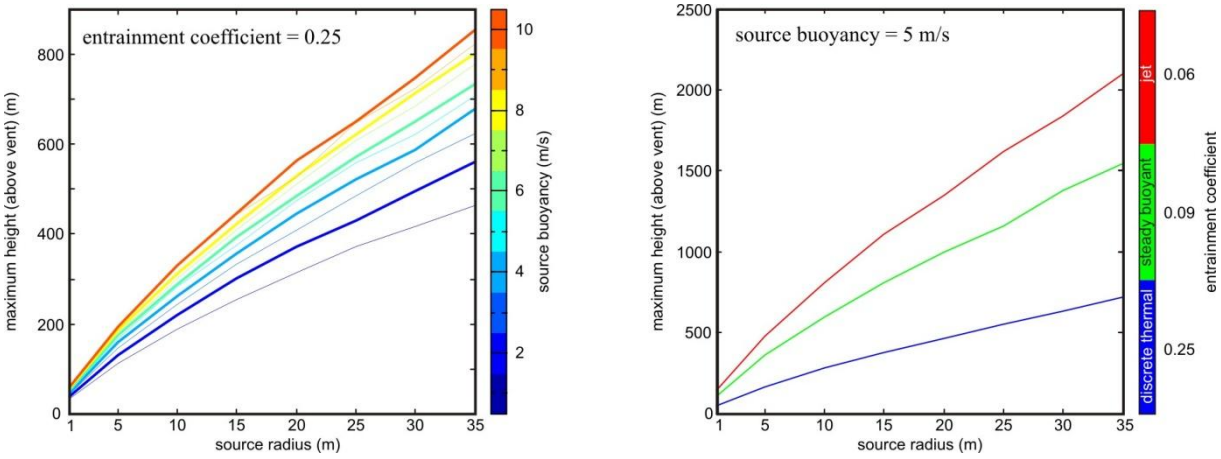

Figure IV.24. Height reached by the plume center above the vent in 100 seconds, with varying source radius, source buoyancy (left), and entrainment coefficient (right), using equations for thermal buoyant plumes (Yamamoto et al., 2008).

IV.2.3.2. Model sensitivity to wind speed and azimuth

Figure IV.25 and Figure IV.26 respectively illustrate how the wind speed (W_s) and azimuth (W_a) affect the plume's trajectory, and the ensuing consequences for the radar signal. It is important to remind that the wind solely influences the plume center's trajectory in the horizontal plane: the particles expand from the center but are not directly influenced by the wind, meaning that at all times the plume conserves it original spheroid-shape. The rise rates are consequently identical whichever the wind speed (lower left plots in Figure IV.25a and b). The trajectories however differ strongly, and result in different radar signals: low wind speed (e.g. 1 m/s, Figure IV.25b) allows the plume to rise quasi vertically, and thus enter few gates (e.g. two) but remain over long periods within each (> 100 s).

Similar observations can be made with varying wind azimuths (Figure IV.26): the rise rates do not change, but the number of gates the plume enters, and the time it remains within each does. With wind azimuth parallel to the radar beam axis (i.e. W_a = 0°), the particles enter 5 gates and may stay up to 60 seconds in each. With wind azimuth 30° away from the beam axis on the other hand, the plume enters only 3 gates, with similar residence time (~60-70 s). A study of the influence the plume exit has on the diminution of the backscattered powers is carried in Chapter VI.

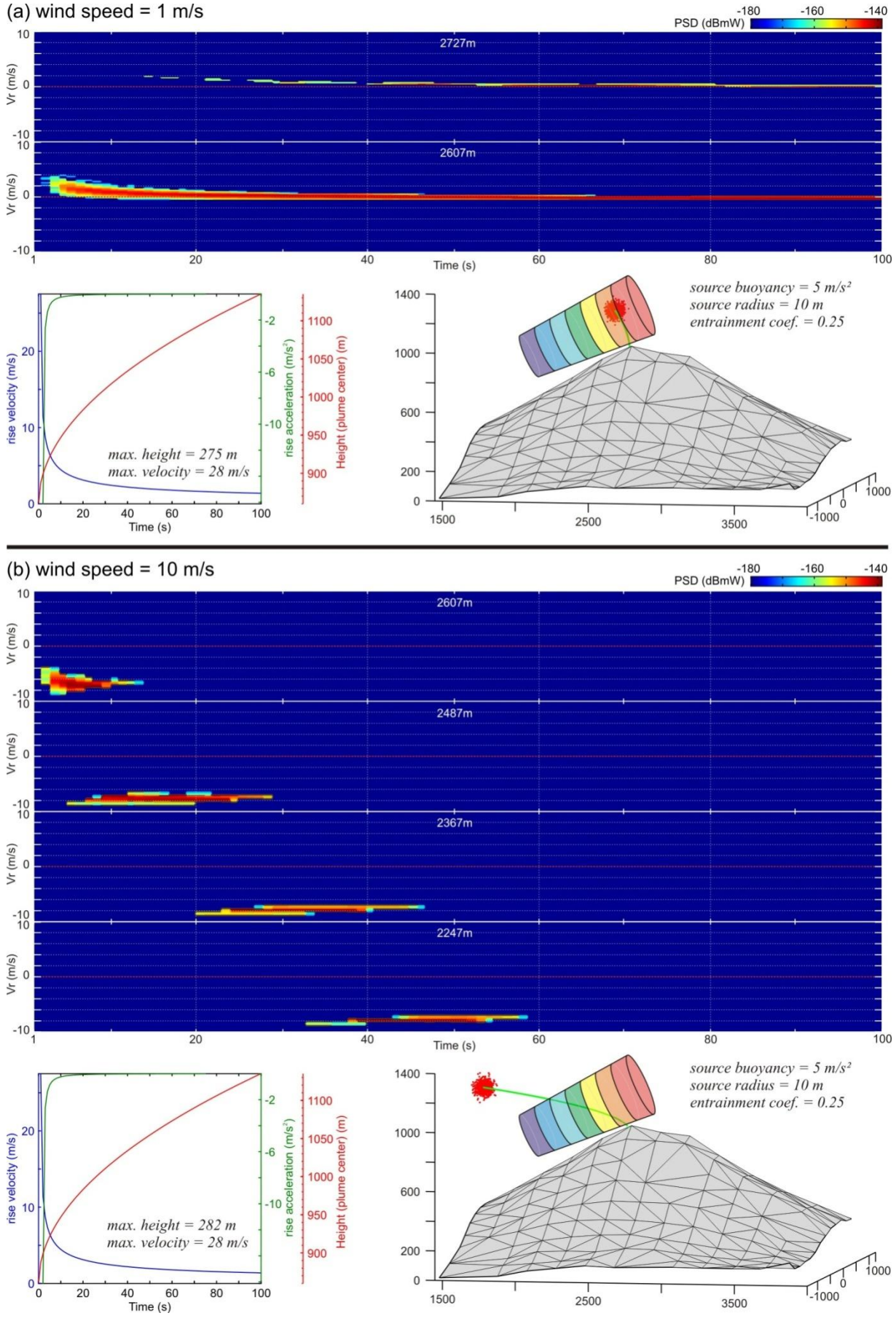

Figure IV.25. Model sensitivity to wind speed (W_s).

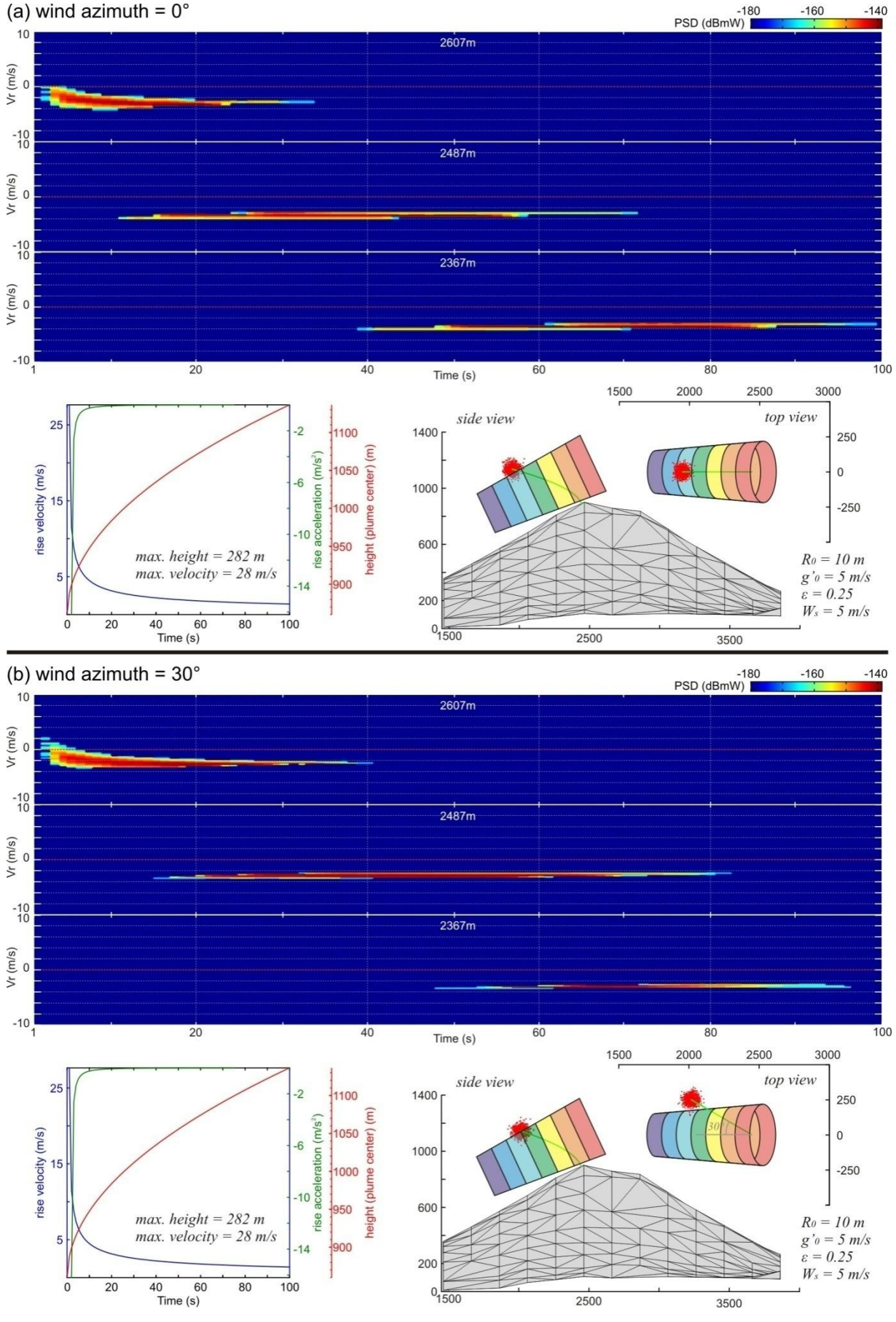

Figure IV.26. Model sensitivity to wind azimuth (W_a).

IV.3. Conclusion

IV.3.1. Successful reproduction of recorded radargrams

Radar recordings of mild eruptions at Arenal (Costa Rica) show the signature of two distinct phenomena occurring simultaneously, evidenced on Doppler radargrams by distinct Doppler signatures (see Chapter III). In this chapter, we have described the physical models used to simulate the 3D transit of both ballistic particles and ash cloud particles through the radar beam, and we have shown how synthetic radargrams resulting from these simulations can be reconstructed. For this purpose, a user-friendly software entitled *eject3D* has been designed, which enables the user to easily select the inputs and outputs to the model (see appendix C for details). Figure IV.27 shows the result of a simulation runned by *eject3D*, in which both the ash cloud and the ballistic particles are ejected simultaneously.

Modeling of particles thrown with ballistic trajectories through the radar beam successfully reproduced the main characteristics of the short-lived part of the signal described in see Chapter III. In particular, the shapes (i.e. time-velocity distribution), durations, and transit times within the gates were reproduced with reasonable match. Most notably, the characteristic curveted shape of the radargram directly above the vent (i.e. with radial velocities progressively drifting from positive values towards negative ones), can be interpreted as resulting from the progressive bending of the ballistic trajectories through the radar beam.

On the other hand, modeling of a cloud of particles behaving as a thermal drifted by trade winds has successfully reproduced most characteristics of the long-lived signal in the observed radargrams. Despite the fact that sedimentation, convection, and internal turbulences were not considered, the long life spans, emergent power onsets, slow transit times through the gates, and low negative radial velocities (resulting from the opposing effects between buoyancy and wind drift towards the radar) were adequately reproduced.

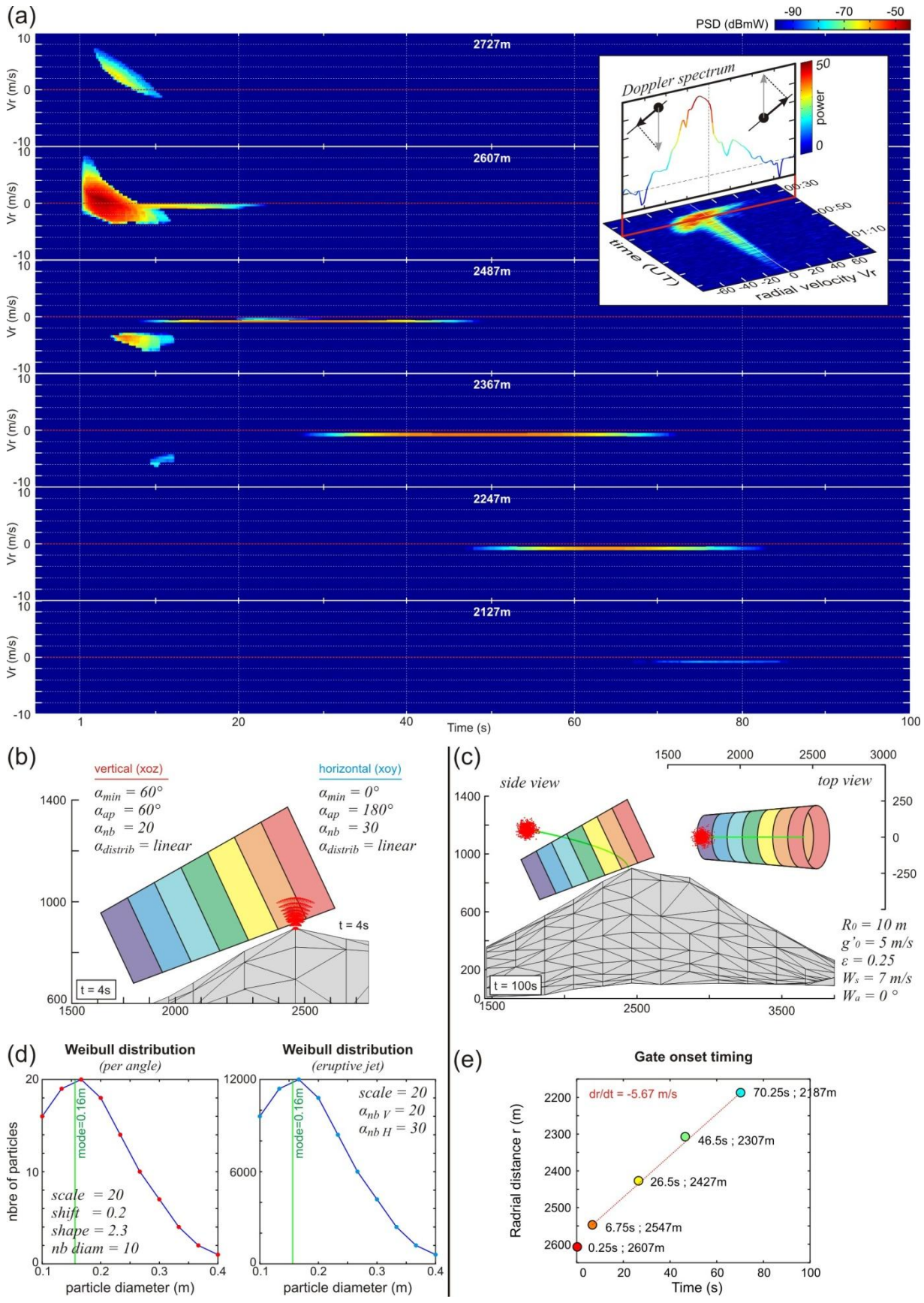

Figure IV.27. (a) Synthetic Doppler radargrams resulting from the simultaneous 3D transit of (b) ballistic particles and (c) ash plume particles. The particle size distribution of the ballistics, ejected at each ejection angle, is shown in (d). Various graphical outputs may be generated by* eject3D*, such as the onset timing of the ash plume in each range gate (e), which can be used for hazard mitigation (see Chapter VI).

IV.3.2. Improvements for future forward models

IV.3.2.1. Future improvements for modeling of ballistics

Several improvements could be made to the algorithm driving the particles. We list a few below, without any sense of prioritization among the suggestions:

- have particles ejected during a certain time lapse rather than in a single pulse and have source gas velocities vary over the duration of the emission (e.g. *Scharff et al.*, in press for numerical simulations, *Clarke et al.*, 2009 for analogue experiments),
- account for more evolved definition of the drag coefficient, such as reduced drag near the vent (e.g. *Mastin et al.*, 1991),
- use more realistic particle shapes, and account for the subsequent aerodynamical properties (e.g. *Mele et al.*, 2011),
- implement the effect of cross-wind (at the moment particles above a user-defined diameter can be displaced latteraly to simulate the wind (like in the ash plume model), however this does not account for the air resistence).

IV.3.2.2. Future improvements for modeling of ash plumes

The plume model developed in this study, is a very simple model which was not intended to reproduce the complexity of ash plumes dynamics (gas-thrust region, convection, turbulence, sedimentation, drag …), but rather to test the radar signals obtained by the transit of a simple finite-volume spheroidal plume having realistic size and speed. Nevertheless, it is obvious that much is to be learned on the internal dynamics of the ash plumes, if more complex algorithms were to be implemented in *eject3D*, or if radar data were coupled to more sophisticated tephra dispersal models for mutual validation and improved interpretations.
Several Volcanic Ash Transport and Dispersion (VATD), such as PUFF (*Searcy et al.*, 1998), HYSPLIT (*Draxler and Hess*, 1998), CANERM (*D'Amours et al.*, 1998), NAME (*Jones et al.*, 2007), or MEDIA (*Piedelievre et al.*, 1990), have been developed to forecast the dispersal of ash clouds. However, these operate on large scales and ignore the small-scale processes in the eruption plume itself, which are more interesting to us. ATHAM (Active Tracer High Resolution Atmospheric Model, *Oberhuber*, 1998) is likely to be a model better suited for our purposes, because it simulates the processes in the volcanic eruption column in great detail. Implementing the radar backscattering equations within this type of algorithm is likely to be very promising (e.g. *Marzano et al.*, 2010b).

IV.3.2.3. Improvements in the model simulating radar signal

The radar aperture angle (9°) refers to the beamwidth where the received/transmitted signal power is equal to -3 dB of the main power lobe. From a physical point of view however, the radiation pattern is progressive, meaning that the beam borders are not sharp but rather consist of zones of varying electromagnetic intensity. In turn, this means that particles located on the beam borders will backscatter less power than those located near the beam center where the transmitted power is maximum. This is an improvement that should be taken into account in future versions of *eject3D*.

Chapter V

Inverse modeling of pyroclastic emissions

V.1. Introduction

In the preceding chapter, we have described physical models simulating both ballistic pyroclastic projections, and ash plume rise. From there, synthetic radargrams have been reconstructed, and have shown that the observed radargrams did comprise the signature of ballistics, and/or ash plume transiting through the radar beam. These models however, require the user to select input parameters (hence the term ***forward modeling***), which will produce synthetic data that match more or less the observed data. ***Inverse modeling*** will come in handy to search for the best input parameter values, i.e. those that will best reproduce the observed data. Inverse modeling will require: (i) an ***exploration algorithm*** that will search the parameter space (e.g. Monte Carlo procedure), (ii) an ***optimization algorithm*** used to sample the parameter space and explore it "intelligently" (e.g. near-neighborhood algorithm), and (iii) a ***misfit function*** (or objective function) that will measure the discrepancy between the observed and modeled data (e.g. least square function).

We present hereafter the methodology developed, and discuss the preliminary results from the inversion of the Doppler signature of both the ballistics and the ash plume, recorded during the eruptive event of February 19, 2004 at 20:00:30 UTC.

V.2. Inverse modeling methodology

V.2.1. Inversion model algorithms

The inversion model is made of an ***exploration algorithm*** that searches the parameter space, and an ***optimization algorithm*** that drives the exploration algorithm. Both are presented below.

V.2.1.1. **Exploration algorithm:** the Monte Carlo approach

The inversion procedure is meant to explore the parameter space (i.e. the range of values the input parameters may take), and search the combination of parameters which minimizes the misfit function (hence the discrepancy between observed and modeled data). Two types of exploration algorithms exit: those *gradient* based, and those *Monte Carlo* based (Figure V.1). The first uses the derivative of the misfit function to reach its minimum (*Gill et al.*, 1981; *Press et al.*, 1992). These algorithms will converge efficiently towards the minimum only if the misfit function is simple (e.g. smooth gradient changes, with few local minima). In the case of geophysical inverse problems however, the data/model relationship is often highly nonlinear, and thus the data misfit function is more complex (e.g. abrupt gradient changes, narrow valleys and multiple minima, often non-differentiable). Consequently, the gradient-based method will either fail to converge, or fall into local minima. Henceforth, for geophysical inversions, direct search methods (i.e. direct sampling of the parameter space) like Monte Carlo are often preferred.

The ***Monte Carlo approach*** can be expressed as a method which "*makes use of repeated trials, or sampling, generated with the use of random numbers, named after the famous French city associated with casinos*" (*Sambridge and Mosegaard*, 2002). In other words, the Monte Carlo procedure will search the parameter space by sampling it pseudo randomly (the sampling will be guided by an optimization algorithm), evaluating by repeated trial the misfit function at given points in the parameter space.

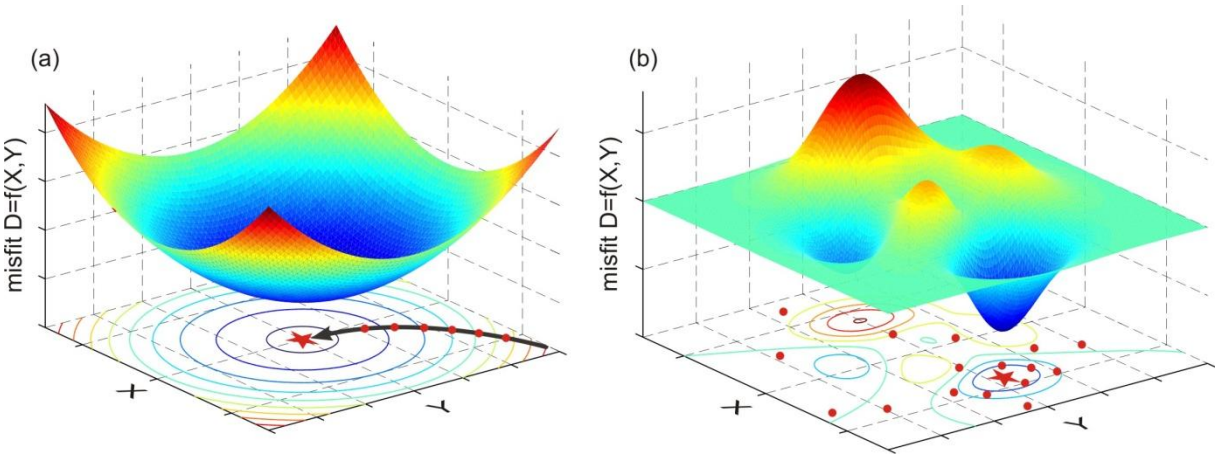

Figure V.1. Minimization of the misfit function D = f(X,Y): search of the minimum misfit value (red star) by iterative trials (red dots). a) Simple function for which a gradient-based search may be applied. b) Complex function for which a direct search by Monte Carlo is preferred, by pseudo random sampling of the parameter space (X, Y).

V.2.1.2. **Optimization algorithm:** the neighborhood algorithm

Optimization algorithms are used to guide the exploration in the parameter space, by seeking only parts of it. Several methods exist, including simulated annealing, genetic algorithms, neighborhood algorithm, and several others (see *Sambridge and Mosegaard* (2002) for a review). We used a ***neighborhood algorithm*** (nasearch), originally developed by *Sambridge* (1999a), and later applied to INSAR inverse modeling by *Fukushima* (2005) and *Augier* (2011). The method uses the spatial properties of Voronoi cells to guide the sampling of the parameter space: when a sampled point gives satisfying results (i.e. low misfit), the algorithm will enhance the search in the neighboring region by subdividing it into smaller cells (Figure V.2). Iteratively, the algorithm will converge towards the misfit minimum.

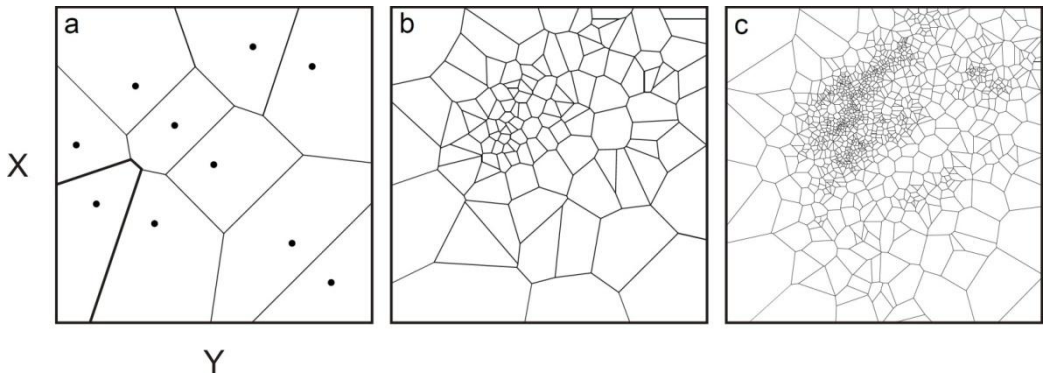

Figure V.2. Iterative sampling of the parameter space using the neighborhood algorithm (modified after Sambridge, 1999a). The thickened region in (a) represents a Voronoi cell. As the algorithm proceeds from (a to c), the Voronoi cells become more concentrated in certain regions of the parameter space, where the misfit value is low.

V.2.1.3. NAsearch code

The NAsearch code (Neighborhood Algorithm) is a *Matlab* code developed by *Fukushima et al.* (2005), based on the method presented by *Sambridge* (1999a), which uses the Monte Carlo and neighborhood algorithms described earlier. The code was later improved by *Augier* (2011), and was used to constrain source geometries responsible for ground deformation monitored by INSAR.

The code enables the user to specify search parameters, such as the number of Voronoi cells to be resampled at each iteration, the maximum number of iterations wanted to end the search, or the convergence criteria value. For more details on the code, refer to *Augier* (2011).

V.2.2. Misfit function: quantification of discrepancy between radargrams

The ***misfit function*** (or objective function) is a measure of the discrepancy between the observed and modeled data (*Sambridge and Mosegaard*, 2002). The misfit function we used is a least-square function, which computes the discrepancy (*d*) as the sum of differences between the synthetic radargram pixels, and the observed radargram pixels:

$$d = \sum_{time}\left\{\sum_{gate}\left[\sum_{V}\left(p_V^{obs} - p_V^{\mathrm{mod}}\right)^2\right]\right\} \qquad \text{V.1}$$

where p_V^{obs} and p_V^{mod} are the pixels' echo power values (respectively in the observed radargram and modeled radargram), at the velocity value *V*, in a given *gate* at a given *time*. As we are dealing with several thousands of pixels, equation (V.1) is rewritten in matrix form (to gain in computational time) as follows:

$$d = \left(P_{obs} - P_{\mathrm{mod}}\right)\cdot\left(P_{obs} - P_{\mathrm{mod}}\right)^T \qquad \text{V.2}$$

where P_{obs} and P_{mod} are vectors containing the power values of the pixels in the observed and modeled radargrams respectively.

Note that the radargram may be subsampled (see following section), so that the discrepancy is not measured on all pixels but on chosen ones. The values in P_{obs} and P_{mod} will change consequently.

V.2.3. Radargram conditioning for inversion

Before computing the discrepancy (*d*), a number of operations must be performed on the radargrams.

V.2.3.1. Radargram filtering

Even though *eject3D* enables the possibility to model simultaneously ballistics and ash plumes, the inversions we carry out try to match only one of the two signals at a time. Indeed, it would be too time consuming to match both, because (i) the forward model would take much longer to compute (i.e. > 100 seconds-long radargrams), and (ii) the inversion procedure would have a larger amount of parameters to inverse (i.e. plume and ballistic input parameters).

The observed (raw) radargram is thus filtered in order to isolate the part of the signal in which we are interested (short-lived or long-lived part, depending on whether we are modeling the ballistic or the plume). To do so, each pixel of the non-wanted part of the signal is replaced by the mean power noise value +/- the standard noise deviation (Figure V.3).

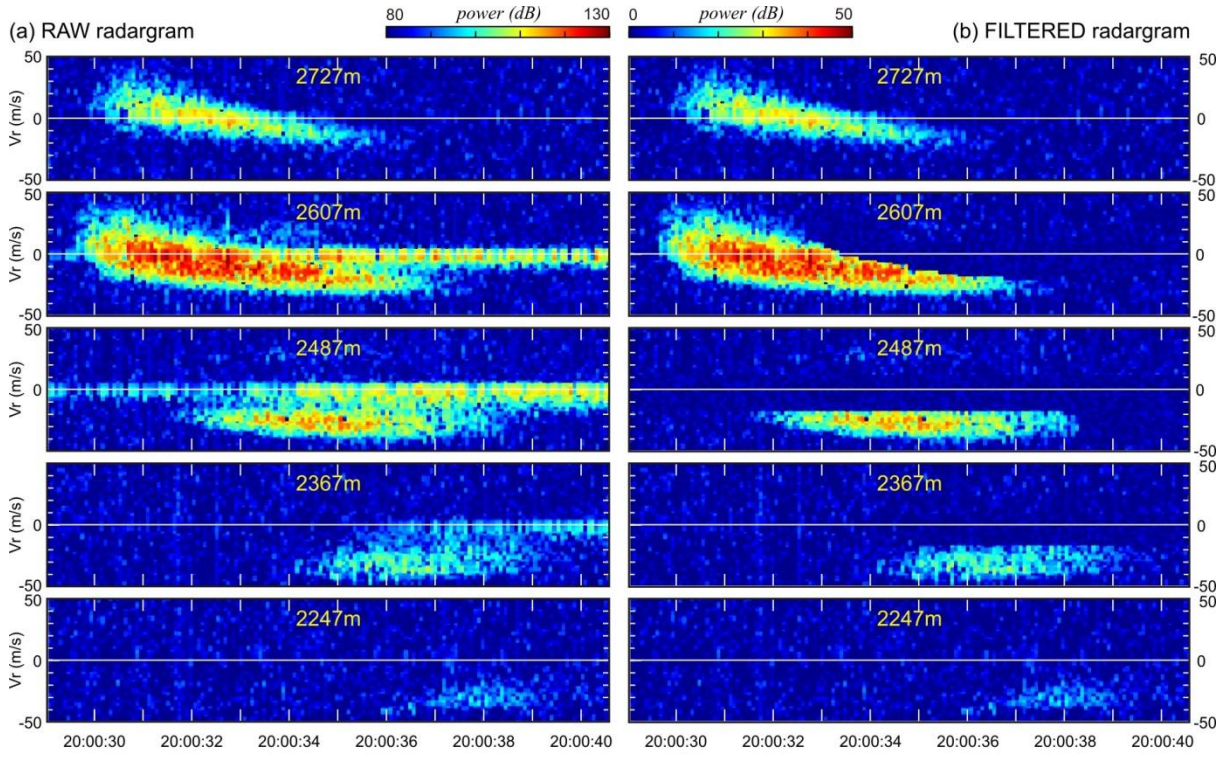

Figure V.3. Filtering of the raw radargram to isolate the part of the signal that is to be matched by the inversion procedure. (a) shows the raw radargam having both the signature of the ballistics and the ash plume (i.e. short-lived and long-lived signal), (b) shows the radargram after filtering of the ash plume signature (i.e. long-lived signal).

V.2.3.2. Radargram resampling

Radargrams need to be resampled before data can be used in the inversion procedure. The resampling method consists of two major steps: the first resamples the time vector in order to get a constant time step (identical to the one in the synthetic radargrams computed), the

second subsamples the signal in order to get more sampling points where radargrams have useful signal. Let us describe hereafter both steps.

V.2.3.2.1. Constant time step

Raw radar data suffer from non-constant sampling rate because of the limited accuracy of the clock of the PC recording the data (Figure V.4). However for synthetic radargrams to be quantitatively compared with observed radargrams (i.e. misfit), the time vectors must be identical. A linear interpolation is performed with the function *interp2* of the *Matlab* toolbox, in order to interpolate the raw time vector into a vector with the same values as the synthetic radargrams (0.1 s time step).

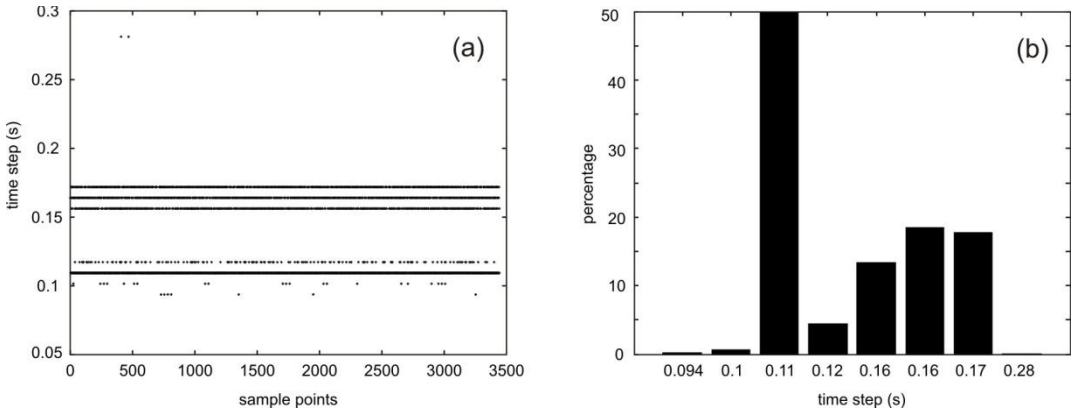

Figure V.4. Unsteady sampling rate from raw radar data (a), and representativeness of each time step in percent (b). The examined time period is that of the eruptive event recorded at Arenal on 2004-02-19 at 20:00 UTC (Figure V.3).

V.2.3.2.2. Quad tree decompositions

The objective of this operation is to increase the proportion of sampled points where there is eruptive signal, in order to optimize the value of the calculated discrepancy. To do so, a *quadtree decomposition* of the observed radargram image is performed (*Finkel and Bentley,* 1974). The idea is to subdivide the radargram into square blocks, and to collect the mean power value of the pixels contained in the block (Figure V.5). The sizes of the created blocks depend on the power variance of the pixels inside them: if there is homogeneity among the values then large blocks are defined, and conversely small blocks are defined when there is large variance among the pixels (e.g. at the boundary of eruptive signal). The mean power value of each block, positioned at the block center, are the values used for the computation of the discrepancy (*d*) between the observed and modeled radargrams (equation V.2). This

implies that the coordinates of the blocks defined on the observed radargram are stored, and that these will be used to compute the mean values of the same blocks on the modeled radargram.

The function *qtdecomp* in the *Matlab* toolbox is used to perform the quadtree decomposition. The user may force the minimum and maximum size of the blocs, as well as the power variance threshold value, which dictates whether the block is subdivided or not.

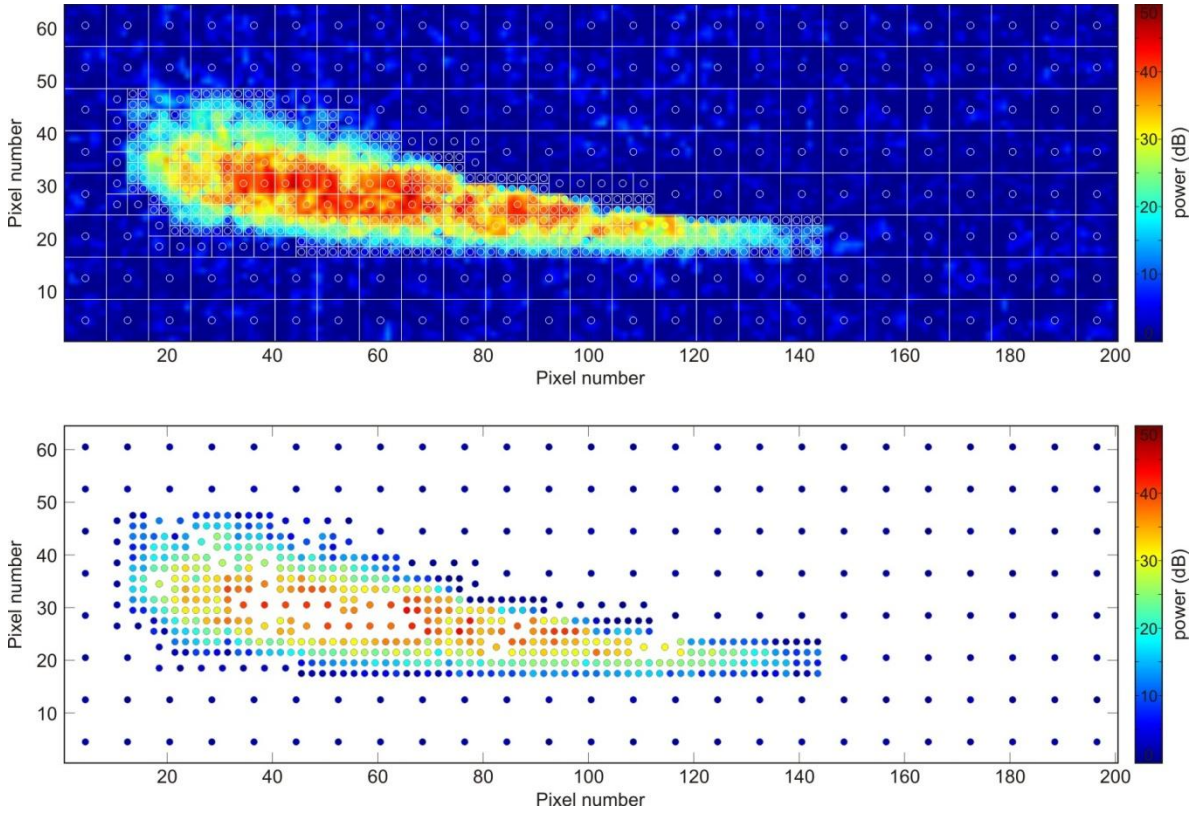

Figure V.5. Quad tree decomposition of the radargram, performed to increase the number of sampled points where there is eruptive signal. The radargram is decomposed into blocks of varying size (top), and the mean power value of the pixels in the bloc is collected (bottom) and used to compute the misfit (i.e. vector P_{obs} in equation V.2).

V.2.3.3. Radargram binarization and normalization

In a first step, we were only interested in matching the time-velocity distribution of the signal, not the absolute power values. The observed and modeled radargrams consequently needed to have their power values normalized for the misfit to have a meaning.

Various power normalizations have been tested. Most notably, normalization of the power values between 0 and 1, or binarization of the power (i.e. values 0 or 1 rather than ranging from 0 to 1). In the latter case, we fix a noise power threshold and force all the values above to 1, and all values below to 0. This operation can be performed directly on the sub-sampled

points collected from the quadtree decomposition (Figure V.6), or on the each pixel of the radargram.

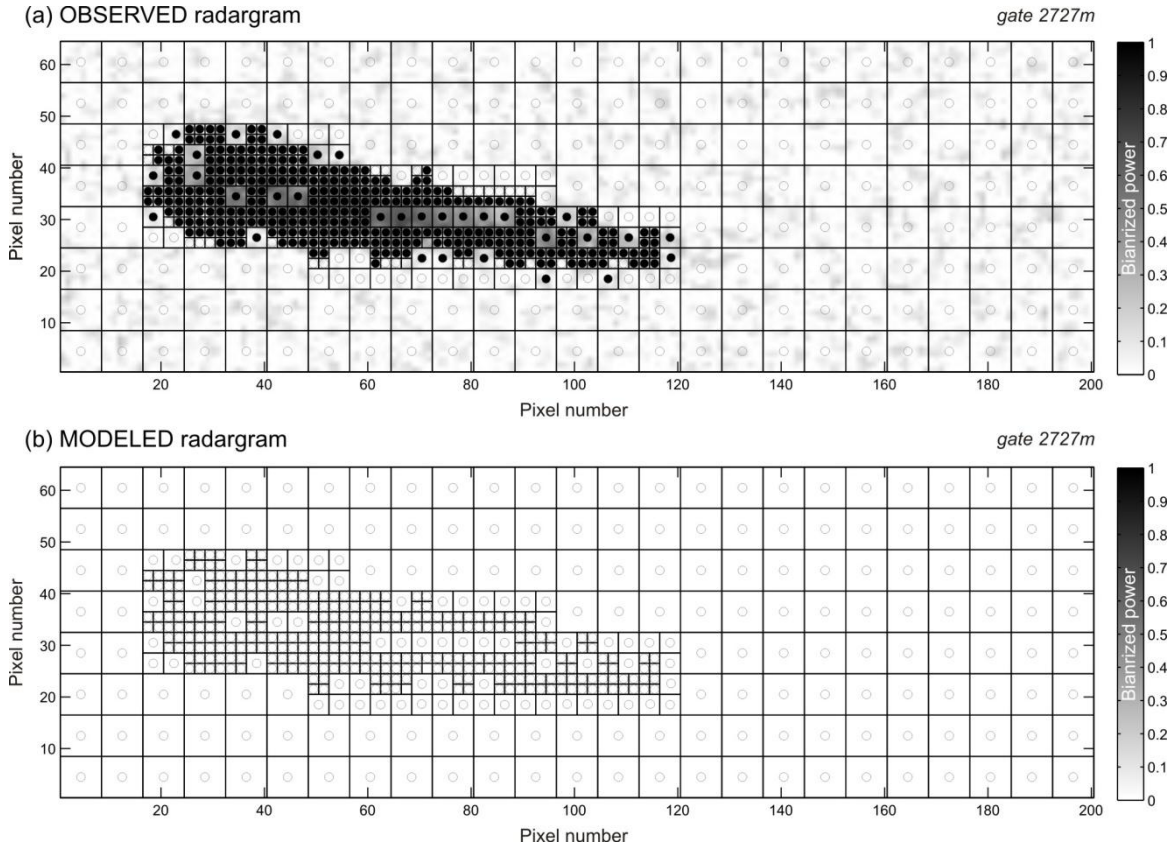

Figure V.6. Binarization of the observed and modeled radargrams (gate 2727 m). (a) Observed radargram: the subsampled points whose power values are above a noise threshold of 3.5 dB are set to 1, those below are set to 0. (b) Modeled radargram: no particle has entered the gate, all points have 0 values.

V.2.3.4. Radargram onset shift

The signal onset in the modeled radargrams, i.e. delay between the time at which particles are launched, and the time at which they first enter the beam, may vary depending on the input parameters in the forward model (e.g. vent coordinates, initial gas velocity …). The signal onset in the observed radargrams however is fixed, yet arbitrarily since we have no precise constraint on the timing at which the particles are actually launched from the vent. Consequently, the onset delay cannot be used as a constraint in the inversion procedure, and must thus be corrected for. Henceforth before the misfit is computed, the onset delay of the modeled radargram is set identical to the one of the observed radargram.

To do so, the onset timing of the modeled radargrams is located (whichever the range gate), and is then shifted to match the one of the observed radargram (the shift affects all range gates), Figure V.7.

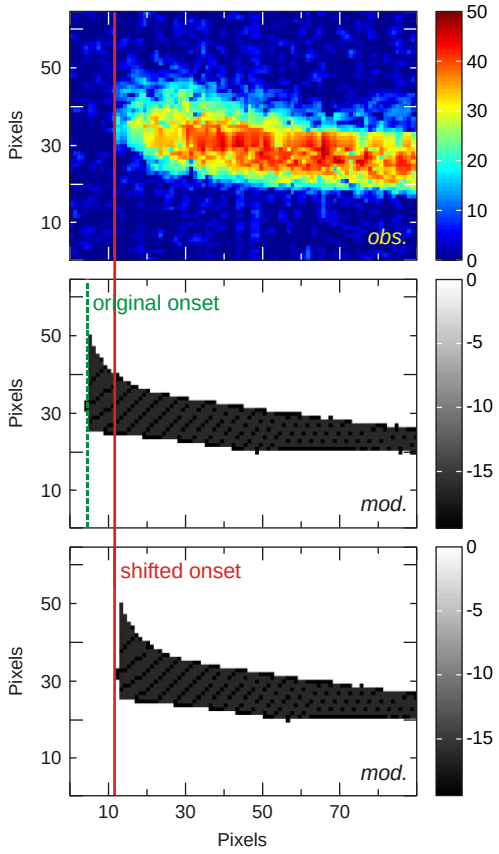

Figure V.7. Shifting of the modeled radagram signal onset (bottom), to match the one of the observed radargram (top).

V.2.4. Inversion model efficiency

The most efficient way to test the inversion model's efficiency is to inverse synthetic data, since the input parameters used to build it are known precisely. If the inversion converges towards the correct values, then the inversion model can be considered as robust, and can thus be applied to real data to infer source eruptive parameters.

Figure V.8 shows an inversion performed on a synthetic radargram, which attempted to recover the following input parameters: initial gas velocity (V_{g0}), particle diameter, and ejection angle distribution. The synthetic radargram (Figure V.8a) was constructed with the following input values: V_{g0} = 100 m/s, particle diameter = 0.1 m, minimum ejection angle = 60°, ejection aperture angle = 60°. The inversion model successfully recovered these values (V_{g0} = 99.9 m/s, particle diameter = 0.099 m, minimum ejection angle = 62°, ejection aperture angle = 58°), consequently reproducing a very similar radargram (Figure V.8b). Note that the

number of angles distributed within the jet aperture angle was imposed during the inversion procedure, and set to be equal to the value of the aperture angle. This explains why the best-fit model uses 58 ejection angles while the reference model only uses 30 (Figure V.8, bottom panels), resulting in a best-fit radargram with more power than the reference one (i.e. darker color).

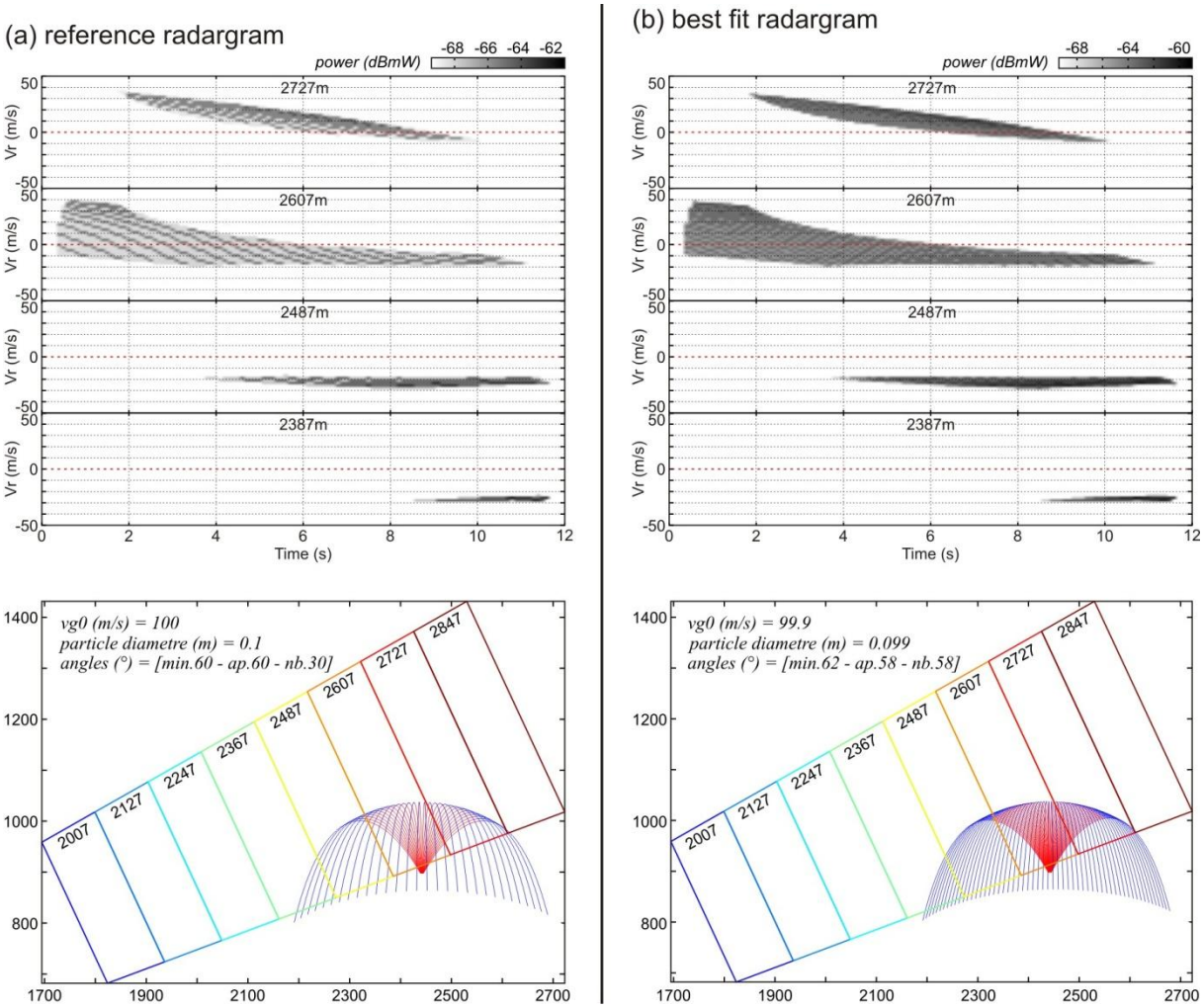

Figure V.8. Illustration of how inversion of synthetic Doppler radargram can test the inversion model's efficiency. The best-fit radargram (b) fits closely to the reference synthetic radargram (a), and the input parameter values searched by the inverse procedure are found with <0.1 % error.

Figure V.9 illustrates the minimization of the misfit value throughout the inversion iterative procedure, indicating that the models improve as the inversion progresses. The convergence towards the correct input values is presented in Figure V.10, where the misfit value is shown by the color code (light blue = high misfit, dark blue = low misfit). Notice that local minima are found during the inversion (e.g. aperture angle ≈ 120°, investigated until iteration n° 25 approximately), but that the inversion model successfully avoids "falling" into them.

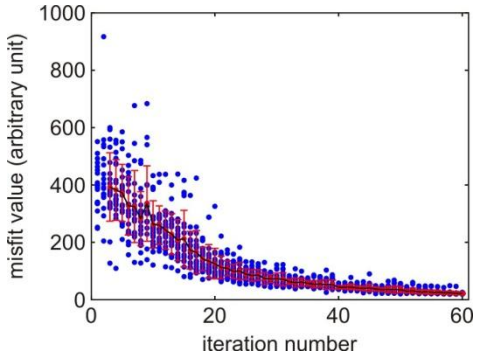

Figure V.9. Minimization of the misfit value throughout the iterative inversion procedure. The black line traces the mean value obtained at each iteration, and the red bars the standard deviation.

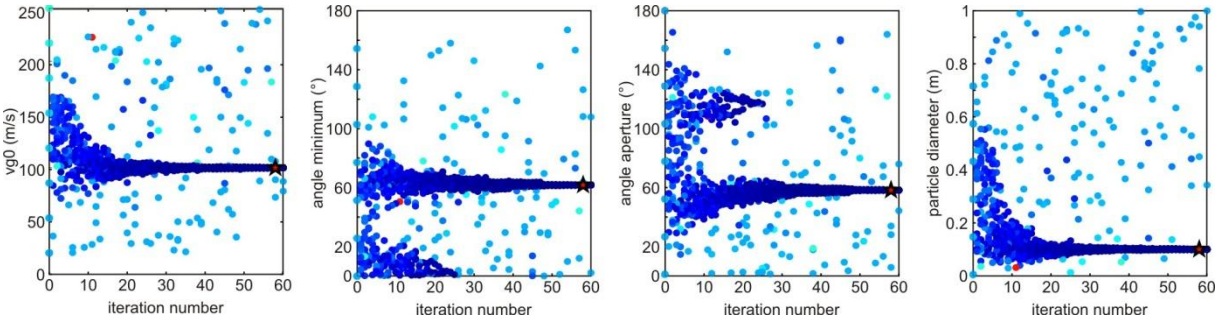

Figure V.10. Convergence towards the best input parameter values as the inversion procedure progresses. At each iteration, a certain number of models are computed, testing a number of values for each input parameters (materialized by the markers). Note that the points apart from the main trends are models which probe the parameter space, independently from the Voronoi cell resampling. The color code of each marker is related to the misfit value: the darker the color is, the lower this value is. In turn, dark blue markers indicate that the model tested by the inversion is close to the reference model. The red star indicates the best model found (i.e. with the lowest misfit value).

The fact that the inversion procedure successfully matched the reference radargram, recovering its input parameters within 97 % accuracy, indicates that it is efficient and robust. In turn, it can confidently be applied to radargrams of recorded eruptive events in order to infer eruptive parameters, such as the eruptive jet geometry, particle sizes, source gas velocities, etc.

V.3. Inversion of a case eruptive event

The inversion methodology described above has been tested on a representative case eruptive event, recorded at Arenal on February 19, 2004, at 20:00:30 UTC. Note that this event is the same that has been used to show that the ash plume and the ballistics may be discriminated, based on their distinctive Doppler signatures (Figure III.4, *Valade and Donnadieu*, 2011).
As said previously, we inverse the ballistics' signature and the plume's signature separately in order to gain in computational time (see section V.2.3.1). The inversion of the ballistics' signature however, clearly is the most challenging of the two, as both the Doppler signature and the model to reproduce it are more complex. We consequently make a much more significant point on it.

V.3.1. Inversion of ballistics' Doppler signature

Because simplicity often ensures robustness and explicitness, the first inversions to be carried out were performed with a ballistic model operating in 2D, with monodisperse particles launched following a linear distribution of angles within the jet aperture. This however, considerably restricted the number of particles within the beam, which in turn meant that the absolute backscattered power (in dBmW) could not be matched (power was consequently either normalized or binarized, thus in arbitrary units). Hence at this stage, we were mostly interested in matching the time-velocity distribution of the signal (or in other words shape of the radargram), neglecting the absolute power distribution within the radargram itself. Two inversion results are presented, the first with normalization of the power, the second with binarization of it (section V.3.1.1.1). We later introduced polydisperse particle size distributions which were ejected in 3D, in order to assess how these improvements could help match the radargram shapes. One inversion run incorporating these changes is presented (section V.3.1.1.2). Only recently, we intended to match the backscattered power absolute values (in dBmW), in addition to the shape of the radargram. This however is still work in progress, for which we show only preliminary results (section V.3.1.2).

V.3.1.1. Matching the time-velocity distribution

V.3.1.1.1. Projections in 2D, with monodisperse particles

Normalized radargrams

Figure V.11 shows the result from an inversion in which the powers were normalized between 0 and 1. The reference radargram was subsampled to optimize the ratio of points where eruptive signal is recorded (minimum bloc side in pixels = 2, maximum bloc size = 8, Figure V.11a). The resulting sampled points, are those used to compute the misfit value. In order to visualize how the best-fit model reproduces the reference radargram's time-velocity distribution, the locations of the subsampled points are shown in the best-fit radargram by empty circles (Figure V.11b). This enables us to notice that the best-fit model: (i) successfully reproduces signal in the gates were signal is indeed observed (i.e. gates 2247 to 2727 m), (ii) successfully matches the successive onset timings and onset velocities in these gates. The eruptive jet appears slightly inclined towards radar (Figure V.11c), which was expected since a majority of gates with eruptive signal are down-beam from the vent. The best particle diameter found by the inversion is of 0.17 m, launched with an initial gas velocity (V_{g0}) of 131 m/s (Figure V.11d).

The results however exhibit two shortcomings: (i) the modeled radargrams are not as wide as the reference radargrams (in terms of velocity range, particularly in gate 2727 m), and (ii) the durations are not properly matched (particularly in gate 2247 m). Several elements may be responsible for these imperfections: the normalization of the power (which may introduce threshold issues), the fixed coordinates of the vent (which may restrict the signal in the gates up-beam), and the subsampling (which may under-sample the eruptive signal itself). These elements were modified in the inversion run presented hereafter.

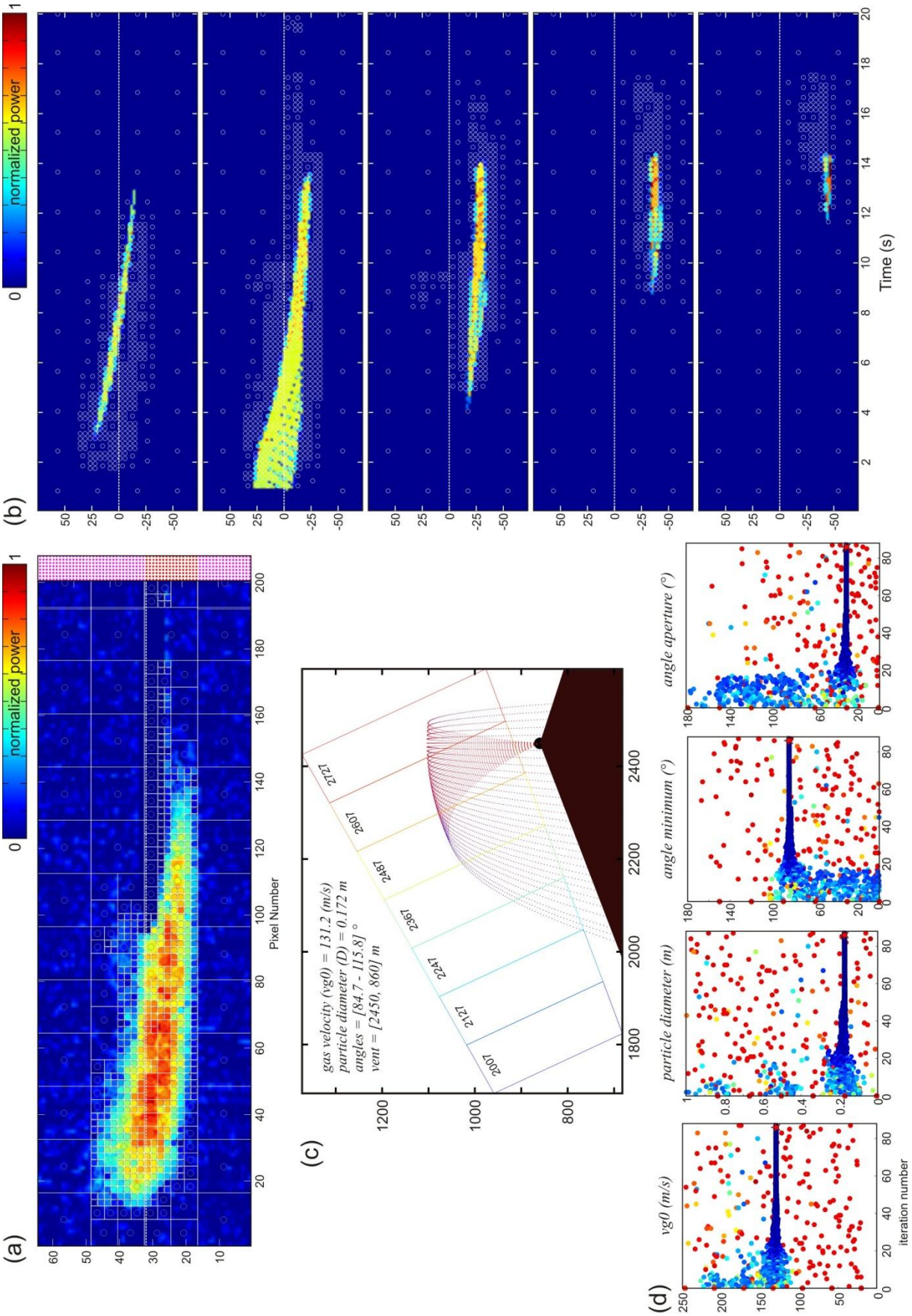

Figure V.11. Results from an inversion with normalized power values. (a) radargram subsampling (gate 2607 m); (b) best-fit radargrams on which are overlaid the locations of the subsampled points (empty circles); (c) 2D trajectories from best-fit model; (d) convergence of the parameters throughout the inversion procedure.

Binarized radargrams

Figure V.12 shows the results from an inversion in which no quadtree subsampling was performed on the radargrams, but where the pixels' power value were binarized (i.e. 0 or 1), and the vent coordinates were left free. The results are similar and consistent with the ones presented above: the eruptive jet is slightly oriented towards the radar, and the onset timing and onset velocities in the gates are well reproduced. The vent coordinates found by the inversion procedure come close to the fixed values used previously, although slightly shifted towards gate 2727 m (X = 2484 m instead of 2450 m, Y = 864 m instead of 860 m). Notice that this shift enables the signal in gate 2727 m to be slightly better matched than in the previous inversion (Figure V.11), in terms of both onset timing and velocity representativeness (although this latter point still remains poorly reproduced for the lowest velocities in that gate). As for the lifespans of the signals in the gates downhill (2247 – 2487 m), these are still underestimated by about 30%, a shortcoming likely related to the fact that the modeled emission pulse is instantaneous, and that the particle size distribution is monodisperse.

Moreover, notice that the particle diameter found by the inversion is much larger than the previous estimate (Figure V.11), i.e. D = 0.47 m instead of 0.17 m, and the initial gas velocity is accordingly higher, i.e. 171 m/s instead of 131 m/s. This highlights the fact that similar matches of the signal's time-velocity distribution are possible with various couples of particle diameter / gas velocity. Figure V.13 plots the various values obtained over a number of inversions carried out, and shows the nearly linear relationship between the two parameters. This calls for the need of another parameter to constrain our inversion: the absolute backscattered power (in dBmW), which will constrain the size of the particles. This is discussed in section V.3.1.2. In the meantime however, improvements are still possible to enhance the match of the radargrams' shapes (i.e. the time-velocity distribution of the signal). Indeed, we have seen in the previous chapter that the particle size distribution could influence both the shape of the radargrams and the power distribution within these. Moreover, we have mentioned that computing eruptive jets in 3D rather than in 2D also affects the power distribution. Consequently, we have launched inversion runs in which the forward model could eject polydisperse particles in 3D, to see if we could better match the observed radargrams. The results from one of these inversions are presented below.

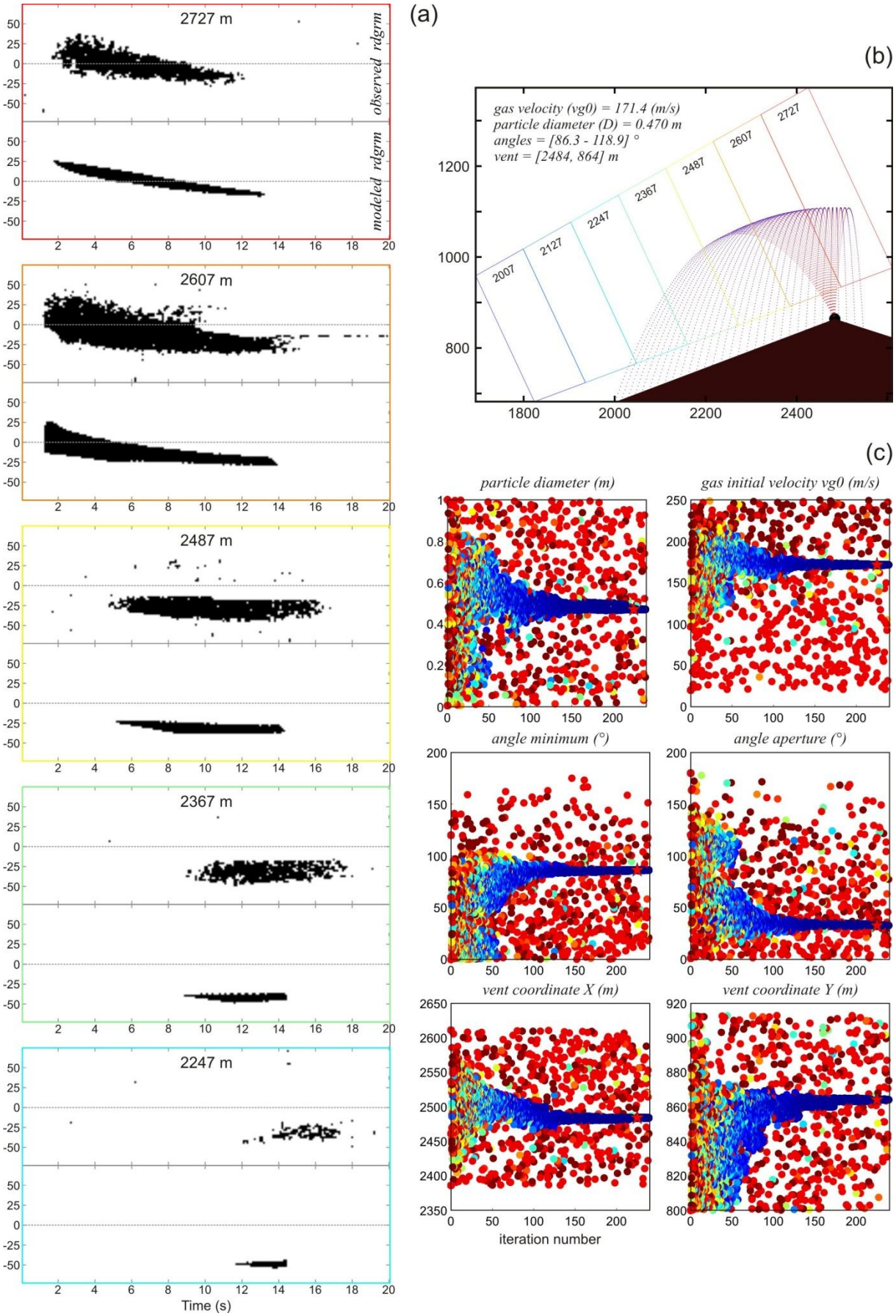

Figure V.12. Results from an inversion with binarized power values. (a) observed and modeled radargrams; (b) 2D trajectories from best-fit model; (c) convergence of the parameters throughout the inversion procedure.

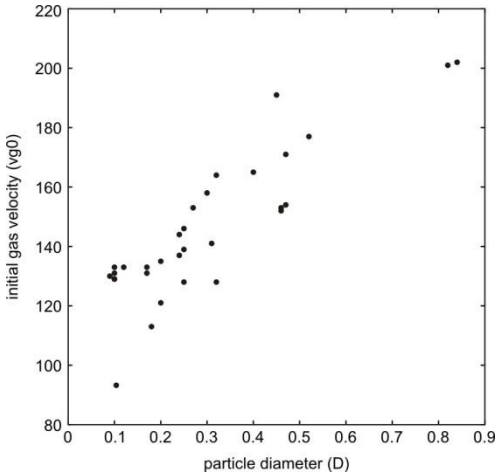

Figure V.13. Relationship found between particle diameter and initial gas velocity for the inversions performed with the ballistic model operating in 2D, and with monodisperse particle size distribution.

V.3.1.1.2. Projections in 3D, with polydisperse particles

Figure V.14 shows the results of an inversion in which polydisperse particles were ejected in 3D. The diameter range was fixed from 5 mm to 50 cm, with 10 diameters taken uniformly within this range. (Note however that at this stage, because we were still interested in matching the shape of the radargram rather than its absolute power values, the displayed powers are in arbitrary units and do not reflect the true backscattered powers which would be obtained from such diameter range). The inversion procedure then searched for the best distribution of angles in 3D (i.e. α_{min}, α_{ap}, and α_{nb} in both the horizontal and vertical planes, see Figure IV.5 in Chapter IV), and for the best initial gas velocity value (V_{g0}).

Figure V.14a shows that the modeled signal (in blue) tends to match the durations of the observed signal (in red) better than what was achieved with the previous 2D monodisperse inversion runs (Figure V.12 and Figure V.13). This is due to the increased number of particle sizes used, which implies a wider range of particle motion and subsequent radial velocity / residence time in the gates. Moreover, we notice that because of the increased number of particles transiting within the 3D beam, the relative power distribution within the radargram exhibits more realistic transition than in the previous 2D runs. Importantly, the ejection cone is orientated towards the radar, which is in agreement with the previous inversion results.

Notice however that the radargrams (i) exhibit isolated streaks departing from the overall signal shape, and (ii) exhibit slightly overestimated onset radial velocities in gate 2607 m located directly above the vent: this results from the fact that the particle size range is fixed, and include in particular fine particles (5 mm) whose ballistic trajectories denote from the rest of the particles (see section IV.1.3.3 for further details).

These results are encouraging, as they show that ballistic projections in 3D with polydispersed particles can be used in the inversion procedure, and can improve certain aspects in the match of the radargrams (i.e. velocity range, duration, and power distribution within the radargrams in particular). Henceforth at this stage, the inversions are able to give insights into the eruptive jet geometry by matching the shape of the radargram, but are still unable to give precise constraints on the particle loading (i.e. exact sizes and number) since the absolute backscattered power is not matched. In the following section, we present some of the preliminary results obtained in that aim.

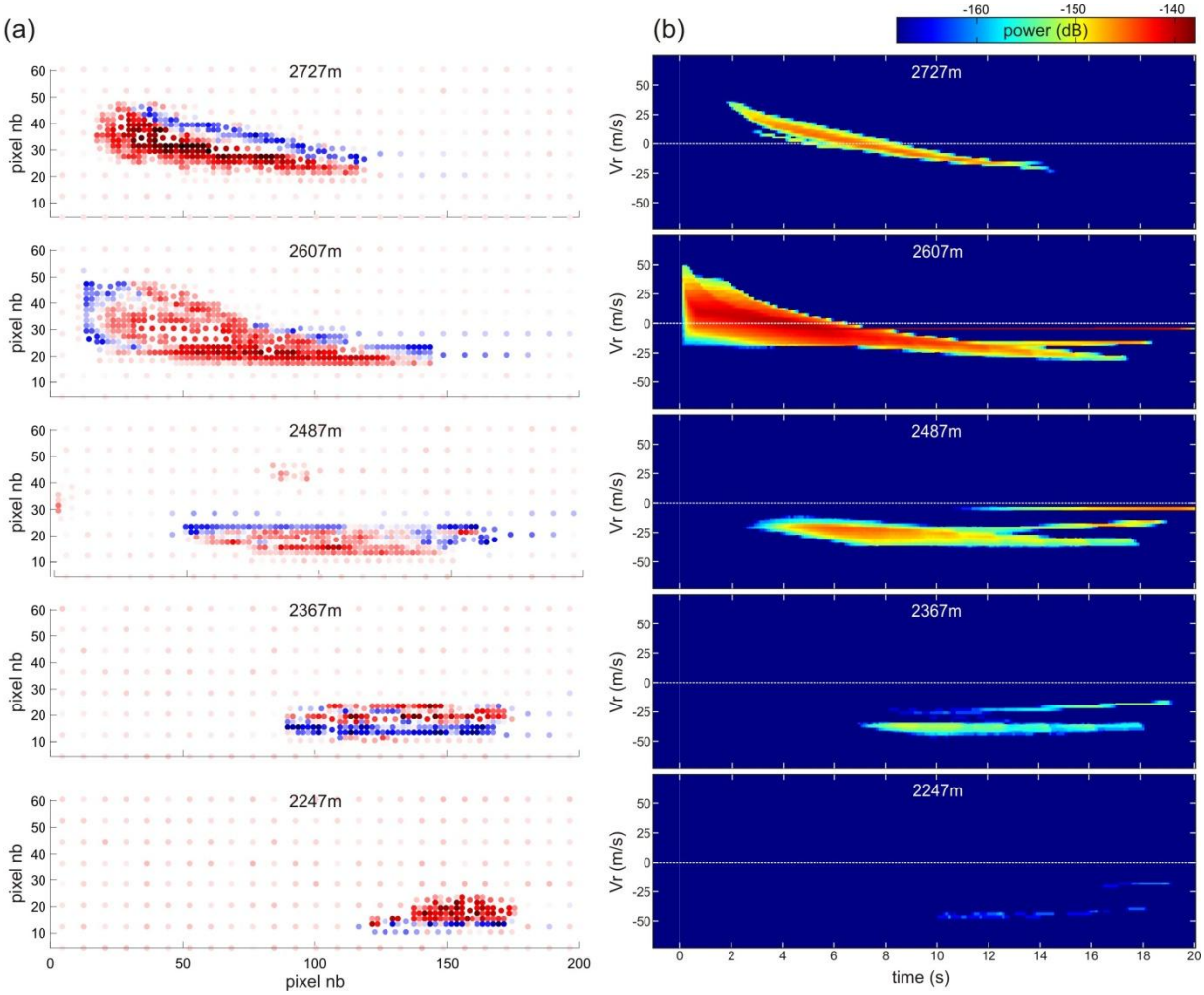

Figure V.14. Inversion run with polydisperse particles ejected in 3D. (a) Residue plot: blue dots are the modeleled data, red dots are the observed radargram; units are in pixels. (b) Synthetic best-fit radargram.

V.3.1.2. Matching the true backscattered power

In order to match the true backscattered power, the recorded radargram must be converted from arbitrary units (dB) to absolute units (dBmW), using VOLDORAD's conversion constant (C_{conv}). This constant is obtained from laboratory measurements, where a frequency

generator transmits an electromagnetic signal of known power (in mW) into the radar receiver. The power which is retrieved by the radar at the output of the whole acquisition line is then compared to the injected power. The conversion constant is then derived from the ratio of injected power to the power at the output of the acquisition line. For the recording campaign at Arenal in 2004 and 2005, the constant was found to be $C_{conv} = 3.67 \cdot 10^{-22}$.

Each pixel of the radargram is first converted from dB unit to decimal units ($P_{decim}=10^{(PdB/10)}$), afterwhat the value is multiplied by the conversion constant ($C_{conv} = 3.67 \cdot 10^{-22}$) to obtain a value in mW. This value is finally set back to decibel units (dBmW) for visualization purposes ($P_{dBmW} = 10 \cdot \log_{10}[P_{mW}]$). The resulting radargram is shown in Figure V.15 (where only gate 2607 m is displayed). The mean noise value in the radargram (ca. -130 dBmW), was then used as the "noise" value in the modeled radargrams, i.e. the pixels which do not have power values (because no particle have the considered radial velocity at the considered time).

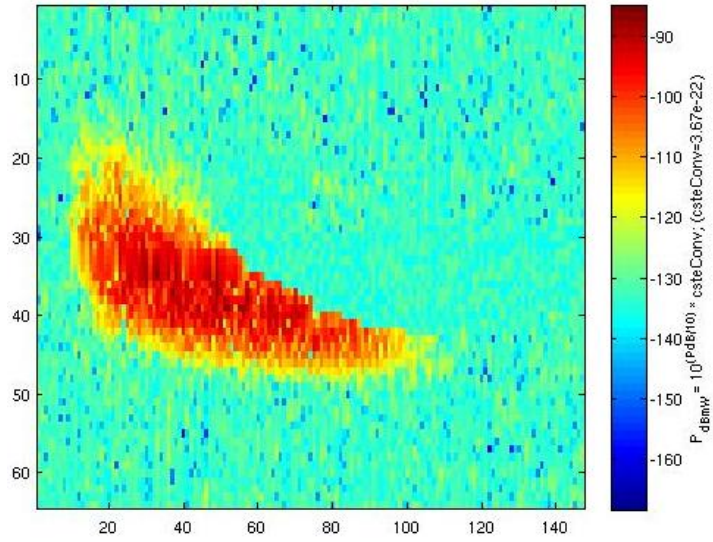

Figure V.15. Radargram of gate 2607 m with power values expressed in dBmW, using the radar conversion constant C_{conv}. Axis units refer to the pixels counted from the top left corner of the radargram.

We hereafter present the results from an inversion run, which attempted to match both the time-velocity distribution of the power (i.e. shape of the radargram), and absolute power values (expressed in dBmW). The following parameters were searched for during the inversion procedure: the 4 parameters controlling the ejection angle distribution in 3D (i.e. α_{min}, α_{ap}, and α_{nb} in both the horizontal and vertical planes, see Figure IV.5), the 3 parameters controlling the particle size distribution (i.e. Weibull's scale factor k, shift factor Λ, and scale factor N_{max}, see Figure IV.7), and the initial gas velocity (V_{g0}). The particle size range was fixed to between 0.01 and 0.5 m, with 10 diameters to be chosen within this range.

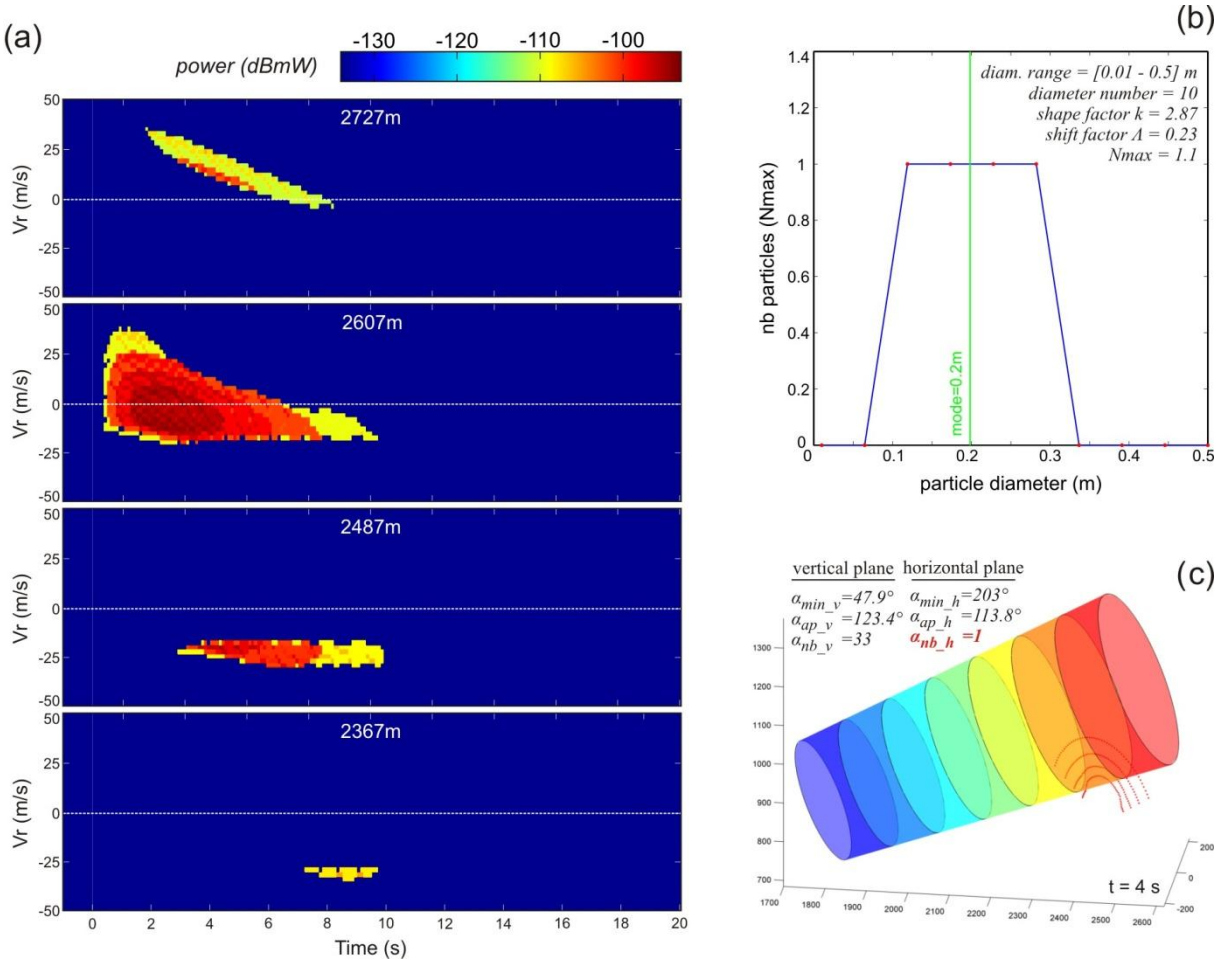

Figure V.16. Inversion run which attempted to match both the shape of the radargram, and the absolute values (dBmW) within it.

The inversion succeeded in matching the absolute power values, since the modeled radargram (Figure V.16a) exhibits the same power range as the reference radargram (Figure V.15). However, both the ejection angle distribution and the particle size distribution of the best-fit model are rather unexpected. Indeed, the particle size distribution (Figure V.16b) shows a maximum value of 1, i.e. the lowest value the N_{max} parameter could take (with a shape factor k = 2.87, i.e. nearly Gaussian). The ejection angle distribution on the other hand, was found to converge towards a 2D trajectory (Figure V.16c), i.e. selecting α_{nb_h} = 1 (number of angles in the horizontal plane), the lowest value this parameter could take. It thus appears as if the inversion procedure converged towards the model which would eject the minimum number of particles possible (to match the power), while reproducing the best it could the shape of radargram. This suggests that in the present state, the forward model causes the particles to backscatter too much power than it should.

Unfortunately we have not yet found a solution to this problem, which is still the subject of ongoing work. The perspectives however are very promising, as inverting the full information

a Doppler radargram holds (i.e. power and velocity distribution through time) can give powerful constraints on the particle size distribution (i.e. shape, amplitude and range) and the subsequent ejected mass load (in kilograms if a mean particle density is defined) notably.

V.3.1.3. Summary of what has been learned from inverse modeling of ballistics' Doppler signature

At this stage, the inversion runs which have been performed on the case eruptive event recorded on February 19, 2004 (20:00:30 UTC) allow us to provide confident constraints on the geometry of the eruptive jet, which appears slightly inclined towards the radar (ca. 10 ° from the vertical). Particles are likely to have reached about 245 m above the vent, and nearly 500 m to the West of it (entering up to 3 range gates down-beam from the vent, i.e. gates 2247 to 2487 m). The eruptive vent was likely positioned about 2484 m above the radar and 864 m away from it, hence below gate 2607 m and slightly towards gate 2727 m. The particle size distribution and subsequent gas velocities on the other hand are still loosely constrained: the particle size mode is likely in the range 0.1 – 0.5 m (consistent with the expected size of bloc at Arenal, see section III.3.5.4), and the source gas velocities in the range 130 – 170 m/s, which infers ejection velocities at the vent in the range of 65 – 85 m/s (from equation IV.1). More stringent constrains on the particle size distribution (i.e. precise shape, amplitude, and range) will be possible with the inversion of the absolute backscattered power, which is subject of ongoing work.

V.3.2. Inversion of the plume's Doppler signature

Because the studied event (19 February 2004, 20:00:30 UTC) exhibits the signal of both the ballistics and the ash plume, we have also intended to invert the plume's Doppler signature. However, because the plume model developed in section IV.2 is very simple (i.e. no sedimentation nor internal turbulences involved), the potential outcomes and instructions from the inversion of the plume's Doppler signature are lesser than for that of the ballistics' signature. Still, we present hereafter some preliminary results.

Figure V.17 shows the result of an inversion which attempted to match the duration of the signal in each range gate by inverting the source radius (R_0) of the plume, as well as the wind speed (W_s) and azimuth (W_a). The plume entrainment coefficient (ε) was set to 0.25 and its shape factor (m) to 3, which are defined for spheroidal discrete thermals (*Turner*, 1979). The power values from the radargrams were normalized between 0-1, and the radargrams were subsampled with a quadtree filter. The best-fit model reproduces fairly well the signal onset and life span of the observed radargrams in each range gate (Figure V.17a). The slight underestimations may likely result from the fact that the modeled plume is released instantaneously, whereas the real plume emission may have lasted a few seconds. The velocity range however is not well reproduced: the synthetic radargrams appear as very narrow streaks whereas the observed radargrams exhibit a wider range of velocities staggered between 0 m/s and -15 m/s (see Figure III.4 in Chapter III for details). As pointed out in section IV.2, this is due to the simplicity of the forward model, which does not account for internal turbulences, sedimentation, etc… Figure V.17b shows that the wind speed is a very discriminative parameter, as only a very narrow range of values gives low misfit values. Contrastingly, the plume azimuth and the source radius are less discriminative, as it appears that several combinations of values can render similar misfit values (this explains why the inversion does not converge towards a unique parameter value like it should be the case, e.g. Figure V.10). It is likely however that this could be improved, especially with *ad hoc* radargram subsampling and power normalizations.

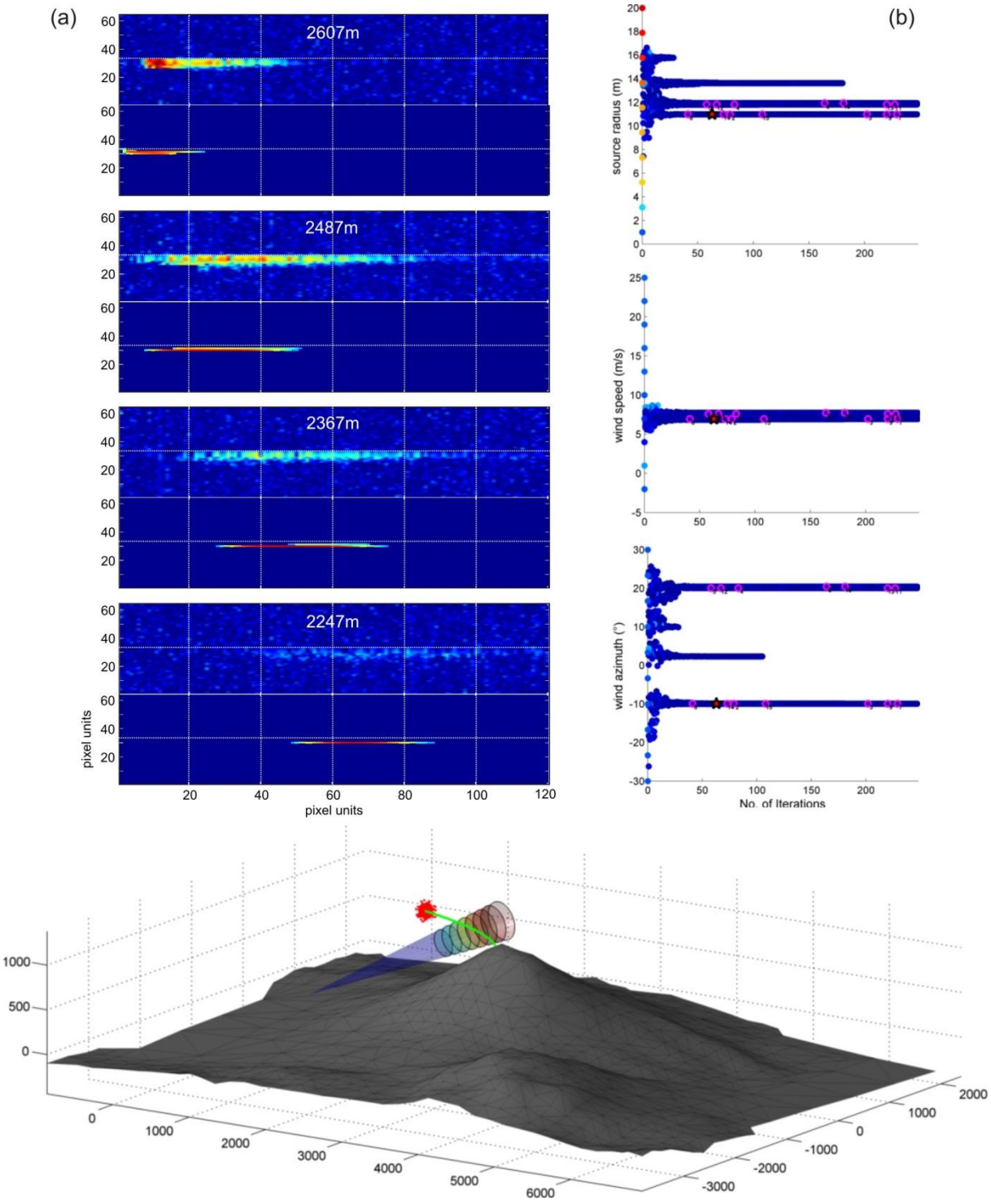

Figure V.17. Inversion run attempting to reproduce the plume Doppler signature of the eruptive event recorded on February 19, 2004 (a). The source radius, wind speed and wind azimuth are searched for by the inversion procedure (b). The plume entrainment coefficient and shape factor are set to 0.25 and 3 respectively (i.e. values defined for spheroidal discrete thermals, Turner, 1979).

Although both the inversion parameterization and the plume model could be improved, the results even at this stage are insightful. In particular, it appears that the spatio-temporal characteristics of the ash plume's Doppler signature (i.e. onset timing and gates of appearance) are strongly controlled by the wind speed. Moreover, the results suggest that the

ash plumes emitted during such transient events at Arenal can adequately be simulated as buoyant thermals, powered by buoyancy and drifted by trade winds. The emission duration is likely to last a few seconds, as the simulated plume (instantaneous release) generates signals whose life-spans underestimate the observed ones. The radial velocities on the other hand are not well reproduced, suggesting that an expanding plume drifted by winds cannot account for the full range of velocities observed (-15 – 0 m/s). We suspect that sedimentation of particles is likely to be the main factor responsible for this range of velocities, and should consequently be implemented into the plume model in the future.

Lastly, the ability to constrain the wind speed with high precision (+/– 5% error) at the actual plume height is particularly valuable, especially for the estimation of SO_2 fluxes from DOAS instruments for which uncertainties on the plume velocity constitute the main source of error in gas flux estimates (e.g. *Gerlach et al.*, 1997; *McGonigle et al.*, 2005).

V.4. Conclusion

Inverse modeling using a Monte Carlo procedure with a near-neighborhood search algorithm was used to find the synthetic Doppler radargrams which best matched the observed ones. Using a representative eruptive event recorded at Arenal on February 19, 2004 (20:00:30 UTC), we intended to inverse independently the Doppler signature of the ballistic particles and the ash plume to gain insights into the eruptive characteristics.

At this stage, we are able to reproduce the shape of the radargrams resulting from the transit of the ballistics within the radar beam. In doing so, we give confident constraints on the eruptive jet geometry, which appeared slightly inclined to the West (~10° from the vertical), ~30-35° in aperture, ejecting particles up to ~245 m above the vent and up to ~500 m to the West. Moreover, we are able to constrain the position of the vent with respect to the radar. The particle size distribution and associated gas velocities however are loosely constrained, between 0.1 – 0.5 m for the mean particle size and between 130 – 170 m/s for the initial gas velocities, which would infer ejection velocities at the vent in the range of 65 – 85 m/s. Additional constraints will be possible with the inversion of the absolute backscattered power (in dBmW), which is still the subject of ongoing work. In particular, this will allow the possibility to define a precise particle size distribution (i.e. shape, amplitude and range, see section IV.1.2.3), and in turn give a precise estimate of the ejected mass load (provided a mean particle density is defined).
Inversion of the ash plume Doppler signature on the other hand showed that the wind speed controlled for the most part the onset and lifespan of the signal, and could be confidently estimated to ~7 m/s. The Doppler velocities however are not well reproduced, most likely because sedimentation of the particles are not taken into account in the plume model.

Future work will aim towards the ability to carry out the "appraisal" of the inversion procedure (*Sambridge*, 1999b), which gives a probabilistic view of the inverted parameter values.

Chapter VI

Operational monitoring of pyroclastic emissions

VI.1. Introduction

In the first section of the manuscript, we have investigated the *source conditions* of pyroclastic emissions by cross-analysis of seismic and radar data (Chapter II). In the second section, we have focused on the *dynamics of the emissions*, by simulating their projection and reconstructing their synthetic radar signals (Chapter III to Chapter V). In this last section, we progress higher up (figuratively speaking), to consider the *monitoring of the emissions*, from the vent to their dispersal downwind.

The chapter is threefold. The first part shows how determination of the 3D transport vector of wind-drifted ash plumes can be made, using both the transit times through the range gates and simple geometric shapes to simulate the plume path (results published in *Geophysical Research Letters* as *Donnadieu, Valade & Moune*, 2011). The second part discusses some results from two years of monitoring of VOLDORAD 2B on the flanks of Mt. Etna, and the challenges which arise to provide real-time notifications on tephra emissions (*Natural Hazards*, *Donnadieu et al.*, in prep). The third and last part, highlights how the integration of ground-based and satellite-based sensors (e.g. Doppler radar, infrared cameras, and MSG's SEVIRI sensor) can complement each other to provide a powerful observational suite of tools, capable of tracking the eruptive event at different spatial resolutions. We particularly emphasize on the interaction between the Doppler radar and the ground-based infrared cameras (stored in the same shelter at Mt. Etna), and thus provide supplementary material to the recently published *Gouhier et al.*, 2011 (*Bulletin of Volcanology*).

VI.2. Ash plume transport speed retrieval

We have previously shown that inverse modeling of Doppler radargrams enables us to retrieve information on the dynamics of tephra emission. In particular, inversion of the ash plume signature observed in Doppler radargrams can tell us about the wind speed at the time of the eruptive event, as well as the most likely plume trajectory through the radar beam. Nevertheless, this inversion process is long and consequently not well suited for situations of volcanic crisis, which require rapid response and near real-time observations to share with the authorities.

In the following section, we show how determination of the 3D transport vector of wind-drifted ash plumes can be made, using both the transit times through the range gates and simple geometric shapes to simulate the plume path. The method, results, and potential applications are published in *Geophysical Research Letters* by *Donnadieu, Valade, & Moune,* 2011), appendix F. My main contribution to this publication has been the simulation of the ash plume transit path using simple geometrical shapes, and the determination of the intersection volumes between this presumed path and the radar beam.

This enabled us to: (i) assess how a plume exiting the beam influences the radar signals, and (ii) constrain the plume trajectory. The method is detailed below, after we recall how the 3D transport vector was retrieved (i.e. *Donnadieu et al.,* 2011), and what the potential applications this may have for volcano monitoring.

Geophysical Research Letters

Three dimensional transport speed of wind-drifted ash plumes using ground-based radar

Franck Donnadieu, Sébastien Valade, Séverine Moune

Received 21 July 2011; revised 31 August 2011; accepted 31 August 2011; published 27 September 2011.

VI.2.1. Simulation of ash plume transit path

When an ash plume gets drifted towards the radar, it enters successive range gates probed by the radar and echoes from backscattering particles are recorded. The power echoes within these gates typically decrease in amplitude with the distance from the emission source (Figure VI.1). In order to evaluate the contribution that plume exiting the beam may have on this

power decrease, we have computed the intersection volumes between the range gates and various geometrical shapes which simulated the plume transit path.

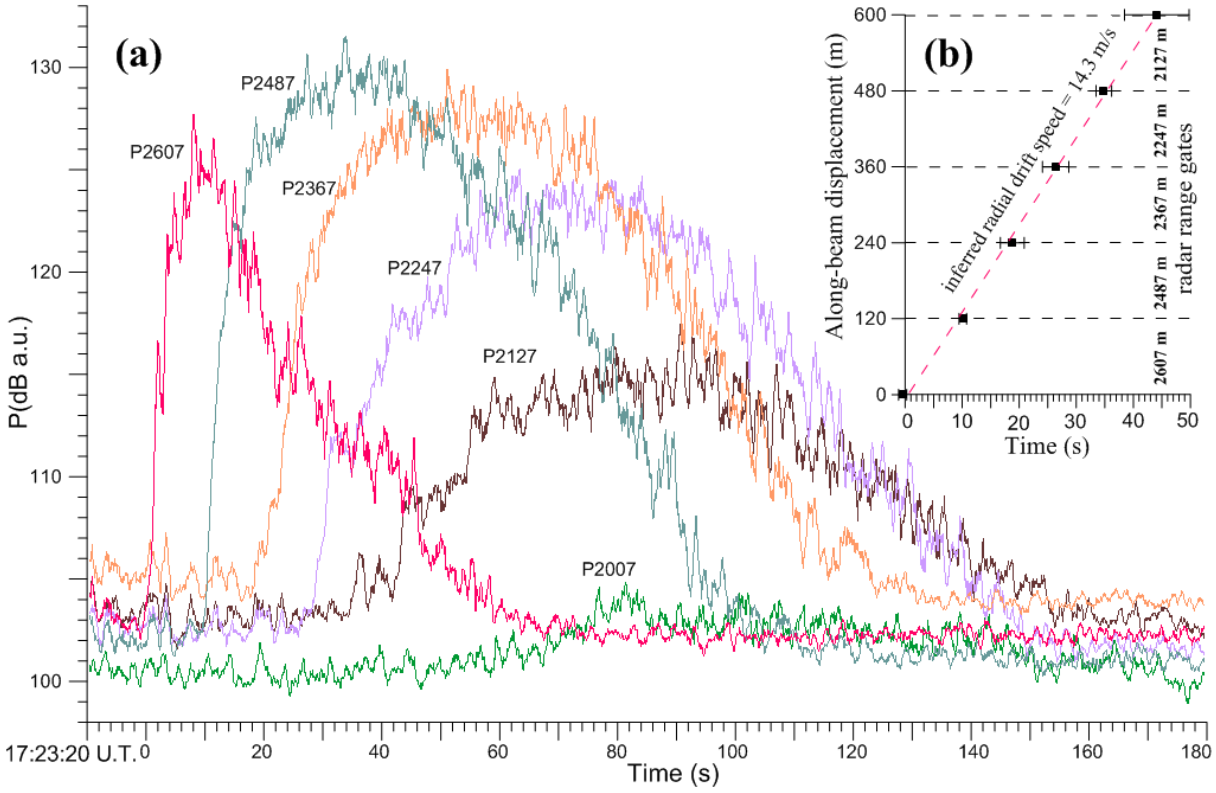

Figure VI.1. (a) Power amplitude (dB Log scale, arbitrary units) recorded as the wind-advected ash plume crosses 6 successive beam volumes probed by the radar (Arenal, 11/02/2005, 17:23'20 UTC). (b) Onset times of ash plume detection in each range gate (120 m radial resolution). The slope of the linear data fit gives the along-beam component of the ash plume transport speed (14.3 m/s, R^2=0.99). From Donnadieu et al. (2011).

Because of the wide variety of shapes and orientations which needed to be tested to simulate the plume transit, we used a software capable of manipulating objects and computing intersection volumes in 3D. *Blender* is a free, open-source, 3D computer graphics software, commonly used for creating animated films. We found it well suited for our purposes for several reasons: (i) it allows the user to generate complex shapes and handles them fairly easily, (ii) it contains built-in functions which enable the creation of new objects resulting from the intersection of several others, and (iii) it enables the use of external scripts (*Python* programming language), allowing personalized mathematical operations to be carried on objects. In particular, we have implemented a script to compute the volume of the intersection objects, which result from the intersection between the conical radar beam (and more specifically the individual range gates), and the various geometric shapes simulating the plume path. Below, we summarize the main steps of the methodology.

1) Create the radar beam and its range gates with realistic sizes and inclination

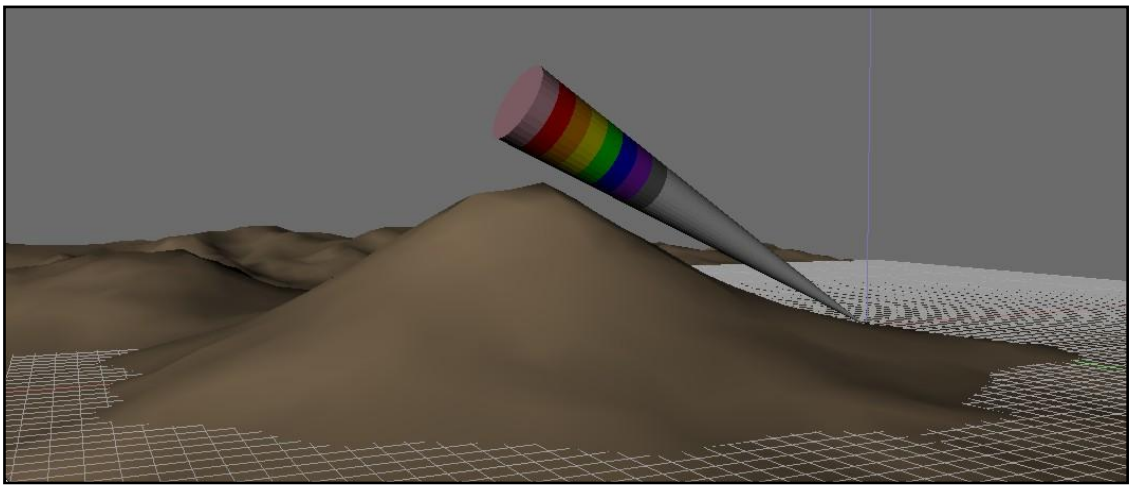

Figure VI.2. Radar beam geometry created with Blender. The radar beam dimensions and inclination are set to be realistic (e.g. beam aperture = 9°, beam inclination = 25°, gate depth = 120 m).

The sounding geometry is first created, with a radar beam set to have realistic dimensions (9° aperture) and inclination (25°). Within this conical beam the range gates are individualized, and set to have the appropriate size (i.e. 120 m slant-wise) and the appropriate distance from the radar (e.g. 2607 m for the gate considered above the vent).

2) Create various geometrical shapes to simulate the plume transit path

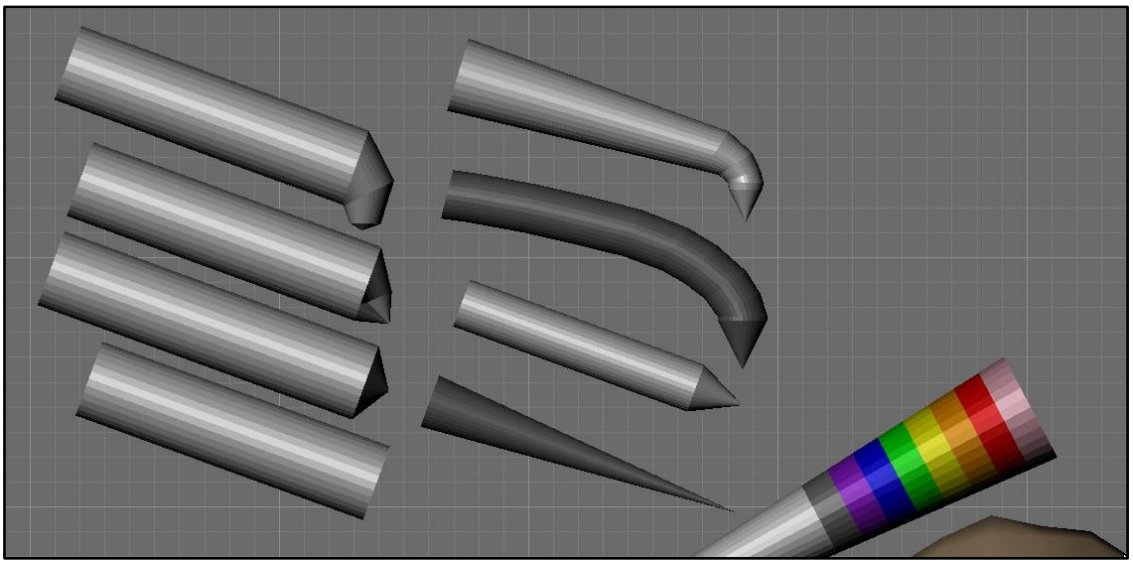

Figure VI.3. Plume transit paths simulated with various geometrical shapes. (These are positioned to the left of the beam for visualization purposes, but are in fact meant to intersect the beam).

Various shapes have been created to simulate the plume transit path. These range from simple cylinders, to more complex, bended funnel shapes. These were then positioned and orientated to intersect the radar beam in a variety of ways.

3) Generate intersection volumes between transit path and range gates

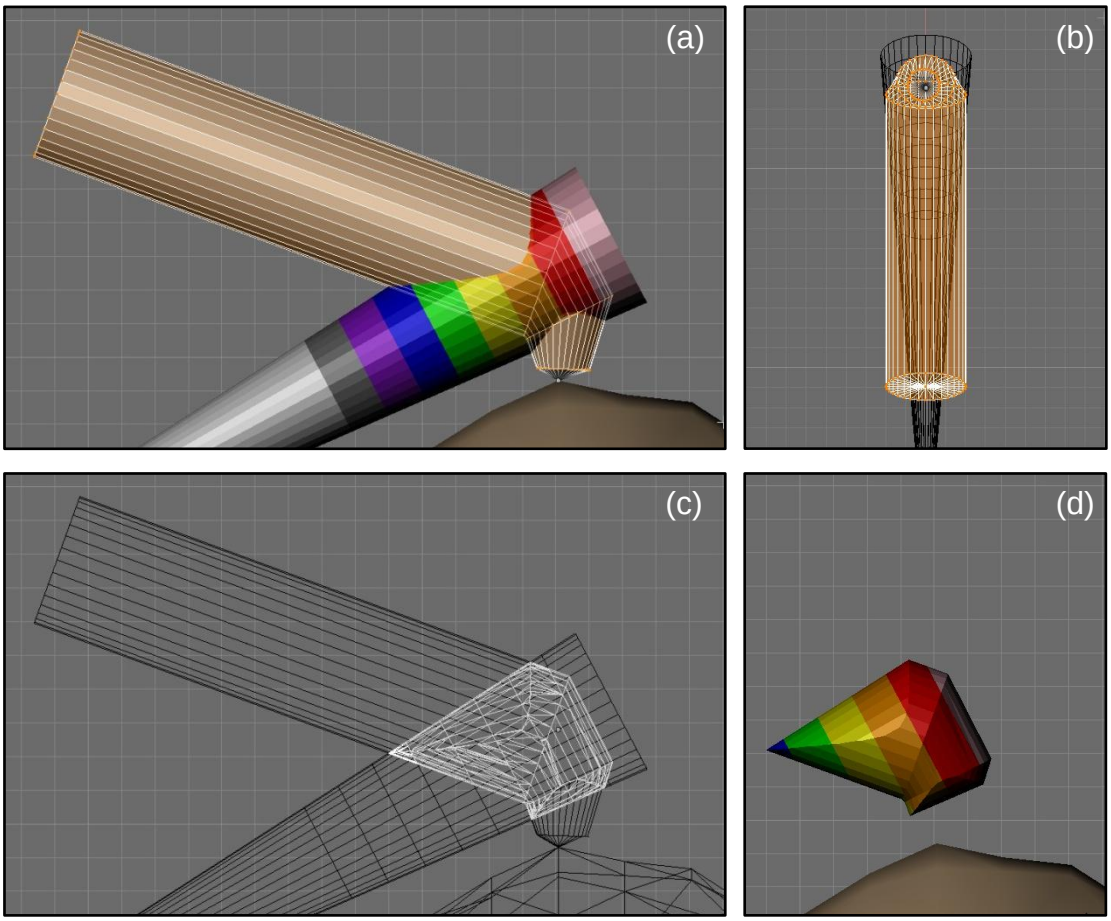

Figure VI.4. Simulated plume path and radar beam viewed in both cross section (a) and aerial view (b), and the resulting intersection volumes with each range gate (c, d).

Once the shape simulating the plume transit path has been created and positioned, the intersection volumes between the path shape and the radar beam were generated (bottom right plot), using a built-in function of *Blender*.

4) Compute intersection volume

The computation of the intersection volumes in each gate (e.g. lower left plot in Figure VI.4) was done using a *Python*-coded script, called from *Blender*'s interface. The script sums the signed volumes of tetrahedrons, which are formed by the triangular mesh's faces and the space origin. The volumes are signed depending on the orientation of the face normal. In doing so, the actual object's volume may be obtained.

We've tested the accuracy of the method, by comparing the intersection volume of two cones, which was computed both analytically (*Beyer et al.*, 1987) and with this method. The result obtained with this method was found with 99.2% accuracy, proving its efficiency for our

purposes. Note that because the radar sounding conditions created with *Blender* are set with realistic units, the created volumes also have realistic units (in m^3).

5) Compare intersection volumes with observed power amplitudes

By assuming comparable particle concentrations and sizes among the range gates, and compensating for the effect of distance on the radar signal amplitude, the relative variations of the intersection volumes between the beam range gates and the plume are equivalent to relative variations in echo power. Values are thus normalized to the intersection volume of the 2487 m range gate, having the maximum amplitude (most filled), and compared to the normalized radar power amplitudes of the successive range gates downwind. Since our objective is to simulate the plume path once it is bent over, the beam filling by the plume in the range gates above the vent and upwind (i.e. 2607 m and 2727 m) is not considered.

In Figure VI.5, all the tested simulations are plotted (black curves, comprising a wide variety of transit shapes and orientations, see Figure VI.3), and compared to the observed radar power amplitudes (red curve, values from Figure VI.1). The evaluation of the simulation quality is done by a least-square between the simulation curve and the data curve. The resulting value is a measure of the discrepancy between the two curves: the best simulation (i.e. smallest discrepancy) is represented by the green curve, the worst by the blue.

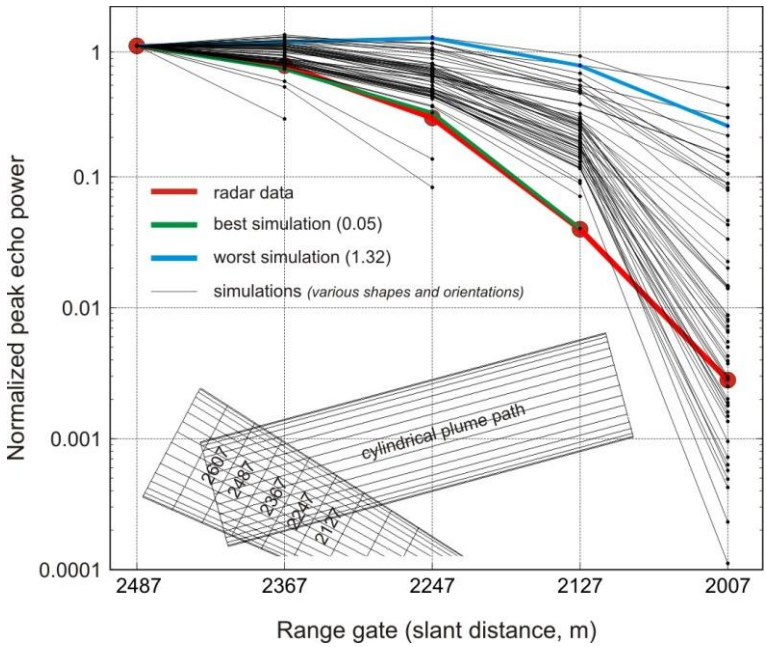

Figure VI.5. Normalized peak echo power from radar range gates crossed by the plume (distance corrected). Red curve is the radar data which recorded an ash plume at Arenal on February 11 2005, at 17:23 UTC (Figure VI.1). Black curves are the various simulations, comprising various plume path shapes, azimuth and elevation angles. The simulation quality (i.e. discrepancy between the simulation curve and the radar data) is evaluated using a least-square value: the blue shows the worst simulation, and the green shows the best. A section of the best-fit is shown as an inset (cylindrical shape, azimuth angle $\alpha = 0°$, inclination angle $\beta = 15°$).

The best simulation uses a cylindrical plume path, with an azimuth angle α = 0° and an inclination angle β = 15°. The diameter of the cylinder (400 m) was chosen in agreement with common values observed for ash plumes at Arenal, and the cylinder's lowest point was set just below the intersection between gates 2607 m and 2487 m. The good agreement between the simulation and the data suggests that the decrease in power amplitude within the first few hundred meters from the vent is dominantly controlled by the progressive exit of drifted ash from the probed volumes, rather than by particle fallout. However since a cylindrical shape does not reproduce plume bending, the modeled plume exits the beam without intersecting the farthest range gates (2007 m). Nevertheless, because the plume and beam intersection volumes decrease dramatically downwind with increasing values of α and β, the plume azimuth and upraise angles can be well constrained. In turn, these are used to obtain the three-dimensional transport speed of the ash cloud, as discussed below (see also *Donnadieu et al.*, 2011, appendix F).

Although more sophisticated shapes (accounting for more realistic plume bending, or plume shape in gates up the vent for example) could provide better matches, simulations using cylindrical shapes are more widely applicable for monitoring purposes because they are quicker to fit.

In the future, such simulations could be implemented into an inversion procedure to test automatically a wide range of plume path geometries and orientations, and find the best match to the data. Also, it would be possible to compare the plots of radial displacements versus gate onset timing, from both the observed data (e.g. Figure VI.1b) and modeled data (e.g. Figure IV.27e from *eject3D*). This latter point could be easily done as the inversion procedure are already in operation with *eject3D* (*nasearch* inversion algorithm, see section V.2.1.3).

VI.2.2. Three dimensional transport speed of wind-drifted ash plumes

The simulation of the ash plume transit path described above, enabled the constrain of the azimuth and inclination angles of the plume path (α and β respectively, Figure VI.6).

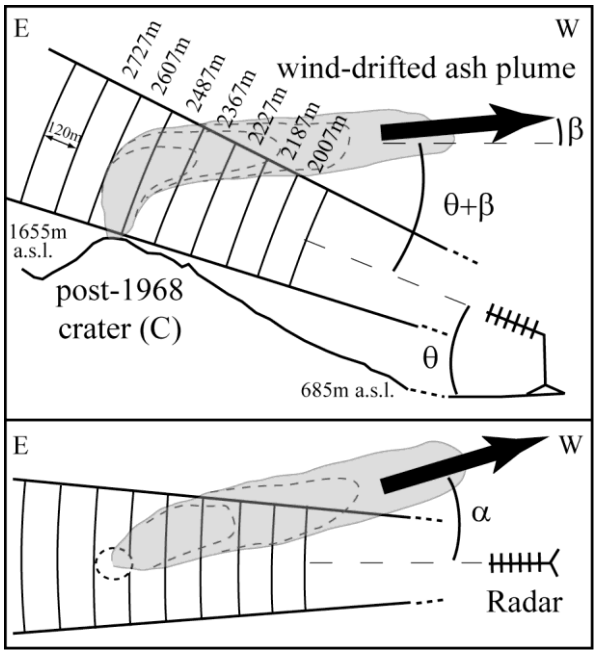

Figure VI.6. Schematic view of the ash plume path's azimuth (α) and inclination (β) angles, seen in lateral view (top) and aerial view (bottom). From Donnadieu et al., 2011.

These angles, along with the plume transit time Δt in the successive range gates (interval between signal onsets), may then be used to obtain the three-dimensional transport speed of the ash cloud u_{ash}. As discussed by *Donnadieu et al.* (2011), u_{ash}.may be formulated as:

$$u_{ash} = \frac{c\tau}{2\Delta t} \times \frac{1}{\cos(\theta+\beta)\cos\alpha} \qquad \text{VI.1}$$

where $c\tau/2$ is the range gate radial resolution, θ the beam elevation angle (27°), β and α the ash cloud elevation and azimuth angles respectively (Figure VI.6).

The first term $c\tau/2\Delta t$ in equation (VI.1) represents the radial (along-beam) speed component of the drifted ash. Its average value can be obtained from the slope of the radial displacements versus the power onset times in the successive range gates (Figure VI.1b). Indeed, the displacements with time commonly follow a linear trend, indicating of a constant transport velocity (which suggests that buoyancy and wind entrainment take over momentum within a few seconds, ca. <10 s). For the event considered here, we determine an along-beam speed component of 14.3 m/s.

Finally, using the above equation with $\alpha = 0°$, $\beta = 15°$ (determined from plume path simulations, Figure VI.5), and $c\tau/2\Delta t$ = 14.3 m/s (Figure VI.1b), the three dimensional transport speed of the considered event (Figure VI.1) may be estimated to 19.2 m/s.

VI.2.3. Potential applications

Determination of the transport speed of volcanic ash plume may be very useful in several aspects. Below, we emphasize two potential applications we consider the most noteworthy.

VI.2.3.1. Implications for gas flux measurements

Ground-based measurements of volcanic SO_2 fluxes by remote spectroscopy have received an increasing attention from the volcanological community in the recent years. The reason for this is that SO_2 fluxes are important indicators of volcanic activity, which can also be used to determine fluxes of other volcanic gas species (*Gerlach et al.*, 1997). Miniature UV spectrometers (e.g. DOAS, FLYSPEC, *Galle et al.*, 2002; *Horton et al.*, 2006) in particular, have recently been used to remotely sense SO_2 emissions. The measures however, require precise knowledge of the plume velocities to accurately calculate gas emission rates. Unfortunately, wind speed at plume altitude can differ significantly from that measured on the ground (e.g. *Archer and Jacobsson*, 2003), and can in turn introduce large errors in the gas estimates (potentially >100 %; *McGonigle et al.*, 2005). The determination of the plume velocity thus appears of prime interest. Using the method described above, the lateral transport speed of ash plumes can now be determined, and could help to reduce errors on gas fluxes down to a few percents. Moreover, estimation of the plume ash-loading might also help to quantify the errors on gas measurements due to the UV absorption by ash (e.g. *Andres and Schmidt*, 2001).

VI.2.3.2. Implications for mass flux measurements

Estimation of the eruptive mass flux ejected into the atmosphere is another important outcome made possible with the described methodology. This type of information is of crucial need for the Volcanic Ash Transport Models (VATD) used by the Volcanic Ash Advisory Centers (VAAC), to forecast the ash propagation downwind and assess the potential hazards to human health and aviation safety (*Zehner*, 2010). The procedure to retrieve the mass flux would be twofold: (i) convert the power time series into mass curves (using the inversion algorithms

from *Gouhier and Donnadieu,* 2008), and (ii), knowing the plume's transport speed and transit time through the beam, integrate the mass curve through time to obtain the mass flux.

VI.3. Automated tephra emission alerts at Mt. Etna

The following section discusses the recent installation of VOLDORAD 2B on the flanks of Mt. Etna, and the challenges which arise to provide real-time notifications on tephra emissions. Some elements of the discussion provided below are part of a publication in preparation for *Natural Hazards Earth Sci. Syst.*, by F. Donnadieu and coauthors, entitled "*A new ground-based Doppler radar system to monitor the volcanic activity of Etna*".

VI.3.1. VOLDORAD monitoring Etna's activity: challenges

Following the first successful recording campaigns in 1998 with the radar prototype VOLDORAD 1 (*Dubosclard et al.,* 1999, 2004) and in 2001 with the compacted radar VOLDORAD 2 (*Donnadieu et al.,* 2003, 2005), a duplicate of the latter has been ordered by the INGV (*Istituto Nazionale di Geofisica e Vulcanologia*) through a research contract, in order to monitor permanently the volcano's explosive activity. We have installed this surveillance radar (VOLDORAD 2B) in July 2009 in a shelter located at La Montagnola, approximately 3 km South from Etna's summit craters, at an altitude of 2610 m above seal level. From this location the radar sounds a conical beam 9°-wide, pointing N342°E and looking at an upward angle of 14° (Figure VI.7). Data are acquired at 0.23 s^{-1}, in 11 range gates of 150 m-deep each, so that the field of view is a 1.65 km-deep sector above the summit craters (*Donnadieu et al.,* 2009). The data are transferred in real-time by WIFI transmission to the operational center in Catania (Sicily), from where it is shared by FTP with the OPGC (*Observatoire Physique du Globe de Clermont-Ferrand*, France), and exploited jointly in the frame of a collaborative research agreement (Figure VI.8). See the VOLDORAD website for more details and real-time data (http://wwwobs.univ-bpclermont.fr/SO/televolc/voldorad/).

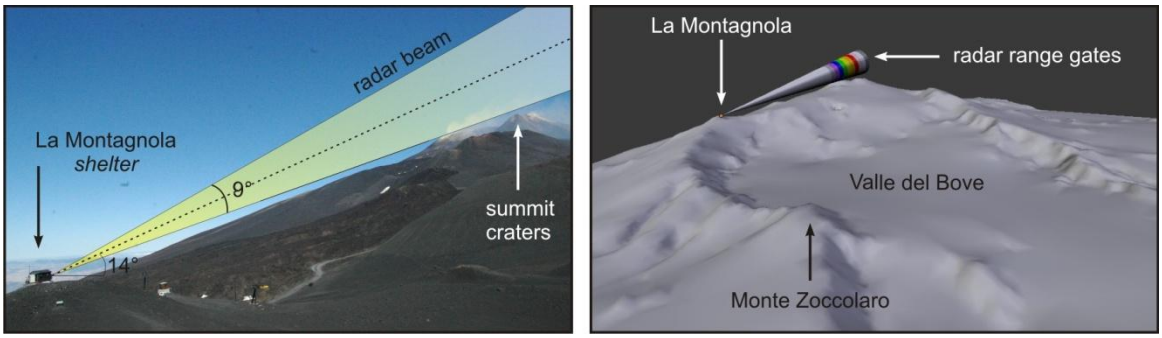

Figure VI.7. VOLDORAD 2B, installed in a shelter located La Montagnola (2610 m a.s.l). The radar 9°-aperture beam, probes a 1.65 km deep sector above the summit craters (3330 m a.s.l).

At present, despite adverse conditions at 2610 m a.s.l. on the volcano, continuous acquisition of data is ensured by: (i) a tension regulator with batteries to prevents shortcomings of short electricity interruptions, (ii) an automatic restart of the radar system (PC, two units of the radar, data acquisition software, and radar power), (iii) a heating system inside the shelter, (iv) a radome for protection of the antenna, (v) an anti-icing system of the northern panel of the shelter hosting the window for video observations and the radar antenna.

This provides an exceptional opportunity to use VOLDORAD within an operational monitoring network, destined for the real-time surveillance and activity alert of one of Europe's most active volcano. It also represents a great challenge for hazard mitigation issues, due to both the highly populated nearby areas (e.g. Catania's metropolitan area, ~750 000 inhabitants), and the intense regional air traffic (e.g. *Scollo et al.*, 2009). In turn, this calls for an efficient set of parameters, capable of providing unambiguous notifications when tephra emissions occur.

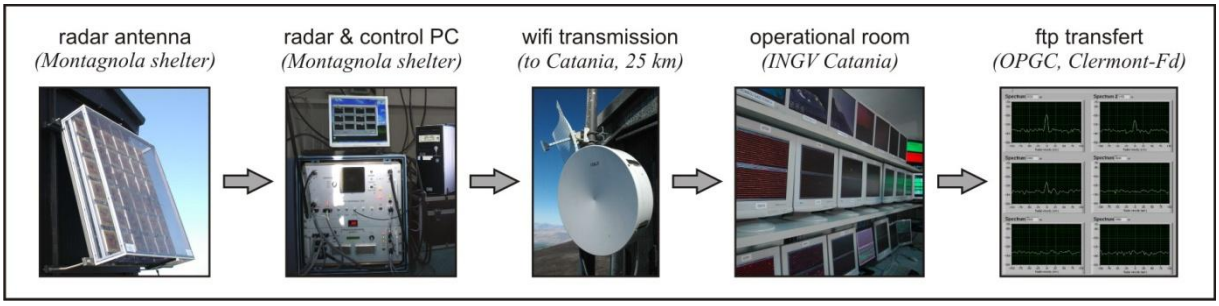

Figure VI.8. Operational diagram illustrating the successive steps the radar data goes through. The radar antenna (without its radome here), located on Etna's southern flank (La Montagnola), transmits an electromagnetic wave and receives the echoes backscattered by the particles in the beam. The radar then amplifies, filters, and digitizes the received signal, which appears in real-time as Doppler spectra on the control PC in the shelter. Data are stored on a server in the shelter. From there the data is transmitted by WIFI to INGV's operational room in Catania (Sicily). At last, they are transferred to the OPGC (Clermont-Ferrand, France) by FTP, and displayed every 2 min on its website (http://wwwobs.univ-bpclermont.fr/SO/televolc/voldorad/TRetna.php).

A real-time procedure for the radar detection of explosive activity was implemented by INGV in the context of the repeated eruptions from the new SE crater. The INGV detection procedure is mainly based on (i) a time series constructed from the power values of Doppler spectra at 3285m, with decreasing weight at increasing velocities, (ii) a STA/LTA algorithm searching for signal deviation from the background noise and indicating the onset time of the eruption, and (iii) the delivery of an automatic alert message by email. An automatic alert email is also sent upon detection of the end of the eruptive signal, so that data can then be quickly processed at OPGC and preliminary reports issued to INGV (cf. reports by Franck Donnadieu on VOLDORAD's website). We explore below some possibilities for future improvements in the radar detection and monitoring at Etna.

VI.3.2. Tephra emission alerts: requirements

The parameter (or set of parameters) destined to notify for tephra emissions should meet a number of requirements in order to be fully efficient:

- ability to discriminate eruptive signal from non-eruptive signal (e.g. rain fall),
- ability to display optimized signal-to-noise ratios,
- enable optimum spatial coverage (i.e. span all eruptive vents),
- enable optimum temporal coverage (i.e. acquisition rate, suited for both short events and long eruptions),
- provide a comprehensive display, suited for operational room monitoring screens,
- be as informative as possible but quickly and easily interpretable,
- give real-time notifications (i.e. excluding lengthy data processing procedures).

Fulfilling all of the above requirements is a very challenging task. Below, we succinctly describe the variability of eruptive events at Etna (e.g. multiple exit vents, variable intensity…), and assess how it can be accounted for to ensure the detection of all of the events by the radar.

VI.3.3. Radar data at Etna: implications for monitoring parameters

Since its installation in the summer of 2009, VOLDORAD 2B has successfully detected 44 tephra emissions (up until November 28, 2011). These however, show variability in terms of:

- eruptive vents/craters: leading to eruptive signal in different range gates,

- eruptive intensity and duration: leading to variable radar waveforms (in terms of impulsivity, duration, number of pulses, amplitudes in power and velocity),
- atmospheric conditions (trade winds) at the time of the eruption: leading to variable amounts of ash in the beam regardless of the real tephra-mass ejected, and to variable distribution of ash among the range gates.

We hereafter discuss and test which data processing seems the most relevant to guarantee the detection and alert of all eruptive events.

VI.3.3.1. Detecting eruptive events emitted from various vents

Four craters have been active at Etna over the past 2½ years (INGV bulletins): the new pit crater on the Southeast Crater's flank (new SEC), the Bocca Nuova (BN), the Voragine crater (VOR), and the Northeast Crater (NEC). Luckily, the radar beam covers the four vents, yet at variable radial distances. In turn, this calls for the need to monitor several gates, as ash can be expelled from all of the four vents.

The new Southeast Crater (SEC) is clearly the most active of the three vents, with 17 paroxysmal events recorded in the year 2011 (counted until November 15). The eruptive signal onset is recorded in gates 3135 and 3285 m, and during the peak of activity, the signal may enter gates 3435 and 3535 m. The Bocca Nuova (BV) on the other, although less active than the new SEC, has proved capable of ejecting strongly loaded ash plumes (e.g. on August 25, 2010, at 13:09 UTC). The signal onset is usually seen in gate 3735 m, and can overlap in gates 3585 or 3885 m (e.g. on December 22 and August 25, 2010, respectively). Finally, dilute ash emissions have been reported from the Northeast Crater (NEC) (e.g. November 15, 2010, at 06:30 UTC), as well as small explosions from the Voragine (VOR) crater (e.g. July 05, 2010, at 05:02 UTC). Although no radar signal was recorded during the Voragine eruptive event, signal was recorded in gate 4485 m during the eruptive event from the NEC. However, because of the weak intensity of the eruptive event, and because the crater is quite deep and the base of the radar beam is quite high, the recorded signal was very weak.

In an operational monitoring room, the data coming from the various remote sensing instruments need to be displayed in a comprehensive manner on the screens. Typically, it would be unrealistic to display the radar data coming from all of the 11 range gates. We suggest instead to make three distinct groups of range gates, each monitoring an eruptive vent (Figure VI.9).

Given the above comments, the following groups could be foreseen:

- Southeast crater group: gates 3135, 3285 and 3435 m (cyan segment),
- Bocca Nuova group (and Voragine): gates 3585, 3735, 3885 and 4035 m (magenta),
- Northeast craters: gates 4185, 4335, 4485 and 4635 m (green).

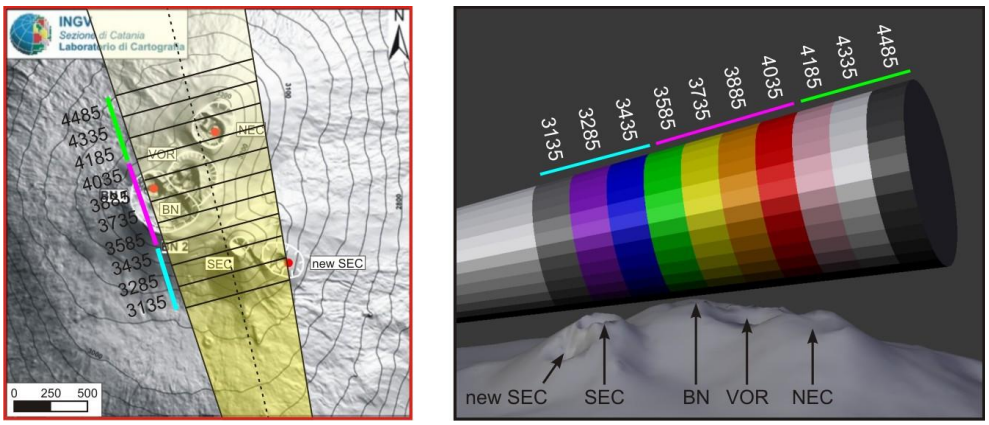

Figure VI.9. Spatial distribution of the range gates above Etna's summit craters. The colored segments highlight the possible gate groups which could be defined to monitor specific eruptive vents: cyan for the new Southeast Crater (SEC), magenta for the Bocca Nova (BN) and Voragine (VOR) craters, and green for the Northeast crater (NEC).

VI.3.3.2. Detecting weak eruptive events

As discussed in section I.2.3 (radar parameter acquisition section), processing of the Doppler spectra through time enables the acquisition of three types of time series: those related to the spectra backscattered power (e.g. P_{+}, P_{-}, P_{gate}, P_{tot}), those related to the radial velocity (e.g. V_{+max}, V_{-max}), and those which combine both to inform about the kinetic energy (e.g. E_k). The questions which now arise are: (i) which of these would be best suited to provide unambiguous notifications on tephra emission, (ii) with what temporal resolution (i.e. number of incoherent integrations), and (iii) with what spatial resolution (i.e. range gates).

We hereafter consider a weak eruptive event (short-lived ash plume from the new SE Crater), recorded on August 28 (2011) at 15:07 UTC. The signal appears only in gate 3135 m, and has a maximum backscattered power which is barely above the background noise, making it particularly challenging to detect automatically. Figure VI.10 illustrates for this event, the time series of various radar parameters computed with two different acquisition rates (related to the number of incoherent integrations): 3 integrations (time step = 0.23 sec, default acquisition rate), and 15 integrations (time step = 1.14 sec). As expected, the first observation is that increasing the number of incoherent integrations clearly flattens the noise level of all

parameters. More importantly, it appears that it does not alter the eruptive signal like a running average would: the gray curve in the bottom plot of Figure VI.10b (i.e. non-filtered curve computed with 15 incoherents) reveals the eruptive peak better than the black curve in the top plot of Figure VI.10b (i.e. running average of a curve computed with 3 incoherents). Hence the first lesson to be drawn from Figure VI.10b is that computing the raw data with 15 incoherent integrations results in an acquisition rate of ca. 1 sec, which seems enough to detect even small events lasting a few seconds only.

Figure VI.10c plots the time series of the total backscattered power in the gate (P_{3135}), which is equivalent to the sum of the negative and positive powers (P_{-3135} + P_{+3135}, respectively referring to the left and right hand of the Doppler spectrum). Notice that because the eruptive signal is visible only in P_{-3135} (none in P_{+3135}, Figure VI.10a), its amplitude on the P_{3135} curve (Figure VI.10c) is slightly lower than on the P_{-3135} curve (Figure VI.10b). Nevertheless, even when using P_{3135} the signal remains detectable, and has the advantage of ensuring its detection regardless of which side of the spectrum it appears on. We thus conclude that it is preferable to use the newly developed P_{gate} parameter rather than P_{+} or P_{-}.

Figure VI.10d and Figure VI.10e plot the maximum radial velocities collected from the left- (V_{-max}) and right-hand (V_{+max}) side of the Doppler spectra, respectively. These are particularly noisy when computed with only 3 incoherent integrations, making them hard to use for monitoring purposes since weak events will often appear "drowned" into the noise. When computed with a higher number of integrations, the signal to noise is significantly improved but erratic values still remain (e.g. between 15:20:00 and 15:21:30). In turn, we suggest that the maximum velocities collected from the automated spectra processing are not well suited for the real-time detection of tephra emissions.

Figure VI.10 (on next page). Detection of a weak eruptive signal recorded on August 28 (2011) at Mt. Etna, using a variety of radar parameters computed in gate 3135 m: power related parameters (left hand column plots: a, b and c, in dB units), velocity related parameters (middle column plots: d and e, in m/s), and kinetic energy proxy (right hand column plots: f, g, and h, in arbitrary units). Gray curves refer to the non-filtered data, while the black curves refer to the data filtered with a running average (window = 5). The dashed vertical red line marks the onset of the eruptive event.

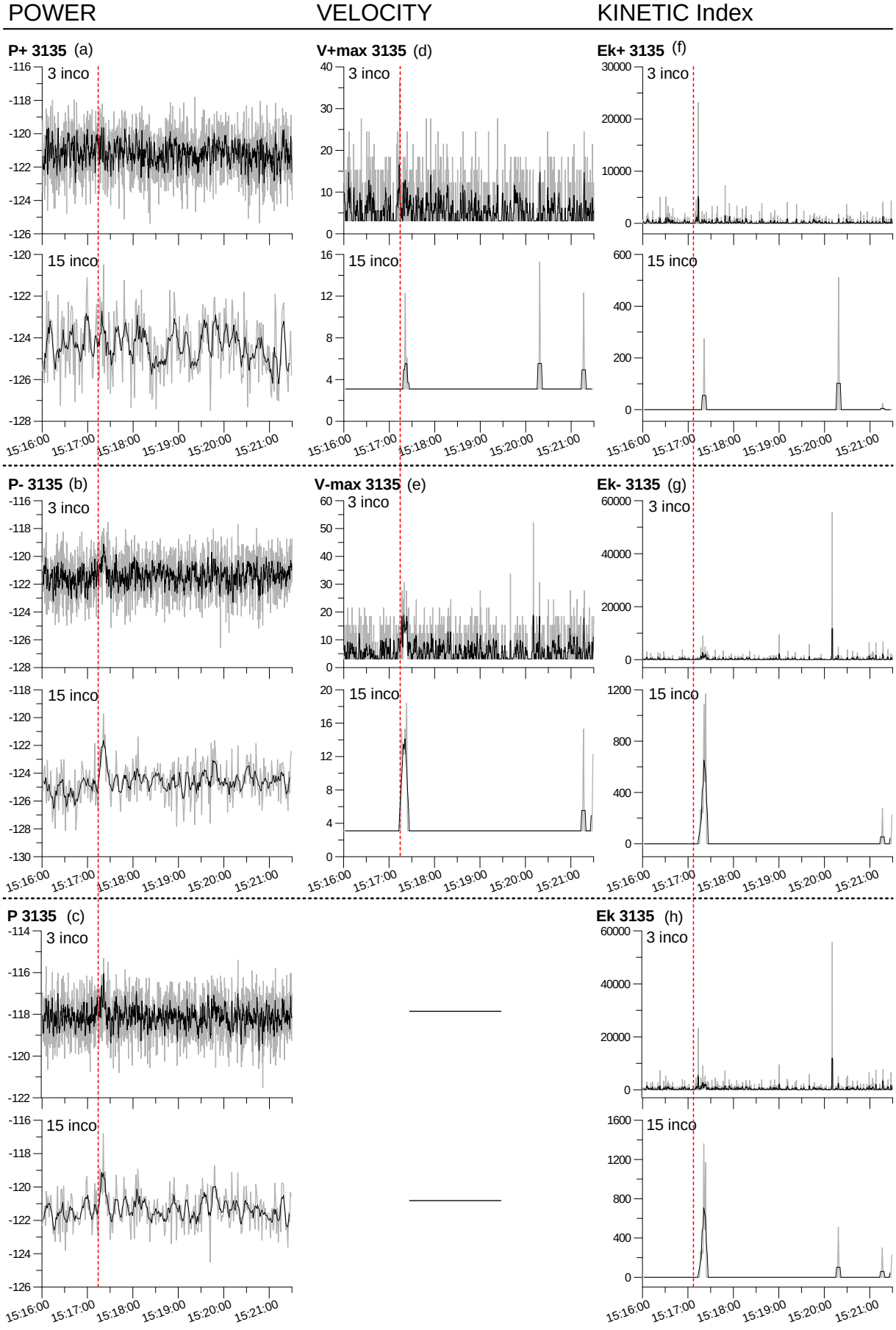
POWER
VELOCITY
KINETIC Index
P+ 3135 (a)
V+max 3135 (d)
Ek+ 3135 (f)
P- 3135 (b)
V-max 3135 (e)
Ek- 3135 (g)
P 3135 (c)
Ek 3135 (h)
3 inco
15 inco
15:16:00
15:17:00
15:18:00
15:19:00
15:20:00
15:21:00

Finally, Figure VI.10f to Figure VI.10h display time series of kinetic indexes, which use both the power and velocity information of Doppler spectra to inform on the kinetic energy of the pyroclasts crossing the radar beam. Basically, the kinetic index[4] is obtained by summing the product of the power and velocity value at each spectral line, until the V_{max} spectral line is reached (e.g. from the central spectral line to V_{+max} if we consider E_{k+}). As a consequence, E_{k+}, E_{k-} and E_k will suffer from similar shortcomings as those for V_{+max} and V_{-max} described previously (i.e. erratic peaks, resulting from abnormal V_{max} values collected). Notice for instance the E_{k-3135} peak at 15:20:10 in Figure VI.10g: it exhibits a value higher than the eruptive signal itself (at 15:17:21), but because it is isolated (i.e. composed of a unique value) it is very unlikely that it is eruptive signal. This is confirmed when looking at the Doppler spectrum recorded at this precise moment: Figure VI.11 shows that due to both the level of noise computed in the spectra (from the lowest average of 8 consecutive power values of the spectrum) and the shape of the spectra itself, V_{-max} is found at an abnormally high negative value. This calls for another filter, deleting the isolated values to leave only the eruptive signal. Although such filtering has been done in the study of eruptive signals at Arenal (Chapter II), it is a supplementary operation which would need to be performed for real-time monitoring at Etna. Hence in the present state, the kinetic energy index E_k is not ready to be used in an operational setting. Further work should focus on improving the algorithms which calculate the mean noise value, as it strongly controls the V_{max} value computed, and in turn the E_k value.

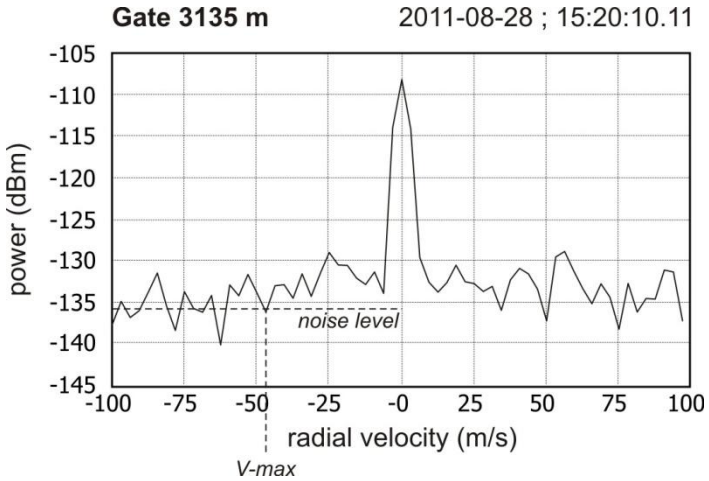

Figure VI.11. Doppler spectrum recorded in gate 3135 m at 15:20:10.11 on August 28, 2011. The abnormal V_{-max} value collected will result in an isolated peak of E_{k-} (Figure VI.10g).

[4] $E_k = \sum_{i=i_{-\max}}^{i_{+\max}} p(i) \cdot V_r(i)^2$, see section I.2.3

We have mentioned in section VI.3.3.1 that the signal from several gates could be merged, in order to keep a limited number of curves for the monitoring of the 4 active craters at Etna. However when the eruptive event is weak, and when it is recorded in only one gate, we expect this merging to lower the signal to noise ratio. Figure VI.12 shows a plot of the power recorded in the gates 3135, 3285, and 3435 m, a combination which seems relevant to monitor the SE crater's activity (see Figure VI.9). We can see that although the signal amplitude is slightly diminished (~2.25 dB at 15 incoherent integration, with respect to ~5 dB for P_{-3135} only in Figure VI.10b), the event remains detectable even if very weak.

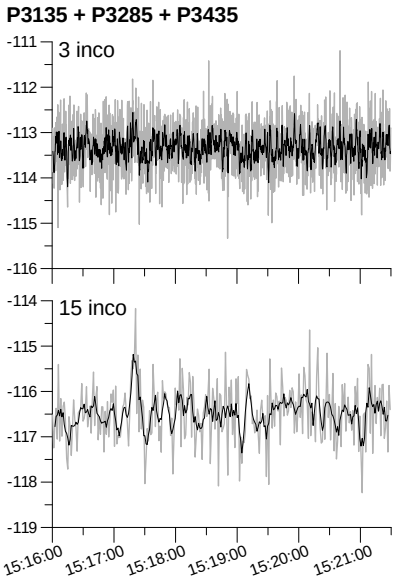

Figure VI.12. Power recorded in gates 3135, 3285, and 3435 m. The power is computed by summing the spectral power in decimal units (linear scale) over the 3 gates, and finally converted again in dB units (log scale).

The real-time detection algorithms should be trained using long sequences of recorded data including a variety of events (in terms of waveform, duration and signal to noise ratios in particular), in order to find the best compromise between most successful detections and fewest false alarms.

VI.3.3.3. Emissions not entering the beam

If trade winds drift the tephra plume in such a way that it does not enter the radar beam, or if small ash plumes originate from locations outside the summit craters area, the radar data will appear useless to warn about the tephra emission. Although this is likely to be restricted to a limited number of weak events, this type of situation highlights the need to integrate the various remote sensing instruments available, and bring together their respective activity-alert systems to ensure successful emission warnings. For instance, the digital cameras (in

particular those positioned at La Montagnola operating in both the visible and thermal spectral ranges), could be combined with the radar's own alert system. In doing so, the strengths of the first will support the weaknesses of the second: the cameras' wide field of view (FOV) will make up for the radar's narrow FOV (see Figure VI.14), and the radar's all-weather capability will make up for the camera's inability to operate in overcast weather.

Figure VI.13 shows the data collected during an the eruptive event which originated from the new SE crater on April 8, 2010. Unfortunately, the vent is located at the edge of the radar beam's main lobe (see Figure VI.9), and the trade winds drifted the plume eastward so that VOLDORAD was only able to record the marginal part of the plume that expanded during the first stage of the eruption (hence low power amplitude in subset (a)). Typically, the alert coming from the video data (b) could complement that of the radar. To another extent, the videos and photographs can be used to evaluate the plume volume fraction entering the radar beam (subset (c) is a schematic view of the spatial relationship between the plume and the radar beam).

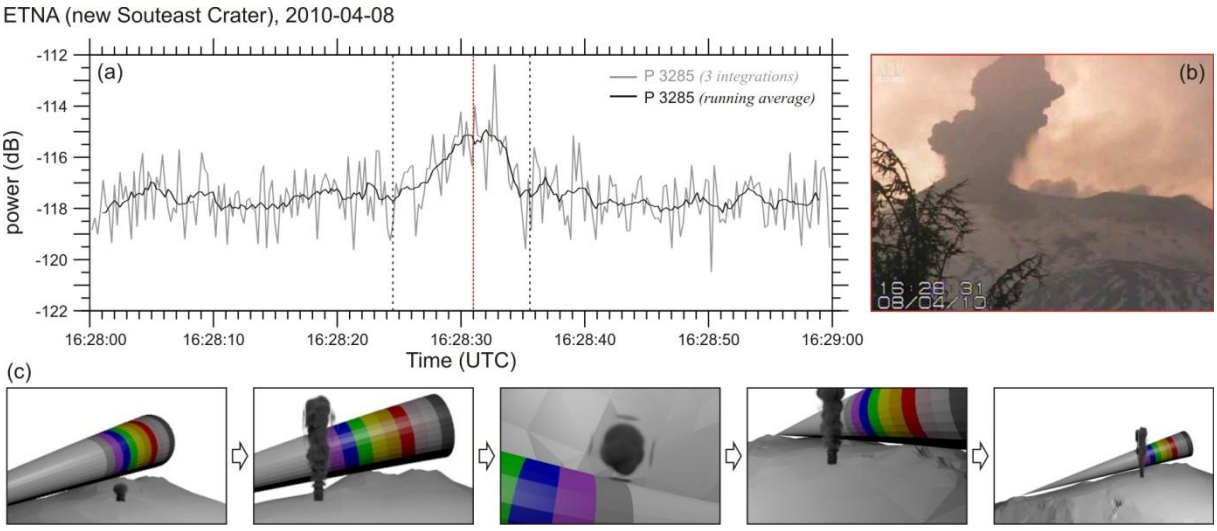

Figure VI.13. Eruptive event originated from the new SEC (Etna), on April 08, 2010. (a) power amplitude from gate 3285 m, (b) snapshot from INGV's monitoring camera taken at 16:28:31 (timing marked by a red line in plot a), (c) schematic view of the spatial relationship between the ash plume and the radar beam.

Obviously, other instruments implemented at Etna like acoustic or seismic sensors can further inform on sub-surface or surface activity, even invisible to cameras or radar (e.g. Strombolian activity confined inside a crater). Ideally, the monitoring network should include all complementary instruments, including those satellite-based. In the following section we focus on the coupling between ground- and satellite-based infrared imagery with Doppler radar data, as they potentially hold rich complementary information on the dynamics of eruptions.

VI.4. Integration of remote sensing techniques to track pyroclastic emissions

Basaltic explosive eruptions commonly generate both ash plumes ejected into the atmosphere, and effusive lava flows emitted on the ground. This implies a partitioning of the magma flux between the two flows, which can be quantified using several sensors, both ground- and satellite-based. The recent study carried by *Gouhier et al.* (2011) at Etna during the January 2011 eruption, provides a compelling example of such integration of remote sensing techniques. In the following section, based on this specific eruption, we show that the use of ground-based infrared cameras and Doppler radar, coupled with satellite-based thermal sensors (MSG's SEVIRI sensor), is a powerful observational suite of tools

Bulletin of Volcanology

Lava discharge during Etna's January 2011 fire fountain tracked using MSG-SEVIRI

Mathieu Gouhier[1,2,3], Andrew Harris[1,2,3], Sonia Calvari[4], Philippe Labazuy[1,2,3], Yannick Guéhenneux[1,2,3], Franck Donnadieu[1,2,3], Sébastien Valade[1,2,3]

VI.4.1. The January 2011 eruption: phenomenology and instrumentation

The January 2011 eruption at Etna began on the 11th, and was initially characterized by weak explosive activity confined to a pit crater on Etna's South East Crater (INGV report n°UFVG2011/05). On January 12, 20:20 UTC, lava began to overflow from the rim of the pit crater. Shortly after, a fountaining phase started, feeding an ash plume which drifted eastward. The remote sensing network of INGV successfully monitored the evolution of the eruptive activity (*Calvari et al.*, 2011). In particular, the radar clearly detected the fountain-fed ash plume associated with the main fountaining phase. In the shelter the radar located, are also two cameras, operating respectively in the visible and thermal spectral domain (Figure VI.14). The thermal images are displayed with a fixed color scale ranging between −20 and 60°C, and are stacked in 15 minute-long movie sequences. Analysis of these images enables exceptional monitoring of the eruptive activity, such as the frequency of strombolian explosions (*Calvari et al.*, 2011). Below, we show how simple *Matlab*-based algorithms can automatically process video sequences, to give for example, the evolution of the lava fountain height with time at high temporal resolution.

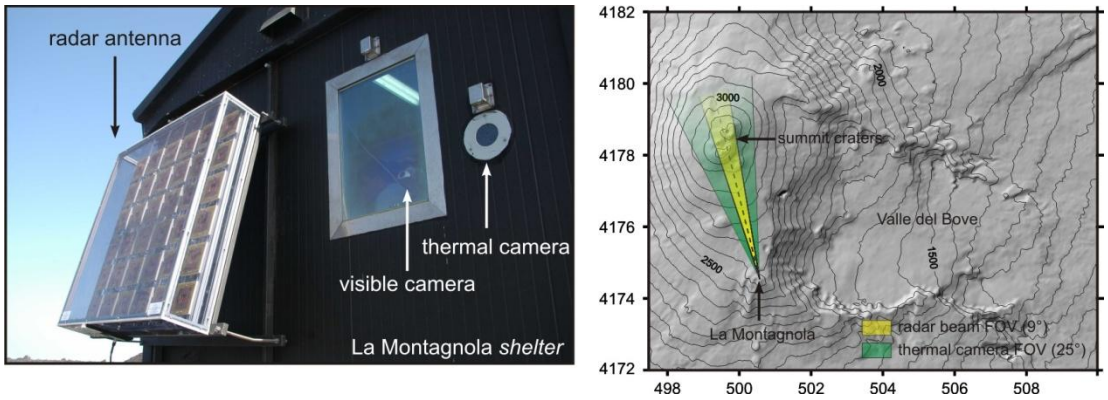

Figure VI.14. Radar antenna and digital cameras located at La Montagnola shelter. The horizontal field of view (FOV) of the radar and the thermal camera are indicated on the map (in yellow and green respectively). The visible camera's FOV is not indicated, because it can vary depending on the optical zoom applied (Calvari et al., 2011).

VI.4.2. Automated retrieval of fountain height from thermal cameras

Figure VI.15a is an image extracted from a video sequence of the INGV thermal camera at La Montagnola, recorded during the paroxysm of the lava fountaining episode on January 12, 2011 (courtesy of M. Coltelli, INGV Catania). The saturated portion of the image, displayed in white (> 60 °C), is attributed to the incandescent lava clots of the fountain. Tracking the maximum height of this saturated area in each movie frame can thus give a time series of the lava fountain height, provided a scale can be established in the image.

To do so, the video is first opened with *Matlab*, after what each image is processed in three steps: (i) extraction of the area of interest in the image (i.e. excluding the bordering information such as the color scale), (ii) conversion of the three-component RGB image into a one-component gray scaled image, and (iii) tracking of the pixels above a defined color threshold (e.g. color index > 249, where 0 is black and 256 is white). The highest saturated pixel in the image was assumed to be representative of the lava fountain height (red line, Figure VI.15b). Note however that the height obtained in this way is just an estimate because (i) the real top of the lava fountain can be hidden by cooled ash, and (ii) uncertainties may arise from the fixed color threshold chosen. Nevertheless, first order height values are quantified and relative variations can be analyzed confidently at very high sampling rate (unlike manual hand-picking operations which are extremely tedious). The number of saturated pixels on the other hand (blackened in Figure VI.15b), was considered as a discharge proxy of the lava fountain. Knowing the equivalent size of an image pixel in reality (~3 by 3 m), we can convert the height in pixels into a height in meters. Note that no correction was applied to account for the perspective distortion (due to the projection of the

assumed plane of the jet onto the video image plane), nor for the lens distortion. However given the distance (~3 km) and the weak slant angle (~15°), these effects are assumed to be small.

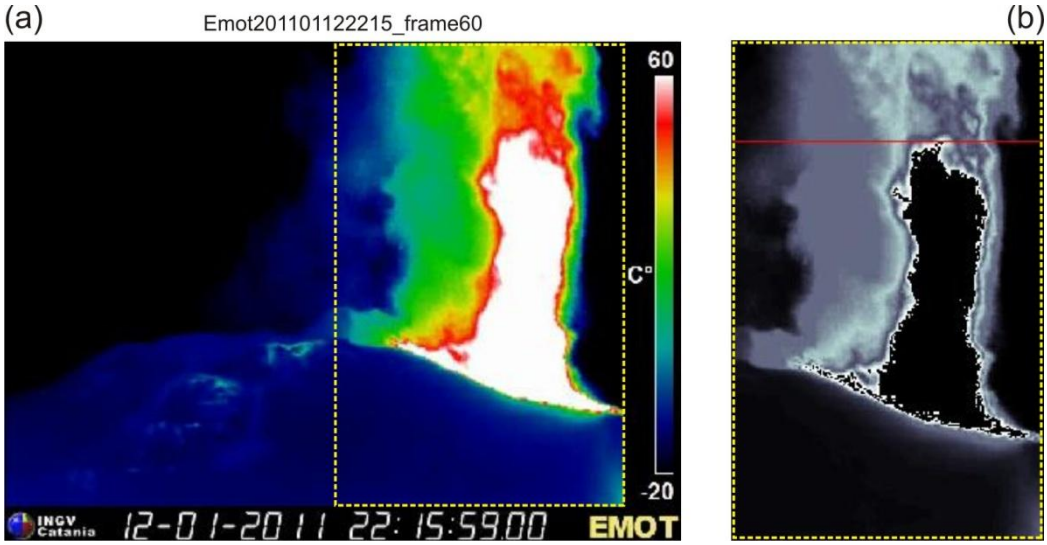

Figure VI.15. Image processing of thermal video to track lava fountain height. The raw RGB image (a) is converted to grayscale (b), and the highest part of the saturated area is considered as the maximum fountain height (red line). The pixels above the defined color threshold were set to black in (b) in order to visualize which pixels were found. (thermal videos, courtesy of INGV Catania)

This processing is performed automatically on each movie frame, which in turn gives us time series of both the fountain height and the lava discharge proxy (Figure VI.16).

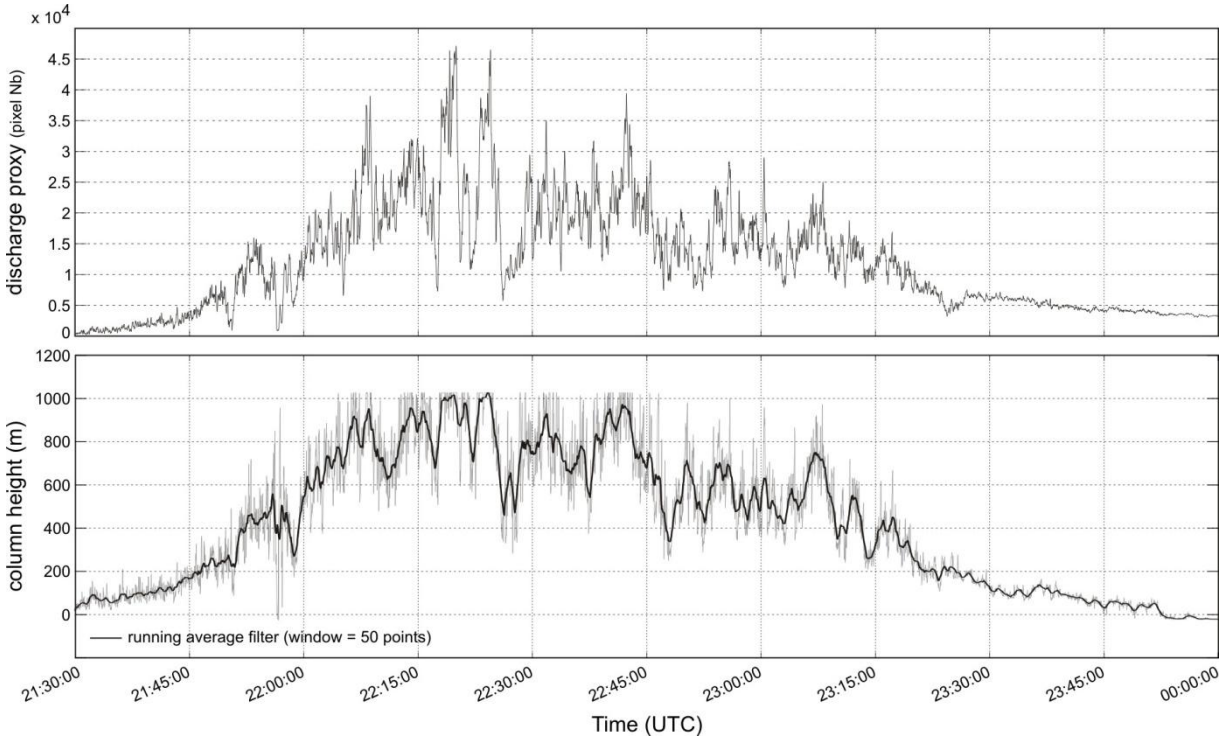

Figure VI.16. Time series of the lava discharge proxy (arbitrary units) and the lava fountain, computed from the automated analysis of INGV thermal videos recorded on January 12, 2011. Note that the height curve is

saturated between ca. 22:00:05 and 22:45:00, because the fountain height goes beyond the camera's field of view (18.8° vertical, 25° horizontal, Calvari et al., 2011). The pixel size in meters was determined using the distance between the western and eastern lip of the South East crater (ca. 100 m = 34 pixels, which yields a pixel width of 2.94 m).

This data is an additional piece of information that can be put in perspective with the other remote sensing instruments which have monitored the eruptive activity (Figure VI.17, completion of the original figure in *Gouhier et al.*, 2011). In turn, we see an interesting complementarity between the satellite- and ground-based measurements.

The satellite thermal sensor (SEVIRI's 3.9 µm channel, Figure VI.17a) was the first to detect a thermal anomaly at 20:00, marking the onset of effusive activity. Around 21:30, this signal vanishes, and the ground-based Doppler radar and thermal imagery detect the onset of the fountaining phase. The coincidence of the trends is explained by the fact that intense fountaining produced a large (relatively) cold tephra plume, which in turn obscured the hot spot associated with the active lavas (3.9 µm band hiatus, Figure VI.17a) and caused low radiances in the 12 µm band (Figure VI.17b). When the radar power and fountain height began to decline shortly after 23:00 (Figure VI.17c and d), the satellite radiances increased on again, which is consistent with clearance of the plume to reveal the hot spot associated with the active lavas.

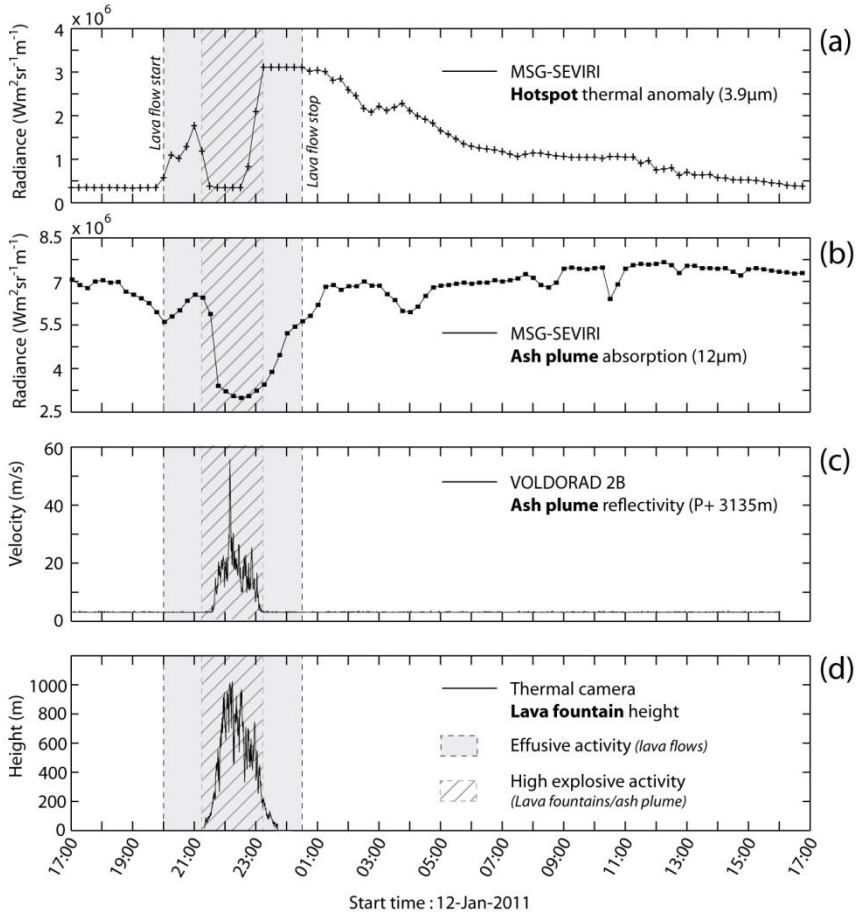

Figure VI.17. Time series from various remote sensing instruments, tracing the evolution of the eruptive activity at Etna, on January 12, 2011. (a) and (b) MSG satellite SEVERI thermal sensors (3.9 µm and 12 µm band respectively); (c) radar backscattered power in the 3135 m range gate; (d) lava fountain height obtained from thermal video processing (running average in Figure VI.16). Modified after Gouhier et al. (2011).

The above figure illustrates how satellite-based sensors and ground-based sensors can complement each other, to provide a complete synopsis of the eruptive event. In the following section, we shortly mention what potential benefits could be drawn from the interaction of the radar and thermal data.

VI.4.3. Potential insights from coupling of thermal cameras and Doppler radar

The interaction of thermal and radar data is very promising in various aspects. Firstly, because thermal cameras image the spatial distribution of the pyroclastic ejecta (in a perpendicular plane to the radar beam), they can tell us how and when the ejecta enters the radar beam. In particular, this type of correlation enabled us to explain the delay between the radar and thermal waveforms, recorded during the eruptive event on August 25, 2010, 13:09 UTC. Indeed, Figure VI.18 shows that the peak temperature recorded by the thermal camera precedes by approximately 15 seconds the radar power peak. This results from the fact that when tephra radiates most of their heat, they have not yet entered the radar beam, and when they do, they have cooled sufficiently to radiate only little thermal energy.

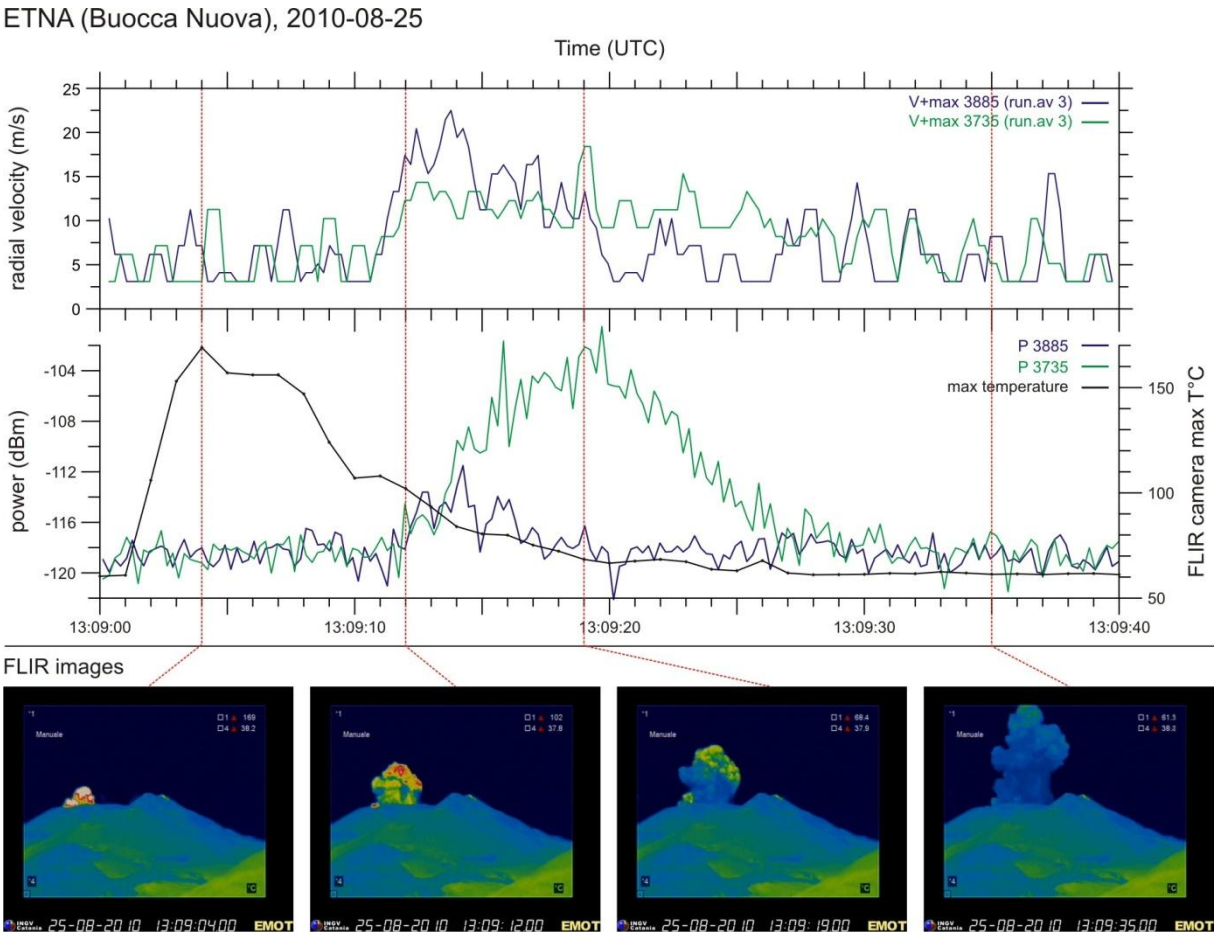

Figure VI.18. Tephra emission from the Buocca Nuova (Etna), recorded on August 25, 2010, by both VOLDORAD 2B and the infrared camera located at La Montagnola (courtesy of INGV Catania). The maximum temperature recorded by the camera (snap shots) is collected, and put in perspective with the radar power and velocity power curves (data from F. Donnadieu, unpublished).

Another interesting aspect is the mutual feedback possible, on the tephra mass and particle size distribution inferred from both techniques. Indeed, because the heat radiated to the thermal cameras is mainly conveyed by particles (rather than the gas), it is possible to recover the particle size distribution and the mass of the erupted material (e.g. *Prata and Bernardo*, 2009 using a filter-wheel infrared camera). The inferred size distribution could in turn be used to derive an eruptive mass estimate from the radar data (*Gouhier and Donadieu*, 2008), and thus assess the validity of both techniques.

VI.5. Conclusion

Firstly, we have simulated ash plume transit paths using simple geometrical shapes, and computed the intersection volumes between these and the radar range gates. The good agreement between the intersection volumes and the radar power amplitudes, suggests that the decrease in power amplitude within the first few hundred meters from the vent is dominantly controlled by the progressive exiting of the plume from the beam. Moreover, the simulations give constraints on the plume's path azimuth and upraise angles. These, coupled with the radial speed component of the drifted ash plume, are used to obtain the three-dimensional transport speed of the ash cloud. In turn, the method has applications for volcano monitoring, and for quantitative assessment of volcanic gas and tephra mass fluxes.

Secondly, we have discussed the challenges and the subsequent requirements the radar parameters must fulfill in order to provide unambiguous, real-time notifications on tephra emissions at Mt. Etna. Using a weak eruptive event, we assess the ability for various parameters to detect the emission. We suggest making three distinct groups of range gates, in order to restrict the number of analyzed radar time series, while ensuring the monitoring of all the active vents at Etna. The power recorded from each group, and analyzed with 15 incoherent integrations (i.e. 1.14 s time step), seems like the most adequate parameter to alert from tephra emissions.

Lastly, we show how automated analysis of thermal video imagery can provide high frequency, time evolution of the lava fountain height and discharge rate. We emphasize on the complementarity between the satellite- and ground-based measurements, to provide a synopsis of the January 2011 eruption at Mt. Etna. In addition, we highlight the promising interaction expected that could be foreseen between the Doppler radar and infrared camera data. We particularly emphasize on the feedback that could operate between both techniques, to give mutual constraints on the eruptive mass and particle size distribution.

Conclusion

The aim of this study was to investigate the source explosive mechanisms and the subsequent pyroclastic emissions dynamics of mildly explosive volcanoes, which expel frequent small-scale ash plumes and ballistic projections. Using Arenal (Costa Rica) as a case study volcano, we combined seismic and Doppler radar to unravel the eruptive mechanisms from depth to surface. The study is composed of three parts, arranged in an order reflecting the sequence from the *sub-surface* source mechanisms, through to the *surface* emission dynamics, and lastly to the operational monitoring of tephra emissions and their *dispersal* of downwind.

Source mechanisms of explosive activity at Arenal

In the first part of the study, we have investigated the relationship between subsurface source mechanisms and surface pyroclastic emissions, from the cross-analysis of seismic and radar data (*Valade et al.*, 2012). The study shows a non-systematic relationship between the two, both geophysical signals exhibiting a large variety of behaviors and features. Notably, no clear pattern is found on seismic signals that can be associated to tephra emissions, as these are encountered in association with explosion-quake events, during episodes of tremor, and even during aseismic intervals. Energy proxies of coeval radar and seismic eruptive signals show significant scattering, suggesting that at Arenal the seismic energy is not a good indicator of the kinetic energy nor mass loading of pyroclastic emissions. This observation is particularly important for volcano observatories, for whom seismic data remain the most common tool to inform on the eruptive activity of the monitored volcanoes.

A conceptual model was proposed to account for the complex interplay between seismic and radar signals. It echoes and completes the tremor clarinet-model proposed by *Lesage et al.* (2006), providing a complementary explanation to the explosion quake signals and their relationship with tephra emissions. The key idea is that the conduit is topped by a rigid lava cap, which is cross-cut by fractures that control the degassing of the shallow system. In turn, the seismic signals are controlled by the degassing regime through these fractures: when gas release is intermittent, the repetitive pressure pulses act as a source of tremor, whereas when it is sudden, the gas release will cause fracture walls to slap one against the other, acting as a source mechanisms to the recorded explosion quakes. Because variable amounts of tephra may be entrained by the gas, the seismic events may or may not be accompanied by radar signals, depending on the tephra load of the emission and the radar detection threshold (ca. 15

g/m^3 for 1 mm particles, *Donnadieu et al.*, 2011). All of these mechanisms however are sensitive to small changes of the state of the conduit and plug. In semi open-system volcanoes such as Arenal, the shallow system conditions (e.g. the presence of a solidified cap, its rheology, heterogeneous fracturing, thickness, debris residing above it, and subsequent permeability to gas) are constantly evolving, which is likely to account for some of the variability observed between both the seismic and radar signals.

Further understanding of these complex systems is limited by our capacity to measure enough parameters to adequately constrain conduit models, and to consider their time-dependent and inter-dependent evolution. In particular, volcanoes undergoing recurrent explosive activity such as Arenal, must be considered as unstable dynamic systems, very sensitive to boundary conditions which can trigger transitions from one state of stability to another (*Schick*, 1988). Furthermore, the parameters and processes characterizing these boundary conditions, notably at the conduit upper-end (rheology and gas-permeability of cap), lower-end (magma/gas influx), and lateral-margins (outgassing and shear), are likely to be non-linear, time-dependent and with complex feedback mechanisms. In particular, variations in the physical properties of the shallow plug-cap structure are governed by parameters which are all interdependent and difficult to model: degassing of magma triggers crystallisation and pore pressure evolution, which in turn controls its viscosity, its fracture network evolution, and its cycles of destruction/generation etc... Further geophysical studies, involving continuous radar measurements over a long period, accompanied by acoustic sensors and proximal broad-band seismic stations, should allow us to better analyze the variability of the geophysical signals on longer time scales. Such studies may help to further constrain the complex processes and feedbacks operating in the shallow system of Arenal, and to better understand the mechanism and evolution of its persistent activity.

Dynamics of pyroclastic emissions at Arenal

The second part of this manuscript was devoted to the study of the dynamics of pyroclastic emissions at Arenal, using exclusively Doppler radar data. The section was threefold.

Firstly, we developed a new method to visualize at once all the information the radar data holds, namely the evolution of the velocity and mass load of the ejecta through time and space. The method simply consists in the juxtaposition through time of the Doppler spectra,

using a color code to display the power variations. The resulting image, entitled Doppler radargrams, enables the possibility to visualize the evolution of the shape of the Doppler spectra through time and within all the range gates, informing on the dynamics of the ejecta crossing the beam. In turn, the time-velocity distribution of the power, or Doppler signature, revealed two distinct dynamics recorded simultaneously during several eruptive events. The discriminative characteristics of each show that they result from two distinct phenomena occurring simultaneously: the rapid transit of ballistic particles projections, and the slower transit of a wind drifted ash plume (*Valade and Donnadi*eu, 2011). The first imprints as a short lived-signal (5-21 s), which may enters up to 5-6 range gates in a few seconds. In each gate, the signal exhibits high and contrasted velocities: in the gates above the vent and up-beam, the ballistic particles imprint on radargrams as oblique streaks, with high impulsive positive radial velocities (+10 – +80 m/s) that progressively shift towards negative values (in 5-17 s); in the gates below and down-beam from the vent however, the ballistics sketch a signal which exhibits high negative values (onset velocities -12.5 – -47 m/s) which usually span a narrow velocity range (i.e. short-lived horizontal streak). Contrastingly, the ash plume Doppler signature is a long-lived signal (20-160 s) which transits slowly in the gates down-wind from the vent (4-15 m/s along-beam), and exhibit low negative radial velocities (< |-30| m/s). The ability to remotely discriminate ballistics and ash plumes expelled simultaneously opens a way to better constrain the eruption mechanisms and source parameters. In particular, we were able to constrain the mass fraction of both the ballistics and the ash plume for a representative eruptive event. The mass of centimeter- to decimeter-sized ballistics was confidently estimated at 0.5–7 tons, whereas mass of the infra-centimeter particles of the ash plume was loosely constrained at $5.8 \cdot 10^2$ tons (assuming an average diameter of 2 mm above the vent).

Secondly, we carried out forward numerical modeling of both ballistics particles and wind-drifted ash plume crossing the radar range gates, and simulated the resulting Doppler radargrams using the Mie scattering theory (*Gouhier and Donnadieu*, 2008). The aim of this section was to reproduce the observed Doppler signature and assess which factors controlled it, with the final aim of understanding what the recorded radar signals can actually tell us about the underlying emission dynamics. Both models operate in 3D, and can be run simultaneously via a graphical *Matlab* interface (*eject3D*). The ballistic model is an improvement of the 2D model developed by *Dubosclard et al.* (2004) and *Gouhier and Donnadieu* (2010). It succeeded in reproducing the main characteristics of the ballistic

Doppler signature, in particular the short life span, the transit times through the range gates, as well as the radial velocities and overall shape of the signal. An important outcome to mention is that the maximum radial velocity retrieved by the radar (i.e. V_{+max}) is strongly dependent on the inclination of the jet, and thus not necessarily representative of the real ejection velocity. In particular, for a vertical jet of 45° aperture entering a beam having 25° of inclination, V_{+max} underestimates by ca. 30% the true vertical speed of the particles. On the other hand, modeling of a cloud of particles behaving as a buoyant thermal (*Yamamoto et al.*, 2008) drifted by cross winds successfully reproduced the main characteristics of the plume Doppler signature. Although sedimentation, convection, and internal turbulences were not considered, the long life spans, slow transit times through the gates, emergent power onset, and low negative radial velocities (resulting from the combined effects of buoyancy and wind drift towards the radar) were adequately reproduced. This emphasizes the strong influence of the wind direction and speed on the Doppler signature and the importance to take these into account in the interpretation of radar signals.

Lastly, we applied inversion algorithms to search for the input model parameters which would best match the observed radargrams. A Monte Carlo near-neighborhood search algorithm (*Sambridge, 1999a*) was used (Nasearch, *Fukushima et al.*, 2005; *Augier*, 2010). Algorithms were developed to condition the radargrams for the inversion (e.g. quadtree subsampling), and a misfit function was designed to measure the discrepancy between the observed and modeled data (least-square). The method was then tested on a representative eruptive event, for which we carried out inversions of the Doppler signature of both the ballistics and the ash plume independently. Concerning the ballistics' signal, the results successfully reproduced for the most part the shape of the Doppler radargram, providing constrains on: (i) the geometry of the eruptive jet (inclined ~10° from the vertical towards the radar, ~30-35° in aperture, ejecting particles up to ~245 m above the vent and ~500 m to the West); (ii) the position of the vent with respect to the radar (~2484 m above and ~864 m away from the radar); as well as the particle size distribution and subsequent gas velocities (0.1-0.5 m and 130-170 m/s respectively, inferring ejection velocities at the vent in the range of 65-85 m/s). In order to further constrain the particle size distribution, inversion of the absolute power values is required, which is still the subject on ongoing research. Inversion of the ash plume Doppler signature on the other hand gives us confident constrains on the wind speed drifting the ash plume, which was estimated to 7 m/s, coherent with the findings of *Donnadieu et al*. (2011).

Monitoring of pyroclastic emissions

Because Doppler radars are also powerful tool for real-time all-weather monitoring of volcanic activity and early warning (high acquisition rate), we addressed issues relative to the operational monitoring of ash plumes in the last section. We firstly simulated ash plume transit path using simple geometrical shapes, to assess the influence on the radar power time series of the volumetric emptying of the beam by an ash plume. The intersection volumes between the simulated path and the range gates were used as proxies to the radar power amplitude. The good agreement between the intersection volumes and the radar power amplitudes, suggested that the decrease in power amplitude within the first few hundred meters from the vent is dominantly controlled by the progressive exiting of the plume from the beam. Such simulations gave constraints on the plume path azimuth and upraise angles, which in turn can be coupled with the radial speed component of the drifted ash plume to obtain the three-dimensional transport speed of the ash cloud (*Donnadieu, Valade and Moune,* 2011).

Finally, we discussed the issues relative to the real time monitoring of tephra emission at Etna. Indeed, in July 2009 we installed a Doppler radar on the southern flank of the volcano to monitor continuously its eruptive activity (*Donnadieu et al.,* 2009). Taking into consideration the several events recorded in the past 2 ½ years (e.g. OPGC-INGV reports by F. Donnadieu), we gave suggestions for the set of radar parameters which could be implemented to provide unambiguous, real-time notifications on tephra emission. In particular, because several vents are active at varying radial distances from the radar, we have suggested to make three distinct groups of range gates. This should restrict the number of analyzed radar time series, while ensuring the monitoring of all the active vents at Etna. Lastly, parametric tests performed on a weak ash emission suggested that the backscattered power is likely to be the most adequate parameter to alert from tephra emissions when computed with 15 incoherent integrations (i.e. 1.14 s time step).

References

A

Adams, R.J., W.F. Perger, W.I. Rose, and A. Kostinski (1996), Measurements of the complex dielectric constant of volcanic ash from 4 to 19 GHz, *J. Geophys. Res.*, 101, 8175– 8185, doi:10.1029/96JB00193.

Allard, P., M. Burton, and F. Muré (2005), Spectroscopic evidence for a lava fountain driven by previously accumulated magmatic gas, *Nature*, 433, 407–410, doi:10.1038/nature03246.

Alvarado, G.E., and R. Barquero (1987), Las señales sísmicas del Volcán Arenal (Costa Rica) y su relación con las fases eruptivas (1968-1986*), Ciencia y Tecnología*, 11(1): 15-35.

Alvarado, G.E., and G.J. Soto (2002), Pyroclastic flow generated by craterwall collapse and outpouring of the lava pool of Arenal Volcano, Costa Rica, *Bull. Volcanol.*, 63, 557–568.

Alvarado, G.E., G.J. Soto, H.U. Schmincke, L.L. Bolge, and M. Sumita (2006), The 1968 lateral blast eruption at Arenal Volcano, Costa Rica, *J. Volcanol. Geotherm. Res.*, doi:10.1016/j.jvolgeores.2006.03.035.

Alvarado, G.E., W. Taylor, M. Ohrnberger, G.J. Soto, and L.Madrigal (1997), First observations of volcanic seismicity at Arenal volcano (Costa Rica) using a new three componen seismic digital network, *Bol. Obs. Vulc. Arenal*, 8 (15-16): 11-45.

Andres, R.J., and W.I. Rose (1995), Remote sensing spectroscopy of volcanic plumes and clouds. In: McGuire, B., Kilburn, C.R.J., Murray, J. (Eds.), Monitoring Active Volcanoes. University College London Press, pp. 301–314.

Andres, R.J., and J.W. Schmid (2001), The effects of volcanic ash on COSPEC measurements, *J. Volcanol. Geotherm. Res*., 108, 1-4:237-244.

Archer, C.L., and M.Z. Jacobson (2003), Spatial and temporal distributions of U.S. winds and wind power at 80 m derived from measurements, *J. Geophys. Res.*, 108 (D9), 4289,doi:10.1029/2002JD002076.

Arrowsmith, S.J., J.B. Johnson, D.P. Drob, and M.A.H. Hedlin (2010), The seismo-acoustic wavefield: a new paradigm in studying geophysical phenomena, *Rev. Geophys.*, 89 (D3), 4895–4904.

Atlas, D., M. Kerker, and W. Hitschfeld (1953), Scattering and attenuation by non-spherical atmospheric particles, *J. Atmospheric and Terrestrial Physics*, Vol. 3, pp.108-119.

Augier, A. (2011), Étude de l'éruption d'avril 2007 du Piton de la Fournaise (île de la Réunion) à partir de données d'interférométrie radar et GPS, développement et application de procédures de modélisation. Mémoire de Thèse, Université Blaise Pascal, Laboratoire Magmas et Volcans, 239 pp.

B

Balcerak, E. (2012), Observing volcanic ash plumes and ballistics using Doppler radar, *Eos Trans. AGU*, 93(2), 28, doi:10.1029/2012EO020025.

Barboza, V., and W. Melson (1990), Correlación entre las señales sísmicas y los sonidos de las erupciones del volcán Arenal, *Boletin de Vulcanología*, 21: 8-12.

Barquero, R., G.E. Alvarado, and T. Matumoto (1992), Arenal Volcano (Costa Rica) Premonitory Seismicity. En: P. Gasparini, R. Scarpa, K. Aki (eds.): *Volcanic Seismology. Springer-Verlag*, Berlin Heidelberg.

Battaglia, J., V. Ferrazzini, T. Staudacher, K. Aki, and J.L. Cheminée (2005), Pre-eruptive migration of earthquakes at the Piton de la Fournaise volcano (Réunion Island), *Geophysical Journal International*, 161, 449–458.

Baxter, P.J. (1999), Impacts of eruptions on human health. In:Siggurdson, H. (Ed.), *Encyclopaedia of Volcanoes. Academic Press, New York*, pp. 1035–1043.

Benoit, J.P., and S.R. McNutt (1996), Global volcanic earthquake swarm database and preliminary analysis of volcanic earthquake swarm duration, *Ann. Geofis.*, 39, 221-299.

Benoit, J.P., and S.R. McNutt (1997), New constraints on source processes of volcanic tremor at Arenal Volcano, Costa Rica, using broadband seismic data, *Geophysical Research Letters*, 24 (4), 449–452.

Benson, P.M., S. Vinciguerra, P.G. Meredith, and R.P. Young (2008), Laboratory simulation of volcano seismicity, *Science*, 322, 249–252.

Bertolino, S., C. Cigolini, and G.E. Alvarado (2009), Viscosity and explosive volcanism: the case of Arenal volcano (Costa Rica), *Am. Geophys. Un. Fall Meeting*, V11B, 1943.

Beyer, W., L. Fawcett, R. Mauldin, and B. Swartz (1987), The volume common to two congruent circular cones whose axes intersect symmetrically, *Journal of Symbolic Computation*, *4*(3), 381-390, doi:10.1016/S0747-7171(87)80014-7.

Blackburn, E.A., L Wilson, and R.S.J. Sparks (1976), Mechanisms and dynamics of strombolian activity, *J. Geol. Soc. London*, 132, 429–440.

Bluth, G.J.S., T.J. Casadevall, C.C. Schnetzler, S.D. Doiron, L.S. Walter, A.J. Krueger, and M. Badruddin (1994), Evaluation of sulfur dioxide emissions from explosive volcanism: the 1982–1983 eruptions of Galunggung, Java, Indonesia, *J Volcanol Geotherm Res*, 63:243–256.

Bluth, G.J.S., and W.I. Rose (2004), Observations of eruptive activity at Santiaguito volcano, Guatemala, *J. Volcanol. Geotherm. Res.*, *136* (3-4), 297–302, doi: 10.1016/j.jvolgeores.2004.06.001.

Bluth, G.J.S., M. Shannon, I.M. Watson, A.F. Prata, and V.J. Realmuto (2007), Development of an ultra-violet digital camera for volcanic SO2 imaging, *J. Volcanol. Geotherm. Res.*, 161, 47–56.

Bohren, C. F., and D.R. Huffman (1983), Absorption and Scattering of Light by Small Particles, 489 pp., Wiley-Interscience, New York.

Bonadonna, C., R. Genco, M. Gouhier, M. Pistolesi, R. Cioni, F. Alfano, Á. Höskuldsson, and M. Ripepe (2011), Tephra sedimentation during the 2010 Eyjafjallajökull eruption (Iceland) from deposit, radar and satellite observations, *J. Geophys. Res.*, 116, B12202, doi:10.1029/2011JB008462.

Bonadonna, C., and J.C. Phillips (2003), Sedimentation from strong volcanic plumes, *J. Geophys. Res.*, 108(B7), 2340, doi:10.1029/2002JB002034.

Bouche, E., S. Vergniolle, T. Staudacher, A. Nercessian, J.C. Delmont, M. Frogneux, F. Cartault, and A. Le Pichon (2010), The role of large bubbles detected from acoustic measurements on the dynamics of Erta 'Ale lava lake (Ethiopia), *Earth and Planetary Science Letters*, 295, 37–48.

Branan, Y., A. Harris, I. Watson, J. Phillips, K. Horton, G. Williamsjones, and H. Garbeil (2008), Investigation of at-vent dynamics and dilution using thermal infrared radiometers at Masaya volcano, Nicaragua, *Journal of Volcanology and Geothermal Research*, *169*(1-2), 34-47, doi:10.1016/j.jvolgeores.2007.07.021.

Burden, R.E., J.C. Phillips, and T.K. Hincks (2011), Estimating volcanic plume heights from depositional clast size, *J. Geophys. Res.*, 116, B11206, doi:10.1029/2011JB008548.

Burton, M., P. Allard, F. Mure, and C. Oppenheimer (2003), In Volcanic Degassing (eds Oppenheimer, C., Pyle, D. & Barclay, J.) 281–293 (Special Publication 2213, *Geological Society*, London, 2003).

Burton, M., C. Oppenheimer, L.A. Horrocks, and P.W. Francis (2000), Field measurement of CO2 and H2O emissions from Masaya Volcano, Nicaragua, by Fourier transform spectrometry, *Geology*, 28, 915–918.

C

Calvari, S., G.G. Salerno, L. Spampinato, M. Gouhier, A. La Spina, E. Pecora, A.J.L. Harris, P. Labazuy, E. Biale, and E. Boschi (2011), An unloading foam model to constrain Etna's 11–13 January 2011 lava fountaining episode, *J. Geophys. Res.*, 116, B11207, doi:10.1029/2011JB008407.

Carn, S.A., A.J. Prata, and S. Karlsdottir (2008), Circumpolar transport of a volcanic cloud from Hekla (Iceland), *J. Geophys. Res. Atmos.*, 113(D14).

Carr, M.J., and R.E. Stoiber (1977), Geologic setting of some destructive earthquakes in Central América, *Bull. Geol. Soc. Amer*, 5: 387-401.

Chazette, P., M. Bocquet, P Royer, V Winiarek, J.C. Raut, P. Labazuy, M Gouhier, M Lardier, and J.P. Cariou (2012), Eyjafjallajökull ash concentrations derived from both Lidar and modeling, *J. Geophys. Res*., 117, D00U14, doi:10.1029/2011JD015755.

Chouet, B.A. (1996), Long-period volcano seismicity: its source and use in eruption forecasting, *Nature*, 380:309–16.

Chouet, B.A., N. Hamisevicz, and T.R. McGetchin (1974), Photoballistics of volcanic jet activity at Stromboli, Italy, *J. Geophys. Res.*, 79, 4961–4976.

Chow, C.Y. (1979), An introduction to computational fluid mechanics,Hoboken, New Jersey: John Wiley & Sons.

Cigolini, C., and A. Borgia (1980), Consideraciones sobre la viscosidad y la estructura de las coladas: volcán Arenal, Costa Rica, *Rev. Geogr. Am. Central*, 11/12, doi: 10.1016/0377-0273(84)90072-6.

Cigolini, C., A. Borgia, and C. Casertano (1984), Intercrateric activity, aa-block lava viscosity and flow dynamics, *J. Volcanol. Geotherm. Res*., 20, 155–176.

Clarke, A.B., J.C. Phillips, and K.N. Chojnicki (2009), An investigation of Vulcanian eruption dynamics using laboratory analogue experiments and scaling analysis, *Methods*, 155-166.

Cole, P.D., E. Fernandez, E. Duarte, and A.M. Duncan (2005), Explosive activity and generation mechanisms of pyroclastic flows at Arenal volcano, Costa Rica between 1987 and 2001, *Bull. Volcanol.*, 67, 695–716.

D

Daag, A.S., B.S. Tubianosa, C.G. Newhall, N.M., Tungol, D. Javier, M.T Dolan, P.J.D Reyes, R.A. Arboleda, M.M.L Martinez, and M.T.M. Regalado (1996), Monitoring Sulfur Dioxide Emission at Mount Pinatubo, in Newhall, C.G. and Punongbayan, R.S. (Eds.), Fire and Mud: Eruptions and Lahars of Mount Pinatubo, Philippines; Philippine Institute of Volcanology and Seismology, Quezon City, and University of Washington Press, Seattle, 409–414.

D'Amours, R., R. Servranckx, J.P. Toviessi, and S. Trudel (1998), The operational use of the Canadian Emergency Response Model: Data assimilation, processing, storage, and dissemination. In: OECD Nuclear Energy Agency (Editor), Nuclear Emergency Data management: Proceedings of an International Workshop. Organisation for Economic Cooperation and Development. Nuclear Energy Agency, pp. 215–221.

Davi, R., G. O'Brien, L. De Barros, I. Lokmer, C. Bean, P. Lesage, M. M. Mora, and G.J. Soto (2012), Seismic source mechanisms of tremor events recorded on Arenal volcano, Costa Rica, retrieved by waveform inversion, *J. Volcanol. Geotherm. Res.*, 213-214, 1-13, doi:/10.1016/j.jvolgeores.2011.10.008.

Davi, R., G. O'Brien, I. Lokmer, C. Bean, P. Lesage, and M.M. Mora (2010), Moment tensor inversion of explosive long period events recorded on Arenal volcano, Costa Rica, constrained by synthetic tests, *J. Volcanol. Geotherm. Res.*, *194* (4), 189–200, doi: 10.1016/j.jvolgeores.2010.05.012.

De la Cruz-Reyna S., and G. Reyes-Dávila (2001), A model to describe precursory material-failure phenomena: application to short-term forecasting at Colima volcano, Mexico, *Bull. Volcanol.* 63, 297–308, doi: 10.1007/s004450100152.

Denlinger, R.P., and R.P. Hoblitt (1999), Cyclic eruptive behavior of silicic volcanoes, *Geology*, *27* (5), 459–462, doi:10.1130/0091-613(1999)027!0459:CEBOSV.2.3.CO;2.

Divoux, T., V. Vidal, F. Melo, and J.C. Geminard (2008), Acoustic emission associated with the bursting of a gas bubble at the free surface of a non-Newtonian fluid, *Phys. Rev. E*, 77, 056310, doi:10.1103/PhysRevE. 77.056310.

Doloire J. (2006), Traitement des signaux acquis par un radar Doppler volcanologique au sol lors d'une éruption de l'Arenal en février 2004. Rapport de stage ENGEES, Univ. Strasbourg, pp. 40.

Donnadieu F. (2012). Volcanological applications of Doppler radars: A review and examples from a transportable pulse radar in L-band. In "Doppler Radar", Intech, ISBN 979-953-307-352-0.

Donnadieu F., T. Druitt, C. Hervier (2004), Ground-based Doppler radar data from explosions of Arenal volcano. *IAVCEI Gen. Ass*., Pucon (Chile).

Donnadieu, F., G. Dubosclard, P. Allard, R. Cordesses, C. Hervier, J. Kornprobst, and J.F. Lénat (2003), Sondages des jets volcaniques par radar Doppler:applications à l'Etna. *Rapport quadriennal C.N.F.G.G. 1999-2002*, p.119-124.

Donnadieu, F., G. Dubosclard, R. Cordesses, T. Druitt, C. Hervier, J. Kornprobst, J. Lénat, P. Allard, and M. Coltelli (2005), Remotely monitoring volcanic activity with groundbased Doppler radar, *Eos Trans. AGU,* 86, 21, doi:10.1029/2005EO210001.

Donnadieu F., M. Gouhier, J. Fournet-Fayard, and C. Hervier (2008), Applications of pulsed ground-based Doppler radar to the study and monitoring of volcanoes, Ground-based radar observations for volcanoes workshop, Univ. Reading UK, p.6-8.

Donnadieu F., M. Gouhier, S. Valade, C. Hervier, and J. Fournet-Fayard (2009), Quantifying the dynamics of explosive eruptions using ground-based Doppler radar, *Workshop of the IAVCEI Commission on Explosive Volcanism, Clermont-Ferrand, France*, 26-29 Oct. 2009.

Donnadieu, F., C. Hervier, P. Freville, M. Coltelli, S. Scollo, L. Boccia, G. Di Massa, P. Cacault, M. Prestifilipo, C. Reymond, S. Rivet, and S. Valade (In prep), A new ground-based Doppler radar system to monitor the volcanic activity of Etna, *Natural Hazards and Earth System Sciences.*

Donnadieu, F., C. Hervier, P. Freville, J. Fournet-Fayard, J.-F. Fournol, P. Menny, C. Reymond, and C. Bernard (2009), The VOLDORAD 2B radar: Operational handbook, Note OPGC 07.09, Univ. Blaise Pascal Clermont-Ferrand, July 2009, 15p.

Donnadieu F., M. Mora, T.H. Druitt, and G.E. Alvarado (2006), Eruption dynamics of Arenal volcano, Costa Rica: insights from Doppler radar and seismic measurements. *Cities on Volcanoes 4,* Quito, Ecuador, p.89. Invited talk.

Donnadieu, F., S. Valade, and S. Moune (2011), Three dimensional transport speed of wind-drifted ash plumes using ground-based radar, *Geophys. Res. Lett.*, 38, L18310, doi:10.1029/2011GL049001.

Draxler, R.R., Hess, G.D. (1998), An overview of the Hysplit-4 modeling system or trajectories, dispersion, and deposition, *Australian Meteorological Magazine*, 47 (4), 295–308.

Dubosclard, G., R. Cordesses, P. Allard, C. Hervier, M. Coltelli, and J. Kornprobst (1999), First testing of a volcano doppler radar (VOLDORAD) at Mount Etna, Italy, *Geophys. Res. Lett.*, 26(22), 3389–3392, doi:10.1029/1999GL008371.

Dubosclard, G., F. Donnadieu, P. Allard, R. Cordesses, C. Hervier, M. Coltelli, E. Privitera, and J. Kornprobst (2004), Doppler radar sounding of volcanic eruption dynamics at Mount Etna, *Bull. Volc.*, 66, 443–456, doi:10.1007/s00445-003-0324-8.

E

Ebmeier, S.K., J. Biggs, T.A. Mather, G. Wadge, and F. Amelung (2010), Steady downslope movement on the western flank of Arenal volcano, Costa Rica, *Geochem. Geophys. Geosyst.*, 11, Q12004, doi:10.1029/2010GC003263.

Edmonds, M., R.A. Herd, B. Galle, and C.M. Oppenheimer (2003), Automated, high time-resolution of SO_2 flux at Soufrière Hills Volcano, Montserrat, *Bulletin of Volcanology*, 65, 578–586.

Endo, E.T., and T. Murray (1991), Real-time Seismic Amplitude Measurement (RSAM): a volcano monitoring and prediction tool, *Bull. Volcanol., 53*, 533-545, doi: 10.1007/BF00298154.

Eychenne, J. (2012), Budgets éruptifs et origine des paroxysmes explosifs andésitiques en système ouvert: l'éruption d'août 2006 du Tungurahua en Equateur. Mémoire de Thèse, Université Blaise Pascal, Laboratoire Magmas et Volcans, 249 pp.

Eychenne, J., J.L. Le Pennec, L. Troncoso, M. Gouhier, J.M. Nedelec (2011), Causes and consequences of bimodal grain-size distribution of tephra fall deposited during the August 2006 Tungurahua eruption (Ecuador), *Bull Volcanol*, DOI 10.1007/s00445-011-0517-5.

F

Finkel, R.A., and J.L. Bentley (1974), Quad trees a data structure for retrieval on composite keys, *Acta Informatica, Springer Berlin / Heidelberg, 4*, 1-9.

Formenti, Y., T.H. Druitt, and K. Kelfoun (2003), Characterisation of the 1997 vulcanian explosions of Soufrie`re Hills Volcano, Montserrat, by video analysis, *Bulletin of Volcanology*, 65, 587– 605.

Francis P, M.R. Burton, C. Oppenheimer (1998), Remote measurements of volcanic gas compositions by solar occultation spectroscopy, *Nature*, 396:567–570.

Francis, P., and D. Rothery (2000), Remote sensing of active volcanoes, *Annu Rev Earth Planet Sci*, 28:81–106.

Fudali, R.F., and W.G. Melson (1972), Ejecta Velocities Magma Chamber pressure and Kinetic asocieted with the 1968 Eruption Arenal volcano, *Bull. Volcanol.*, 35: 383-340.

Fukushima, Y., V. Cayol, and P. Durand (2005), Finding realistic dike models from interferometric synthetic aperture radar data: The February 2000 eruption at Piton de la Fournaise, *J. Geophys. Res., 110*, B03206, doi: 10.1029/2004JB003268.

G

Galle, B., C. Oppenheimer, A. Geyer, A. McGonigle, and M. Edmonds (2003), A mini-DOAS spectrometer in remote sensing of volcanic SO2 emissions, *Journal of Volcanology and Geothermal Research*, 119, 241–254.

Galle B., C. Oppenheimer, A. Geyer, A.J.S. McGonigle, M. Edmonds, and L. Horrocks (2002), A miniaturised ultraviolet spectrometer for remote sensing of SO_2 fluxes: a new tool for volcano surveillance, *J. Volcanol. Geotherm. Res.*, 119 (2002): 241-254.

Garcés, M.A. (1997), On the volcanic waveguide, *J. Geophys. Res.*, 102, p. 22 547, 22 564.

Garcés, M.A. (2000), Theory of acoustic propagation in a multi-phase stratified liquid flowing within an elastic-walled conduit of varying cross-sectional area, *J. Volcanol. Geotherm. Res.*, 101, 1–17.

Garcés, M. A., M.T. Hagerty, and S.Y. Schwartz (1998), Magma acoustics and time-varying melt propoerties at Arenal volcano, Costa Rica, *Geophys. Res. Lett.*, 25, 2293-2296.

Garcés, M.A., and S.R. McNutt (1997), Theory of the sound field generated by a resonant magma conduit, *J. Volcanol. Geotherm. Res.*, 78, 155–178.

Gardner, C.A., and R.A. White (2002), Seismicity, gas emission and deformation from 18 July to 25 September 1995 during the initial phreatic phase of the eruption of Soufriere Hills Volcano, Montserrat. In: Druitt, T.H., Kokelaar, B.P. (Eds.), The Eruption of

Soufriere Hills Volcano, Montserrat, from 1995 to 1999. . Memoirs, vol. 21. Geological Society, London, pp. 567–581.

Gerlach, T.M., H. Delgado, K.A. McGee, M.P. Doukas, J.J. Venegas, and L. Cárdenas (1997), Application of the LI-COR CO2 analyzer to volcanic plumes: A case study, Volcán Popocatéptl, Mexico, June 7 and 10, 1995, *J. Geophys. Res.*, 102(B4), 8005–8019, doi:10.1029/96JB03887.

Gerst, A. (2010), The First Second of a Strombolian Volcanic Eruption, Ph. D. Thesis, Hamburg University, Germany.

Gerst, A., M. Hort, P. Kyle, and M. Vöge (2006), The first second of a Strombolian eruption:velocity observations at Erebus volcano, Antarctica, *Eos Trans. AGU, Fall Meet. Suppl.*, 87(52), Abstr. V31G–04.

Gerst, A., M. Hort, P. Kyle, and M. Vöge (2008), 4D velocity of Strombolian eruptions and man-made explosions derived from multiple Doppler radar instruments, *J. Volc. Geotherm. Res.*, 177, 648–660, doi:10.1016/j.jvolgeores.2008.05.022.

Gill, P.E., W. Murray, and M.H. Wright (1981), Practical Optimization, Academic San Diego, Calif.

Glaze, L.S., P.W. Francis, S. Self, D.A. Rothery (1989), The 16 September 1986 eruption of Lascar Volcano, north Chile: satellite investigations, *Bull Volcanol*, 51 :149–160.

Goldstein, S. (1938), Modern Developments in Fluid Dynamics, Vol.1, Clarendon Press, Oxford, England.

Gonnermann, H.M., and M. Manga (2003), Explosive volcanism may not be an inevitable consequence of magma fragmentation, *Nature*, *426* (6965), 432–435, doi: 10.1038/nature02138.

Gouhier, M. (2008), Application du radar Doppler (VOLDORAD) à l'étude de la dynamique des éruptions Stromboliennes de l'Etna. Mémoire de Thèse, Université Blaise Pascal, Laboratoire Magmas et Volcans, 245 pp.

Gouhier, M., and D. Coppola (2011), Satellite-based evidence for a large hydrothermal system at Piton de la Fournaise volcano (Reunion Island), *Geophys. Res. Lett.*, 38, L02302, doi:10.1029/2010GL046183.

Gouhier, M., and F. Donnadieu (2008), Mass estimations of ejecta from Strombolian explosions by inversion of Doppler radar measurements, *J. Geophys. Res.*, 113, B10,202, doi:10.1029/2007JB005383.

Gouhier M., and F. Donnadieu (2010), The geometry of Strombolian explosions: insight from Doppler radar measurements, *Geophys. J. Int.* (2010) 183, 1376–1391 doi: 10.1111/j.1365-246X.2010.04829.x.

Gouhier M., and F. Donnadieu (2011), Systematic retrieval of ejecta velocities and gas fluxes at Etna volcano using L-Band Doppler radar, *Bull. Volcanol.*, 73, 9, 1139-1145. DOI 10.1007/s00445-011-0500-1.

Gouhier M., A. Harris, S. Calvari, P. Labazuy, Y. Guéhenneux, F. Donnadieu, and S. Valade (2011), Lava discharge during Etna's January 2011 fire fountain tracked using MSG-SEVIRI, V, *Bull Volcanol*, DOI 10.1007/s00445-011-0572-y.

Gorshkov, G.S. (1959), Gigantic eruption of the Volcano Bezymianny, *Bull. Volcan.*, 20, 77–109.

Gudmundsson, G. (2011), Respiratory Health Effects of Volcanic Ash with Special Reference to Iceland. A review, *The Clinical Respiratory Journa*l, Vol.5, pp. 2–9, (January 2011), ISSN 1752-6981.

Gurioli, L., A.J.L. Harris, B.F. Houghton, M. Polacci, and M. Ripepe (2008), Textural and geophysical characterization of explosive basaltic activity at Villarrica volcano, *J. Geophys. Res.*, 113, B08206, doi:10.1029/2007JB005328.

H

Hagerty, M.T., S.Y. Schwartz, M.A. Garces, and M. Protti (2000), Analysis of seismic and acoustic observations at Arenal Volcano, Costa Rica, 1995–1997, *Journal of Volcanology and Geothermal Research*, 101 (1–2), 27–65.

Harris, A., and M. Ripepe (2007), Synergy of multiple geophysical approaches to unravel explosive eruption conduit and source dynamics—A case study from Stromboli, *Chem. Erde, 67*, 1–35.

Harris, D., and W. Rose (1983), Estimating particle sizes, concentrations, and total mass of ash in volcanic clouds using weather radar, *J. Geophys. Res.*, 88(No. C15), 10,969–10,983.

Harris, D., W. Rose, R. Roe, and M. Thompson (1981), Radar observations of ash eruptions, *USGS Professional Paper*, 1250, 322–333.

Hellweg, M. (2000), Physical models for the source of Lascar's harmonic tremor, *J. Volcanol. Geotherm. Res., 101* (1-2), 183–198, doi: 10.1016/S0377-0273(00)00163-3.

Hofton, M.A., E. Malavassi, and J.B. Blair (2006), Quantifying recent pyroclastic and lava flows at Arenal Volcano, Costa Rica, using medium-footprint Lidar. *Geophysical Research Letters, 33,* L21306, doi:10.1029/2006GL027822.

Holland, A.C., and G. Gagne (1970), Rayleigh-Gans-Born Light Scattering by Ensembles of Randomly Oriented Anisotropic Particles, *Appl. Opt.*, 9, 1113.

Hort, M.K., L. Scharff, A. Gerst, K. Meier, M. Ripepe, and J.B. Johnson (2010), How do volcanoes deform immediately prior to an eruption: Observations of deformation inside a vent and on an active dome, *American Geophysical Union, Fall Meeting 2010*, abstract #V32B-03.

Hort, M., and R. Seyfried (1998), Volcanic eruption velocities measured with a micro radar, *Geophys. Res. Lett.*, 25(1), 113–116, doi:10.1029/97GL03482.

Hort, M., R. Seyfried, and M. Vöge (2001), Monitoring volcanic eruption velocities in three dimensions: First results from Doppler radar measurements at Stromboli volcano, *Eos Trans. AGU Fall Meet. Suppl.*, 82(47), F1400.

Hort, M., R. Seyfried, and M. Vöge (2003), Radar Doppler velocimetry of volcanic eruptions:theoretical considerations and quantitative documentation of changes in eruptive behavior at Stromboli Volcano, Italy, *Geophys. J. Int.*, 154, 515–532, doi:10.1046/j.1365-246X.2003.01982.x.

Hort, M., M. Vöge, R. Seyfried, and A. Ratdomopurbo (2006), In situ observation of dome instabillities at Merapi Volcano, Indonesia: A new tool for hazard mitigation, *J. Volc. Geotherm. Res.*, 153, 301–312, doi:10.1016/j.jvolgeores.2005.12.007.

Horton, K.A., G. Williams-Jones, H. Garbeil, T. Elias, A.J. Sutton, P. Mouginis-Mark, J.N. Porter, and S. Clegg (2006), Real-time measurement of volcanic SO_2 emissions: validation of a new UV correlation spectrometer (FLYSPEC), *Bull. Volcanol.*, 68, 4:323-327.

J

Jaupart, C., and S. Vergniolle (1988), Laboratory models of Hawaiian and Strombolian eruptions, *Nature, 331* (6151), 58–60, doi: 10.1038/331058a0.

Johnson, J.B. (2003), Generation and propagation of infrasonic airwaves from volcanic explosions, *J. Volcanol. Geotherm. Res.*, 121, 1–14.

Johnson, J.B. (2005), Vent mapping and source location variability at Stromboli mapped with small-aperture infrasound array, *Bull. Volcanol.*, 67, 1–14.

Johnson, J.B., and J.M. Lees (2000), Plugs and chugs–seismic and acoustic observations of degassing explosions at Karymsky, Russia and Sangay, Ecuador, *J. Volcanol. Geotherm. Res.*, *101* (1-2), 67–82, doi: 10.1016/S0377-0273(00)00164-5.

Johnson, J.B., J.M. Lees, and E.I. Gordeev (1998), Degassing explosions at Karymsky Volcano, Kamchatka, *Geophys. Res. Lett.*, *25* (21), 3999–4002, doi: 10.1029/1998GL900102.

Johnson, J.B., J.M. Lees, and N. Varley (2010), Characterizing complex eruptive activity at Santiaguito Volcano, Guatemala using infrasound semblance in networked arrays, *J. Volc. Geotherm. Res.*, 199, 1–14.

Johnson, J.B., M. Ripepe (2011), Volcano infrasound: A review, *Journal of volcanology and geothermal research*, 206, 61-69.

Johnson, J.B., M.C. Ruiz, J.M. Lees, and P. Ramon (2005), Poor scaling between elastic energy release and eruption intensity at Tungurahua Volcano, Ecuador, *Geophys. Res. Lett., 32* (15), L15304, doi: 10.1029/2005GL022847.

Johnson, J.B., R. Sanderson, J. Lyons, R. Escobar-Wolf, G. Waite, and J.M. Lees (2009), Dissection of a composite volcanic earthquake at Santiaguito, Guatemala, *Geophys. Res. Lett.*, 36 (L16308).

Jones, A., D. Thomson, M. Hort, B. Devenish (2007), The U.K. Met office's next-generation atmospheric dispersion model, NAME III. In: Borrego, C., Norman, A.-L. (Eds.), Air Pollution Modeling and Its Application XVII. Springer, Berlin, pp. 580–589.

K

Kaminski, E., S. Tait, F. Ferrucci, M. Martet, B. Hirn, and P. Husson (2011), Estimation of ash injection in the atmosphere by basaltic volcanic plumes: The case of the Eyjafjallajökull 2010 eruption. *Journal of Geophysical Research*, *116*(July), 1-10. doi:10.1029/2011JB008297.

Kawakatsu, H., S. Kaneshima, H. Matsubayashi, T. Ohminato, Y. Sudo, T. Tsutsui, K. Uhira, H. Yamasato, H. Ito, and D. Legrand (2000), Aso94: Aso seismic observation with broadband instruments, *J. Volcanol. Geotherm. Res.*, 101:129–54.

Kazahaya, R., T. Mori, and M. Iguchi (2010), The degassing fluctuation concerning sealing process before eruptions at Sakurajima volcano, Japan, *Am. Geophys. Un. Fall Meeting*, V52C-06.

Kittleman, L.R.J. (1964), Application of Rosin's distribution in size frequency analysis of clastic rocks, *J. Sediment. Petrol.*, 34, 483– 502.

Konstantinos, K.I., and V. Schlindwein (2002), Nature, wavefield properties and source mechanism of volcanic tremor: a review, *J. Volcanol. Geotherm. Res.*, 119, 161–187.

L

Labazuy, P., et al. (in press), Near real-time monitoring of the April-May 2010 Eyjafjallajökull ash cloud: an example of a web-based, satellite-data-driven, reporting system, *International Journal of Environment and Pollution*.

Lacasse, C., S. Karlsdottir, G. Larsen, H. Soosalu, W.I. Rose, and G.G.J. Ernst (2004), Weather radar observations of the Hekla 2000 eruption cloud, Iceland, *Bull. Volcanol.*, 66, 457– 473, doi:10.1007/s00445-003-0329-3.

Lautze, N.C., and B.F. Houghton (2007), Linking variable explosion style and magma textures during 2002 at Stromboli volcano, Italy, *Bull. Volcanol.*, 69, 445– 460.

Lavallée, Y., P.M. Benson, M.J. Heap, a Flaws, K.U. Hess, and D.B. Dingwell (2011), Volcanic conduit failure as a trigger to magma fragmentation, *Bulletin of Volcanology*, 2-4, doi:10.1007/s00445-011-0544-2.

Lees, J.M., M. Ruiz (2008), Non-linear explosion tremor at Sangay, Volcano, Ecuador, *J Volcanol Geotherm Res*, 176:170–178.

Leonardi, S., S. Gresta, and F. Mulargia (2000), Searching for a significant correlation between volcanic tremor amplitude and SO2 emissions at Mount Etna volcano, Sicily, *Geophys. J. Int ., 141*, 832-834.

Lesage, P. (2009), Interactive Matlab software for the analysis of seismic volcanic signals, *Computers and Geosciences*, 35 (10), 2137–2144, doi: 10.1016/j.cageo.2009.01.010.

Lesage, P., M.M. Mora, G.E. Alvarado, J. Pacheco, and J.P. Métaxian (2006), Complex behavior and source model of the tremor at Arenal volcano, Costa Rica, *J. Volcanol. Geotherm. Res.*, 157 (1-3), 49–59, doi: 10.1016/j.jvolgeores.2006.03.047.

M

Malavassi, E. (1979), Geology and petrology of Arenal Volcano, Costa Rica, Ms thesis, Univ. Hawaii at Manoa. 111 pp.

Malinconico Jr., L.L. (1987), On the variation of SO2 emission from volcanoes, *Journal of Volcanology and Geothermal Research*, 33, 231–237.

Marchetti, E., M. Ripepe, A.J.L. Harris, and D. Delle Donne (2009), Tracing the differences between Vulcanian and Strombolian explosions using infrasonic and thermal radiation energy, *Earth Planet. Sci. Lett., 279*, 273–281, doi:10.1016/j.epsl.2009.01.004.

Marignier, J.-L. (1999), Nicéphore Niépce 1765 - 1833: l'invention de la photographie. Paris : Belin.

Marzano F.S., S. Barbieri, E. Picciotti and S. Karlsdottir (2010a), Monitoring sub-glacial volcanic eruption using C-band radar imagery, *IEEE Trans. Geosci. Rem. Sensing*, vol. 58, n. 1, pp. 403-414.

Marzano, F., S. Barbieri, G. Vulpiani, and W. Rose (2006b), Volcanic ash cloud retrieval by ground-based microwave weather radar, *IEEE Trans. Geosci. Rem. Sens.*, 44(11 Part 2), 3235–3246, doi:10.1109/TGRS.2006.879116.

Marzano, F. S., S. Marchiotto, C. Textor, and D. J. Schneider (2010b), Model-Based Weather Radar Remote Sensing of Explosive Volcanic Ash Eruption, *IEEE Transactions on Geoscience and Remote Sensing*, *48*(10), 3591-3607, doi:10.1109/TGRS.2010.2047862.

Marzano, F.S., E. Picciotti, G. Vulpiani, and M. Montopoli (2012), Synthetic signatures of volcanic ash cloud particles from X-band dual-polarization radar, *IEEE Trans. Geosc. Remote Sens.*, 50(1), 193-211, doi:10.1109/TGRS.2011.2159225.

Marzano, F.S., G. Vulpiani, and W.I. Rose (2006a), Microphysical characterization of microwave radar reflectivity due to volcanic ash clouds, *IEEE Trans. Geosci. Remote Sens*., 44, 313 – 327, doi:10.1109/TGRS.2005.861010.

Mastin, L.G. (1991), A simple calculator of ballistic trajectories for blocks ejected during volcanic eruptions, *US Geol Surv*, Open-File Rep 01-45, v. 1.2. (Code available online at http://vulcan.wr.usgs.gov/Projects/Mastin)

Mastin, L.G., M. Guffanti, R. Servranckx, P. Webley, S. Barsotti, K. Dean, A. Durant, J.W. Ewert, A. Neri, W.I. Rose, D. Schneider, L. Siebert, B. Stunder, G. Swanson, A. Tupper, A. Volentik, and C.F. Waythomas (2009), A multidisciplinary effort to assign realistic source parameters to models of volcanic ash-cloud transport and dispersion during eruptions, *J. Volcanol. Geotherm. Res.*, doi:10.1016/j.jvolgeores.2009.01.008.

Matumoto, T. (1976), Predictions of a volcanic eruption implied from seismic data, *Rev. Geogr. Inst. Panamericano de Geografia e Historia.*, 5: 285-293.

Mauk, F.J. (1983), Utilization of seismically recorded infrasonic–acoustic signals to monitor volcanic explosions: the El Chichon sequence 1982 – a case study, *J. Geophys. Res.*, 88 (B12), 10,385–10,401.

McGetchin, T.R., M. Settle, and B. Chouet (1974), Cinder cone growth modeled after northeast crater, Mount Etna, Sicily, *J. Geophys. Res.*, 79, 3257– 3272, doi:10.1029/JB079i023p03257.

McGonigle, A.J.S., P. Delmelle, C. Oppenheimer, V.I. Tsanev, T. Delfosse, G. Williams-Jones, K. Horton, and T.A. Mather (2004), SO2 depletion in tropospheric volcanic plumes, *Geophysical Research Letters 31*, doi:10.1029/2004GL019990.

McGonigle, A.J.S., S. Inguaggiato, A. Aiuppa, A.R. Hayes, and C. Oppenheimer (2005), Accurate measurement of volcanic SO_2 flux: Determination of plume transport speed and integrated SO_2 concentration with a single device, *Geochem. Geophys. Geosyst.*, 6, Q02003, doi:10.1029/2004GC000845.

McNutt, S.R. (2002), Volcano seismology and monitoring for eruptions, *International Handbook of Earthquake and Engineering Seismology*, Int. Geophys. Ser., vol. 81, edited by W. H. K. Lee et al., pp. 383–406, Elsevier, New York.

McNutt, S.R., H. Rymer, and J. Stix (2000), Synthesis of volcano monitoring, H. Sigurdsson, B.F. Houghton, S.R. McNutt, H. Rymer, J. Stix, Editors , *Encyclopedia of Volcanoes*, Academic Press, San Diego, pp. 1165–1183.

Mele, D., P. Dellino, R. Sulpizio, and G. Braia (2011), A systematic investigation on the aerodynamics of ash particles, *Journal of Volcanology and Geothermal Research*, *203*(1-2), 1-11, doi:10.1016/j.jvolgeores.2011.04.004.

Melnik, O., and R.S.J. Sparks (2002), Dynamics of magma ascent and lava extrusion at Soufrière Hills Volcano, Montserrat, *Geological Society, London, Memoirs*, *21* (1), 153–171, doi:10.1144/GSL.MEM.2002.021.01.07.

Melson, W. (1989), Las erupciones del volcán Arenal: 1 al 13 de abril de 1989, *Boletin de Vulcanología*, 20: 15-22.

Melson, W., and R. Sáenz (1968), The eruption of Volcán Arenal, Costa Rica: Preliminary summary of field and laboratory studies. Smithsonian Institution Center for Short-Lived Phenomena, *Report 7. Cambridge, Massachussetts*, 35 pp. Rapport Interne, ICE.

Métaxian, J.P., P. Lesage, R. Barquero, and A. Creusot-Eon (1996), Características espectrales de las señales sísmicas y estimación de Vp en la estructura superficial del Volcán Arenal, *Bol. Obs. Vulc. Arenal*, 6 (11-12): 23-44.

Métaxian, J.P., G.S. O'Brien, C.J. Bean, B. Valette, M. Mora (2009), Locating volcanoseismic signals in the presence of rough topography: wave simulations on Arenal volcano, Costa Rica, *Geophysical Journal International*, 179, 3. doi:10.1111/j.1365-246X.2009.04364.x.

Mie, G. (1908), Beiträge zur Optik trüber Medien, speziell kolloidaler Metallösungen, *Ann. Phys.*, 330(3), 377– 445.

Millan, M.M., A.J. Gallant, H.E. Turner (1976), The application of correlation spectroscopy to the study of dispersion from tall stacks, *Atmospheric Environment*, 10, 499–511.

Miller, T.P., and T.J. Casadevall (2000), Volcanic Ash Hazards to Aviation. In: Sigurdsson, H., Houghton, B.F., McNutt, S.R., Rymer, H., Stix, J. (Eds.), Encyclopedia of Volcanoes. Academic Press, San Diego, pp. 915–930.

Minakami, T., S. Utibori, and S. Hiraga (1969), The 1968 Eruption of Volcano Arenal, Costa Rica, *Bull. Earth. Res. Inst.*, 47,783-802.

Mishchenko, M.I., L.D. Travis, D.W. Mackowski (1996), *T* -matrix computations of light scattering by nonspherical particles: a review, *JQSRT*, 55:535–75.

Moffat, A.J., M.M. Millan (1971), The applications of optical correlation techniques to the remote sensing of SO2 plumes using sky light, *Atmospheric Environment*, 5, 677–690.

Mora, M. (2003), Etude de la structure superficielle et de l'activité sismique du volcan Arenal, Costa Rica, Ph.D. thesis, Laboratoire de Géophysique Interne et Tectonophysique, Univ. de Savoie, Le Bourget du Lac, France.

Mora, M., P. Lesage, F. Donnadieu, S. Valade, A. Schmidt, G. Soto, W. Taylor, and G. Alvarado (2009), Joint seismic, acoustic and Doppler radar observations at Arenal volcano, Costa Rica: preliminary results, in *VOLUME Project*, edited by C. J. Bean, A. K. Braiden, I. Lokmer, F. Martini, and G. S. O'Brien, pp. 330–340, VOLUME Project Consortium, Dublin.

Mora, M., P. Lesage, J. Dorel, P.Y. Bard, J.P. Métaxian, G.E. Alvarado, C. Leandro (2001), Detection of seismic site effects by using H/V spectral ratios at Arenal volcano (Cost Rica), *Geophys. Res. Lett*., 28, 2991– 2994.

Mora, M.M., P. Lesage, B. Valette, G.E. Alvarado, C. Leandro, J.P. Métaxian, and J. Dorel (2006), Shallow velocity structure and seismic site effects at Arenal volcano, Costa Rica, *J. Volcanol. Geotherm. Res.*, *152* (1-2), 121–139, doi: 10.1016/j.jvolgeores.2005.09.013.

Morales, L.D., J.F. Soley, G. Alvarado, A. Borgia, and G Soto (1988), Análisis espectral de algunas señales de los volcanes Arenal y Poás (Costa Rica) y su relación con la actividad eruptive, *Bol. Obs. Vulc. Arenal*, 1 (2): 1-25.

Mori, T., and M. Burton (2006), The SO2 camera: A simple, fast and cheap method for ground-based imaging of SO2 in volcanic plumes, *Geophys. Res. Lett.*, 33, L24804, doi:10.1029/ 2006GL027916.

Mori, T., K. Notsu, Y. Tohjima, H. Wakita, P.M. Nuccio, and F. Italiano (1995), Remote detection of fumarolic gas chemistry at Vulcano, Italy, using an FT-IR spectral radiometer, *Earth Planet. Sci. Lett.*, 134.

Mori, J., H. Patia, C. McKee, I. Itikarai, P. Lowenstein, P. De Saint Ours, and B. Talai (1989), Seismicity associated with eruptive activity at Langila Volcano, Papua New Guinea, *J. Volcanol. Geotherm. Res.*, 38, 243–255, doi:10.1016/0377-0273(89)90040-1.

Morton, B.R., G. Taylor, and J.S. Turner (1956), Turbulent Gravitational Convection from Maintained and Instantaneous Sources, *Proceedings of the Royal Society of London. Series A. Mathematical and Physical Sciences, 234*, 1-23.

Mouginis-Mark, P.J., J.A. Crisp, and J.H. Fink (Eds.), (2000), Remote sensing of active volcanism, *American Geophysical Union, Geophysical*, Monograph 116, *American Geophysical Union*, Washington, DC.

Murillo, S., and P. Ruiz (2004), Datos paramétricos de las coladas de lava del volcán Arenal (Costa Rica) entre 1968 y 2002, *Boletín del Observatorio Sismológico y Vulcanológico de Arenal y Miravalles*, 15 (27), 25–33.

N

Nadeau, P.A., J.L. Palma, and G.P. Waite (2011), Linking volcanic tremor, degassing, and eruption dynamics via SO_2 imaging., *Geophys. Res. Lett.*, 38, L01304, doi: 10.1029/2010GL045820.

Nakamura, Y. (1984), The 1888 eruption of Bandai volcano, Japan: Grain size distribution, paper presented at IAVCEI Meeting, Int. Assoc. of Volcanol. and Chem. of the Earth's Interior, Rome, 13– 17 Aug.

Neuberg, J. (2000), Characteristics and causes of shallow seismicity in andesite volcanoes, *Phil. Trans. R. Soc. Lond. A*, *358* (1770), 1533–1546, doi: 10.1098/rsta.2000.0602.

Neuberg, J.W. (2006), Multi-parameter monitoring and modelling of 607 volcanic processes. In: Mader, H.M., Coles, S.G., Connor, C.B. (Eds.), Statistics in Volcanology. Special Publications of IAVCEI, *Geological Society*, London, pp. 215–230.

Neuberg, J., R. Luckett, M. Ripepe, and T. Braun (1994), Highlights from a seismic broadband array on Stromboli volcano, *Geophys. Res. Lett*, 21:749–52.

O

Oberhuber, J. (1998), Volcanic plume simulation on large scales, *Journal of Volcanology and Geothermal Research*, *87*(1-4), 29-53, doi:10.1016/S0377-0273(98)00099-7.

Oppenheimer, C., P. Francis, M. Burton, A.J.H. Maciejewski and L. Boardman (1998), Remote measurement of volcanic gases by Fourier transform infrared spectroscopy, *Applied Physics B*, 67, pp. 505–515.

Ozerov, A.Y. (2010), The Mechanism of Basaltic Explosions: Experimental Modeling., *Journal of Volcanology and Seismology*, *4* (5), 295309, doi: 10.1134/S0742046310050015.

P

Patrick, M.R. (2007), Dynamics of strombolian ash plumes from thermal video: motion, morphology, and air entrainment, *J. Geophys. Res.*, 112, B06202. doi:10.1029/2006JB004387.

Patrick, M.R., A.J.L. Harris, M. Ripepe, J. Dehn, D.A. Rothery, and S. Calvari (2007), Strombolian explosive styles and source conditions: insights from thermal (FLIR) video, Bull. *Volcanol.*, 69, 769–784.

Platt, U. (1994), Differential optical absorption spectroscopy (DOAS). In: Sigrist, M.W. (Ed.), Air monitoring by spectroscopic techniques, Wiley, Chichester, pp. 27–84.

Piedelievre, J.P., L. Musson-Genon, F. Bompay (1990), MEDIA — An Eulerian model of atmospheric dispersion: First validation on the Chernobyl release, *Journal of Applied Meteorology*, 29 (12), 1205–1220.

Pouchol, L. (2005), Étude des mécanismes éruptifs de l'Arénal grâce au radar Doppler. Rapport de stage T.E.R. Master 1 Sciences de la Terre, *Univ. Blaise Pascal, Clermont-Ferrand II*, pp. 33.

Prata, A.J. (1989), Radiative transfer calculations for volcanic ash clouds, *Geophysical Research Letter*., 16 (11), 1293–1296.

Prata, A.J., I.J. Barton (1993), Detection and discrimination of volcanic ash clouds by infrared radiometry I. In: Casadevall, T. (Ed.), Theory, International Symposium on Volcanic Ash and Aviation Safety. USGS.

Prata, A.J., and C. Bernardo (2009), Retrieval of volcanic ash particle size, mass and optical depth from ground-based thermal infrared camera, *J. Volcanol. Geotherm. Res.*, 186, 91–107.

Press, W.H., B.P. Flannery, A.T. Saul, and W.T. Vetterling (1992), Numerical Recipes, 2nd ed., *Cambridge Univ. Press*, New-York.

Punongbayan, R.S., C.G. Newhall, M.L.P. Bautista, D. Garcia, D.H. Harlow, R.P. Hoblitt, J.P. Sabit, and R.U. Solidum (1996), Eruption hazard assessments and warnings, in: C.G. Newhall, R.S. Punongbayan (Eds.), Fire and Mud: Eruptions and Lahars of Mount Pinatubo, Phillipines, University of Washington Press, Seattle, WA, pp. 67-85.

R

Ramsey, M.S., and L.P. Flynn (2004), Strategies, insights, and the recent advances in volcanic monitoring and mapping with data from NASA's Earth Observing System, *J Volcanol Geotherm Res*, 135(1–2):1–11.

Riley, C.M., W.I. Rose, and G.J.S. Bluth (2003), Quantitative shape measurements of distal volcanic ash, *J. Geophys. Res.*, 108(B10), 2504, doi:10.1029/2001JB000818.

Ripepe, M., and T. Braun (1994), Air-wave phases in strombolian explosion-quake seismograms: a possible indicator for the magma level?, *Acta Vulcanol.*, 5, 201–206.

Ripepe, M., S. Ciliberto, and M. Della Schiava (2001), Time constraints for modeling source dynamics of volcanic explosions at Stromboli, *J. Geophys. Res.*, 106 (B5), 8713–8727.

Ripepe, M., and E. Gordeev (1999), Gas bubble dynamics model for a shallow volcanic tremor at Stromboli. *J. Geophys. Res.*, 104 (B5), 10,639–10,654.

Ripepe, M., A.J.L Harris, and R. Carniel (2002), Thermal, seismic and infrasonic evidences of variable degassing rates at Stromboli volcano, *J. Volcanol. Geotherm.*, Res. 118, 285–297.

Ripepe, M., and E. Marchetti (2002), Array tracking of infrasonic sources at Stromboli volcano, *Geophys. Res. Lett.*, 29 (22), 2076.

Ripepe, M., P. Poggi, T. Braun, and E. Gordeev (1996), Infrasonic waves and volcanic tremor at Stromboli, *Geohys. Res. Lett.*, 23, 181–184.

Ripepe, M., P. Poggi, and E. Marchetti (2004), Small aperture infrasonic array monitors activity of Stromboli volcano, *Inframatics*, 7, 1–14.

Ripepe, M., M. Rossi, and G. Saccorotti (1993), Image processing of explosive activity at Stromboli, *J. Volcanol. Geotherm.*, Res. 54, 335–351.

Rose, W.I., A.B. Kostinski, and L. Kelley (1995), Real time C band Radar 891 observations of 1992 eruption clouds from Crater Peak, Mount Spurr 892 Volcano, Alaska, U.S. *Geol. Surv. Bull.*, 2139, 19– 28, 1995.

Rowe, C.A., R.C. Aster, P.R. Kyle, R.R. Dibble, and J.W. Schlue (2000), Seismic and acoustic observations at Mount Erebus Volcano, Ross Island, Antarctica, 1994–1998, *Journal of Volcanology and Geothermal Research*, 101 (1–2), 105–128.

Rust, A.C., N.J. Balmforth, and S. Mandre (2008), The feasibility of generating low-frequency volcano seismicity by flow through a deformable channel, in Fluid motions in volcanic conduits; a source of seismic and acoustic signals, ed. Lane, S.J. and J.S. Gilbert, *London Geological Society*, Special Publications, 307, 45–56, doi: 10.1144/SP307.4.

S

Sahetapy-Engel, S.T.M., and A.J.L Harris (2009), Thermal structure and heat loss at the summit crater of an active lava dome, *Bull. Volcanol.*, 71, 15–28.

Sahetapy-Engel, S.T.M., A.J. Harris, and E. Marchetti (2008), Thermal, seismic and infrasound observations of persistent explosive activity and conduit dynamics at Santiaguito lava dome, Guatemala, *J. Volcanol. Geotherm. Res.*, *173* (1-2), 1–14, doi: 10.1016/j.jvolgeores.2007.11.026.

Sambridge, M. (1999a), Geophysical inversion with a neighbourhood algorithm, I, Searching a parameter space, *Geophys. J. Int.*,*138*, 479–494.

Sambridge, M. (1999b), Geophysical inversion with a neighbourhood algorithm, II, Appraising the ensemble, *Geophys. J. Int.*, *138*, 727–746.

Sambridge, M., and K. Mosegaard (2002), Monte Carlo Methods in Geophysical Inverse Problems, *Rev. Geophys, 40(3)*, 1009, doi:10.1029/2000RG00089.

Sanderson, R., J.B. Johnson, and J.M. Lees (2010), Ultra-long period seismic signals and cyclic deflation coincident with eruptions at Santiaguito volcano, Guatemala, *J. Volcanol. Geoth. Res.*, 198, pp. 35–44.

Sauvageot, H. (1992), Radar Meteorology, 366 pp., Artech House, Boston, Mass.

Scharff, L., M. Hort, A. Harris, M. Ripepe, J. Lees, and R. Seyfried (2008), Eruption dynamics of the SW crater of Stromboli volcano, Italy – An interdisciplinary approach, *J. Volc. Geotherm. Res.*, 176(4), 565–570, doi:10.1016/j.jvolgeores.2008.05.008.

Scharff, L., F. Ziemen, M. Hort, A. Gerst, and J.B. Johnson (in press), A Detailed View Into the Eruption Clouds of Santiaguito Volcano, Guatemala, Using Doppler Radar*J. Geophys. Res*., doi:10.1029/2011JB008542.

Schick, R. (1988), Volcanic tremor-source mechanisms and correlation with eruptive activity, *Natural Hazards*, *1*(2), 125–144.

Scollo, S., M. Coltelli, F. Prodi, M. Folegani, and S. Natali (2005), Terminal settling velocity measurements of volcanic ash during the 2002-2003 Etna eruption by an X-band microwave rain gauge disdrometer, *Geophysical Research Letters*, *32*(10).

Scollo, S., M. Prestifilippo, G. Spata, M. D'Agostino, and M. Coltelli (2009), Monitoring and forecasting Etna volcanic plumes, *Nat. Hazards Earth Syst. Sci.*, 9, 1573–1585.

Scorer, R.S. (1957), Experiments on convection of isolated masses of buoyant fluid, *J. Fluid Mech.*, *2*, 583–594.

Searcy, C., K. Dean, and W. Stringer (1998), PUFF: A high-resolution volcanic ash tracking model, *Journal of Volcanology and Geothermal Research*, 80, 1–16.

Self, S., R.S.J. Sparks, B. Booth, and G.P.L. Walker (1974), The 1973 Heimaey Strombolian Scoria deposit, Iceland, *Geol. Mag.*, 111, 539–548.

Self, S., L. Wilson, and I.A. Nairn (1979), Vulcanian eruption mechanisms, *Nature*, 277, 440-443.

Sheridan, M.F. (1971), Particle-size characteristics of pyroclastic tuffs, *J. Geophys. Res.*, 76, 5627– 5634, doi:10.1029/JB076i023p05627.

Sheridan, M.F., K.H. Wohletz, and J. Dehn (1987), Discrimination of grain-size subpopulations in pyroclastic deposits, *Geology*, 15, 367– 370, doi:10.1130/0091-7613(1987)15<367:DOGSIP>2.0.CO;2.

Soltzberg, L.J., P.G. Bowers, and C. Hofstetter (1997), A computer model for soda bottle oscillations: "the bottelator", *J. Chem. Educ.*, *74* (6), 711–714, doi: 10.1021/ed074p711.

Soto, G.J., G.E. Alvarado (2006), Eruptive history of Arenal volcano, Costa Rica, 7 ka to present, *Journal of Volcanology and Geothermal Research*, 157. doi:10.1016/j.volgeores.2006.03.041.

Soto, G., G. Alvarado, and M. Ghigliotti (1998), El registro eruptivo de Arenal en el lapso 3000-7000 años antes del presente y nuevas deducciones sobre la edad del volcán, *Bol. Obs. Vulc. Arenal*, 9 (17-18): 19-49, 1996.

Spampinato, L., S. Calvari, C. Oppenheimer, E. Boschi (2011), Volcano surveillance using infrared cameras, *Earth Sci Rev*,106:63-91.

Sparks, R.S.J. (2003), Frontiers: Forecasting volcanic eruptions, *Earth Planet. Sci. Lett.*, 210, 1 –15.

Sparks, R.S.J., M.I. Bursik, S.N. Carey, J.S. Gilbert, L.S. Glaze, H. Sigurdsson, and A.W. Woods (1997), Volcanic Plumes, John Wiley, Chichester, U. K.

Sparks, R.S.J., and L. Wilson (1982), Explosive volcanic eruptions V. Observations of plume dynamics during the 1979 Soufriere eruption, St Vincent. *Geophys J R Astron Soc*, 69:551–570.

Spieler, O., M. Alidibirov, and D.B. Dingwell (2003), Grain-size characteristics of experimental pyroclasts of 1980 Mount St. Helens cryptodome dacite: Effects of pressure drop and temperature, *Bull. Volcanol.*, 65, 90–104.

Steinberg, G., and J. Babenko (1978), Experimental velocity and density determination of volcanic gases during eruption, *Journal of Volcanology and Geothermal Research, 3*, 89 – 98.

Steinbger, G., and V. Lorenz (1983), External ballistic of volcanic explosions, *Bull. Volcanol.*, 46, 333–348.

Stix, J., R.C. Torres, L. Narváez M, G.P. Cort**é**s J, J.A. Raigosa, D. G**ó**mez M, and R. Castonguay (1997), A model of vulcanian eruptions at Galeras volcano, Colombia, *J. Volcanol. Geotherm. Res.*, *77* (1-4), 285–303, doi: 10.1016/S0377-0273(96)00100-X.

Stohl, A., F. Prata, H. Elbern, S. Scollo, and S. Varghese (2010), Description of Some European Ash Transport Models. In: C. Zehner, Ed. (2010). Monitoring Volcanic Ash from Space. Proceedings of the ESA-EUMETSAT workshop on the 14 April to 23 May 2010 eruption at the Eyjafjoll volcano, South Iceland. Frascati, Italy, 26-27 May 2010. ESA-Publication STM-280. doi:10.5270/atmch-10-01.

Stoiber, R.E., L.L. Malinconico Jr., and S.N. Williams (1983), Use of the correlation spectrometer at volcanoes. In: Tazieff, H., Sabroux, J.C. (Eds.), Forecasting Volcanic Events, pp. 425–444. Amsterdam-New York.

Symonds, R.B., W.I. Rose, G.J.S Bluth, and T.M. Gerlach (1994), Volcanic-gas studies: Methods, results, and applications. In: Carroll, M.R., Holloway, J.R. (Eds.), Volatiles in Magmas. *Reviews in Mineralogy*, vol. 30, pp. 1–60.

Szramek, L., J.E. Gardner, and J. Larsen (2006), Degassing and microlite crystallization of basaltic andesite magma erupting at Arenal Volcano, Costa Rica, *J. Volcanol. Geotherm. Res.*, 157, 182–201.

T

Thomas, H.E., and I.M. Watson (2009), Observations of volcanic emissions from space: current and future perspectives, *Nat. Hazards*, (2010) 54, 323–354, doi:10.1007/s11069-009-9471-3,283.

Toda, S., RS. Stein, and T. Sagiya (2002), Evidence from AD 2000 Izu islands earthquake swarm that stressing rate governs seismicity, *Nature*, 419:58–61.

Turner, J. S. (1979), Buoyancy Effects in Fluids, Cambridge Univ.Press, Cambridge, UK.

U

Urbanski, N., M. Vöge, R. Seyfried, L. Rüpke, T. Petersen, T. Hanebuth, and M. Hort (2002), Fifteen days of continuous activity survey at Stromboli volcano, Italy, in late September 2000: Doppler radar, seismicity, infrared, soil humidity, and mapping of the crater region, *Int. J. Earth Sci.*, 91(4), 712–722, doi:10.1007/s00531-001-0242-y.

V

Valade, S., and F. Donnadieu (2011), Ballistics and ash plumes discriminated by Doppler radar, *Geophys. Res. Lett*., 38, L22301, doi:10.1029/2011GL049415.

+ GRL cover image (Volume 38, No 22.)

+ EOS research spotlight (Volume 93, No 2):

Balcerak, E. (2012), Observing volcanic ash plumes and ballistics using Doppler radar, *Eos Trans. AGU*, 93(2), 28, doi:10.1029/2012EO020025.

Valade, S., F. Donnadieu, A. Augier, and M. Gouhier (in prep), Tracking and modelling of pyroclastic emissions using ground Doppler radar: constraints on eruptive parameters from inversion modelling, Geological Society Special Publication, Remote sensing of volcanoes & volcanic processes: integrating observation & modelling, William Smith Meeting, London, 2011.

Valade, S., F. Donnadieu, P. Lesage, M. M. Mora, A. J. L. Harris, and G. Alvarado (2012), Explosion mechanisms at Arenal volcano, Costa Rica: an interpretation from integration of seismic and Doppler radar data, *J. Geophys. Res.*, doi:10.1029/2011JB008623.

Van der Laat, R., and M.J. Carr (1989), In: McClelland, L., Simkin, T., Nielsen, M., Summers, E., Stein, T.C. (Eds.), Global Volcanism 1975–1985: The First Decade of Reports from the Smithsonian Institution's Scientific Event Alert Network (SEAN). Prentice Hall, Englewood Cliffs, NJ, pp. 510–511.

Vergniolle, S., M. Boichu, and J. Caplan-Auerbach (2004), Acoustic measurements of the 1999 basaltic eruption of Shishaldin volcano, Alaska 1. Origin of strombolian activity, *J. Volcanol. Geotherm*., Res 137, 109–134.

Vergniolle, S., and G. Brandeis (1994), Strombolian explosions. 1. A large bubble breaking at the surface of a lava column as a source of sound, *Journal of Geophysical Research*, Solid Earth 101 (B9), 20433–20447.

Vergniolle, S., G. Brandeis, and J.C. Mareschal (1996), Strombolian explosions: 2. Eruption dynamics determined from acoustic measurements, *J. Geophys. Res.*, 101(B9), 20,449–20,466, doi:10.1029/96JB01925.

Vöge, M., and M. Hort (2008), Automatic classification of dome instabilities based on Doppler radar measurements at Merapi volcano, Indonesia: Part I, *Geophys. J. Int.*, 172(3), 1188–1206, doi:10.1111/j.1365-246X.2007.03605.x.

Vöge, M., and M. Hort (2009), Installation of a Doppler radar monitoring system at Merapi volcano, Indonesia, *IEEE Trans. Geosci. Rem. Sens.*, 47(1 Part 2), 251–271, doi:10.1109/TGRS.2008.2002693.

Vöge, M., M. Hort, and R. Seyfried (2005), Monitoring volcano eruptions and lava domes with Doppler radar, *Eos Trans. AGU*, 86(51), 537, 541, doi:10.1029/2005EO510001.

Vöge, M., M. Hort, R. Seyfried, and A. Ratdomopurbo (2008), Automatic classification of dome instabilities based on Doppler radar measurements at Merapi volcano, Indonesia: Part II, *Geophys. J. Int.*, 172(11), 1207–1218, doi:10.1111/j.1365-246X.2007.03665.x.

Voight, B., R.S.J. Sparks, A.D. Miller, R.C. Stewart, R.P. Hoblitt, A. Clarke, J. Ewart, W.P. Aspinall, B. Baptie, T.H. Druitt, R.A. Herd, P. Jackson, A.B. Lockhart, S.C. Loughlin, L. Lynch, J. McMahon, G.E. Norton, R. Robertson, I.M. Watson, and S.R. Young (1999), Magma flow instability and cyclic activity at Soufriere Hills Volcano, Montserrat, B.W.I, *Science*, 283(1999) 1138^1142.

Volten, H., O. Muñoz, J.W. Hovenier, J.F. de Haan, W. Vassen, W.J. van der Zande, L.B.F.M. Waters (2005), WWW scattering matrix database for small mineral particles at 441.6 and 632:8 nm, *Journal of Quantitative Spectroscopy & Radiative Transfer*, 90, 191–206.

Volten H, O. Muñoz, E. Rol, J.F. de Haan, W. Vassen, J.W. Hovenier, K. Muinonen, T. Nousiainen (2001), Scattering matrices of mineral particles at 441:6 nm and 632:8 nm, *J Geophys Res*, 106:17,375–401.

W

Wadge, G. (1983), The magma budget of Volcan Arenal, Costa Rica from 1968 to 1980, *J. Volcanol. Geotherm. Res*, 19, 281–302.

Wadge, G., D. Oramas Dorta, and P. Cole (2006), The magma budget of Volcán Arenal, Costa Rica from 1980 to 2004, *J. Volcanol. Geotherm. Res.*, *157* (1-3), 60–74, doi: 10.1016/j.jvolgeores.2006.03.037.

Wen, S., and W.I. Rose (1994), Retrieval of sizes and total masses of particles in volcanic clouds using AVHRR bands 4 and 5, *J Geophys Res*, 99:5421–5431.

Williams-Jones, G., K.A. Horton, T. Elias, H. Garbeil, P.J. Mouginis-Mark, A.J. Sutton, and A.J.L. Harris (2006), Accurately measuring volcanic plume velocity with multiple UV spectrometers, *Bull. Volcanol.*, 68, 328–332.

Williams-Jones, G., J. Stix, M. Heiligmann, J. Barquero, E. Fernández, and E.D. González (2001), A model of degassing and seismicity at Arenal Volcano, Costa Rica, *J. Volcanol. Geotherm. Res.*, 108: 121-139.

Wilson, L. (1980), Relationships between pressure, volatile content and ejecta velocity in three types of volcanic explosion, *J. Volcanol. Geotherm. Res.*, 8 (2-4), 297–313, doi: 10.1016/0377-0273(80)90110-9.

Wohletz, K.H., M.F. Sheridan, and W.K. Brown (1989), Particle size distributions and the sequential fragmentation/transport theory applied to volcanic ash, *J. Geophys. Res.*, 94, 15,703–15,715, 721, doi:10.1029/JB094iB11p15703.

Woods, A.W. (1988), The fluid dynamics and thermodynamics of eruption columns, *Bull. Volcanol.*, 50, 169– 193.

Y

Yamamoto, H., I.M. Watson, J.C. Phillips, and G.J. Bluth (2008), Rise dynamics and relative ash distribution in vulcanian eruption plumes at Santiaguito Volcano, Guatemala, revealed using an ultraviolet imaging camera, *Geophys. Res. Lett.*, 35, L08314.

Yamasato, H. (1998), Nature of infrasonic pulse accompanying low frequency earthquake at Unzen Volcano, *Japan. Bull. Volcanol. Soc. Japan*, 43, 1–13.

Yokoo, A., and M. Iguchi (2010), Using infrasound waves from eruption video to explain ground deformation preceding the eruption of Suwanosejima volcano, Japan, *J. Volc. Geotherm. Res.*, 196 (3–4), 287–294.

Yokoo, A., T. Tameguri, and M. Iguchi (2009), Swelling of a lava plug associated with a Vulcanian eruption at Sakurajima Volcano, Japan, as revealed by infrasound record: case study of the eruption on January 2, 2007, *Bull. Volcanol.*, 71 (6), 619–630.

Z

Zehner, C. (2010), Ed. Monitoring Volcanic Ash from Space. Proceedings of the ESA-EUMETSAT workshop on the 14 April to 23 May 2010 eruption at the Eyjafjoll volcano, South Iceland. Frascati, Italy, 26-27 May 2010. ESA-Publication STM-280. doi:10.5270/atmch-10-01.

Zobin, V.M., G.A. Reyes, E. Guevara, and M. Bretón (2009), Scaling relationship for Vulcanian explosions derived from broadband seismic signals, *J. Geophys. Res., 114*, B03203, doi: 10.1029/2008JB005983.

Appendixes

Appendix A. *Seismo_Radar_Correlation* software

Seismo_Radar_Correlation is a software designed to carry out correlations between seismic and Doppler radar signals recorded in volcanic settings. It provides several tools that allow to select, filter, zoom and pick on sections of both records, either simultaneously or separately. The software is also able to calculate time-frequency representations of the seismic data, as well as several parameters from the radar time series (signal amplitude, duration, total power, sampling frequency). It enables the possibility to display Doppler radargrams and seismic spectrograms on the same output figure. The program is written using *Matlab* 8.0, its Graphical User Interfaces and Signal Processing Toolbox. Note that the seismic data processing part of *Seismo_Radar_Correlation* uses the same functions as *Seismo_Volcanalysis*, a software specifically developed for the analysis of seismic volcanic signals (*Lesage*, 2009).

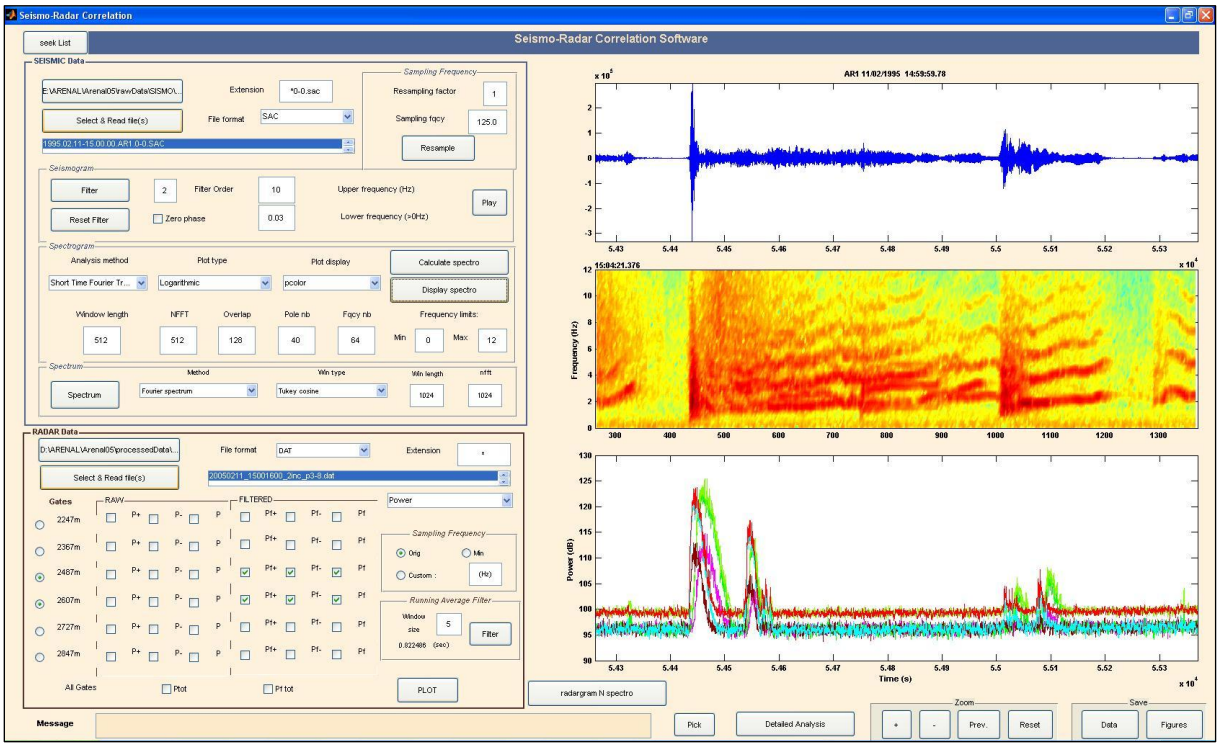

Figure A. Snapshot of Seismo_Radar_Correlation software.

Seismic file types supported include *.sac* and *.suds*. Radar files supported are *.dat* files generated with the CALPV code (CALculation of Power and Velocity).

Appendix B. *Radargram Builder* software

RadargramBuilder is a *Matlab*-coded program designed to easily generate Doppler radargrams, pick, plot, and extract a number of key parameters. The software comes with a package of functions, each of which manage separate parts of program. The program is launched when running the function named *gui_radargramLauncher.m* (gui stands for "graphical user interface"), which opens an interface to upload radargram source files (Figure B) and compute the radargrams.

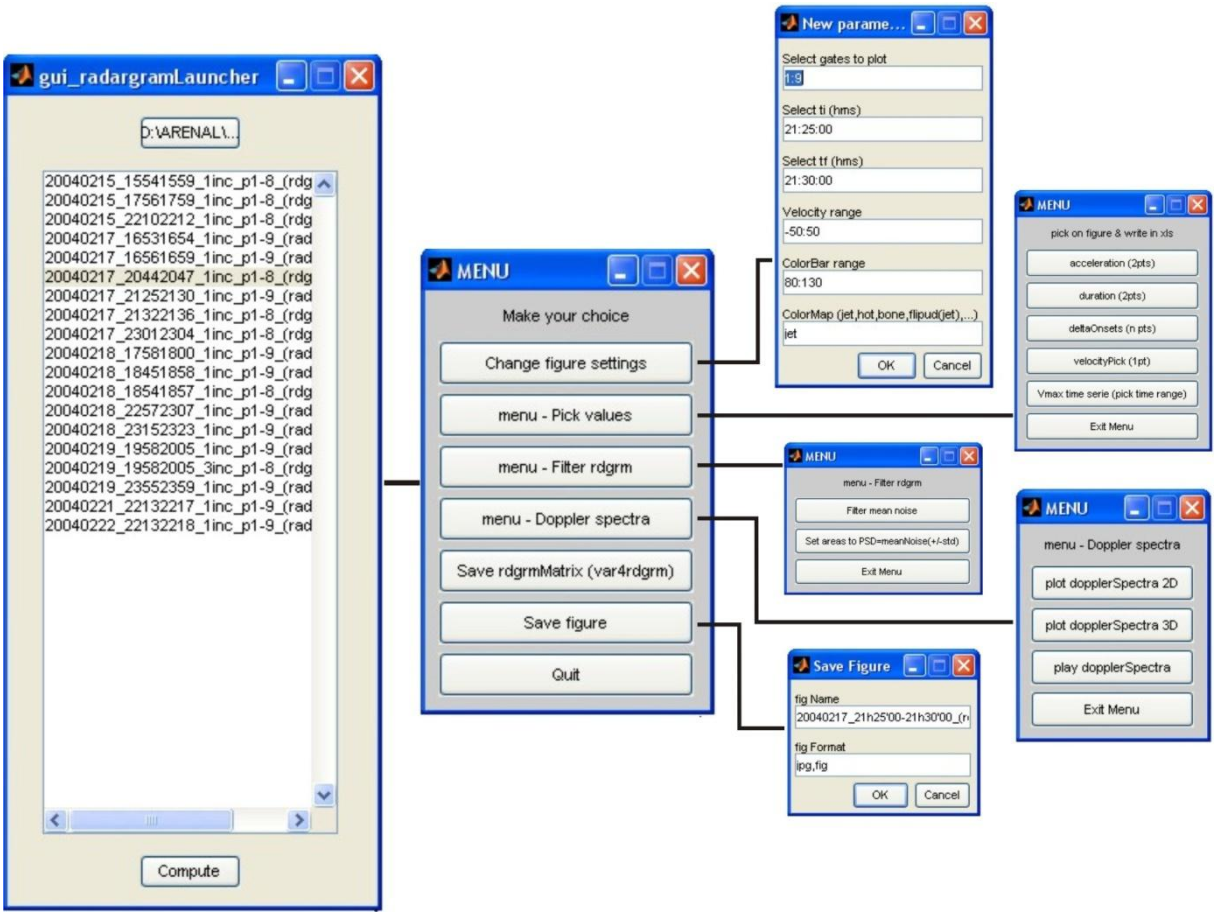

Figure B. Cascade of pop-up menus in RadargramBuilder software, designed to construct Doppler radargrams and extract a number of features from these.

The files which need to be uploaded are *.dat* files, generated with a *Borland Pascal* algorithm that reads the raw radar files (i.e. *.srt* or *.spe* files). The algorithm is called "CALPV_radargram", and is a modified version of the original CALPV code (CALculation of Power and Velocity), originally designed to build Doppler spectra and compute spectral parameter. The output files are structured as follows: each line is a time-step, each column a velocity-step (64 per gate), and each cell at the specified line / column holds the backscattered power value at the corresponding time / velocity. The first column holds the time values

(seconds from midnight), the following 64 hold the power values of the 64 velocity-steps of the first gate to compute, and so on until reaching the last gate. The output files are named according to the time range which is computed: "yyyymmdd_HHMMhhmm_rdgrm" (i.e. year, month, day, starting hour and minute, ending hour and minutes).

Once the wanted radargram file is selected, the user may clic on "Compute", and the radargram will be automatically generated with default values. A pop-up menu will simultaneously open, enabling the user to perform a number of operations on the radargram using a cascade of sub-menus (Figure B). In particular, the user may change the radargram settings (time period, color scale/map, …), pick on certain elements of interest and export in Excel file (e.g. onset velocities, durations, …), filter the radargram, (e.g. mean noise), plot 2D Doppler spectra at times of interest, plot 3D radargrams, export the radargram as an image in a variety of formats, export the radargram in matrix format, etc…

Appendix C. *Eject3D* software

Eject3D is a *Matlab*-coded program designed to simulate the projection of ballistic particles and small scale ash clouds in 3D, and construct the resulting synthetic radar signal as they transit through the radar beam. The program comes with a toolbox which includes a number of functions, each managing a specific part of the program (see Figure IV.2 and IV.19 in Chapter IV to see its architecture). The various input and output parameters can be easily and intuitively defined via user-friendly interface (Figure C, a), which is opened by running the function named *gui_eject3D.m* (gui stands for "graphical user interface").

The user may define parameters controlling the simulation timing (e.g. duration, time step), the sounding conditions (e.g. vent position with respect to the radar, wind speed / azimuth, radar beam angle, gate depth / number, …), as well a variety of parameters controlling the motion of both the ballistics and ash plumes (see driving equations in sections IV.1.1 and IV.2.1 respectively for details). A very handy feature of this interface, is that it automatically enables/disables the context menu items which appear respectively necessary/unnecessary, depending on the selected options and parameters. For instance, if the user wishes to simulate ballistic particles only (by ticking "ballistics" in the white box entitled "DYNAMICS"), all the context menu items which are used to select the input parameters to the plume model are disabled.

Once the program is launched, the particle motion within the beam can be plotted in real time (Figure C, b), along with the number of particles entering each gate through time. The interface also enables the possibility to plot a variety of outputs, such as Doppler radargrams (displaying either radial velocities or real particle velocities), plots of the gate onset timings, maximum radial velocities, particle altitude with time, etc…

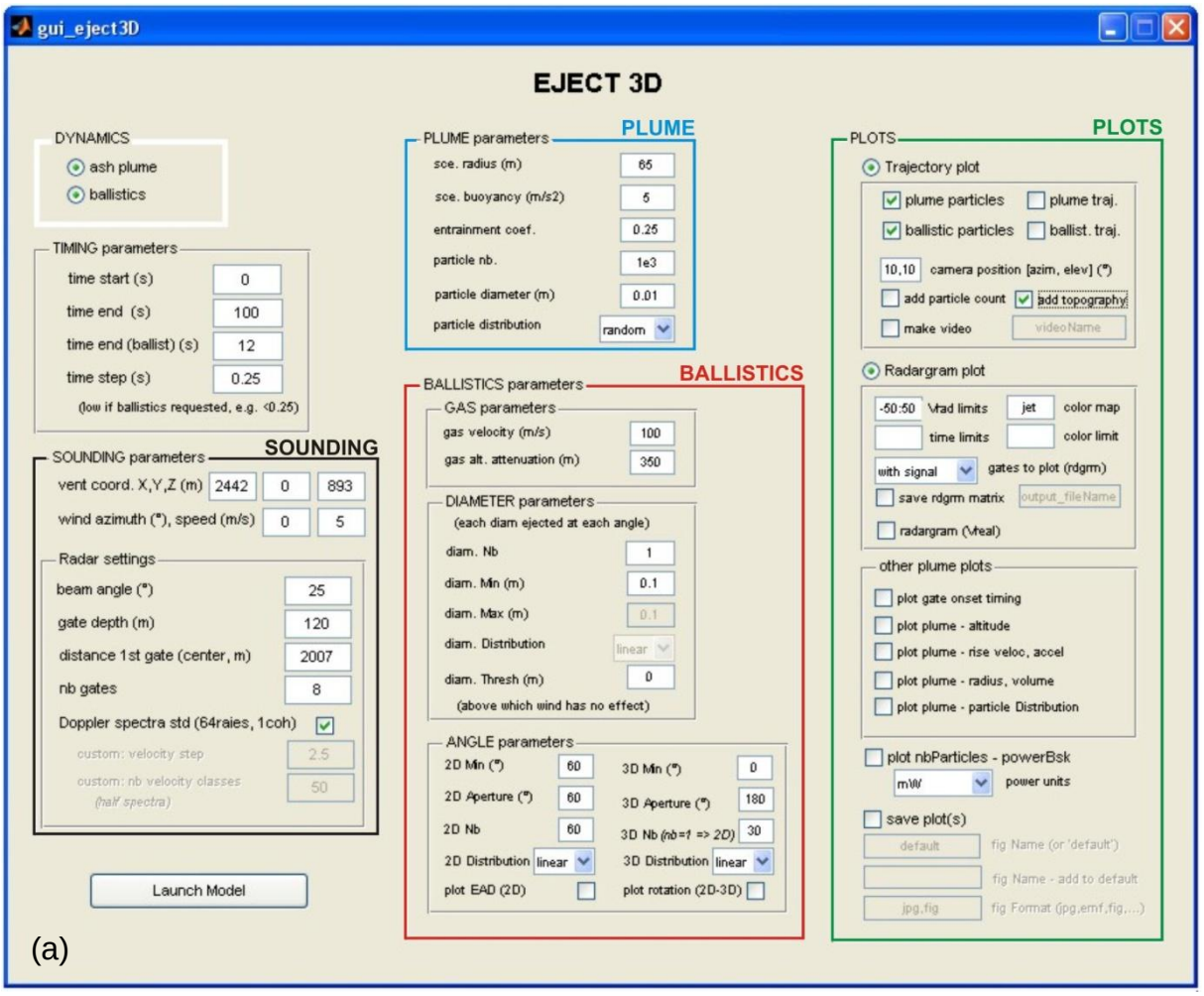

Figure C. Eject3D software, designed to simulate the 3D motion of ballistics and ash clouds, and construct the resulting synthetic radar signal as they transit through the beam. (a) graphical user interface, (b) particle motion plotted in real time (red and gray particles refer respectively to ballistic and ash plume particles).

Appendix D. *Valade et al.*, 2012

Valade, S., F. Donnadieu, P. Lesage, M. M. Mora, A. J. L. Harris, and G. Alvarado (2012), Explosion mechanisms at Arenal volcano, Costa Rica: an interpretation from integration of seismic and Doppler radar data, *J. Geophys. Res.*, doi:10.1029/2011JB008623.

Explosion mechanisms at Arenal volcano, Costa Rica: An interpretation from integration of seismic and Doppler radar data

S. Valade,[1,2,3] F. Donnadieu,[1,2,3] P. Lesage,[4] M. M. Mora,[5] A. Harris,[1,2,3] and G. E. Alvarado[5]

Received 23 June 2011; revised 15 November 2011; accepted 17 November 2011; published 21 January 2012.

[1] We execute an integrated analysis of broadband seismic and Doppler radar data to gain insights into the subsurface mechanisms that drive repetitive, mildly explosive activity of Arenal volcano (Costa Rica). We find large variability of both seismic and radar waveforms, and nonsystematic relationships between the two. Seismic recordings display long-lasting tremor sequences and numerous explosion quakes. Radar measurements show that tephra emissions are poorly correlated, in both time and energy, to the seismic activity. Tephra emissions were found in association with explosion quakes but also during episodes of tremor and seismic quiescence. Moreover, the exit velocity, mass loading, and kinetic energy of the emissions show no clear relationship with the coeval seismic amplitude and frequency content. We propose a conceptual source model whereby degasing is controlled by opening and closing of fractures that crosscut a rigid cap atop the conduit. When the fracture's strength is overcome by the gas pressure building up below, it suddenly opens and high-velocity gas escapes, producing high-frequency elastic waves typical of explosion quakes. Gas release also occurs in relation to periodic opening and closure of the fractures to produce repetitive pressure pulses, this being the source of tremor. In both cases, varying quantities of fragmented material may be carried by the gas, which can be detected by the radar if their concentration is high enough. Moreover, the highly variable, constantly changing state of lava cap (e.g., thickness, fracture network and gas permeability) results in nonrepeatable source conditions and explains the complex relationship between tephra emissions and associated seismic signals.

Citation: Valade, S., F. Donnadieu, P. Lesage, M. M. Mora, A. Harris, and G. E. Alvarado (2012), Explosion mechanisms at Arenal volcano, Costa Rica: An interpretation from integration of seismic and Doppler radar data, *J. Geophys. Res.*, *117*, B01309, doi:10.1029/2011JB008623.

1. Introduction

[2] Arenal, a small stratovolcano (1,710 m asl) located in northern Costa Rica, has experienced near continuous effusive and explosive activity since its reactivation in 1968 [*Minakami et al.*, 1969; *Cigolini and Borgia*, 1980]. Since 1975, the activity has been concentrated in crater C, from which blocky basaltic-andesitic lavas continuously effuse [*Cigolini et al.*, 1984; *Murillo and Ruiz*, 2004]. In addition, pyroclastic flows and numerous small ash plumes (ascending ≤1–3 km above the crater) are emitted recurrently [*Cole et al.*, 2005]. The frequency of ash emissions in the 1980s and 1990s was nearly one event every 30 min [*Williams-Jones et al.*, 2001], but this frequency has been progressively decreasing so that only a few per day were recorded during the time of our recording campaign in 2005. Arenal's lava discharge rate also fell from ~2 m^3/s in the 1980s to between 0.1 and 0.2 m^3/s in 2004 [*Wadge et al.*, 2006], and a rigid degassed plug capping the conduit has developed [*Cole et al.*, 2005].

[3] A number of geophysical studies have been carried at Arenal in order to constrain its shallow structure and the mechanisms operating within it. Studies using seismic data have constrained the shallow velocity structure of the edifice [*Mora et al.*, 2006], as well as the source mechanism of both tremor [*Benoit and McNutt*, 1997; *Lesage et al.*, 2006] and long period signals [*Davi et al.*, 2010]. *Hagerty et al.* [2000]

[1]Clermont Université, Université Blaise Pascal, Observatoire de Physique du Globe de Clermont-Ferrand, Laboratoire Magmas et Volcans, Clermont-Ferrand, France.
[2]Also at CNRS, UMR 6524, Laboratoire Magmas et Volcans, Clermont-Ferrand, France.
[3]Also at Institut de Recherche pour le Développement, R 163, Laboratoire Magmas et Volcans, Clermont-Ferrand, France.
[4]Institut des Sciences de la Terre, Université de Savoie, CNRS, Le Bourget-du-Lac, France.
[5]Escuela Centroamericana de Geología, Universidad de Costa Rica, San José, Costa Rica.

0148-0227/12/2011JB008623

cross-correlated seismic and acoustic data, and achieved a detailed analysis of the waveforms to give further constraints on the generation of these signals. *Williams-Jones et al.* [2001] cross-correlated seismic data with both SO_2 fluxes (from COSPEC data) and Earth tides to investigate the link between degassing, seismicity, and the influence of cyclic drivers. No study, however, has been able to cross-correlate quantitative information regarding both the pyroclastic emissions and subsurface processes that drive the explosions.

[4] We here quantify the exit velocity, mass-loading and kinetic energy proxies of pyroclastic emissions using ground-based Doppler radar (VOLDORAD), which we cross-correlate with broadband seismic data. We use these data to constrain a conceptual model which accounts for the complex interplay between tremor, explosion earthquakes and tephra emissions recorded in this study.

2. Background: Seismic Activity at Arenal

[5] Arenal exhibits intense and varied seismic activity, including tremor, explosion quakes, long-period (LP) events, rockfall events, and (rarer) volcano-tectonic events. Tremor is the most common signal, it being recorded several hours per day on average. Two types of tremor are commonly distinguished depending on the way the energy is distributed across the spectrum [*McNutt*, 2002]: when the energy is evenly distributed with no dominant peak (generally confined to the 1–6 Hz band at Arenal), it is referred to as "spasmodic tremor"; if the spectrum contains several regularly spaced peaks, composed of a fundamental frequency and its overtones, it is termed "harmonic tremor." The fundamental frequency at Arenal is generally in the range 0.9–2 Hz [*Hagerty et al.*, 2000; *Mora*, 2003], and the frequencies of overtones are integer multiples of it. Tremor at Arenal shows striking characteristics, such as [*Lesage et al.*, 2006]: frequency gliding episodes (whereby the fundamental and corresponding harmonic frequencies fluctuate in time while maintaining their regular spacing [*Benoit and McNutt*, 1997; *Garcés et al.*, 1998; *Hagerty et al.*, 2000]), frequency jumps (with either positive or negative increments), progressive transitions from spasmodic to harmonic tremor (with variable quantities of harmonic overtones), and coexistence of multiple frequency systems (with distinct spectral peaks and independent gliding). Several source models have been proposed to explain tremor at many volcanoes worldwide; at Arenal the clarinet model defined by *Lesage et al.* [2006] appears to be well-adapted to describe the complex behavior of the tremor. In particular, harmonic and spasmodic tremor are thought to have the same source mechanism, i.e., intermittent flow of gas through fractures in the cap atop the conduit. Frequency gliding is attributed to pressure fluctuations in the magmatic conduits [*Neuberg*, 2000; *Lesage et al.*, 2006], which depends on the mechanical state of the plug, and also potentially affects its permeability to gas flow. The coexistence of different frequency systems, each evolving independently, may be the expression of different resonators, i.e., different conduits in the shallow feeding system.

[6] Long-period (LP) transients and explosion quakes are regularly superimposed on the nearly continuous tremor, and are both characterized by spindle-shaped envelopes and narrow band-width (1–3 Hz) frequencies [*Chouet*, 1996; *Hagerty et al.*, 2000]. The coda may in some cases evolve into harmonic tremor [*Barquero et al.*, 1992; *Benoit and McNutt*, 1997; *Hagerty et al.*, 2000]. Both LP and explosion quake signals are thought to have the same source mechanism, but with differing source depths. Following *Mori et al.* [1989], explosion quakes should occur at shallow levels within the conduit, allowing the propagation of an acoustic air wave which couples with the ground as a high frequency seismic phase and arrives shortly after the P wave onset. LP events, on the other hand, should occur at greater depths in the conduit, preventing the propagation of an acoustic air wave. Because there is probably no fundamental difference in their mechanisms, we follow *Lesage et al.* [2006] and consider both LP events and explosion quakes as part of the same type of event, defined as "explosion quakes." Note that this term will refer to this particular seismic signal, regardless of whether it is accompanied by tephra emission or not. On the contrary, the term "eruptive event" will refer to tephra emission, regardless of the presence and type of associated seismic signal.

[7] High frequency events are also frequently observed and show a progressive onset followed by a progressive decay, generally lasting 50–180 s. Energy is well staggered between 5 and 35 Hz with no dominant frequency and a sharp onset in the 5–15 Hz band. At Arenal, radar signals are always recorded ahead of these seismic signals. *Johnson and Lees* [2000] described similar events at Karymsky volcano, and suggested that they may result from energetic gas jetting when the vent is unobstructed by debris.

[8] Volcano-tectonic events are less frequent at Arenal as the open state of the vent prevents the accumulation of high stresses. The rarity of such events also suggests the absence of a shallow magma storage body [*Mora*, 2003].

3. Data Acquisition and Processing

[9] VOLDORAD 2 (Volcano Doppler Radar) is a ground-based, pulsed, Doppler radar specifically designed for active remote sensing of volcanic pyroclastic emissions [*Dubosclard et al.*, 1999, 2004; *Donnadieu et al.*, 2003, 2005, 2011; *Gouhier and Donnadieu*, 2008, 2010; *Valade and Donnadieu*, 2011]. It was set up at an altitude of about 690 m asl, around 2.3 km west, and downwind, of active crater C (Figure 1a), from where we recorded activity for several hours per day between February 10 and 22, 2005. The antenna pointed along an azimuth toward the crater, and then lowered until ground echoes appeared in the Doppler spectra, indicating that the base of the beam was aligned with Arenal's summit. At Arenal, there is no deep crater, but rather an irregular dome-like surface. This ensures that the beam skims the eruptive vent. The radar should thus capture all ash emissions, provided the particle concentration is above the detection threshold (ca. 15 g/m^3 for 1 mm particles, *Donnadieu et al.* [2011]). The radar beam is divided into successive sampling volumes, termed range gates, whose radial resolution depend on the pulse duration (τ), and whose location and azimuthal resolution depend on the beam aperture (conical 9° beam width) and the distance from the radar. During the recording campaign, data were recorded in range gates with radial resolutions of 120 m (τ = 0.8 μs), and with slant distances ranging

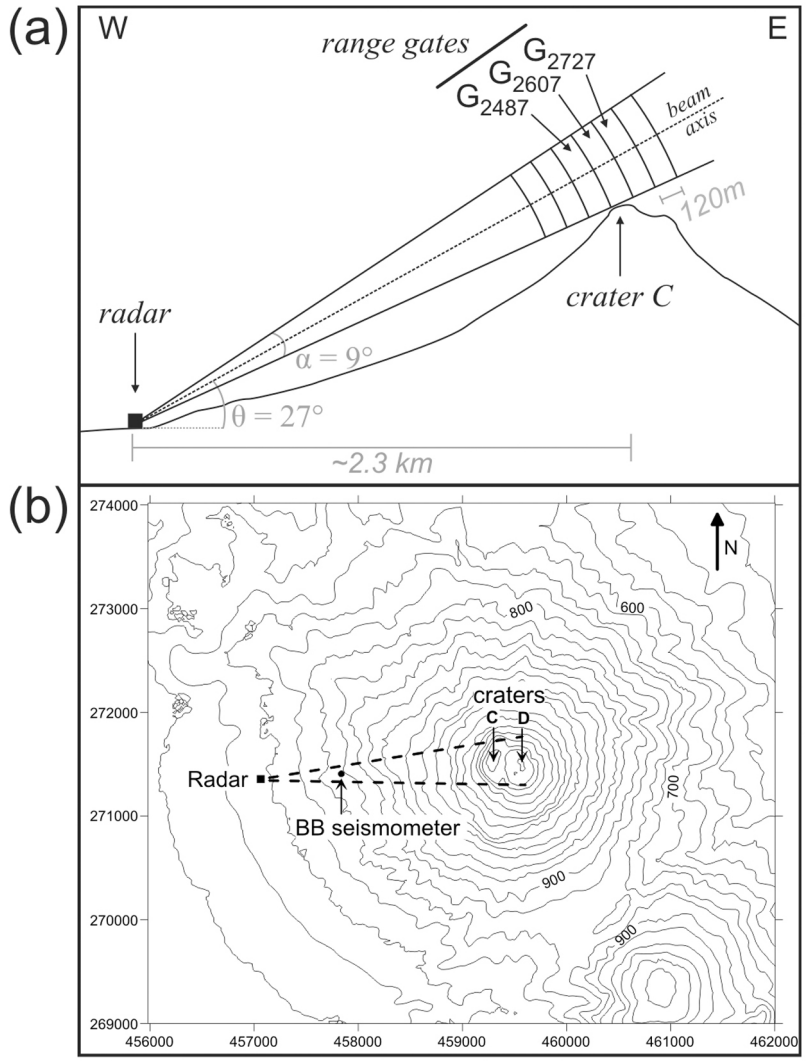

Figure 1. (a) Radar beam geometry during the recording campaign. (b) Location map of the broadband seismometer and Doppler radar. At the time of the recording campaign in February 2005, the estimated altitude of crater C is 1710 m above sea level (asl) [*Wadge et al.*, 2006].

between 2007 and 2847 m (i.e., between gates G_{2007} and G_{2847}). Two range gates were located above the active crater area: gates G_{2607} and G_{2727} (Figure 1a). Volcanic ejecta crossing the beam scatter the electromagnetic signal repeatedly transmitted by the radar (sampling rate 100 μs^{-1}), part of which is scattered back to the radar and can be recorded. Real-time processing of this signal gives information on (1) the backscattered power (which is a complex function of the number and size of the ejecta, and so is a proxy for the mass loading of the pyroclastic emissions), and (2) the radial velocity of the ejecta (i.e., the component of the exit velocity projected along the beam axis). These data are displayed for each range gate as Doppler spectra, representing the backscattered power (P in dB) versus the radial velocity (V in m/s). Processing of the Doppler spectra gives, for each range gate, two sets of parameters: positive parameters, which refer to signal backscattered by particles with a radial component of motion away from the radar, and negative parameters, which refer to particles with a radial motion toward the radar.

[10] For each range gate, the following parameters were defined and calculated: backscattered powers (P_+, P_-, and $P = P_+ + P_-$), and maxima of radial velocities (V_{+max}, V_{-max}) [*Dubosclard et al.*, 2004]. We also implemented a proxy for the kinetic energy E_k of the tephra emission following:

$$E_k = \int_{V-\max}^{V+\max} \left(P(V) \cdot V^2\right).dV \qquad (1)$$

in which V is the radial velocity of particles and P(V) is the power backscattered by all particles with radial velocity V.

[11] Seismic observations were carried out 1.8 km west of the active crater using a permanent 30-s GURALP CMG-6TD broadband seismometer (Figure 1b). The vertical component was generally used, because tremor and explosion quakes are mainly composed of Rayleigh waves [*Mora et al.*, 2006, *Zobin et al.*, 2009], which are polarized in the vertical plane.

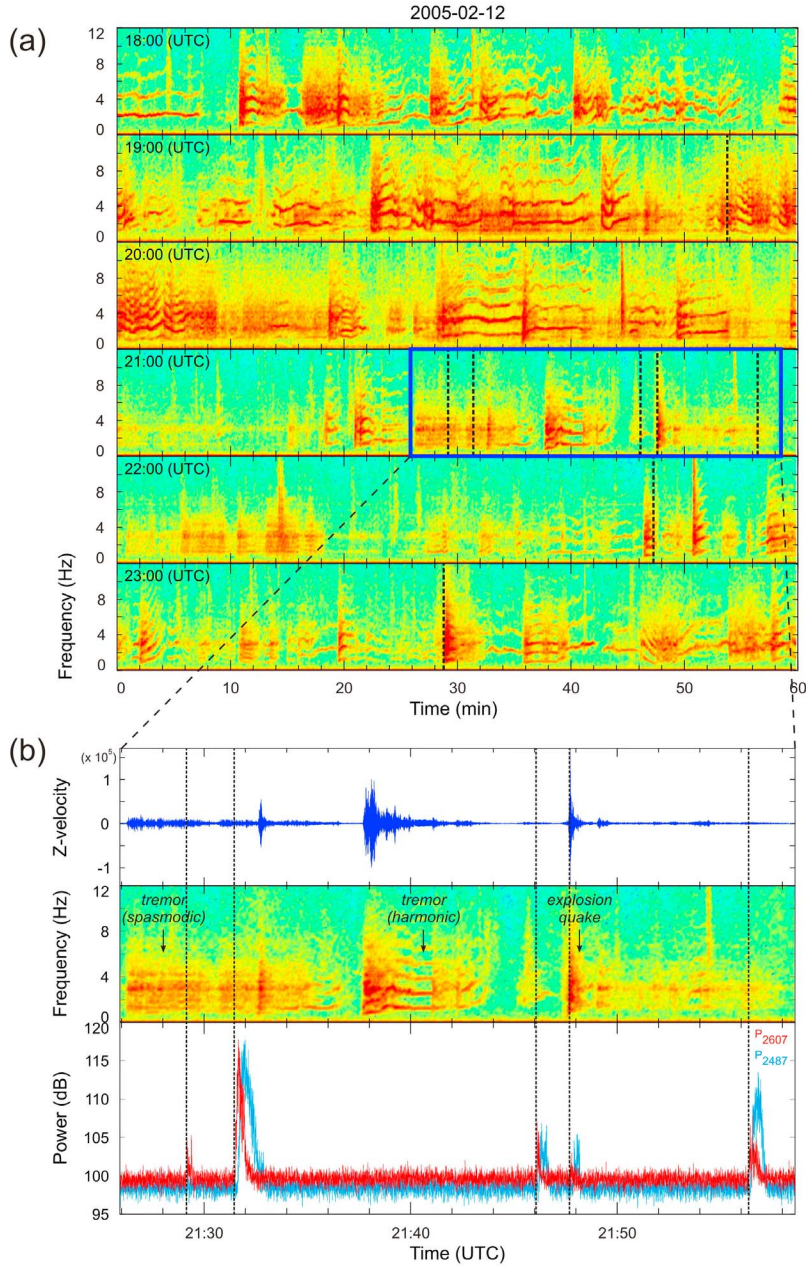

Figure 2. (a) Spectrograms of the seismic signal recorded on February 12, 2005 from 18:00 to 24:00 UTC. Each line corresponds to 1 hour. Vertical dashed lines indicate radar eruptive events. (b) Enlargement of the sequence enclosed by the box in Figure 2a, which presents (from top to bottom) the seismic trace (vertical component), the corresponding Fourier spectrogram, and the power backscattered to the radar in gates G_{2607} (red) and G_{2487} (blue).

[12] Detailed analyses of radar and seismic data were carried out using MATLAB-based software [*Mora et al.*, 2009], we specifically designed for the purpose of this study. This software enables the display of the different data types on a graphical interface and the application of high resolution time-frequency methods [*Lesage*, 2009] to extract the main features from the different geophysical data sets collected. During the 11-day-long field campaign, a total of 132 eruptive events were recorded by the radar, from which we defined a subset of 68 events comprising medium- and large-amplitude radar events, and/or the events having a good seismo-radar temporal correlation.

4. Results

[13] We herein consider the correlation between radar and seismic records on two distinct time-scales: (1) over the time scale of seconds to minutes, to analyze the coeval seismic and radar signals during individual pyroclastic emissions, and (2) at the time scale of several hours, to understand how

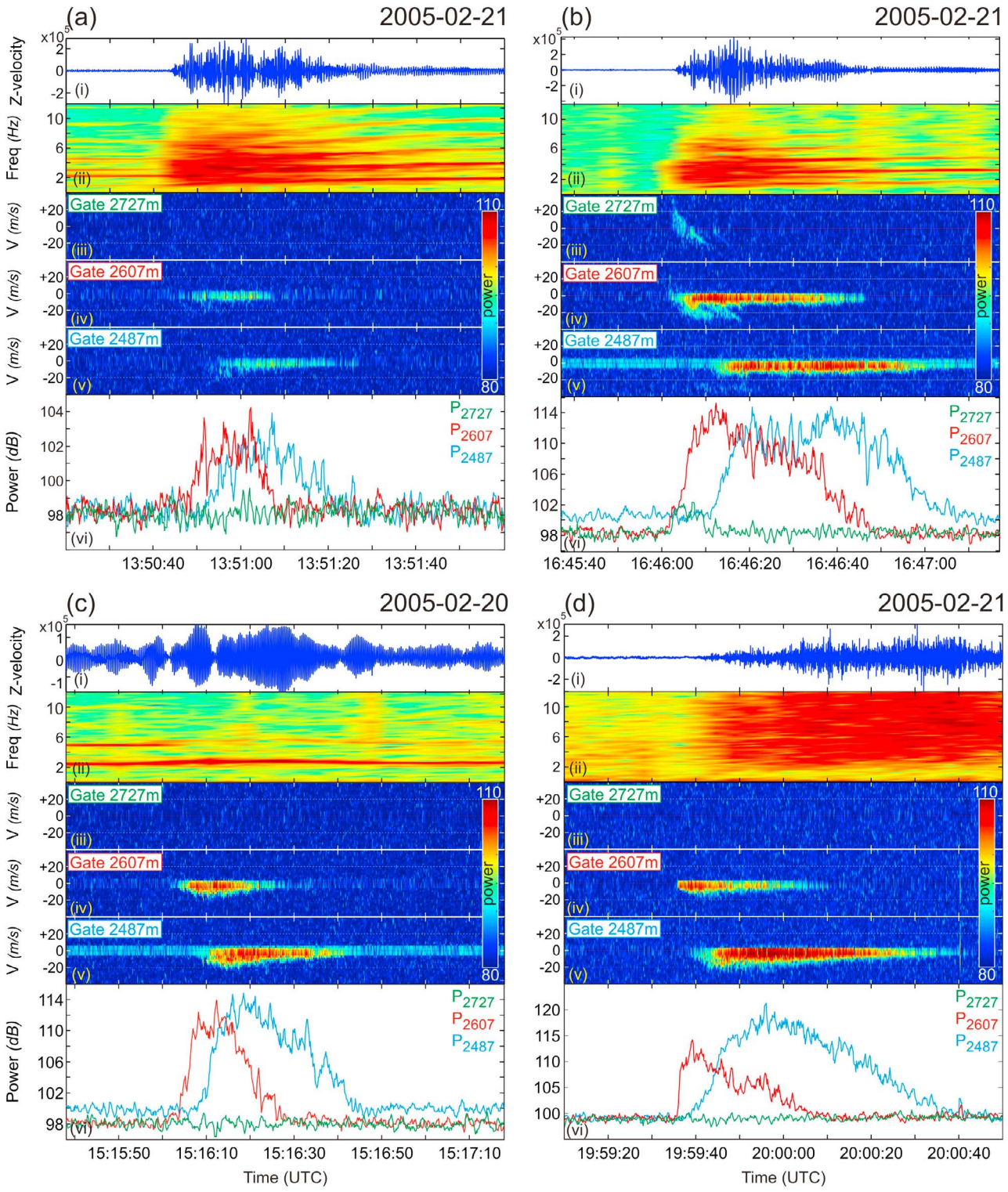

Figure 3. Four representative seismic events and the associated radar signal: (a and b) explosion quakes, (c) harmonic tremor, and (d) no seismic signal at emission onset, post-onset, high-frequency signal only. Figures 3a–3d display the seismic record (plot i); the seismic spectrogram (plot ii); the Doppler radargrams (time-velocity distribution of backscattered radar signal) in gates G_{2727} (plot iii), G_{2607} (plot iv), and G_{2487} (plot v); and the corresponding time series of backscattered power in gates G_{2727} (green), G_{2607} (red), and G_{2487} (blue) (plot vi).

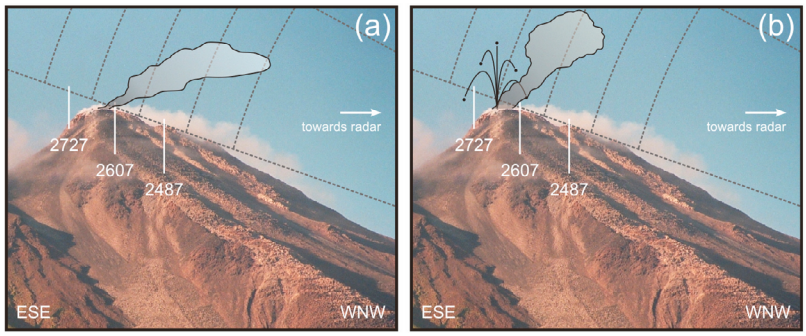

Figure 4. Schematic illustration of pyroclastic emission dynamics, interpreted in terms of spatial motion in the radar range gates. (a) Weakly loaded ash plume drifts in trade winds toward the radar, resulting in Doppler radargrams which exhibit low negative velocities and low backscattered power (e.g., Figure 3a, plots iii–v). (b) Strongly loaded ash plume accompanied by ballistic projections. In this case (e.g., Figure 3b), the resulting radargrams contain an additional signal to the plume signature described previously; the ballistics causing diagonal streaks which exhibit high positive velocities (mostly in gate 2727 m) that progressively shift toward negative velocities.

subsurface and surface activity may interact on longer time scales.

4.1. Short-Term Correlation Between Seismic and Radar Observations

[14] Spectrograms were computed from the seismic data, and radar signals recorded during emissions were traced over it to visualize how surface and sub-surface activity were related on short time scales (Figure 2). Figure 2a shows spectrograms from six consecutive hours of seismic data recorded on the 12 February 2005, with eruptive events detected by the radar being indicated by vertical dashed lines. Figure 2a illustrates the variety of seismic activity discussed in section 2, with sequences of both harmonic and spasmodic tremor, multiple frequency systems that glide independently, numerous explosion quakes, and periods of quiescence all being apparent. Surprisingly, the surface tephra emissions are poorly correlated with this seismic activity. Indeed, tephra emissions detected by the radar are not always associated with distinct seismic events, and emissions can be found associated with explosion quakes (e.g., 23:28:48 UTC), in the middle of tremor sequences (e.g., 21:31:29 UTC), and during periods of very weak seismic activity (e.g., 21:56:23 UTC). This observation applies throughout the entire record in which, of the 68 radar events subset, ~44% of the signals are associated with explosion quakes, ~43% occur during episodes of tremor, and ~13% occur during periods when only background seismic noise is recorded. Figure 2b shows a magnification of the sequence identified by the box in Figure 2a, and highlights that the strongest ash emissions (i.e., the events giving the highest backscattered power, such as that occurring at 21:31:29 UTC) do not occur when they are most expected (i.e., during high amplitude explosion quakes, at 21:37:30 UTC, for example). Hence, it seems that there is no simple relationship between tephra emission and coeval seismic events. Pyroclast emissions do not have a unique repetitive seismic signature and, more importantly, emissions cannot always be identified by the seismic signals alone, even for emissions with high mass loadings.

[15] The radar signals and associated seismic records show a large variability in their respective characteristics. Radar signals show variable backscattered power (varying by more than 30 dB), particle velocities, and Doppler signatures (i.e., time-velocity distribution of the power), which respectively reflect the diversity of the emissions' mass loading, impulsivity and dynamics. Figures 3a–3d display, for several eruptive events, the seismic trace (plot i); its spectrogram (plot ii); (iii-v) the Doppler radargrams (time-velocity distribution of backscattered power) for gates G_{2727} (plot iii), G_{2607} (plot iv), and G_{2487} (plot v); and the radar backscattered power time series for the same gates (plot vi). Figures 3a and 3b are explosion quakes with similar seismic amplitudes, durations and spectral contents. However, the corresponding radar signals are quite different in terms of both backscattered power and radial velocity. While the event given in Figure 3a has a maximum backscattered power that is +7 dB above the noise level and has no positive velocities, the event of Figure 3b has a higher backscattered power (+17 dB), and radial velocities that exceed 20 m/s. Moreover, the radargrams exhibit distinctive Doppler signatures. Figure 3b shows distinctive diagonal streaks during the first few tens of seconds following the eruptive event onset, which is not the case for the event in Figure 3a. These streaks are short-lived (~10 s), are spread across a large velocity range (reaching more than +20 m/s and −20 m/s in gates G_{2727} and G_{2607}, respectively), and seem to superimpose a longer–lived signal (tens of seconds) with low negative radial velocities (less than −10 m/s). *Valade and Donnadieu* [2011] have modeled these short-lived diagonal streaks and show that they result from ballistic blocks crossing the range gates. The longer-lived signal (observed in Figures 3a–3d) instead results from the slow transit of the ash plume through the beam. Hence, although the two events in Figures 3a and 3b have similar seismic signals, the differences in the radar signals reveal two emissions with very different properties, in terms of mass loading, duration, impulsivity and eruptive dynamics. An interpretative sketch of the dynamics of these two events in terms of spatial motion within the range gates, is given in Figure 4. In the case of the event in Figure 3c, a strong radar signal

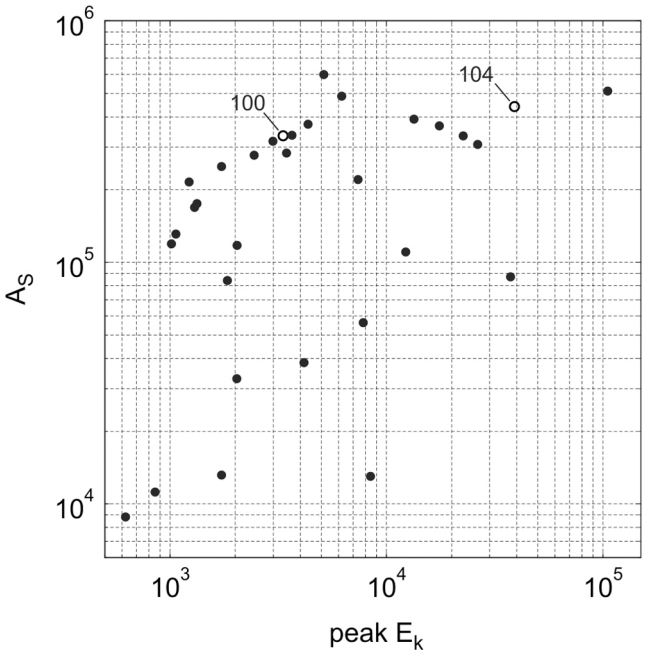

Figure 5. Maximum seismic amplitude A_s (vertical velocity component) versus radar peak amplitude of the kinetic energy proxy E_k, for all the tephra emissions associated with explosion quake events. Values of A_s and E_k are in arbitrary units. Events indexed 100 and 104 refer to the events displayed in Figures 3a and 3b, respectively.

(maximum recorded power ~+17 dB, similar to the event in Figure 3b) occurs without perturbing the harmonic tremor. The event of Figure 3d produces an even stronger signal (with a maximum recorded power of +22 dB). This event is not preceded by any seismic signal, but is followed by a high frequency emergent seismic waveform which begins a few seconds after the radar signal onset. The seismic signal could be interpreted as a rockfall signal, however we doubt that the associated radar signal results from a rockfall-generated cloud. Indeed, the radar signal onset is very impulsive (i.e., sharp P_{2607} increase) and exhibits strong backscattered power (+22 dB), suggesting that a highly concentrated ash plume rapidly entered the beam. In the case of rockfall-originated clouds, we expect much less backscattered power due to both (1) the fine granulometry of the elutriated material and (2) the low particle concentration (compared to ash plumes resulting from an explosive event). Moreover, the radar signal begins before the seismic signal, which is not consistent with a cloud of rockfall-origin. During the recording campaign of 2005, rockfalls were concentrated in a ravine perpendicular to the radar beam axis. This location would increase the time needed for the cloud to rise from its source and drift into the beam. Hence we conclude that this was a highly loaded ash plume, emitted without an associated seismic signal (unlike events in Figures 3a and 3b). All of these observations show that the mass loading (i.e., backscattered power), exit velocities, and dynamics of the tephra emissions at Arenal are highly variable, and do not show apparent correlation with the coeval seismic signal amplitudes or spectral contents.

[16] It is worth noting that both paired and pulsed emissions are commonly observed. Paired eruptions refer to eruptions less than 3 min apart and represent 22% of all the recorded radar events. In most cases, the second event's power amplitude is similar to, or lower than, that of the first (e.g., Figure 2b, 21:46 UTC); only in some rare cases is it higher (e.g., Figure 2b, 21:29 UTC). Pulsed emissions, on the other hand, refer to eruptive events which comprise several pulses, spaced by a few seconds only, as evidenced by the successive streaks in Figure 3b (plot iv). From a seismic point of view, these double-features are rarely recorded, highlighting once again the complex relationship linking the pyroclastic emissions and the coeval seismic signals at Arenal.

[17] Seismic and radar energy proxies were computed for all pyroclastic emissions associated with explosion quake seismic signals. The maximum seismic amplitude (vertical component, A_s) was considered as a suitable proxy for the intensity of the sub-surface process. The use of seismic amplitudes (i.e., velocity trace amplitude) rather than seismic energies (i.e., time-integration of the squared velocity) was preferred because many explosion quakes occurred during background tremor (e.g., Figure 3c), which makes the estimation of the explosion energy problematic. For the radar signal, we computed the kinetic energy, as defined in section 3, for the two gates above the active crater (i.e., $E_{k\ 2607}$ and $E_{k\ 2727}$), and define their sum as the kinetic energy (E_k) of the pyroclastic emissions. Figure 5 displays the maximum seismic amplitude versus the maximum kinetic energy for these events. The data points show a positive trend, which is particularly apparent in the cluster of points in the upper left corner of the plot (i.e., those having A_s between 10^5 and 10^6, and E_k between 10^3 and 10^4, in arbitrary units). The events of this cluster share an emergent onset, a relatively weak power amplitude (<12 dB), and low radial velocities (<16 m/s). Despite this weak positive trend, Figure 5 shows a wide scatter of data points indicating that the ratio between subsurface seismic energy and surface kinetic energy is highly variable. For example, although the events in Figure 3a and 3b (respectively indexed 100 and 104 in Figure 5) have similar seismic amplitudes, they have considerably different kinetic energy values. Whatever the type of energy proxies used for the seismic and radar signals (signal amplitudes, time-integrated energies, various frequency bands, etc.), they all show similarly poor correlation. This suggests poor scaling between the seismic energy and the energy of the subsequent emission. Similar observations were reported by *Johnson et al.* [2005] at Tungurahua. Nevertheless, pyroclastic emissions may be the result of long pressurization processes, which can only be revealed by examining data records on longer time-scales, as reported next.

4.2. Long-Term Correlation Between Seismic and Radar Observations

[18] The time-averaged amplitude of the seismic trace, termed RSAM (Real-time Seismic Amplitude Measurement [*Endo and Murray*, 1991]), has proved capable of revealing long-term cyclic patterns [e.g., *Denlinger and Hoblitt*, 1999]. The cumulative squared amplitude of the seismic trace, or cumulative RSEM (Real-Time Seismic Energy

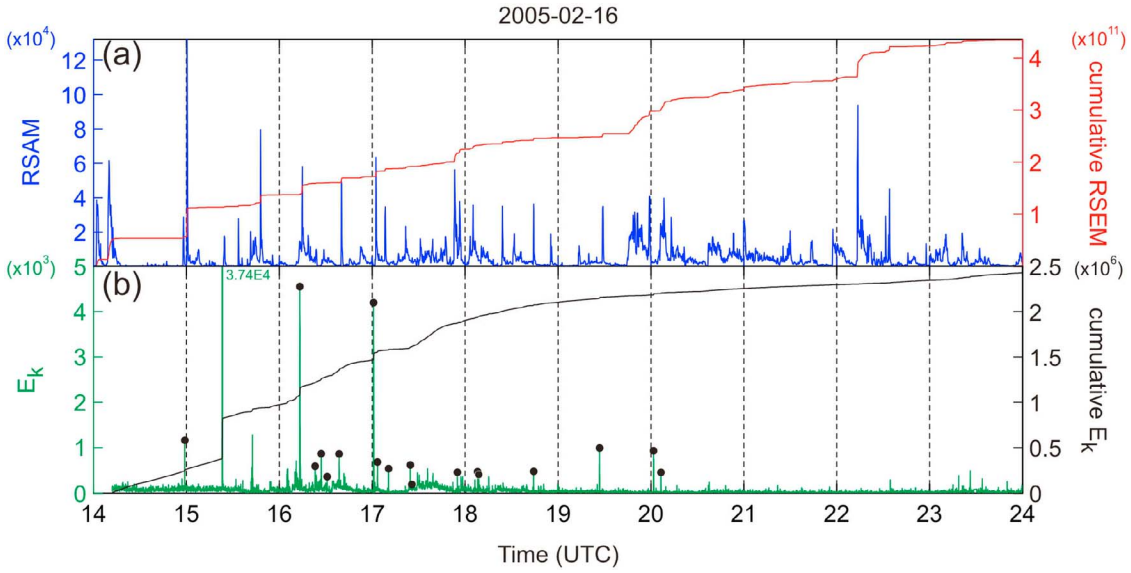

Figure 6. (a) RSAM and cumulative RSEM recorded on the 16 February 2005 and (b) radar kinetic energy (E_k) with its cumulative curve. The kinetic energy curve (E_k) is filtered with a running average, and the recorded eruptive events are indicated by black dots. The peaks which are not topped by black dots are noneruptive peaks (e.g., rain, noise, etc.). For visualization purposes the E_k ordinate axis was clipped at $E_k = 5 \times 10^3$, truncating the major radar event at 15:23 UTC ($E_k = 3.74 \times 10^4$, in arbitrary units).

Measurement [*De la Cruz-Reyna and Reyes-Dávila*, 2001]), enables a better visualization of the seismic energy release rate through time. RSAM, RSEM and E_k time series were thus computed and plotted together to search for relationships between the seismic activity and the tephra emissions on time scales of several hours. Figure 6a and 6b show 10 h of continuous seismic and radar recordings on the 16 February 2005. The RSAM plot displays successive transients with sharp onsets followed by slow decays, which mostly relate to tremor amplitude fluctuations. When an explosion quake triggers a tremor sequence, the RSAM shows a high peak marking the transient onset. The cumulative RSEM curve, on the other hand, shows a gradual increase, punctuated by sudden increments (or steps) when strong explosion quakes are recorded. Similarly, the E_k curve shows successive peaks (or steps in the cumulative E_k curve), indicating the occurrence of pyroclastic emissions with strong kinetic energies. Comparison of Figures 6a and 6b shows poor correlation between the seismic and radar signals: neither the fluctuations (i.e., amplitude oscillations in the RSAM and E_k curves), nor the sudden energy releases (i.e., the steps in the RSEM and E_k cumulative curves), show correlation in time or amplitude. This was observed throughout the entire recording period,

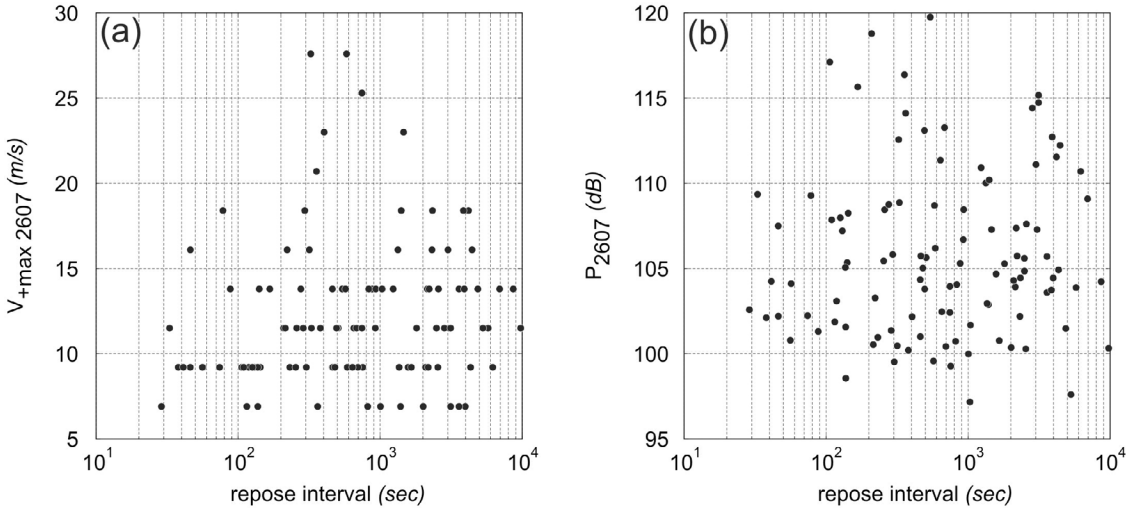

Figure 7. Relationship between the repose interval separating successive tephra emissions and their (a) maximum radial velocities and (b) maximum backscattered power. Values are taken from the main gate G_{2607}.

indicating that there is no simple relationship between the energy of tephra emissions and the energy of seismic vibrations, even on daily time scales.

[19] Classically, exit velocities of volcanic ejecta are thought to be related to overpressures in the volcanic conduit prior to the explosion [*Wilson*, 1980]. If pressure builds-up progressively beneath a cap which obstructs degassing, and if this pressure is released during eruptive events, then the longer the repose intervals between successive eruptions, the longer the period of pressurization and, thus, exit velocities should be higher. Note that this statement holds only if we assume that passive degassing is minor compared to the degassing during an explosion. We consequently investigated whether the measured exit velocities were proportional to the repose interval separating successive emissions. Figure 7a plots the maximum positive radial velocity recorded in gate G_{2607} as a function of repose time, and shows a wide scatter, indicating no correlation between repose time and exit velocity. This suggests that overpressures do not increase steadily during repose intervals, probably because of the fractured nature of the lava cap which allows gas to escape between eruptive events. Figure 7b displays the maximum power recorded in gate G_{2607} as a function of repose time. Again no correlation is observed, which indicates that ejecta mass loadings do not appear to be controlled by the duration of repose.

[20] In summary, analysis of simultaneous seismic and radar recordings show complex, nonrepeatable relationships, on both short and long time scales. Tephra emissions are not systematically associated with a specific type of seismic signal (Figure 2), and show variable properties (i.e., mass loading, exit velocity, dynamics) that do not correlate with seismic amplitude or spectral content (Figure 3). When considering the emissions associated with explosion quakes, poor scaling is found between the kinetic energy of the emission and the amplitude of the seismic signal (Figure 5). Even on daily time scales, we find that the energy of the emissions do not correlate with fluctuations in the seismic amplitude and energy (Figure 6).

5. Existing Models for Arenal-Type Eruptive Activity and Associated Geophysical Signals

[21] Several models have been proposed to account for the style of repeated, mildly explosive eruptive activity and associated geophysical signals at persistently active volcanoes such as Arenal. The physical processes involved in each model depend mainly on the magma viscosity. The bubble-bursting model is widely accepted at volcanoes with low-viscosity magmas. Laboratory experiments [*Jaupart and Vergniolle*, 1988; *Ozerov*, 2010] model the phenomenon as bubbles rising up the conduit to burst intermittently at the surface. This mechanism, however, requires low viscosity magma (10^3 and 10^5 Pa/s [*Ozerov*, 2010]) if the slugs that generate the explosion are to ascend buoyantly through the magma column and burst at the free surface. At Arenal these conditions are not fulfilled: average viscosities of lavas close to the crater range between 10^5 and 10^6 Pa/s [*Cigolini and Borgia*, 1980; *Cigolini et al.*, 1984; *Bertolino et al.*, 2009], and the vent is capped by a degassed, cooled plug of lava [*Cole et al.*, 2005].

[22] The pressure build-up model is often invoked to explain repeated, discrete, short-lived explosions characteristic of the Vulcanian activity. These are attributed to the steady build-up of pressure below a plug obstructing the conduit, which is suddenly released when the plug's resistance threshold is overcome [*Stix et al.*, 1997; *Melnik and Sparks*, 2002; *Yokoo et al.*, 2009]. This sudden failure and decompression causes both brittle failure of the plug and rupture of numerous small gas bubbles trapped in the viscous melt, both of which generate fine ash. At Arenal, petrological observations show that a rigid degassed cap has progressively developed and muzzled the summit vent [*Cole et al.*, 2005]. *Cole et al.* [2005] studied tephra clast morphologies and reported a dominance of blocky textured clasts over fluidal ones, thus arguing for fragmentation of rigid degassed magma with only a minor molten component, typical of Vulcanian-type explosions. The presence of such a degassed body could act as a plug, which blocks the vent and impedes the release of gas.

[23] The idea that such plugs can possess a network of fractures has led several authors to believe that the small pathways represented by the fractures can control the degassing periodicity and, in turn, the associated geophysical signals [*Hellweg*, 2000; *Johnson and Lees*, 2000; *Lesage et al.*, 2006]. The soda-bottle model was proposed by *Hellweg* [2000] as a possible source model for Lascar's harmonic tremor and cyclic degassing behavior. Following *Soltzberg et al.* [1997], *Hellweg* [2000] described how a small opening in a soda bottle may generate cycles of pressure drop beneath the cap, which triggers bubble nucleation and ascent. *Johnson et al.* [1998] and *Johnson and Lees* [2000], on the other hand, proposed a mechanism analogous to a pressure-cooker for Karymsky, in which the plug atop the conduit acts as a valve. In this case, harmonic tremor is the result of rhythmic gas release through the valve, producing source pulses that are sufficiently regular to generate harmonics. More recently, *Lesage et al.* [2006] proposed a process similar to that of a clarinet to explain Arenal's tremor. This model is close to the pressure-cooker idea of *Johnson and Lees* [2000] in the sense that both suggest that gas periodically escapes through fractures in a solid plug. The clarinet model, however, includes a stabilization mechanism for the pressure pulses. As fractures open intermittently, pressure waves are emitted in the conduit, which allow a standing pressure wave to be maintained. This, in turn, controls the pressure state below the plug and consequently the fracture oscillations. This feedback is thought to be an efficient way to produce pressure transients with a stable repeating period, responsible for the harmonic tremor [*Rust et al.*, 2008]. Lack of period stability, however (if rubble chokes the fractures for instance), would result in spasmodic tremor. If the repeat frequency slowly varies with time, the spectral peaks will also vary, and appear as frequency gliding episodes. Nevertheless, if the clarinet-model is an adequate model for the source of tremor at Arenal, it does not explain the source mechanisms of the explosion quakes.

[24] Stick-slip movement of the uppermost part of the conduit has been proposed as a possible conduit model for several volcanoes with high-viscosity magmas, such as Soufriere Hills (Montserrat) and Santiaguito (Guatemala). *Denlinger and Hoblitt* [1999] first suggested that the cyclic

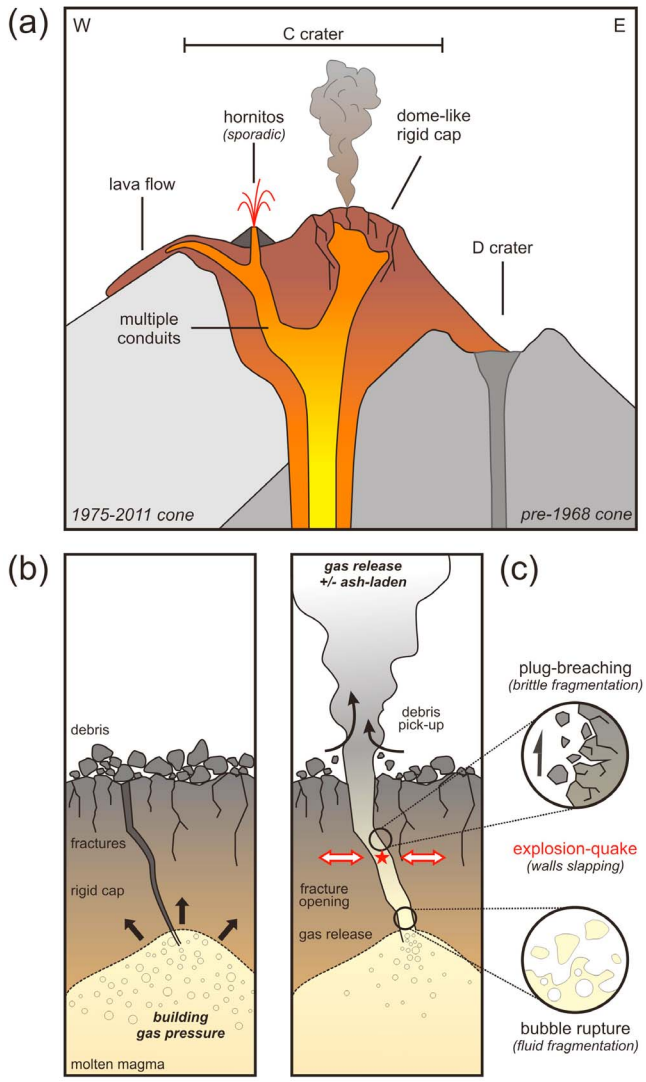

Figure 8. (a) Cross section of Arenal's shallow structure and (b and c) conceptual model of the mechanism of gas and ash emissions at Arenal. In Figure 8b, pressure builds up under a viscous degassed cap crosscut by fractures. When the fracture strength is overcome, the gas is suddenly released (Figure 8c): Fracture walls slap together, triggering high-frequency seismic vibrations characteristic of the explosion quake signals. The turbulent gas may in turn pull out varying quantities of pyroclast, which can be detected by the radar if enough is expelled. The expelled tephra may result from syn-eruptive fragmentation (brittle or fluid fragmentation), or may result from remobilization of loose fragmented material residing atop the cap, or within its permeable fractures.

eruptive behavior at Soufriere Hills might be controlled by boundary conditions along the upper part of the conduit, where stick–slip boundary conditions would generate periodic conduit flow. Field evidence (at Santiaguito, Guatemala [*Bluth and Rose*, 2004]) and numerical modeling [*Gonnermann and Manga*, 2003] have suggested that nonexplosive fragmentation of magma near conduit walls (where strong shear-stress is expected) could generate fine ash during slip events and result in repetitive ash plumes during stick-slip cycles, a hypothesis which was supported by a ring-shaped vent structure and ash emission patterns observed at Santiaguito [*Bluth and Rose*, 2004; *Sahetapy-Engel et al.*, 2008; *Sahetapy-Engel and Harris*, 2009]. Santiaguito, in particular, is very similar to Arenal in terms of eruptive style, intensity and frequency. Both volcanoes show repeated low energy explosions (several per day), sending ash-plumes up to ≤1–4 km, occasionally generating small pyroclastic flows, with a viscous lava cap plugging a conduit from which lava flows continuously extrude. However, at Arenal the characteristic vent structure and emission pattern reported for Santiaguito have not been observed. Furthermore, the constantly evolving crater morphology and the multiplicity of the feeding conduits at Arenal suggest that the persistence of such annular stick-slip zones is unlikely. However, we cannot exclude the possibility that shear-induced fragmentation may occur locally, along limited surfaces of conduit walls.

[25] In summary, pressure build-up under a viscous degassed cap, which is crosscut by fractures, seems the most adequate model to characterize the eruptive periodicity and associated tremor signal at Arenal. Nevertheless, the mechanism explaining the explosion quakes, and the way these are related to the pyroclastic emissions remains unclear. Hence for now, no model can fully account for the complexity of Arenal's activity.

6. Discussion

[26] The joint observation of gas and ash emissions by seismic and Doppler radar measurements reveals complex behavior at Arenal. The seismicity displays a great diversity of event types, which include tremor (both spasmodic and harmonic, with complex frequency gliding episodes) and explosion quakes (of variable amplitude, sometimes followed by a harmonic tremor coda). The radar measurements also reveal great variability in the mass loading and exit velocities of pyroclastic emissions. However, there is poor correlation with the seismicity, and while some mild explosion quakes observed in the seismic records are not accompanied by ash emission, some radar events are not coeval with a seismic signal. Sometimes ash emissions occur during harmonic tremor, or are associated with high frequency (5–35 Hz) seismic events. When pyroclastic emissions and explosion quakes are concomitant, low correlation is obtained between the kinetic energy of the emission and the seismic amplitude. Moreover, no clear relationship can be observed between repose time and exit velocity of solid particles or mass loading of the plume. All of these observations point to a mechanism of gas and ash emission that is highly variable and probably very sensitive to small perturbations in the system.

6.1. Conceptual Model

[27] To explain these observations, we propose the conceptual model of Figure 8. According to this model, fractures in the solid plug control degassing, which in turn controls the seismic signal. If gas release is frequent and intermittent, repetitive pressure pulses will generate low-frequency tremor signal, whereas if gas release is sudden, flow induced vibrations will generate high-frequency explosion quake signals. We hereafter define an explosion as

the release of a given volume of gas, more or less laden with solid particles, through a fracture in the solid plug which becomes suddenly opened to release the gas pressure. We suggest that the high-frequency components of the associated seismic signal (i.e., the explosion quake) result mainly from the interaction between the pressurized turbulent flow of gas and the rough channel walls. Two mechanisms of flow-induced vibration can be considered, whereby hydrodynamic flow instabilities and oscillations occur at the channel walls [*Rust et al.*, 2008]. In the first case, the fluid flow in a thin channel generates roll waves (i.e., waves of channel thickness variation) in the elastic walls when the flow speed is higher than

$$U_{crit\ roll} \approx \beta \sqrt{\frac{\rho_s}{\rho_f}} \frac{H}{L}, \quad (2)$$

where β is the shear wave velocity of the walls, ρ_s/ρ_f the rock to fluid density ratio, and H and L are the thickness and length of the channel, respectively. If we consider typical rock property values of β = 1 km/s and ρ_s = 2000 kg/m^3, with a gas density (ρ_f) of 300 kg/m^3 (H_20 at 500°C and 50 MPa) and, because the fracture is closed at the beginning of the explosion, $H \sim 0$ so that the ratio H/L is small ($\sim 10^{-5}$ to 10^{-3}) during the opening of the fracture, the threshold condition for roll waves to be generated is easily met. However, the channel must be long enough for these instabilities to develop.

[28] The second mechanism is the excitation of normal modes of the conduit walls. Instability occurs when the flow velocity is higher than

$$U_{crit\ wall} \approx fL, \quad (3)$$

where f is the modal frequency and L the characteristic length, or width, of the channel. *Rust et al.* [2008] carried out laboratory experiments of gas flow between an elastic membrane and a rigid plate to show that the amplitude of oscillations increases with increased flow speed (when $U > U_{crit\ wall}$). In another experiment where air was forced to flow through a slit in a block of gelatine, they showed that at very high flow velocities, the channel walls slap together producing large and nonperiodic high-frequency elastic waves. We propose that this process could be considered as an analog for the explosion quakes at Arenal (Figure 8c). In the case of strong explosions, the fracture and part of the plug are destroyed and the conduit remains partly open. However, for most explosions in 2005 at Arenal, the gas volume and pressure associated with each explosion was small, so that the fractures were not, or only slightly, damaged by the gas flow and so that they could close again after the event.

[29] The turbulent gas flow may entrain varying quantities of pyroclasts, and depending on its mass loading, may be recorded by the radar. Explosions expelling only gas will not be detected by the radar (and thus will result in explosion quakes without a coeval radar signal, e.g., Figure 2b, 21:38 UTC). On the other hand, those expelling ash-laden gas flow will produce a radar echo (i.e., explosion quakes with coeval radar signal, Figure 2a, 23:29 UTC). Depending on the fracture strength and the underlying gas pressure, the pyroclasts will not necessarily be expelled all at once, and may result in paired eruptions (i.e., eruptions that are ≤3 min apart, Figure 2b at 21:29 and 21:46 UTC) or pulsed emissions (i.e., pulses ≤10 s apart, Figure 3b, plot iv). In most cases, the second event releases less tephra than the first, ejecting the remaining unevacuated material. The short time lapse separating each eruptive event (minutes to tens of minutes, Figure 2) suggests a high capacity for the system to regenerate overpressure over a very short time scale.

[30] When the gas-flow is intermittent through the fractures of the solid plug, it is believed to act as the source mechanism of tremor [*Lesage et al.*, 2006; *Rust et al.*, 2008]. It results from the periodic opening and closure of the fracture triggered by pressure oscillations associated with standing waves in the conduit. The periodic pulses generate evenly spaced spectral peaks by a Dirac comb effect. This is consistent with the results of moment tensor inversion of tremor waveforms which have been interpreted as the opening and closure of a shallow crack [*Davi et al.*, 2012]. It is also consistent with the repeated large amplitude oscillations (1–2 s) observed in many radar signals associated with ash emissions that suggest staccato pressure release [*Donnadieu et al.*, 2008], and with recent observations of correlation between SO_2 emission rate and tremor amplitude at Fuego volcano [*Nadeau et al.*, 2011]. Furthermore, it explains the frequently observed tremor-like coda of explosions, which occur if the fracture can still act as a valve and if the residual pressure below the plug is high enough after the explosion, or if another crack is opened by the main event. During this kind of post-explosive tremor, the pressure is progressively released by the gas escaping through the fracture. Therefore, the gas flow rate in the upper part of the conduit decreases, the average wave velocity in the resonating conduit increases and thus the fundamental frequency and overtones of the tremor also increases. Simultaneously, the pressure reduction induces an increase of gas exsolution of the magma that tends to counterbalance the gas loss. However, the characteristic time of exsolution and gas transfer inside the conduit is larger than that of the gas loss through the fracture. As a consequence, the dominant effect is a pressure release during the first minutes after mild explosions. This process gives an explanation to the positive frequency gliding observed in the post-explosion tremor (e.g., Figure 2a, 23:02 UTC). On the other hand, during tremors that are not associated with explosion, either constant frequency content, or positive/negative frequency gliding can be obtained according to the balance between gas escape through the plug and gas input in the resonating conduit from exsolution and transfer.

6.2. Model Sensitivity to Evolving Summit Conditions

[31] All the mechanisms considered in the model described above are quite sensitive to small changes of the state of the conduit and plug. In open-system volcanoes such as Arenal, shallow system conditions may evolve rapidly, causing high temporal variability in both the seismic and radar waveforms associated with explosions. In particular, the presence of a solidified cap, its rheology, heterogeneous fracturing, thickness, debris residing above it, and consequently its permeability to gas, may evolve over time scales ranging from days to seconds (e.g., disruption following an explosion). Variable degrees of "gas-tightness" cause variable gas output through the plug fractures, and thus result in complex frequency gliding episodes in the tremor signal (Figure 2). Temporal

variations in fracture strength cause differential mechanical responses to pressure increases from one event to another. Consequently, gas and ash may be expelled from one or several fractures (or vents) simultaneously or at slightly delayed intervals, and the eruption focus may change from one event to another. In this context, the partitioning of the total eruptive energy (i.e., its distribution among the various types of energy: kinetic and seismic [see *Gerst*, 2010]), is likely to vary significantly, and will thus act as a contributing factor to the lack of seismo-radar correlation. The variation in explosion depth, in particular, is likely to have a major impact as it strongly controls the coupling efficiency of the elastic energy radiated into the ground and atmosphere [*Johnson and Aster*, 2005]. Deep explosions (i.e., ~200 m [*Davi et al.*, 2010]) may produce strong seismic signals and low radar signals (exiting of the fragmented material is impeded), and vice versa for shallow explosions. Eventually, due to the distance between the vent and the seismometers, very shallow explosions might not be recorded seismically if they are not strong enough. This may provide an explanation to the occurrence of eruptions unrecorded by seismometers [*Williams-Jones et al.*, 2001], and to radar events which show high exit velocities with no coeval seismic counterpart.

[32] Furthermore, explosions may fragment variable quantities of magma, either molten (i.e., fluidal fragmentation of juvenile magma) or solid (i.e., breaching of the solid plug) (Figure 8c), as attested by tephra clast analysis [*Cole et al.*, 2005]. In turn, the turbulent gas flow may entrain varying quantities of pyroclasts from the plug fracture system, which may be unrecorded by the radar if the ash load is too low. Moreover, magma fragmentation and tephra emissions may not necessarily be synchronous with explosions-quake signals. Indeed, magma fragmentation may result from viscous shear near the conduit walls [*Gonnermann and Manga*, 2003], and loose particles may remain in the permeable fractured regions to be entrained in ensuing events [*Sahetapy-Engel and Harris*, 2009]. Ash emissions can thus result from remobilization of loose, previously fragmented material residing atop the lava cap and/or in the fractured region of conduit walls, remobilized during degassing events (e.g., tremor episodes, Figure 3c).

6.3. Perspectives

[33] Further geophysical studies are needed to constrain the conceptual model proposed here. Acoustic measurements were carried out during this recording campaign, but unfortunately the data were extremely noisy and thus unusable. Nevertheless, acoustic records are likely to hold crucial information on the mechanical processes operating in both the magmatic conduit and the magma-air interface [e.g., *Hagerty et al.*, 2000]. Thus further seismo-acoustic measurements, coupled with coincident Doppler mreasurements, would greatly increase our ability to constrain a shallow system model. Because the mechanism of the eruptions is thought to be closely related to degassing processes, coincident gas flux measurements would also be helpful. In particular, SO_2 fluxes measured by UV cameras have shown to decrease prior to ash-bearing eruptions at Sakurajima [*Kazahaya et al.*, 2010], which suggests that sealing processes were operating between each eruption. Coupling gas flux and radar measurements is thus likely to be very promising. These additional geophysical measurements, if performed continuously over a long period, should allow us to better analyze the variability of the geophysical signals over longer time scales. Such studies may help to further constrain the complex processes, patterns and feedbacks operating in the shallow system of Arenal, and to better understand the mechanism and evolution of its persistent activity.

7. Conclusion

[34] Joint observation of tephra emissions and subsurface processes was carried out at Arenal using broadband seismometers and a ground-based Doppler radar to quantify surface tephra emissions. Cross-correlation of both signals shows complex, nonrepeatable relationships. Indeed, tephra emissions are not systematically associated to a unique type of seismic event, and seem to occur with no clear correlation with the tremor amplitude fluctuation, the seismic energy release rate, or the repose time between successive emissions. Moreover poor correlations are found between the features of both signals (e.g., kinetic energies, backscattered powers, exit velocities of radar signals, versus seismic amplitude, frequency content). We propose a conceptual model that accounts for the generation of the tremor, the explosion quakes, and their relationship with tephra emissions. We suggest that fractures through a solid cap tapping the conduit control degassing of the shallow system, which in turn control the seismic waveforms and tephra emissions. If the gas release is intermittent, it will produce repetitive pressure pulses and thus generate low-frequency tremor signal. On the contrary if gas is suddenly released after the fracture's strength has been overcome by the underlying pressure, flow induced vibrations will generate high-frequency, explosion quake signals. Depending on the amount of fragmented material carried by the gas, the degassing event will either be accompanied by a radar signal (i.e., ash-laden gas output), or not (i.e., ash-free gas output). The variable shallow system conditions (plug thickness, rheology, fracturing, permeability) are likely to be reset on short timescales, and thus result in nonrepetitive conditions that may account for the variability of the gas and ash emission mechanisms (and resulting seismic and radar signals).

[35] **Acknowledgments.** The 2005 radar and seismic campaign was funded through the INSU-CNRS ACI program and the BQR B2005–09 project of Université de Savoie. Financial support from projects 113-A5-503 and 830-A7-511 from University of Costa Rica, Ministry of Science and Technology (MICIT) and National Council for Scientific and Technological Research (CONICIT) and European Commission 6th Framework Project VOLUME (Contract N° 018471) are acknowledged. Acknowledgments are also due to Claude Hervier for technical assistance, Harold Clenet and Laure Pouchol for help in data processing, and Mathieu Gouhier for fruitful discussions on the topic. The Escuela de Geologia and the Instituto Costarricense de Electricidad provided very helpful logistic support, and particular thanks are due to Luis-Fernando Brenes for his great help in the field. We also thank the staff of the Parque Nacional Volcán Arenal for facilitating fieldwork. M. Mora benefited from the visiting researcher program of OPGC. Reviews of the manuscript by Mathias Hort, Micol Todesco, and Geoff Wadge, as well as editorial handling by Tom Parsons, are warmly acknowledged.

References

Barquero, R., G. Alvarado, and T. Matumoto (1992), Arenal volcano (Costa Rica) premonitory seismicity, in *Volcanic Seismology*, edited by P. Gasparini, R. Scarpa, and K. Aki, pp. 84–96, Springer, Berlin.

Benoit, J. P., and S. R. McNutt (1997), New constraints on source processes of volcanic tremor at Arenal volcano, Costa Rica, using broadband seismic data, *Geophys. Res. Lett.*, *24*(4), 449–452, doi:10.1029/97GL00179.

Bertolino, S., C. Cigolini, and G. E. Alvarado (2009), Viscosity and explosive volcanism: The case of Arenal volcano (Costa Rica), *Eos Trans. AGU*, *90*(52), Fall Meet. Suppl., Abstract V11B-1943.

Bluth, G. J. S., and W. I. Rose (2004), Observations of eruptive activity at Santiaguito volcano, Guatemala, *J. Volcanol. Geotherm. Res.*, *136*(3–4), 297–302, doi:10.1016/j.jvolgeores.2004.06.001.

Chouet, B. A. (1996), Long-period volcano seismicity: Its source and use in eruption forecasting, *Nature*, *380*(6572), 309–316, doi:10.1038/380309a0.

Cigolini, C., and A. Borgia (1980), Consideraciones sobre la viscosidad y la estructura de las coladas: Volcán Arenal, Costa Rica, *Rev. Geogr. Am. Central*, *1*(11–12) 131–140.

Cigolini, C., A. Borgia, and L. Casertano (1984), Intra-crater activity, aa-block lava, viscosity and flow dynamics: Arenal volcano, Costa Rica, *J. Volcanol. Geotherm. Res.*, *20*(1–2), 155–176, doi:10.1016/0377-0273(84)90072-6.

Cole, P., E. Fernandez, E. Duarte, and A. Duncan (2005), Explosive activity and generation mechanisms of pyroclastic flows at Arenal volcano, Costa Rica between 1987 and 2001, *Bull. Volcanol.*, *67*(8), 695–716, doi:10.1007/s00445-004-0402-6.

Davi, R., G. O'Brien, I. Lokmer, C. Bean, P. Lesage, and M. M. Mora (2010), Moment tensor inversion of explosive long period events recorded on Arenal volcano, Costa Rica, constrained by synthetic tests, *J. Volcanol. Geotherm. Res.*, *194*(4), 189–200, doi:10.1016/j.jvolgeores.2010.05.012.

Davi, R., G. O'Brien, L. De Barros, I. Lokmer, C. Bean, P. Lesage, M. M. Mora, and G. J. Soto (2012), Seismic source mechanisms of tremor events recorded on Arenal volcano, Costa Rica, retrieved by waveform inversion, *J. Volcanol. Geotherm. Res.*, *213–214*, 1–3, doi:10.1016/j.jvolgeores.2011.10.008.

De la Cruz-Reyna, S., and G. Reyes-Dávila (2001), A model to describe precursory material-failure phenomena: Application to short-term forecasting at Colima volcano, Mexico, *Bull. Volcanol.*, *63*, 297–308, doi:10.1007/s004450100152.

Denlinger, R. P., and R. P. Hoblitt (1999), Cyclic eruptive behavior of silicic volcanoes, *Geology*, *27*(5), 459–462, doi:10.1130/0091-7613(1999)027<0459:CEBOSV>2.3.CO;2.

Donnadieu, F., G. Dubosclard, P. Allard, R. Cordesses, C. Hervier, J. Kornprobst, and J. F. Lénat (2003), Sondages des jets volcaniques par radar Doppler: Applications à l'Etna, in *Rapport Quadriennal de Comité National Français de Géodésie et de Géophysique (C.N.F.G.G.), 1999–2002, XXIII^e Assemblée Générale de l'Union Géodésique et Géophysique Internationale*, edited by J.-P. Barriot, pp. 119–124, Acad. des Sci., de Paris, Paris.

Donnadieu, F., G. Dubosclard, R. Cordesses, T. Druitt, C. Hervier, J. Kornprobst, J. F. Lénat, P. Allard, and M. Coltelli (2005), Remotely monitoring volcanic activity with ground-based Doppler radar, *Eos Trans. AGU*, *86*(21), 201, doi:10.1029/2005EO210001.

Donnadieu, F., M. Gouhier, J. Fournet-Fayard, and C. Hervier (2008), Applications of pulsed ground-based Doppler radar to the study and monitoring of volcanoes, in *Proceedings of the Ground-Based Radar Observations for Volcanoes Workshop*, edited by G. Wadge and R. A. Robertson, pp. 6–8, Environ. Syst. Sci. Cent., Reading, U. K.

Donnadieu, F., S. Valade, and S. Moune (2011), Three-dimensional transport speed of wind-drifted ash plumes using ground-based radar, *Geophys. Res. Lett.*, *38*, L18310, doi:10.1029/2011GL049001.

Dubosclard, G., R. Cordesses, P. Allard, C. Hervier, M. Coltelli, and J. Kornprobst (1999), First testing of a volcano Doppler radar (Voldorad) at Mt. Etna, *Geophys. Res. Lett.*, *26*, 3389–3392, doi:10.1029/1999GL008371.

Dubosclard, G., F. Donnadieu, P. Allard, R. Cordesses, C. Hervier, M. Coltelli, M. Privitera, and J. Kornprobst (2004), Doppler radar sounding of volcanic eruption dynamics at Mount Etna, *Bull. Volcanol.*, *66*, 443–456, doi:10.1007/s00445-003-0324-8.

Endo, E. T., and T. Murray (1991), Real-time Seismic Amplitude Measurement (RSAM): A volcano monitoring and prediction tool, *Bull. Volcanol.*, *53*, 533–545, doi:10.1007/BF00298154.

Garcés, M. A., M. T. Hagerty, and S. Y. Schwartz (1998), Magma acoustics and time-varying melt properties at Arenal volcano, Costa Rica, *Geophys. Res. Lett.*, *25*(13), 2293–2296, doi:10.1029/98GL01511.

Gerst, A. (2010), The first second of a Strombolian volcanic eruption, Ph.D. thesis, Hamburg Univ., Hamburg, Germany.

Gonnermann, H. M., and M. Manga (2003), Explosive volcanism may not be an inevitable consequence of magma fragmentation, *Nature*, *426*(6965), 432–435, doi:10.1038/nature02138.

Gouhier, M., and F. Donnadieu (2008), Mass estimations of ejecta from Strombolian explosions by inversion of Doppler radar measurements, *J. Geophys. Res.*, *113*, B10202, doi:10.1029/2007JB005383.

Gouhier, M., and F. Donnadieu (2010), The geometry of Strombolian explosions: Insights from Doppler radar measurements, *Geophys. J. Int.*, *183*, 1376–1391, doi:10.1111/j.1365-246X.2010.04829.x.

Hagerty, M. T., S. Y. Schwartz, M. A. Garcés, and M. Protti (2000), Analysis of seismic and acoustic observations at Arenal Volcano, Costa Rica, 1995–1997, *J. Volcanol. Geotherm. Res.*, *101*, 27–65, doi:10.1016/S0377-0273(00)00162-1.

Hellweg, M. (2000), Physical models for the source of Lascar's harmonic tremor, *J. Volcanol. Geotherm. Res.*, *101*(1–2), 183–198, doi:10.1016/S0377-0273(00)00163-3.

Jaupart, C., and S. Vergniolle (1988), Laboratory models of Hawaiian and Strombolian eruptions, *Nature*, *331*(6151), 58–60, doi:10.1038/331058a0.

Johnson, J., and R. Aster (2005), Relative partitioning of acoustic and seismic energy during Strombolian eruptions, *J. Volcanol. Geotherm. Res.*, *148*(3–4), 334–354, doi:10.1016/j.jvolgeores.2005.05.002.

Johnson, J. B., and J. M. Lees (2000), Plugs and chugs—Seismic and acoustic observations of degassing explosions at Karymsky, Russia and Sangay, Ecuador, *J. Volcanol. Geotherm. Res.*, *101*(1–2), 67–82, doi:10.1016/S0377-0273(00)00164-5.

Johnson, J. B., J. M. Lees, and E. I. Gordeev (1998), Degassing explosions at Karymsky volcano, Kamchatka, *Geophys. Res. Lett.*, *25*(21), 3999–4002, doi:10.1029/1998GL900102.

Johnson, J. B., M. C. Ruiz, J. M. Lees, and P. Ramon (2005), Poor scaling between elastic energy release and eruption intensity at Tungurahua volcano, Ecuador, *Geophys. Res. Lett.*, *32*, L15304, doi:10.1029/2005GL022847.

Kazahaya, R., T. Mori, and M. Iguchi (2010), The degassing fluctuation concerning sealing process before eruptions at Sakurajima volcano, Japan, Abstract V52C-06 presented at 2010 Fall Meeting, AGU, San Francisco, Calif., 13–17 Dec.

Lesage, P. (2009), Interactive Matlab software for the analysis of seismic volcanic signals, *Comput. Geosci.*, *35*(10), 2137–2144, doi:10.1016/j.cageo.2009.01.010.

Lesage, P., M. M. Mora, G. E. Alvarado, J. Pacheco, and J.-P. Métaxian (2006), Complex behavior and source model of the tremor at Arenal volcano, Costa Rica, *J. Volcanol. Geotherm. Res.*, *157*(1–3), 49–59, doi:10.1016/j.jvolgeores.2006.03.047.

McNutt, S. R. (2002), Volcano seismology and monitoring for eruptions, in *International Handbook of Earthquake and Engineering Seismology*, *Int. Geophys. Ser.*, vol. 81, edited by W. H. K. Lee et al., pp. 383–406, Elsevier, New York.

Melnik, O., and R. S. J. Sparks (2002), Dynamics of magma ascent and lava extrusion at Soufrière Hills Volcano, Montserrat, *Geol. Soc. London, Mem.*, *21*(1), 153–171, doi:10.1144/GSL.MEM.2002.021.01.07.

Minakami, T., S. Utibori, and S. Hiraga (1969), The 1968 eruption of volcano Arenal, Costa Rica, *Bull. Earthquake Res. Inst. Univ. Tokyo*, *47*, 783–802.

Mora, M. (2003), Etude de la structure superficielle et de l'activité sismique du volcan Arenal, Costa Rica, Ph.D. thesis, Lab. de Géophys. Interne et Tectonophys., Univ. de Savoie, Le Bourget du Lac, France.

Mora, M. M., P. Lesage, B. Valette, G. E. Alvarado, C. Leandro, J.-P. Métaxian, and J. Dorel (2006), Shallow velocity structure and seismic site effects at Arenal volcano, Costa Rica, *J. Volcanol. Geotherm. Res.*, *152*(1–2), 121–139, doi:10.1016/j.jvolgeores.2005.09.013.

Mora, M., P. Lesage, F. Donnadieu, S. Valade, A. Schmidt, G. Soto, W. Taylor, and G. Alvarado (2009), Joint seismic, acoustic and Doppler radar observations at Arenal volcano, Costa Rica: Preliminary results, in *VOLUME Project*, edited by C. J. Bean et al., pp. 330–340, VOLUME Proj. Consortium, Dublin.

Mori, J., H. Patia, C. McKee, I. Itikarai, P. Lowenstein, P. De Saint Ours, and B. Talai (1989), Seismicity associated with eruptive activity at Langila volcano, Papua New Guinea, *J. Volcanol. Geotherm. Res.*, *38*, 243–255, doi:10.1016/0377-0273(89)90040-1.

Murillo, S., and P. Ruiz (2004), Datos paramétricos de las coladas de lava del volcán Arenal (Costa Rica) entre 1968 y 2002, *Boletín Obs. Sismol. Vulcanológico Arenal Miravalles*, *15*(27), 25–33.

Nadeau, P. A., J. L. Palma, and G. P. Waite (2011), Linking volcanic tremor, degassing, and eruption dynamics via SO_2 imaging, *Geophys. Res. Lett.*, *38*, L01304, doi:10.1029/2010GL045820.

Neuberg, J. (2000), Characteristics and causes of shallow seismicity in andesite volcanoes, *Philos. Trans. R. Soc. London A*, *358*(1770), 1533–1546, doi:10.1098/rsta.2000.0602.

Ozerov, A. Y. (2010), The mechanism of basaltic explosions: Experimental modeling, *J. Volcanol. Seismol.*, *4*(5), 295–309, doi:10.1134/S0742046310050015.

Rust, A. C., N. J. Balmforth, and S. Mandre (2008), The feasibility of generating low-frequency volcano seismicity by flow through a deformable channel, in *Fluid Motions in Volcanic Conduits: A Source of Seismic*

and Acoustic Signals, edited by S. J. Lane and J. S. Gilbert, *Geol. Soc. Spec. Publ.*, *307*, 45–56, doi:10.1144/SP307.4.

Sahetapy-Engel, S., and A. Harris (2009), Thermal structure and heat loss at the summit crater of an active lava dome, *Bull. Volcanol.*, *71*(1), 15–28, doi:10.1007/s00445-008-0204-3.

Sahetapy-Engel, S. T., A. J. Harris, and E. Marchetti (2008), Thermal, seismic and infrasound observations of persistent explosive activity and conduit dynamics at Santiaguito lava dome, Guatemala, *J. Volcanol. Geotherm. Res.*, *173*(1–2), 1–14, doi:10.1016/j.jvolgeores.2007.11.026.

Soltzberg, L. J., P. G. Bowers, and C. Hofstetter (1997), A computer model for soda bottle oscillations: "The bottelator, *J. Chem. Educ.*, *74*(6), 711–714, doi:10.1021/ed074p711.

Stix, J., R. C. Torres, L. Narváez M, G. P. Cortés J, J. A. Raigosa, D. Gómez M, and R. Castonguay (1997), A model of vulcanian eruptions at Galeras volcano, Colombia, *J. Volcanol. Geotherm. Res.*, *77*(1–4), 285–303, doi:10.1016/S0377-0273(96)00100-X.

Valade, S., and F. Donnadieu (2011), Ballistics and ash plumes discriminated by Doppler radar, *Geophys. Res. Lett.*, *38*, L22301, doi:10.1029/2011GL049415.

Wadge, G., D. Oramas Dorta, and P. Cole (2006), The magma budget of Volcán Arenal, Costa Rica from 1980 to 2004, *J. Volcanol. Geotherm. Res.*, *157*(1–3), 60–74, doi:10.1016/j.jvolgeores.2006.03.037.

Williams-Jones, G., J. Stix, M. Heiligmann, J. Barquero, E. Fernandez, and E. D. Gonzalez (2001), A model of degassing and seismicity at Arenal volcano, Costa Rica, *J. Volcanol. Geotherm. Res.*, *108*(1–4), 121–139, doi:10.1016/S0377-0273(00)00281-X.

Wilson, L. (1980), Relationships between pressure, volatile content and ejecta velocity in three types of volcanic explosion, *J. Volcanol. Geotherm. Res.*, *8*(2–4), 297–313, doi:10.1016/0377-0273(80)90110-9.

Yokoo, A., T. Tameguri, and M. Iguchi (2009), Swelling of a lava plug associated with a Vulcanian eruption at Sakurajima Volcano, Japan, as revealed by infrasound record: Case study of the eruption on January 2, 2007, *Bull. Volcanol.*, *71*, 619–630, doi:10.1007/s00445-008-0247-5.

Zobin, V. M., G. A. Reyes, E. Guevara, and M. Bretón (2009), Scaling relationship for Vulcanian explosions derived from broadband seismic signals, *J. Geophys. Res.*, *114*, B03203, doi:10.1029/2008JB005983.

G. E. Alvarado and M. M. Mora, Escuela Centroamericana de Geología, Universidad de Costa Rica, San José, Costa Rica.

F. Donnadieu, A. Harris, and S. Valade, Clermont Université, Université Blaise Pascal, Observatoire de Physique du Globe de Clermont-Ferrand, Laboratoire Magmas et Volcans, BP 10448, F-63000 Clermont-Ferrand, France. (f.donnadieu@opgc.univ-bpclermont.fr; s.valade@opgc.univ-bpclermont.fr)

P. Lesage, Institut des Sciences de la Terre, Université de Savoie, CNRS, F-73376 Le Bourget-du-Lac, CEDEX, France.

Appendix E. *Valade and Donnadieu*, 2011

Valade, S., and F. Donnadieu (2011), Ballistics and ash plumes discriminated by Doppler radar, *Geophys. Res. Lett*., doi: 10.1029/2011GL049415.

+ GRL cover image (Volume 38, No 22.)

+ EOS research spotlight (Volume 93, Number 2, January 2012)

Observing volcanic ash plumes and ballistics using Doppler radar, *Eos Trans. AGU*, 93(2), 28, doi:10.1029/2012EO020025.

Ballistics and ash plumes discriminated by Doppler radar

Sébastien Valade[1,2,3] and Franck Donnadieu[1,2,3]

Received 23 August 2011; revised 12 October 2011; accepted 12 October 2011; published 16 November 2011.

[1] Small scale eruptive ash plumes at Arenal volcano (Costa Rica) were recorded using a ground-based Doppler radar (VOLDORAD). The time-velocity distribution of the mass load (i.e., Doppler radargrams) exhibits two contrasted dynamics recorded simultaneously, evidenced by distinctive velocities, life spans, and transit speeds through the radar beam. Synthetic Doppler radargrams computed with a simple ballistic model indicate that the short-lived signal is consistent with the instantaneous projection of ballistics blocks accompanying the ash plume emission. The mass of centimeter- to decimeter-sized ballistics is confidently estimated at 0.5–7 tons, whereas the ash plume mass is loosely constrained at 5.8×10^2 tons, assuming a particle diameter of 2 mm close to the vent. These quantitative estimates of the mass proportion either falling on the slopes of the volcano or ejected into the atmosphere could help in the modeling and monitoring of tephra dispersal. **Citation:** Valade, S., and F. Donnadieu (2011), Ballistics and ash plumes discriminated by Doppler radar, *Geophys. Res. Lett.*, *38*, L22301, doi:10.1029/2011GL049415.

1. Introduction

[2] Small-scale volcanic eruptions commonly expel a wide range of pyroclast sizes, ranging from coarse blocks with ballistic trajectories, to fine ash driven away within ash plumes. As both the plume and the ballistics are emitted simultaneously, it is often difficult to discriminate and to collect quantitative data on both phenomena. Thermal [*Patrick et al.*, 2007; *Marchetti et al.*, 2009] and ultraviolet imagery [*Yamamoto et al.*, 2008] have provided powerful insights into the dynamics of mild strombolian and vulcanian eruptions, shedding light onto the plume rise dynamics and the relative ash/ballistics distribution of the ejecta. In this paper, we describe similar small-scale transient eruptions at Arenal (Costa Rica), monitored with a ground-based Doppler radar (VOLDORAD) [*Dubosclard et al.*, 2004; *Donnadieu et al.*, 2005]. The radar provides quantitative information on exit velocities and mass loading of the ejecta. We show that the time-velocity distribution of the mass load (i.e., Doppler radargram) reveals two distinct dynamics, which discriminates the ballistics and the ash plume transiting through the radar beam. We compute synthetic Doppler radargrams by numerical modeling of the ballistics, and constrain the dynamics and mass loadings of both the ballistics and the ash plume. Such characterization of the near-vent eruptive dynamics has strong potential applications, as the degree of fragmentation and the mass proportion injected into the atmosphere are of interest for hazard mitigation issues.

[1] Laboratoire Magmas et Volcans, OPGC, Clermont Université, Université Blaise Pascal, Clermont-Ferrand, France.
[2] LMV, UMR 6524, CNRS, Clermont-Ferrand, France.
[3] LMV, IRD, R 163, Clermont-Ferrand, France.

0094-8276/11/2011GL049415

2. Radar Data Acquisition

[3] VOLDORAD is a ground-based, pulsed Doppler radar, specifically designed for active remote sensing of volcanic jets and plumes [*Dubosclard et al.*, 2004]. The radar was set 2.4 km West of Arenal's active crater C, at an altitude of 685 m. The 27° antenna elevation enabled the beam to skim the summit crater (Figure 1). The spatial resolution is defined by the beam aperture (9°) and the radial depth (120 m) of the successive volumes (range gates) sampled in the beam, referenced by their radial distance to the radar (e.g., 2247 to 2727 m). When volcanic ejecta cross the beam, they scatter some energy of the pulsed electromagnetic waves (100 μs^{-1}) back to the radar. Doppler spectra (acquired at 0.14 s^{-1}), express the power backscattered by the ejecta during the pulse duration (0.8 μs) as a function of their radial velocity (Figure 2a). The backscattered power is a complex function of the number and size of the ejecta. The measured radial velocities inferred from the frequency shift between the transmitted and the backscattered signal correspond to the along-beam components of the ejecta velocities. Positive and negative radial velocities are induced by particles having a radial component of motion respectively away from and towards the radar. Consequently, in the range gates up the vent, ascending ballistics generate mainly positive radial velocities, whereas falling blocks tend to produce negative radial velocities. The juxtaposition of Doppler spectra constitute Doppler radargrams (Figure 2b), which reveal the evolution through time (x-axis) of both the velocities (y-axis) and echo power (color scale) of the ejecta in each range gate. All the useful spatio-temporal information characterizing the target (velocimetry, mass loading, shape of spectra, evolution through the gates) is plotted at once and constitute its Doppler signature.

3. Results

[4] Figure 2b shows the Doppler signature of an eruptive event recorded on February 19, 2004 at 20:00:31 UT. The recording shows two distinct features, characterized by contrasted dynamics, i.e., different life spans, radial velocities, and transit speeds through the radar range gates. The first feature is a short-lived (<15 s) impulsive signal, first appearing at 2607 m as a curved streak. It spreads on a large velocity range (both positive and negative velocities), and transits rapidly through the beam (~3–4 s per gate in average). In the gates above the vent and uphill (i.e., 2607 m and 2727 m), it exhibits sharp onsets, with relatively high positive velocities (>+40 m/s) and high backscattered power

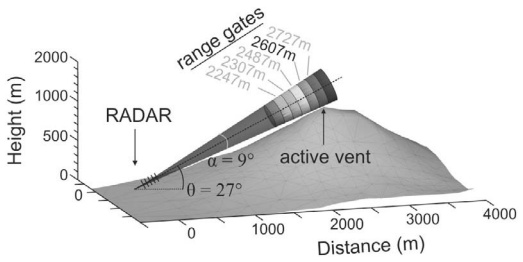

Figure 1. Geometry of the radar sounding at Arenal showing the sampled volumes in the beam. The radar was set up at an altitude of 685 m, 2.4 km West and downwind of the active crater.

(~34 dB in gate 2607 m) reached in <2 s. In both gates, the peak echo power shifts progressively from positive to negative velocities in ~10–13 s (e.g., reaches −30 m/s in gate 2607 m at 20:00:44 UT). In the gates downhill from the vent however (i.e., 2487 m to 2247 m), only negative velocities are recorded: in gate 2487 m for instance, the onset velocity is of −25 m/s, and reaches −48 m/s in ~5 s. Contrastingly, the second feature is a longer-lived signal (≥60 s), whose Doppler signature differs significantly from the short-lived signal: the onsets of both the echo power and the Doppler velocities are progressive, the peak power is 50 times lower (~17 dB), the range of Doppler velocities is similar in all range gates (0 to −15 m/s), the signal lasts 1–2 minutes (e.g., ~84 s in gate 2367 m), and it transits slowly throughout the range gates (~15–20 s per gate in average) with decreasing amplitude. Such Doppler signature is characteristic of an ash plume entrained towards the radar by the wind whose transport speed can be determined in 3-D [*Donnadieu et al.*, 2011].

[5] The occurrence of these two features is observed in several recordings of eruptive events, either simultaneously (e.g., Figure 2), or independently. The differences in the Doppler signature of both point out different dynamics, which suggests that the radar records more than just an ash plume. We hereafter model the short-lived part of the signal to explain its origin.

4. Interpretation and Discussion

[6] Mild explosions typically occur several times a day at Arenal, resulting in small ash-plumes rising to a few hundreds of meters above the vent [*Cole et al.*, 2005]. They are sometime accompanied by blocks impacting the volcano upper slopes, and visible at night as incandescent ballistic projections. We show below with a simple model example that the features of the short-lived signal are consistent with ballistic projections, and we discuss the mass loadings of both the ballistics and the ash plume.

4.1. Modeling Ballistic Projections

[7] We use the 2-D model of *Dubosclard et al.* [2004], to compute the ballistic trajectories of ejecta and the associated synthetic echo power in each range gate. Spherical particles are instantaneously released at selected angles with a velocity depending on the initial gas velocity. Their trajectories are determined by solving the equations of motion

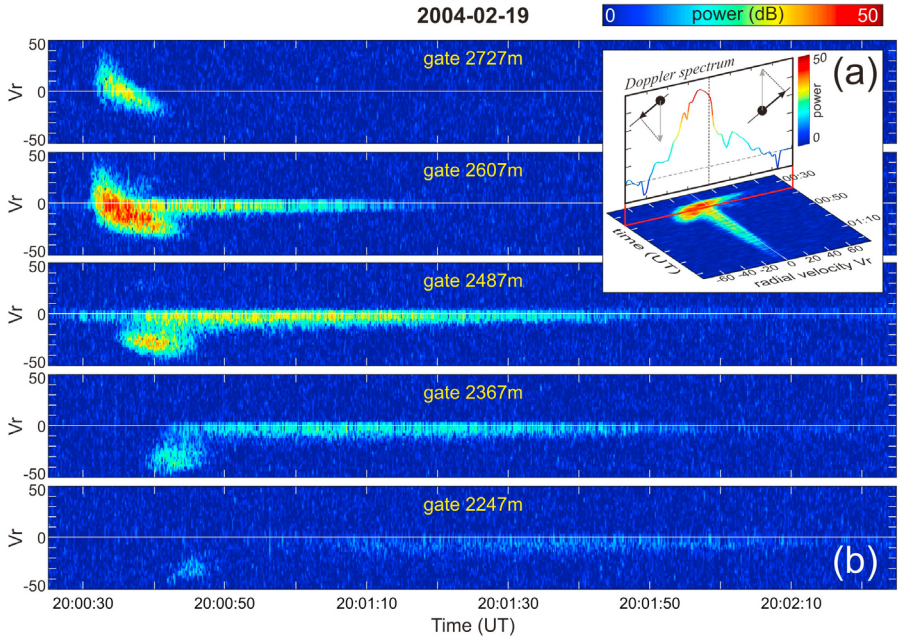

Figure 2. Doppler radargrams recorded during an ash plume emission at Arenal on February 19, 2004 at 20:00:31 UT. (a) The Doppler radargram is built from the succession through time of Doppler spectra. The echo power in the spectrum (dB arbitrary units) is related to the number and size of the particles in the range gate. Positive (right part of the spectrum) and negative (left part) radial velocities correspond to particles with an along-beam velocity component respectively away from the radar antenna and towards it. (b) Doppler radargrams recorded in gates 2247 m to 2727 m, revealing the spatio-temporal evolution of two contrasted event dynamics: the short-lived signal with rapidly changing radial velocities and quickly transiting through the range gates is induced by ballistics, whereas the longer-lived signal with low negative velocities is induced by the wind-drifted ash plume.

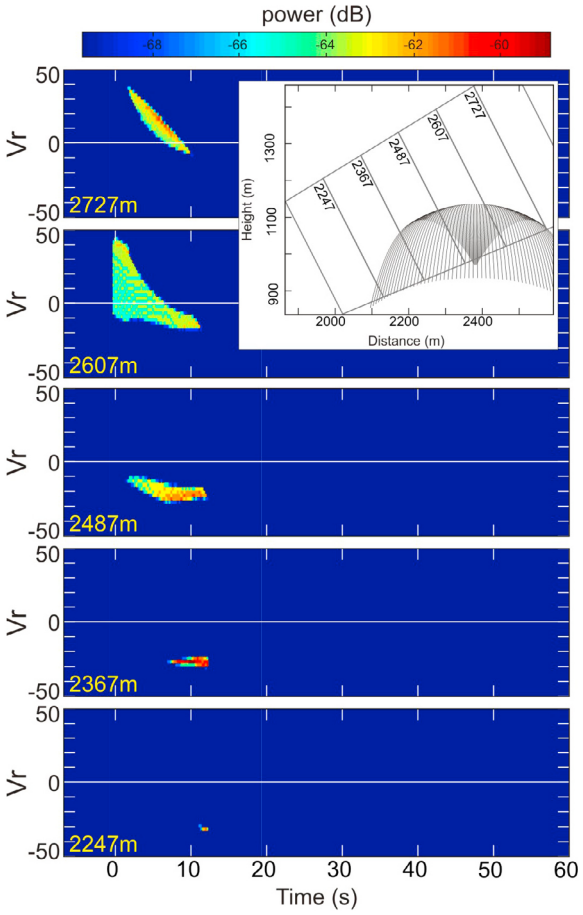

Figure 3. Example of synthetic Doppler radargrams generated with a 2-D ballistic model [*Dubosclard et al.*, 2004; *Gouhier and Donnadieu*, 2010]. 60 spherical particles of diameter 0.1 m were uniformly released in a vertical cone of 60° aperture, with an initial gas velocity of 105 m/s. The source is 20 m below the 2607 m range gate, at x = 2381 m and y = 966 m from the radar. The main features of the short-lived signal observed in Figure 2 are reproduced, indicating its ballistic origin.

under the influence of gas drag and gravity (see *Dubosclard et al.* [2004] for details on the driving equations). The synthetic Doppler spectra are then constructed at each time step by splitting particle radial velocities into classes, and summing the backscattered powers of the particles in each velocity class [*Gouhier and Donnadieu*, 2010]. To reconstruct the evolution of the Doppler signature in the different range gates, Doppler spectra are juxtaposed in time, and a color scale is used for the echo amplitude. Note that this admittedly simple ballistic model was not intended to recover the true eruptive parameters by matching the exact time-velocity distribution of the echo power (which would require inversion procedures, subject of ongoing work), but only to reproduce the main characteristics of the Doppler signature of the short-lived signal using realistic block size and gas velocities.

[8] Figure 3 shows an example of synthetic Doppler signature produced by spheres of 0.1 m in diameter, launched within a vertical cone 60° wide, with an initial gas velocity of 105 m/s. The Doppler radargrams successfully reproduce the main characteristics of the short-lived signal observed in Figure 2b, in particular the transit times, the shape and the number of range gates crossed. The sharp onset in positive velocities at gates 2607 m and 2727 m (+44 and +37 m/s respectively) is successfully reproduced, as well as the decay towards negative velocities during about 10 s. The obtained characteristic curved shape can henceforth be interpreted as mostly resulting from the progressive bending of the ballistic trajectories through the radar beam. As for the gates closer to the radar, the simulation reproduces the onset at moderate and increasing negative radial velocities (−14 m/s in gate 2487 m), the signal onset in the next gate again at higher radial velocities (−27.5 m/s in gate 2367 m), and the progressive diminution of signal duration at increasing distances from the vent (~10.5 s in gate 2487 m against ~1 s in gate 2247 m). Because of the voluntarily simple model, several features of lower importance are not reproduced well: (i) the synthetic power is not as high as the recorded power because of the small number of particles launched in the model; (ii) the spectral width is too narrow, probably because only one particle size and 2-D trajectories are considered. Nevertheless, the reasonable match of the synthetic and observed Doppler signatures strengthens the origin of the short-lived signal as being the instantaneous projection of ballistic blocks crossing the successive range gates.

4.2. Constraints on Mass Loadings

[9] Radar recordings (Figure 2b) have shown that ballistics emitted simultaneously with an ash plume could be discriminated by their distinctive Doppler signature. Using the Mie scattering theory [*Gouhier and Donnadieu*, 2008], the peak echo power of both signals can then be used to constrain the respective masses and volumes of tephra comprising the ballistics and the plume.

[10] Figure 4 shows the solutions for the reflectivity factors close to those measured during the emissions of the ballistics and the ash plume (74.5 and 57.5 dBZ respectively) for

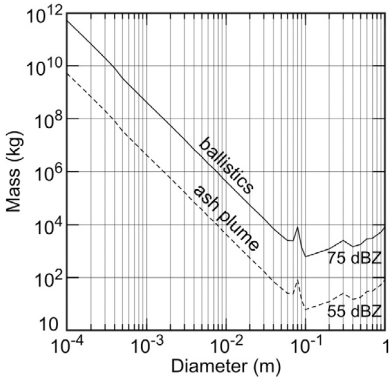

Figure 4. Tephra mass inferred from the Mie scattering theory for various average particle diameters. The two curves indicate the solutions for reflectivity factors close to those measured during the emissions of the ballistics and the ash plume. The mass (assumed density: 1700 kg/m^3) can be well constrained in the case of centimeter- to decimeter-sized ballistics, whereas in the case of the ash plume, it critically depends on the assumed diameter because of the finer grain size distribution.

various particle diameters assumed. The strong power values observed in the short-lived signal (Figure 2b) suggest that they were produced by coarse ballistic particles (blocks), because large particles backscatter much more energy than fine ones. If we consider block sizes ranging between 0.04–1 m and 1700 kg/m^3 in density, the mass of ballistics would fall in the range 0.5–7 tons, i.e., a DRE volume of ballistics of 0.2–2.8 m^3 (density of 2500 kg/m^3). Comparatively, *Cole et al.* [2005] give crude estimates of the total tephra volume of individual explosions at Arenal in the region 10–50 m^3.

[11] For finer grain size distributions, the inferred mass becomes critically dependent on the assumed diameter (Figure 4). Accessing the particle size distribution within the ash plume near the vent is particularly challenging, so we used the coarsest diameter (2 mm) of particles collected by *Cole et al.* [2005] between 2 and 3 km downwind of the vent. Assuming a density of 1000 kg/m^3 (2 mm andesitic ash [*Bonadonna and Phillips*, 2003]), the estimated mass is in the order of 5.8×10^2 tons. Our value likely represents an upper limit for the mass of ash in the plume because (i) the particle size distribution above the vent is highly polydisperse with a diameter mode certainly coarser than the assumed 2 mm diameter, (ii) the particle shapes are likely to deviate from the spherical assumption of the Mie theory, which increases the energy backscattered to the radar [e.g., *Sauvageot*, 1992], and (iii) the ash plume might not completely fill the range gates probed by the radar. To a lesser extent, the ash mass estimate is slightly underestimated because the duration of the ash emission exceeds the plume transit time through the range gates, unlike the ejection of ballistics. More precise estimation of the mass loading of ash plumes would require more stringent constraints on the grain size distribution close to the vent.

5. Conclusions

[12] Ground-based Doppler radars allow the discrimination of ballistics and ash plumes expelled simultaneously. The Doppler radar signatures show two distinct dynamics characterized by different evolutions of the velocity range with time, distinct durations and transit speeds through the radar range gates. In the event analyzed, the ballistics are released instantaneously and transit through 3 range gates in <10 s at radial velocities exceeding 40 m/s. The mass of centimeter- to decimeter-sized ballistics is confidently estimated at 0.5–7 tons. Contrastingly, the ash plume emission lasts several tens of seconds, exhibits lower along-beam velocities (<15 m/s in the radar direction) and longer transit times in the beam, depending on the wind speed and direction. Because the inferred mass becomes critically dependent on the assumed diameters for infra-centimeter particles, the ash plume mass is loosely constrained at 5.8×10^2 tons assuming an average diameter of 2 mm above the vent. The ability to remotely discriminate ballistics and ash plumes expelled simultaneously opens a way to better constrain the eruption mechanisms and source parameters. In particular, refining the mass fraction prone to be ejected in the atmosphere during large eruptions would help in the modeling and monitoring of tephra dispersal. Furthermore, inversion procedures to obtain numerical models matching the exact time-velocity distribution of the echo power in the observed signal, are the subject of ongoing research. These will enable the retrieval of initial eruptive parameters, such as initial gas velocities, particle size distribution, ejecta trajectories and exit velocities.

[13] **Acknowledgments.** The radar campaign was funded by the ACI Risques Naturels program of the French CNRS-INSU. Facilities for radar soundings were kindly provided by the Universidad de Costa Rica, ICE and Arenal National Park. We are indebted to M. Mora, G. Alvarado, C. Hervier, T.H. Druitt, M. Gouhier L.-F. Brenes, F. Arias and C. Ramirez for assistance in the field.

[14] The Editor wishes to thank Iain Matthew Watson for his assistance evaluating this paper.

References

Bonadonna, C., and J. C. Phillips (2003), Sedimentation from strong volcanic plumes, *J. Geophys. Res.*, *108*(B7), 2340, doi:10.1029/2002JB002034.

Cole, P., E. Fernandez, E. Duarte, and A. Duncan (2005), Explosive activity and generation mechanisms of pyroclastic flows at Arenal volcano, Costa Rica between 1987 and 2001, *Bull. Volcanol.*, *67*(8), 695–716, doi:10.1007/s00445-004-0402-6.

Donnadieu, F., G. Dubosclard, R. Cordesses, T. Druitt, C. Hervier, J. Kornprobst, J. F. Lénat, P. Allard, and M. Coltelli (2005), Remotely monitoring volcanic activity with ground-based Doppler radar, *Eos Trans. AGU*, *86*(21), 201, doi:10.1029/2005EO210001.

Donnadieu, F., S. Valade, and S. Moune (2011), Three dimensional transport speed of wind-drifted ash plumes using ground-based radar, *Geophys. Res. Lett.*, *38*, L18310, doi:10.1029/2011GL049001.

Dubosclard, G., F. Donnadieu, P. Allard, R. Cordesses, C. Hervier, M. Coltelli, M. Privitera, and J. Kornprobst (2004), Doppler radar sounding of volcanic eruption dynamics at Mount Etna, *Bull. Volcanol.*, *66*, 443–456, doi:10.1007/s00445-003-0324-8.

Gouhier, M., and F. Donnadieu (2008), Mass estimations of ejecta from Strombolian explosions by inversion of Doppler radar measurements, *J. Geophys. Res.*, *113*, B10202, doi:10.1029/2007JB005383.

Gouhier, M., and F. Donnadieu (2010), The geometry of Strombolian explosions: Insights from Doppler radar measurements, *Geophys. J. Int.*, *183*, 1376–1391, doi:10.1111/j.1365-246X.2010.04829.x.

Marchetti, E., M. Ripepe, A. J. L. Harris, and D. Delle Donne (2009), Tracing the differences between Vulcanian and Strombolian explosions using infrasonic and thermal radiation energy, *Earth Planet. Sci. Lett.*, *279*, 273–281, doi:10.1016/j.epsl.2009.01.004.

Patrick, M., A. Harris, M. Ripepe, J. Dehn, D. Rothery, and S. Calvari (2007), Strombolian explosive styles and source conditions: Insights from thermal (FLIR) video, *Bull. Volcanol.*, *69*, 769–784, doi:10.1007/s00445-006-0107-0.

Sauvageot, H. (1992), *Radar Meteorology*, 366 pp., Artech House, Boston, Mass.

Yamamoto, H., I. M. Watson, J. C. Phillips, and G. J. Bluth (2008), Rise dynamics and relative ash distribution in vulcanian eruption plumes at Santiaguito Volcano, Guatemala, revealed using an ultraviolet imaging camera, *Geophys. Res. Lett.*, *35*, L08314, doi:10.1029/2007GL032008.

F. Donnadieu and S. Valade, Laboratoire Magmas et Volcans, OPGC, Clermont Université, Université Blaise Pascal, 5 rue Kessler, F-63038 Clermont-Ferrand CEDEX, France. (s.valade@opgc.univ-bpclermont.fr)

Geophysical Research Letters

28 NOVEMBER 2011
Volume 38 Number 22
Articles published online
16 November – 30 November 2011
AGU American Geophysical Union

Observing volcanic ash plumes and ballistics using Doppler radar • Sea ice controls variability in microseismicity • Stratospheric ozone affects mesospheric temperature trends

RESEARCH SPOTLIGHT

Highlighting exciting new research from AGU journals

PAGE 28

Observing volcanic ash plumes and ballistics using Doppler radar

When volcanoes erupt, they often emit coarse rocks with ballistic trajectories that fall onto the slopes of the volcano, as well as a plume of fine ash that drifts into the atmosphere. It can be challenging to monitor both simultaneously and discriminate between the two to collect quantitative data, but *Valade and Donnadieu* have done that with a ground-based Doppler radar, which they used to make measurements of small-scale eruptions at Arenal volcano in Costa Rica. They were able to estimate the mass of the ballistic rocks and the mass of ash particles ejected into the atmosphere. Such studies could be useful for understanding and mitigating the hazards associated with volcanic eruptions. (*Geophysical Research Letters*, doi:10.1029/2011GL049415, 2011) —EB

Arabian Sea eddies promote seasonal phytoplankton blooms

In the Arabian Sea, two phytoplankton blooming periods occur each year, one during the winter northeast monsoon and one during the summer southwest monsoon. It has been established that on the large scale the spatial distribution of the seasonal blooms is driven by mesoscale structures, including eddies and filaments, but studies have not resolved the details linking the physical and biogeochemical processes involved. To improve understanding of mechanisms regulating blooms, *Resplandy et al.* studied the mesoscale process contribution to nutrient transport using a high-resolution physical circulation model. The model reproduces the seasonal phytoplankton blooms and shows how physical mesoscale processes such as eddies bring increased nutrient supply to the upper layer of the sea during monsoon seasons, thus promoting the growth of phytoplankton blooms twice a year. (*Journal of Geophysical Research-Oceans*, doi:10.1029/2011JC007006, 2011) —EB

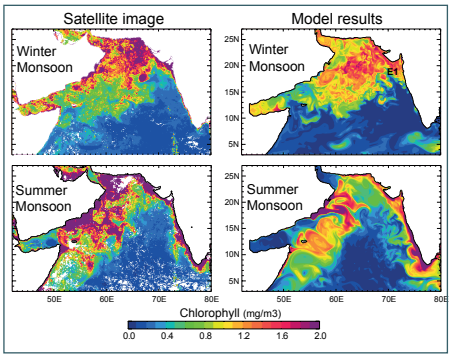

Monsoonal phytoplankton blooms of the Arabian Sea viewed by the ocean color satellite Sea-viewing Wide Field-of-view Sensor (SeaWiFS) and reproduced by a model used by Resplandy et al. *The bloom spatial distribution highlights the crucial role of mesoscale eddies and filaments in promoting the growth of phytoplankton. (Chlorophyll data are provided by the SeaWiFS Project and NASA's Distributed Active Archive Center.)*

Continued volcanic inflation at the Three Sisters

As early as the summer of 1996, a 20- × 30-kilometer patch of earth lying just west of the South Sister volcano in central Oregon began to rise. The Three Sisters volcanoes, which comprise North Sister, Middle Sister, and South Sister, are the most prominent peaks in that stretch of the Cascade Mountains, a landscape littered with the remnants of volcanic activity. Although there has not been an eruption in the region in at least 1200 years, the detected deformations caused concern, and the region was put under continuous monitoring. *Riddick and Schmidt*, continuing the work initiated by other researchers, report on 14 years of satellite-based monitoring, describing the variable rate of the ground's movements and the likely cause of the activity—a sizeable magma intrusion lying 5–7 kilometers underground.

Drawing data from the European Space Agency's European Remote Sensing (ERS) and Envisat radar satellites, the authors found that the terrain deformation went through three distinct phases since its onset. From 1996 to 1998 the ground rose by 1 centimeter per year. The uplift rate rose to 3–4 centimeters per year between 1998 and 2004, then declined to only a few millimeters per year for the rest of the decade, resulting in a total of 25 centimeters of uplift to date. Analyzing the topographic changes led the researchers to suggest that the previously hypothesized magmatic intrusion had a volume of between 50 million and 70 million cubic meters. Whether the uplift is the indication of an imminent eruption depends on whether it is a standalone event or part of a series of similar intrusions, a question that can only be answered through continued monitoring. (*Geochemistry, Geophysics, Geosystems*, doi:10.1029/2011GC003826, 2011) —CS

Internal tides observed to be coherent in shelf sea

Internal tides, waves with tidal frequencies below the ocean's surface, contribute to ocean mixing. They are common in shelf seas, shallow marginal seas located on the continental shelf. These tides are believed to be coherent over hundreds of kilometers before they decay, but spatial coherence of internal tides had not been observationally confirmed in shelf seas. *Inall et al.* conducted in situ observations of internal tides over the continental shelf of the Celtic Sea. They found that the internal tide was coherent over more than 170 kilometers, about five wavelengths. The observations, which provide the first in situ evidence of internal tide coherence over multiple wavelengths in a shelf sea, could be useful for improving models of mixing in shelf seas. (*Geophysical Research Letters*, doi:10.1029/2011GL049943, 2011) —EB

—Ernie Balcerak, Staff Writer, and Colin Schultz, Writer

Appendix F. *Donnadieu, Valade and Moune,* 2011

Donnadieu, F., S. Valade, and S. Moune (2011), Three dimensional transport speed of wind-drifted ash plumes using ground-based radar, *Geophys. Res. Lett.*, 38, L18310, doi:10.1029/2011GL049001.

Three dimensional transport speed of wind-drifted ash plumes using ground-based radar

Franck Donnadieu,[1,2,3] Sébastien Valade,[1,2,3] and Séverine Moune[1,2,3]

Received 21 July 2011; revised 31 August 2011; accepted 31 August 2011; published 27 September 2011.

[1] The main utilization of mobile ground-based Doppler radars is to quantify the dynamics of eruptive activity by aiming directly at the emission source. We show that they can also provide information on the initial lateral transport speed of weak ash plumes bent over by crosswind. The method is illustrated by measurements made with a transportable volcano Doppler radar (VOLDORAD) at Arenal volcano, Costa Rica. The near-source displacements of the plume are tracked through echo onsets induced by ash entering successive probed volumes in the radar beam. A constant transport velocity is commonly reached within a few seconds of the initial ash emission, as wind advection and buoyancy take over momentum. The plume azimuth and upraise angles are constrained by comparing the amplitude decrease of the radar echoes as a function of distance from the source with results from a simple geometric plume model. The three dimensional vector of the ash cloud transport speed is then reconstructed with an accuracy of a few percent. This method may have applications for volcano monitoring, for determining pyroclast fluxes, for the modeling of tephra dispersal, and for remote measurements of volcanic gas fluxes. **Citation:** Donnadieu, F., S. Valade, and S. Moune (2011), Three dimensional transport speed of wind-drifted ash plumes using ground-based radar, *Geophys. Res. Lett.*, *38*, L18310, doi:10.1029/2011GL049001.

1. Introduction

[2] Volcanic ash clouds, even moderate sized ones, can cause direct hazards to aviation as well as severe economic costs, as recently highlighted by the 2010 Eyjafjöll eruption in Iceland. Subsequent ash fallout may also adversely affect the surrounding population and infrastructures. Tracking of large ash clouds is mainly carried out by means of satellite imagery or by ground-based weather radars. Processed satellite data can be used to obtain maps of the eruptive cloud extension (at intervals of 15mn to several hours), the mass of SO_2, and the concentration and sizes of distal particles. Powerful weather radars, because they operate continuously at a minute-scale acquisition rate, and in all weather, have been used to track the path of large ash clouds [e.g., *Harris and Rose*, 1983; *Rose et al.*, 1995; *Lacasse et al.*, 2004; *Marzano et al.*, 2011]. Scanned reflectivity maps indicate the height and extension of the plume (within the limit of the radar sensitivity), and mass estimates of distal ash can be derived. However, weather radars can only scan large ash plumes within a few hundred kilometers of their fixed location, and often the base of the plume cannot be imaged; thus initial information on the characteristics of the ash plume is generally missing. More recently, dedicated transportable Doppler radars with higher temporal and spatial resolutions have been used with the primary goal of studying eruption dynamics [e.g., *Seyfried and Hort*, 1999; *Dubosclard et al.*, 2004; *Donnadieu et al.*, 2005]. Since they are set up at a chosen location, these radars can also monitor short-lived weak ash plumes, sound the gas thrust region and provide source eruptive parameters such as initial velocities [*Donnadieu et al.*, 2005] and mass fluxes [*Gouhier and Donnadieu*, 2008, 2011].

[3] In this paper, we show that they can also provide insights into the dynamics of ash plumes bent-over by crosswinds in the transition region between gas-thrust and lateral spreading, when the beam is wide enough compared to the plume dimensions to capture the bending region. In particular, the 3-D drift speed of ash plumes entrained by wind advection can be retrieved, based on the detection of volcanic ash in beam volumes successively sampled by the radar wave and simple geometric models. The method is illustrated by results obtained from a pulsed Doppler radar on weak ash plumes at Arenal volcano, Costa Rica. Applications for volcano monitoring, estimation of pyroclastic fluxes, remote gas flux measurements, and tephra dispersion models are discussed, along with the limitations of the method.

2. Data Acquisition

[4] Data presented in this study have been collected from Arenal volcano, Costa Rica, using VOLDORAD 2, a compact analog of the first ground-based pulsed VOLcano DOppler RADar successfully used at Mount Etna [*Dubosclard et al.*, 2004]. There is very little signal attenuation by hydrometeors at the operating wavelength of 23.5 cm, which enables volcanic particles in the plume to be detected even in overcast weather. Its all-weather operation capacity, along with its variable range of operation (0.3–11 km), make it an efficient tool both for volcano monitoring and for detailed investigations of ash plume dynamics [*Donnadieu et al.*, 2005]. As released volcanic particles cross the beam aimed at the volcano summit, they backscatter some of the energy transmitted by the radar. Echoes are received back with delay times, which increase from transmission due to the two-way distance run by each wave. Thus the sampled time series corresponds to volumes ("range gates") which are successively probed from further inside the beam (Figure 1).

[5] During the period of February 10–22, 2005, the diurnal explosive activity of Arenal volcano, consisting of discrete, weak ash plumes bent over by a crosswind was recorded. Bad weather often prevented direct observations, but these plumes

[1]Clermont Université, Université Blaise Pascal, OPGC, Laboratoire Magmas et Volcans, BP 10448, Clermont-Ferrand, France.
[2]CNRS, UMR 6524, LMV, Clermont-Ferrand, France.
[3]IRD, R 163, LMV, Clermont-Ferrand, France.

0094-8276/11/2011GL049001

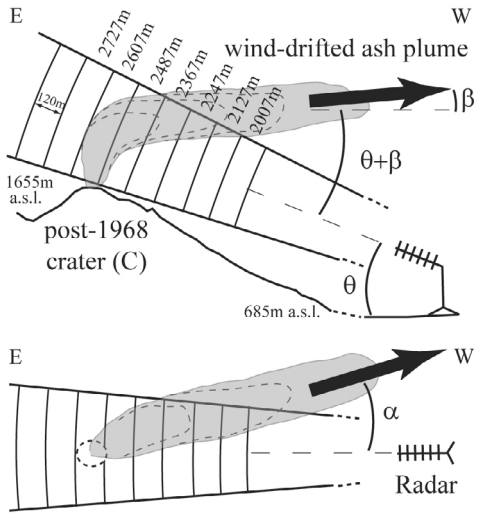

Figure 1. Sketches of the radar sounding at Arenal in (top) section and (bottom) aerial view showing the path of the ash cloud sampled in successive volumes of the radar beam. Whenever the wind direction has a significant along-beam component, the range gates enable the early tracking of the ash cloud displacements through time, providing an estimate of its lateral transport speed. The 3-D transport speed is determined from the plume upraise angle (β) and azimuth relative to the radar (α) obtained by best fitting the echo power from 3-D plume geometrical models to data in all range gates. The antenna beam elevation angle θ is 27°.

commonly reached a few hundred meters in height and were released over a period of seconds to a few tens of seconds. The radar was set up at an elevation of 685 m a.s.l., 2.6 km (slant distance) to the west, downwind of and ca. 1000 m below Arenal's active crater (C). Data were acquired at ~12 Hz in 11 range gates between 2 and 3 km from the radar. The resolution was 120 m along-beam for all range gates, and 410 m in azimuth and elevation for the 2607 m range gate where most of the activity was initially recorded. The antenna elevation angle (θ = 27°) enabled the main lobe of the radar beam to hit the top of the cone (Figure 1) and the antenna aperture (9°) was enough to capture the bending of the plume to the WSW due to wind activity. In this way, ash plume displacements could be recorded through up to 7 range gates (>720 m) before they passed beyond the beam, along with their dynamics right above the emission source.

3. Methodology

3.1. Radar Signals

[6] Whenever an ash plume forms, volcanic particles cross the antenna beam above the eruptive vent and backscatter some energy to the radar. As the ash plume is pushed by the wind, its front successively enters the sampled volumes downwind and causes power echoes to appear in succession. Meanwhile, the plume body still produces echoes in the previous range gates. Figure 2a shows typical power echoes from an ash plume at Arenal. Echoes are first recorded in the range gate above the eruptive vent at 2607 m distance slantwise, and then in 5 more gates down to 2007 m, as the ash plume was bent over by the wind and drifted towards the WSW. Strong ash emissions commonly exhibit a relatively sudden signal onset in the range gate located above the eruptive vent, reaching their maximum amplitude (signal-to-noise ratio up to 10^3) in a matter of seconds, and then follow a more gentle decrease over ca. one minute. For this type of event, the ash release may last for several tens of seconds and radial velocities are generally low (<25 m/s).

3.2. Along-Beam Ash Plume Displacements

[7] An average value of the along-beam speed component of the drifted ash can easily be obtained from the slope of the radial displacements versus the power onset times in the

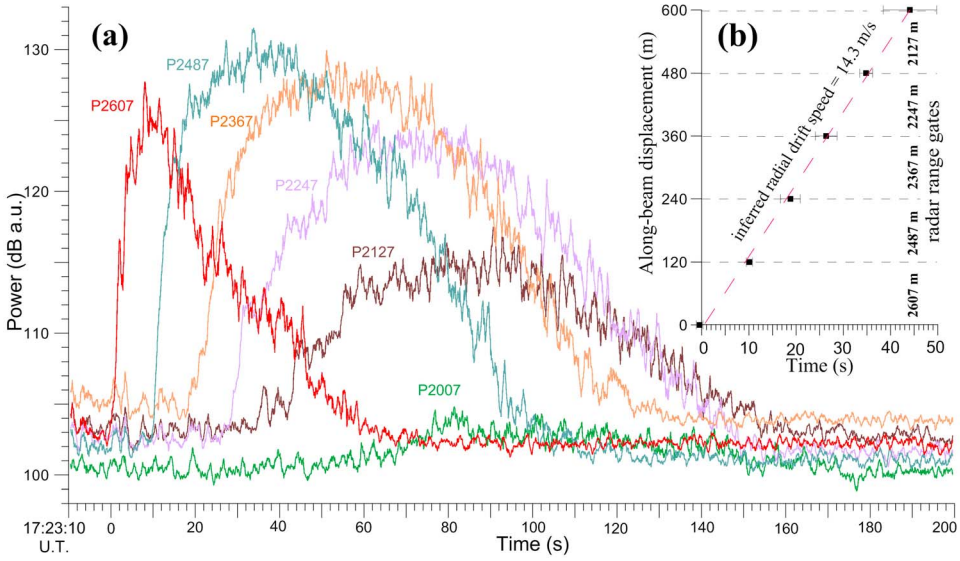

Figure 2. (a) Power amplitude (dB Log scale, arbitrary units) recorded as the wind-advected ash plume crosses 6 successive beam volumes probed by the radar (Arenal, 11/02/2005, 17:23′20 UT). (b) Onset times of ash plume detection in each range gate (120 m radial resolution). The slope of the linear data fit gives the along-beam component of the ash plume transport speed (14.3 m/s, R^2 = 0.99).

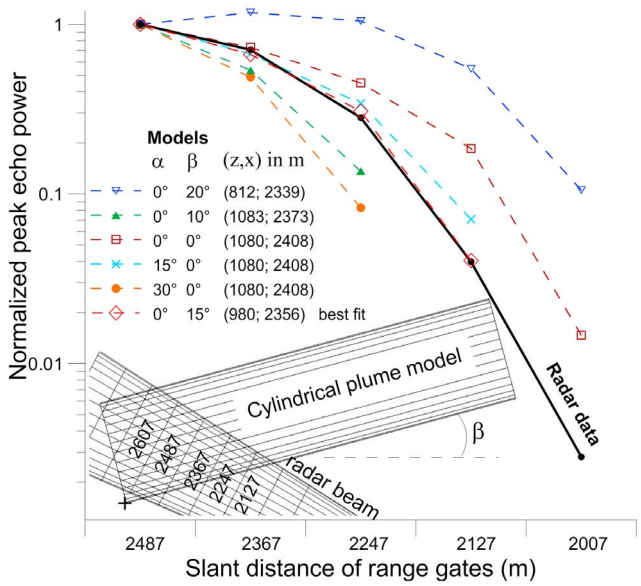

Figure 3. Normalized peak echo power from radar probed volumes crossed by the plume (distance corrected). Black curve is radar data measured on ash plume at Arenal on February 11 2005, at 17:23 UT (Figure 2). Dashed curves are models of cylindrical plume (200 m in radius) with varied azimuth and upraise angles (α, β). A section of the best-fit 3D model is shown as an inset (α = 0°, β = 15°). The cylinder base is positioned by coordinates (x, z) relative to the radar.

successive range gates. Ash plume along-beam displacements with time commonly follow a linear trend, indicative of a constant transport velocity (14.3 m/s, Figure 2b). This suggests that buoyancy and wind entrainment take over momentum within a few seconds (<10 s) of the initial ash release, and is consistent with the low initial radial velocities recorded (<20 m/s). The data point from the first range gate (2607 m) sometimes departs from the overall trend and should not be used in the determination of the drift speed since the plume dynamics and geometry are still controlled by vent location and exit conditions. Slightly concave-upward trends of radial displacements versus time are sometimes observed; they probably reflect an increase in the angle of the plume bending, hence a shorter path through the range gates away from the source, as the wind drag progressively overwhelms the plume buoyancy and residual momentum.

[8] We analysed 8 events with this method and radial components of ash transport speed lie between 6.1 m/s and 15.2 m/s, which is consistent with ordinary wind velocities at the ash cloud altitude (~2 km a.s.l.), for which they also provide a lower limit. At this stage, errors on radial speed values (slope of data fit) range from 3 to 10% as a result of the difficulty in picking onset times when the signal becomes more emerging in the farthest range gates.

3.3. Transport Speed of 3-D Ash Plume

[9] The three-dimensional transport speed of the ash cloud u_{ash} can be inferred from the sounding geometry and plume direction, and from the transit time Δt (interval between signal onsets) in the successive range gates:

$$u_{ash} = \frac{c\tau}{2\Delta t} \times \frac{1}{\cos(\theta + \beta)\cos\alpha} \quad (1)$$

where $c\tau/2$ is the range gate radial resolution, θ the beam elevation angle (27°), β and α the ash cloud elevation and azimuth angles respectively (Figure 1). The first term in equation (1) represents the radial (along-beam) speed component of the drifted ash determined previously. Below we show how to deduce α and β in the second term.

[10] As observed in Figure 2a, radar signals tend to flatten out and decrease in amplitude with distance from the emission source. The relative power backscattered by the volumetric fraction of the ash plume within each range gate can be modeled using simple 3-D geometric shapes to simulate the plume path. By assuming comparable particle concentrations and sizes among the sampled volumes, and compensating for the effect of distance on the radar signal amplitude, the relative variations of the intersection volumes between the beam range gates and the plume are equivalent to relative variations in echo power. Values are thus normalized to the intersection volume of the 2487 m range gate, having the maximum amplitude (most filled), and compared to the normalized radar power from range gates downwind. Since our objective is to simulate the plume path once it is bent over, the beam filling by the plume in the range gates above the vent and upwind is not considered. Although more sophisticated shapes, for example a reversed funnel progressively bending downwind, could provide better matches for the data in the range gates above the vent, only cylinders are shown because they are quicker to fit and therefore more widely applicable for monitoring purposes. In Figure 3, the normalized power is modeled using a cylindrical plume path for various combinations of α and β and cylinder positions above the vent. The diameter of the cylinders (400 m) was chosen in agreement with common heights observed for ash plumes at Arenal. Since a cylindrical shape does not reproduce plume bending, the modeled plume may exit the beam without intersecting the farthest sampling volumes. Yet, because the plume and beam intersection volumes decrease dramatically downwind with increasing values of α and β, the plume azimuth and upraise angles can still be well constrained. In the case of Figure 3, both angles amount to <15°, with a good fit for $\alpha = 0°$ and $\beta = 15°$. Using equation (1), the three dimensional vector of the ash plume transport speed (19.2 m/s for the event in Figures 2 and 3) can then be reconstructed from the values of α and β with an accuracy of a few percent.

[11] Figure 3 also suggests that the decrease in power amplitude within the first few hundred meters from the vent is dominantly controlled by the progressive exit of drifted ash from the probed volumes, rather than by fallout. This may indicate that, for this type of event, the initial plume emission essentially comprises fine material (ash size) and lacks ballistics.

4. Potential Applications

4.1. Implications for Monitoring and Modeling of Tephra Dispersal

[12] The early detection and evaluation of the transport direction and speed of an ash plume may improve risk assessment in real-time, particularly for the prediction of areas likely to be affected by ash fallout, and for the early release of alerts. For instance, the along-beam speed component of the drifted ash determined directly from echo onsets, can be used as a minimum transport speed for quickly estimating plume impact times at given locations even without precise knowledge of the plume trajectory parameters.

[13] Another possible outcome is, importantly, the estimation of the mass flux of tephra and its temporal evolution. Firstly, tephra mass could be derived from radar power time series (as in Figure 2a) by inversion [*Gouhier and Donnadieu*, 2008]. Then, using the ash plume transit time through the radar beam, the mass curve could be integrated through time to obtain the mass flux evolution. Although this requires assumptions on an average particle size (e.g. from analysis of previous similar events) and unchanged plume bending, the mass flux of tephra is a key parameter needed for plume monitoring and modeling. For long-lasting ash emissions, mass fluxes could be refined repeatedly, possibly within hours, as field observations of particle size distribution are made available.

[14] The quantitative estimates from the radar of the kinetic [*Donnadieu et al.*, 2005; *Gouhier and Donnadieu*, 2011] and loading parameters [*Gouhier and Donnadieu*, 2008] could feed volcanic ash transport and dispersion (VATD) models in quasi real-time to help in the assessment of the fallout impact in terms of timing and quantity on nearby areas. Besides, such eruptive parameters, inferred from ground-based Doppler radars measurements near the emission source with high temporal and spatial resolutions, can also complement ash cloud tracking by satellite imagery.

4.2. Improving Accuracy of Gas Flux Measurements by Remote Spectroscopy

[15] Uncertainties on the plume velocity constitute the main source of error in volcanic gas flux measurements by miniature UV spectrometers (DOAS, FLYSPEC) or correlation spectrometers (COSPEC) [e.g., *Gerlach et al.*, 1997]. Wind-based methods traditionally used to obtain a proxy for the plume transport speed, such as ground-based anemometers, provide poor estimations of the true velocity and introduce large flux errors, potentially exceeding 100% [*McGonigle et al.*, 2005]. This is because the wind speed at the plume height can differ significantly from that measured on the ground. Moreover, ash cloud transport speeds may differ from the wind velocity at the altitude of the ash cloud, due to the inertia induced by particle loading [e.g., *Graf et al.*, 1999].

[16] When detectable ash is present (cf. Section 5), transportable high-sensitivity radars like VOLDORAD can provide the real plume transport speed in 3-D with greater accuracy. This could help to reduce errors on gas fluxes down to a few percent, especially when an optimum device number or configuration cannot be achieved. In addition, measurements with a single instrument are often made (i) vertically, assuming horizontal plume motion and thus neglecting a possible plume upraise angle β, and (ii) along existing roads or pathways, not always strictly orthogonal to the plume azimuth α. Thus, accuracy can be improved by correcting for the angle components (α and β) of the transport speed determined by our method. Moreover, the particle concentration in the radar sampling volumes [*Gouhier and Donnadieu*, 2008] might also help to quantify errors on gas and aerosols measurements (e.g. SO_2) due to the ash content increasing UV absorption [e.g. *Andres and Schmid*, 2001].

5. Limitations of the Method

[17] Inaccurate estimates of ash cloud transport speeds will result if the chosen plume geometry strongly diverges from the simple model shape chosen, if plume bending changes with time, or if sedimentation from the ash plume within the first hundred meters has a non-negligible influence on the measured power evolution with distance. The accuracy of u_{ash} decreases as the ash cloud drift becomes very oblique to the beam because (i) the error propagated from α and β increases, (ii) ash is detected in fewer range gates, making data fitting more sensitive to errors on individual data points, and (iii) data are more difficult to match by simple geometric models if only the most bent-over part of the plume trajectory is captured, hence there are less constraints on α and β. However, an estimate of α can be readily estimated in the field from the approximate wind direction. Transport velocity estimates by this method will be made difficult, or even impossible, in the following cases: (i) side wind is null or blows normal to the beam, (ii) the bending region has a strong upward component or is above the beam (e.g. strong vertical plumes), (iii) degassing involves little or no ash. For instance, 1 mm ash particles with a concentration inferior to 15 g/m^3 would remain undetected by our radar in this sounding configuration. For dilute plumes, the transport speed retrieval method could be applied even more efficiently using shorter wavelength radars, as these have generally a higher sensitivity to fine ash particles.

6. Conclusions

[18] In most cases, a single ground-based radar can ensure the accurate determination of the 3-D vector of the transport speed of wind-drifted ash plumes, using transit times in radar sampling volumes and simple geometrical models. This method may have applications for volcano monitoring, for determining tephra mass fluxes, for the modeling of tephra dispersal and for reducing errors on gas flux measurements. Besides, Doppler radar measurements could also help to constrain the transition from the momentum-controlled ash plume dynamics close to the source to its bending and lateral spreading brought about by wind advection. For this purpose, further modeling on the effects of wind advection on weak plumes, e.g. a continuation of *Bonadonna et al.* [2005], is also needed.

[19] **Acknowledgments.** We are indebted to C. Hervier, T. H. Druitt and M. Gouhier for assistance in the field, and to A. Clenet, L. Pouchol and R. Doucelance for help in data processing. Facilities for radar soundings were kindly provided by the Universidad de Costa Rica, ICE and Arenal National Park. Particular thanks are due to M. Mora, G. Alvarado, L.-F. Brenes, F. Arias and C. Ramirez. Funding by the ACI Risques Naturels program of the French CNRS-INSU. We thank Dave Schneider for his review and Ruth Harris for handling the manuscript.

[20] The Editor thanks the anonymous reviewers for their assistance in evaluating this paper.

References

Andres, R. J., and J. W. Schmid (2001), The effects of volcanic ash on COSPEC measurements, *J. Volcanol. Geotherm. Res.*, *108*(1–4), 237–244.

Bonadonna, C., J. C. Phillips, and B. F. Houghton (2005), Modeling tephra sedimentation from a Ruapehu weak plume eruption, *J. Geophys. Res.*, *110*, B08209, doi:10.1029/2004JB003515.

Donnadieu, F., G. Dubosclard, R. Cordesses, T. H. Druitt, C. Hervier, J. Kornprobst, J.-F. Lénat, P. Allard, and M. Coltelli (2005), Remotely monitoring volcanic activity with ground-based Doppler radar, *Eos Trans. AGU*, *86*(21), 201, doi:10.1029/2005EO210001.

Dubosclard, G., F. Donnadieu, P. Allard, R. Cordesses, C. Hervier, M. Coltelli, E. Privitera, and J. Kornprobst (2004), Doppler radar sounding of volcanic eruption dynamics at Mount Etna, *Bull. Volcanol.*, *66*(5), 443–456, doi:10.1007/s00445-003-0324-8.

Gerlach, T. M., H. Delgado, K. A. McGee, M. P. Doukas, J. J. Venegas, and L. Cárdenas (1997), Application of the LI-COR CO_2 analyzer to volcanic plumes: A case study, Volcán Popocatéptl, Mexico, June 7 and 10, 1995, *J. Geophys. Res.*, *102*(B4), 8005–8019, doi:10.1029/96JB03887.

Gouhier, M., and F. Donnadieu (2008), Mass estimations of ejecta from Strombolian explosions by inversion of Doppler radar measurements, *J. Geophys. Res.*, *113*, B10202, doi:10.1029/2007JB005383.

Gouhier, M., and F. Donnadieu (2011), Systematic retrieval of ejecta velocities and gas fluxes at Etna volcano using L-band Doppler radar, *Bull. Volcanol.*, in press, doi:10.1007/s00445-011-0500-1.

Graf, H.-F., M. Herzog, J. M. Oberhuber, and C. Textor (1999), Effect of environmental conditions on volcanic plume rise, *J. Geophys. Res.*, *104*(D20), 24,309–24,320, doi:10.1029/1999JD900498.

Harris, D. M., and W. I. Rose Jr. (1983), Estimating particle sizes, concentrations, and total mass of ash in volcanic clouds using weather radar, *J. Geophys. Res.*, *88*(C15), 10,969–10,983, doi:10.1029/JC088iC15p10969.

Lacasse, C., S. Karlsdóttir, G. Larsen, H. Soosalu, W. I. Rose, and G. G. J. Ernst (2004), Weather radar observations of the Hekla 2000 eruption cloud, Iceland, *Bull. Volcanol.*, *66*, 457–473, doi:10.1007/s00445-003-0329-3.

Marzano, F. S., M. Lamantea, M. Montopoli, S. Di Fabio, and E. Picciotti (2011), The Eyjafjöll explosive volcanic eruption from a microwave weather radar perspective, *Atmos. Chem. Phys. Discuss.*, *11*, 12,367–12,409, doi:10.5194/acpd-11-12367-2011.

McGonigle, A. J. S., S. Inguaggiato, A. Aiuppa, A. R. Hayes, and C. Oppenheimer (2005), Accurate measurement of volcanic SO_2 flux: Determination of plume transport speed and integrated SO_2 concentration with a single device, *Geochem. Geophys. Geosyst.*, *6*, Q02003, doi:10.1029/2004GC000845.

Rose, W. I., A. B. Kostinski, and L. Kelley (1995), Real time C band radar observations of 1992 eruption clouds from Crater Peak/Spurr Volcano, Alaska, *U.S. Geol. Surv. Bull.*, *2139*, 19–26.

Seyfried, R., and M. Hort (1999), Continuous monitoring of volcanic eruption dynamics: A review of various techniques and new results from a frequency-modulated radar Doppler system, *Bull. Volcanol.*, *60*, 627–639, doi:10.1007/s004450050256.

F. Donnadieu, S. Moune, and S. Valade, Laboratoire Magmas et Volcans, Clermont Université, Université Blaise Pascal, OPGC, BP 10448, F-63000 Clermont-Ferrand, France. (f.donnadieu@opgc.univ-bpclermont.fr)